THE ALPHA FOUNDATION FOR THE IMPROVEMENT OF
MINE SAFETY AND HEALTH

Collecting Mine Dust Particles with Liquid-Coated Vibrating Meshes
Final Report

Alpha Foundation Grant Number:
AFC-518SP-89

Organization:
Virginia Tech,
Blacksburg, VA 24061-0001

Principal Investigators:
Aaron Noble || Virginia Tech || 865-250-0498 || aaron.noble@vt.edu
Sunghwan Jung || Cornell University || 607-255-5798 || sunnyjsh@cornell.edu
Lei Pan || Michigan Tech || 906-487-2569 || leipan@mtu.edu
Shima Shahab || Virginia Tech || 540-231-6516 || sshahab@vt.edu
Hassan Amini || West Virginia University || 859-536-3295 || hassan.amini@mail.wvu.edu

Period of Performance:
October 1, 2019 through May 31, 2023

Table of Contents

1. Executive Summary

Over the last 20 years, the flooded bed dust scrubber has been an integral component of dust control strategies for underground continuous mining operations. These units have been shown to be effective and robust in mining environments; however, several technical challenges and knowledge gaps limit their performance and efficiency. Most significantly, the filter mesh can easily be clogged, which leads to reduced cleaning capacity and frequent maintenance. This issue is further amplified given the natural tradeoff between mesh fineness, dust capture efficiency, and sustained air flow rate.

The objective of this project was to develop, design, and test a novel flooded bed dust scrubber that mitigates these operational issues while improving overall dust capture. The key to the technical approach is the integration of controlled vibration to the filter mesh. The vibration not only provides a larger effective wetted area to increase dust capture, but it also provides a self-cleaning mechanism that sheds clogged particles and sustains high air flow rates. Our prior studies verified the critical functions of this approach in a laboratory setting, and the current project seeks to further mature the technology, through testing of a full-scale prototype in a high-fidelity simulated environment.

To support the development of the prototype, several modeling, laboratory-scale, and field studies were conducted. Computational fluid dynamics modeling was used to investigate the influence of mesh vibrational properties with performance indicators such as mesh wetted area, number of droplet-particle contacts, and predicted collection efficiency. These results provided bounds on the optimal vibration conditions later validated in laboratory and prototype testing. In addition, laboratory-scale mesh clogging tests showed that a hydrophilic mesh provided superior clogging mitigation and better performance.

To implement the vibrating mesh concept, we investigated the feasibility of an innovative energy harvesting approach, whereby the necessary mesh vibrations are supplied by capturing and translating the natural vibrations of the continuous miner during operation. Working with a bituminous coal mine in West Virginia, the team collected vibrational data from an operating continuous miner. The data showed that the characteristic frequencies were consistent between operating modes, suggesting that a robust solution is feasible. Multiphysics modeling and laboratory testing showed how these vibrations could be translated to the filter mesh through the design of an elastic housing with a controlled spring constant.

Technology evaluation was conducted in two phases: laboratory-scale testing with a bench-scale (6 inch x 6 inch cross section) scrubber system and high-fidelity testing with a full-scale prototype. Both cases utilized experimental design techniques and several analytical methods to fully investigate the parameters influencing scrubber performance. Of note, high-speed videography provided direct observations of particle-droplet behavior, which may be leveraged in future scrubber designs. Data from the bench-scale testing largely confirmed the benefits of the project technology, with the vibrating mesh outperforming the static mesh in every configuration tested. Typical results showed nearly a 10% increase in dust collection efficiency with as much as a 40% reduction in clogged mass. The prototype testing was less conclusive, with deviations between the static mesh and vibrating mesh depending on the mesh density and operating conditions. Nevertheless, under the highest mesh density (30-layer), the vibrating mesh notably outperformed the static mesh with superior collection efficiency and reduced air flow loss.

Altogether, this project has successfully scaled the technology from the proof-of-concept stage to the engineering prototype stage. Future technology efforts should focus on the design and construction of a mine-worthy retrofit unit to provide operational performance data and mechanical stress testing.

2. Technology Description and Mission Statement

2.1. Background Information

Dust is an inherent byproduct of any mining activity. In particular, dust particulates less than 10 microns raise notable health and safety concerns. In coal mining, concentrated airborne dust can generate explosive mixtures that are easily ignited and self-propagating, and the inhalation of small, respirable dust particles can cause incurable lung diseases, including silicosis and coal worker's pneumoconiosis. Mine operators have typically employed preventative particle-collecting devices in underground mines to suppress airborne dust, and Mine Safety and Health Administration's (MSHA) 2014 respirable dust rule mandates even further reductions to respirable dust concentrations.

The flooded-bed scrubber (depicted in Figure 1) has been developed and widely used for over 20 years as a preventative dust remover in continuous mining operations and has been recently tested on longwall shearers. Despite the proficiency and prevalence of the scrubber, four technical key challenges limit overall performance and operability:
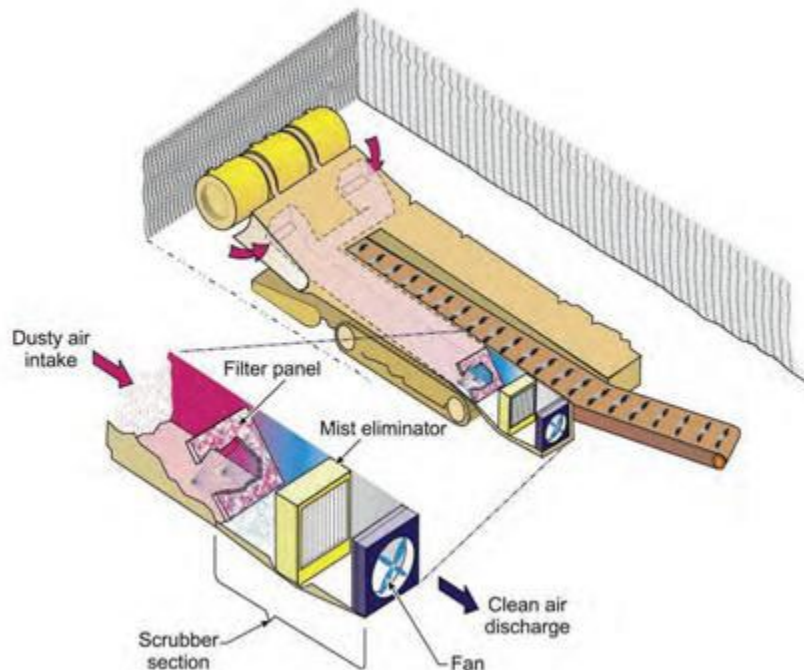
Figure 1. Schematic of flooded bed dust scrubber mounted on a continuous miner. (NIOSH, 2010)

- First, a filter mesh easily gets clogged as dust-laden air flows through. Clogging is a very common problem in stationary porous membranes or filters as they capture dust particles. Moreover, fouled regions become hydraulically overloaded, which significantly reduces the efficiency of dust collection and air flow speed. Therefore, removing particles from clogged regions is necessary to enhance the overall efficiency of dust removal.
- The second challenge is a tradeoff between mesh fineness and air flow rate. Free hole areas (FHA) are defined as a total clear area of a filter panel for air to pass through. In general, the air flow rate

4

through a porous material depends on FHA and the pressure drop, as expressed in Darcy's law. As the filter mesh gets closely packed, the flow rate is decreased. Hence, to maintain a certain flow rate, coarse filter meshes should be used, but the coarse meshes cannot capture the particles effectively.

- Third, poorly wetted areas allow unfiltered dust-laden air to pass through. Adhesion between liquids and silica particles is a key mechanism to hold particulate liquid droplets in the flooded-bed scrubbers. If some regions in the filter do not have moisture or liquid interfaces, the dust particles likely slide through the mesh because the attractive Van der Waals force between the mesh and coal/silica particles is an order of magnitude weaker than the force between the liquid interface and dust particles.

- Finally, the attractive force between fluid interface and particles should be optimized. When mine dust particles get close to a fluid interface on a filter, short-range force plays an important role in controlling a number of particles and stability of particles on the interface. By modifying the attraction strength of the liquid interface, more particles will be captured and held in close proximity.

2.2. Mission Statement

Based on these challenges, the overall goal of the current project was to design, develop, and test a working prototype of an improved flooded bed dust scrubber that can simultaneously increase dust capture and mitigate clogging potential. The team's approach was primarily based on the use of a vibrating, rather than a static, filter mesh in the dust scrubber system. Fundamentally, a vibrating mesh screen has the capacity to capture more particles by creating a larger effective surface area, thus encouraging a greater number of water-particle interactions. Figure 2 shows this phenomenon as a simplified cartoon.
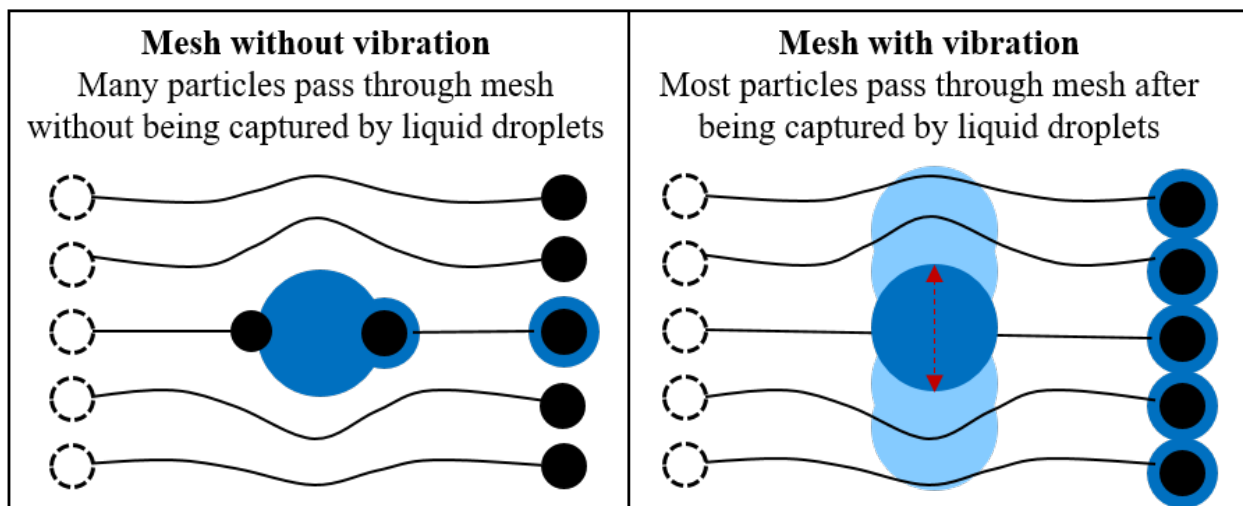

Figure 2. Principles of liquid-coated vibrating meshes in improving the collection efficiency in flooded-bed scrubber.

In a prior proof-of-concept study (AFC-518-25), the project team investigated this concept and found that the addition of a vibrating mesh panel could improve dust collection efficiency over that of a static unit. This work was primarily conducted at the laboratory scale, yielding a technology readiness level (TRL) of 3[1]. Given those findings, the current project sought to continue the technology maturation to a TRL level of 5-6[2] through the detailed design and testing of a prototype scrubber unit in a high-fidelity simulated environment, namely the NIOSH Dust Gallery. To facilitate the prototype design, the team first constructed a laboratory bench-scale scrubber whereby detailed testing could provide the engineering and optimization data needed for scale-up. In addition, laboratory studies, multi-physics modeling, and high-speed videography also supported the research effort by characterizing key operational parameters and providing design specifications.

In addition to the scrubber development, the team investigated the feasibility of an energy harvesting technique whereby the vibration of an operating continuous miner could be a suitable source of vibrational energy for the filter mesh. As depicted in Figure 3, an elastic foundation of known spring constant can be used to transmit the system vibration to the mesh. The vibrational energy transmitted to the mesh can thus be controlled by proper selection of the spring constants of the elastic foundation. To evaluate this hypothesis, the team first collected field data from an operating continuous miner, and through both modeling and experimentation identified a range of spring constants that properly transmitted the optimal vibrational frequencies. This vibrational translation concept was also evaluated through the high-fidelity testing campaign.
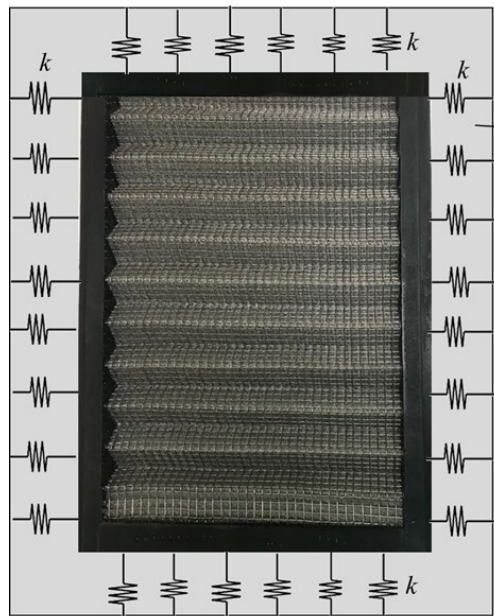
Figure 3. Conceptual design of a scrubber mesh secured to a spring housing.

---

[1] TRL 3 = Analytical and experimental critical function and/or proof-of-concept validated. TRL Definitions provided at: https://www.directives.doe.gov/directives-documents/400-series/0413.3-EGuide-04a-admchg1/@@images/file.
[2] TRL 5 = Basic technology components integrated and validated in a relevant environment. TRL 6 = Prototype validated in a relevant environment.

3. Technology Description and Design Strategy

3.1. In-Mine Vibration Measurements

3.1.1. Motivation

During this project, the team conducted a systematic computational numerical modeling study and laboratory-scale particle shedding experiments to determine appropriate vibration frequencies for maximizing mesh wetted area and dust collection efficiency while minimizing mesh clogging. According to the results of these efforts (see section 3.2, 3.3, and 4.2), vibrations of the filter mesh in the range of 100 to 1000 Hz provided the maximum wetted area (i.e., dust collection) and minimum clogging. While our laboratory tests often use an externally-supplied vibration source, this approach is likely to be infeasible or prohibitive in a mine-setting due to operational and permissibility constraints. As an alternative approach, the project team proposed a novel vibration-based mechanical energy harvesting system. The proposed energy harvesting system captures the pre-existing natural vibration energy of the continuous miner (input vibration) and translates/alters it into the optimal ranges of frequency and amplitude most proper for dust particle capturing and minimum particle clogging (output vibration).

To evaluate the feasibility of this approach, the team conducted a systematic in-mine vibration measurements of an industrial-scale, operating continuous miner under various operating conditions and modes. The project team then utilized raw time-domain acceleration data and performed a detailed vibration data analysis to identify the steadiest vibration frequency levels that may continuously provide the necessary energy for the optimal secondary vibration of the mesh panel. The remaining elements of this subsection describe the team's approach for in-mine vibration measurements and comprehensive data analysis.

3.1.2. Literature Review

3.1.2.1. Background

Very few published studies have provided detailed assessments of the vibrational energy on operating continuous. One notable exception, though, is a technical report provided by Fuchs (1979), which was the primary focus of an initial literature survey. The main objective of this task was to identify and document the acceleration and frequency relationship of continuous miners when they are working under different operating conditions. The data was subsequently used in laboratory experiments as input parameters in the proposed energy harvesting approach to see the possible contribution of the vibrating wet mesh panels to the scrubber collection and capture efficiencies. It was also useful for determining the appropriate material properties of mesh foundation which is necessary for obtaining the optimal vibration characteristic to achieve maximum collection efficiency and minimum clogging rate.

The Fuchs (1979) report shares data of an extensive study in which the team found the vibration acceleration data of various mining machines including four different underground continuous miners. In this report, the researcher utilized accelerometers to measure the vibrational acceleration at different locations of these machines. Figure 4 demonstrates the approximate location of data collecting points.
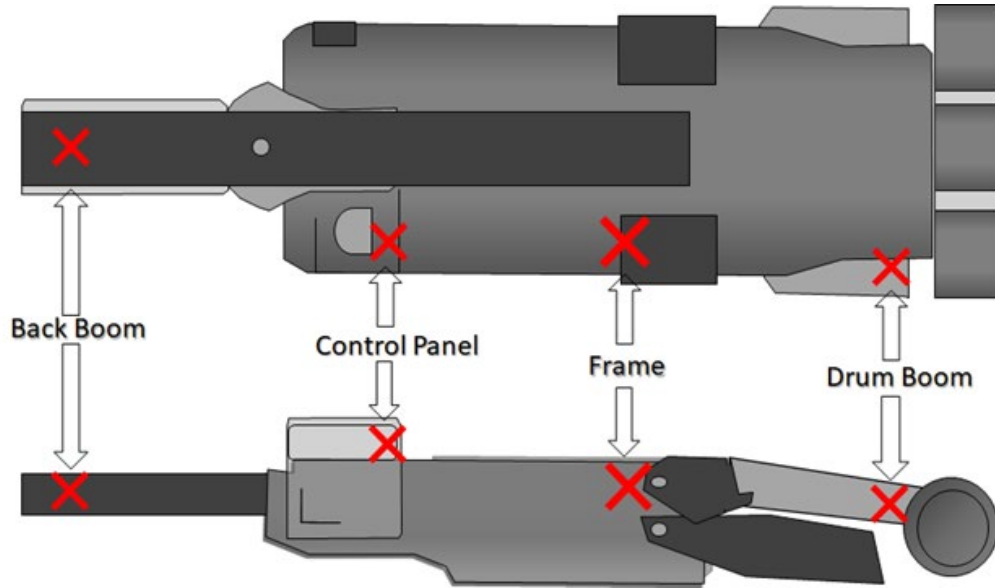
Figure 4. Approximate position of accelerometers on continuous miners. (after Fuchs, 1979)

To effectively assess the data, the acceleration versus frequency plots in the original report were digitized by the project team using WebPlotDigitizer. The extracted data were then systematically categorized to facilitate analysis under various operational conditions at different locations on the continuous miners. Given the variety of data from different continuous miner models under different conditions, the datasets associated with similar operating conditions and location were grouped together. These grouped data sets were finally analyzed following a statistically-sound approach. The statistical mean of the acceleration for each frequency in the grouped data set was calculated along with the confidence intervals based on an alpha value of 0.05. According to the calculated confidence interval values, the upper and lower bounds of acceleration levels were determined for individual frequency values. The determination of mean and upper/lower bounds provide information on the absolute level of acceleration and its associated variation under different operational scenarios. Altogether 19 operational scenarios were evaluated according to two operation mode (i.e., loaded and unloaded), three functionality mode (i.e., cutter head, conveyor, and cutter head & conveyor), and four different accelerators positions (i.e., drum boom, frame, control panel, and back boom).

3.1.2.2. *Influence of Operating Mode*

Figure 5 and Figure 6 show the replotted vibration data from the Fuchs (1979) study. Figure 5 focuses on data collected from the control panel position of continuous miners, while Figure 6 focuses on the frame position. Both figures include loaded and unloaded data from various operational modes. According to these results, as continuous miners began cutting coals, the variation of acceleration level significantly increased as depicted in the shaded confidence limit areas in Figure 5. Interestingly, at the frame position, the acceleration level shows the opposite trends as the acceleration levels were decreased when continuous miners operated under loaded conditions. Altogether, Figure 5 and Figure 6 collectively demonstrate that while the level and variation of natural vibrational acceleration may be different under distinct operating environments, the contradictory observations may be observed at different locations of continuous miners.
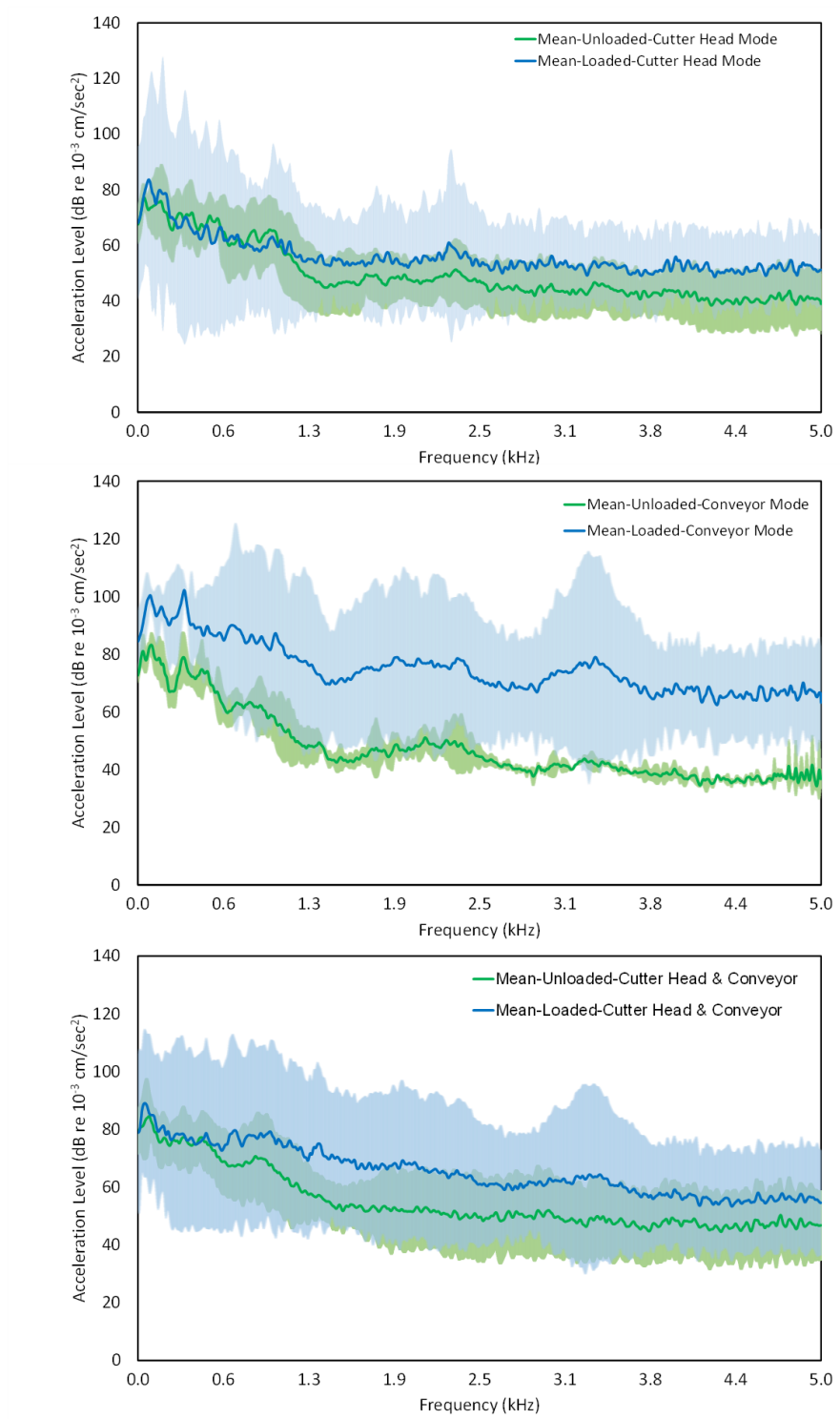
Figure 5. Continuous miner vibrational acceleration at the control panel position under various operating and functionality conditions.
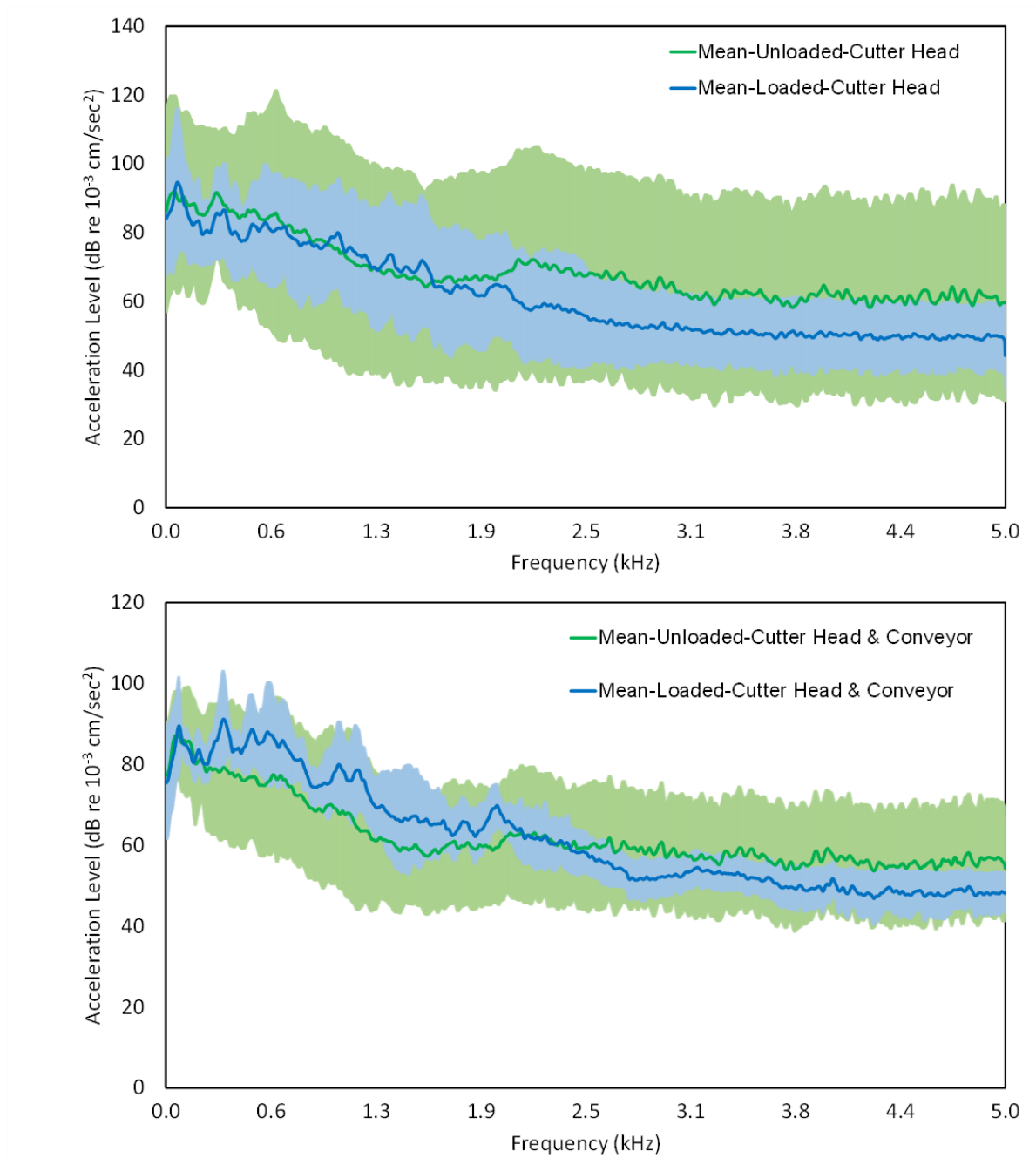
Figure 6. Continuous miner vibrational acceleration at the frame position under various operating and functionality conditions.

3.1.2.3. *Influence of Sampling Location*

To further investigate the vibrational acceleration levels at different locations on continuous miners, the data collected from four different locations were systematically evaluated in a similar fashion as above. As shown in Figure 7, the acceleration level at different locations of continuous miners may be different even under similar operating environments. The back boom location on continuous miners often has the

highest level of acceleration at different ranges of frequencies when the conveyor is running. While no back boom vibration data during the loaded operation mode was available, the structure of the conveyor by itself created a high level of natural vibrational energy. Additionally, the drum boom location has a high vibrational energy when compared with the middle section of the continuous miner, i.e., control panel and frame positions. Given the approximately close distance of the control panel and frame positions, the produced vibration at these two positions may be in a similar range. However, each of these two locations may propagate a higher level of vibrational energy according to the operation status of the cutter head and/or conveyor.
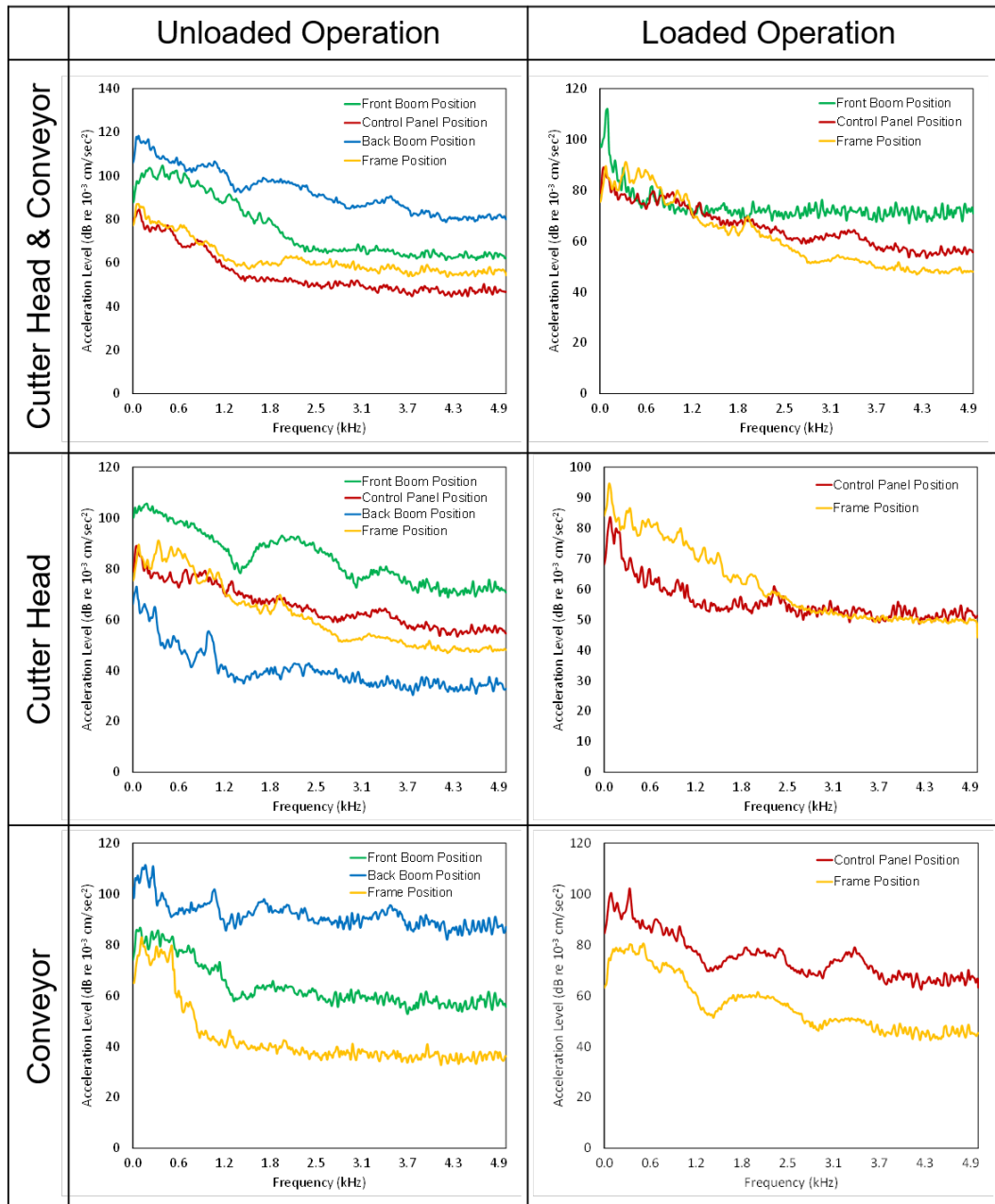

Figure 7. Continuous miner vibrational acceleration at different positions under various operating environments.

11

3.1.2.4.   Detailed Analysis

The vibrational acceleration propagated at the frame and control panel locations are thought to be the best estimate locations for the vibration at the scrubber and mesh filter panel. The team did further analysis on that existing data set and replotted vibration data from the report for the frame location and the control panel location in the specified confidence intervals. Since these two positions are the closest parts to the scrubber, they were pulled off as two separate graphs so that the acceleration data obtained from these graphs can be used as the main inputs for the laboratory testing. Figure 8 shows the change of acceleration levels at the frame location over the range of frequencies between 0 to 5 kHz, whereas Figure 9 shows the change of acceleration levels at the control panel location within the same frequency range. Both figures include different operation modes (loaded/unloaded) and different functionality modes (cutter head/conveyor/cutter head & conveyor). It can be implied from these figures that in the very initial phase of interacting with coal or rock (loaded position), the variation of acceleration level significantly increased. Whole lines in these figures generally follow a downward trend, although there are occasional increases and decreases. However, even though it can be seen that the overall downward trend still continues in the control panel location, when the machine cuts the coal, these increases and decreases are noticeable. According to these implications, the variation of natural vibration acceleration may differ from each other depending on where they are obtained and which operational modes are present.
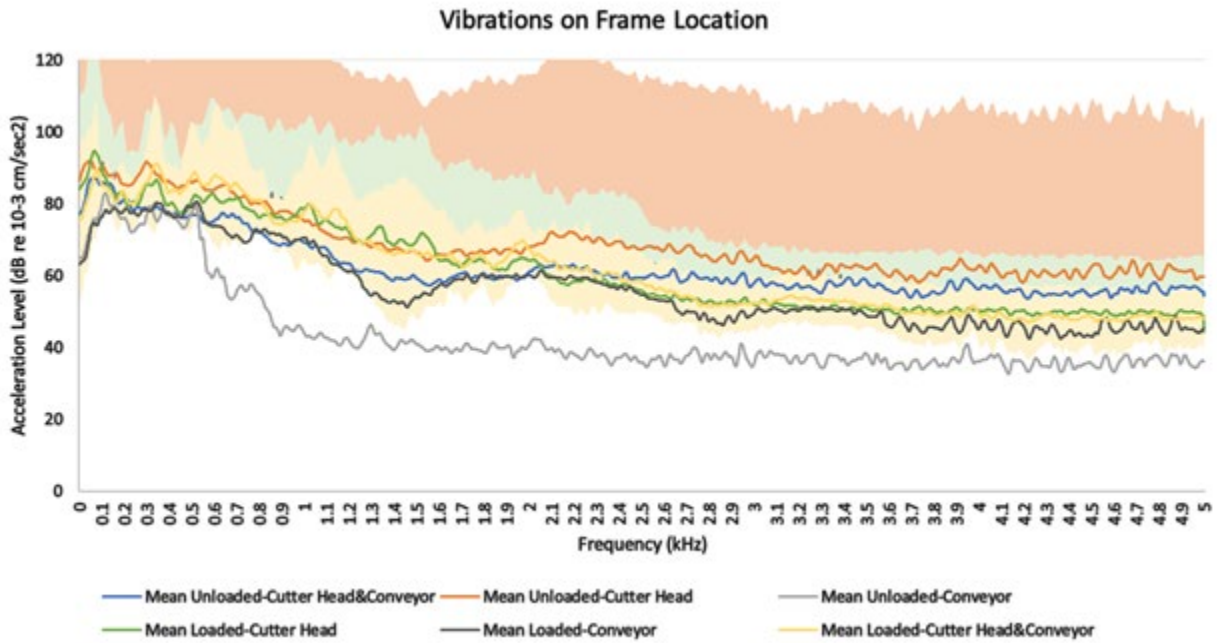

Figure 8. Acceleration level of continuous miner at the frame location under different working conditions.
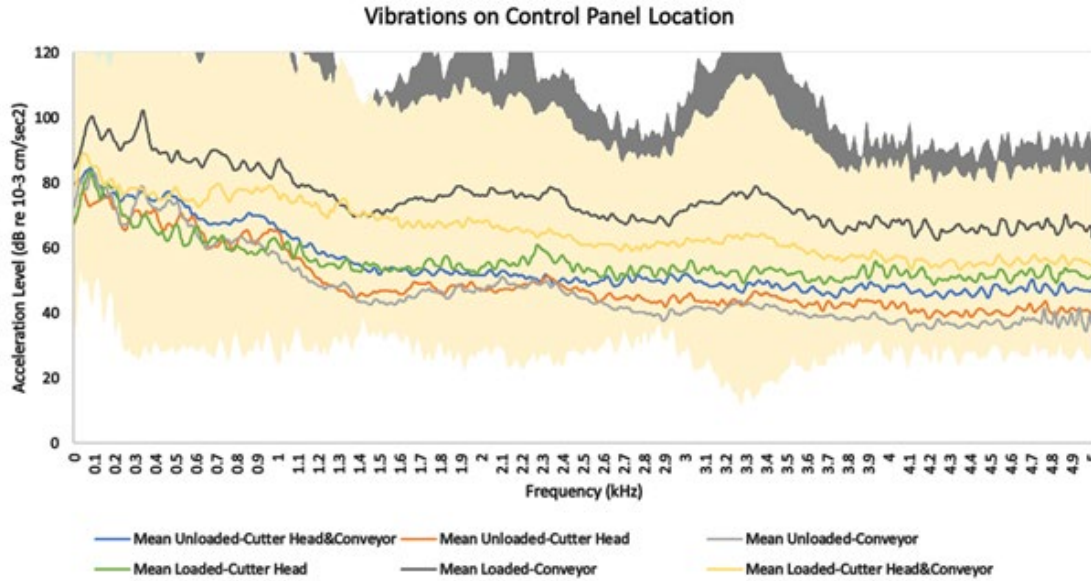
Figure 9. Acceleration level of continuous miner at the control panel location under different working conditions.

In order to demonstrate a single estimate within the %95 confidence interval, Figure 10 has been plotted. This figure shows the overall average and variation of acceleration levels at both control panel and frame positions for the four different continuous miners under all functionality modes and all operating conditions, based on 36 datasets obtained from Fuchs (1979) report. Altogether, these data were used for the initial laboratory and modeling efforts and were also used to set boundary conditions for frequency and acceleration anticipated in the field survey.
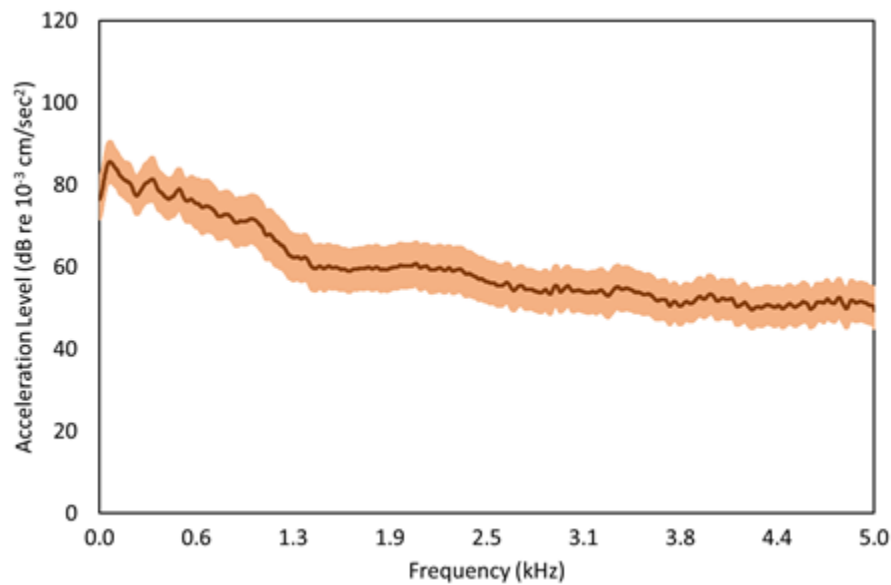

Figure 10. Acceleration level of continuous miner at both the frame and the control panel location under all working environments and operating conditions for the four different continuous miners.

3.1.3. Field Data Collection: Approach

3.1.3.1. Materials and Methods

Following the literature review, the project team successfully performed in-mine vibration measurements of a continuous miner operating in an underground coal mine in West Virginia. The continuous miner assessed during this study was a Joy 14CM15, and during the test period, the miner operated in an outby section away from the active production face. For data collection, the team used a single triaxial ICP accelerometer (Model #356A15). The sensor was mounted on the filter mesh box and aligned so that the principal coordinates were parallel and normal to the mesh panel direction. Figure 11 and Figure 12 show the sensor's location on the continuous miner and the coordinate directions of the sensor with respect to the filter mesh. We selected the mesh box as it is the closest accessible location representing the natural frequency and acceleration levels of filter mesh when the continuous miner is operated under various operational conditions and modes.
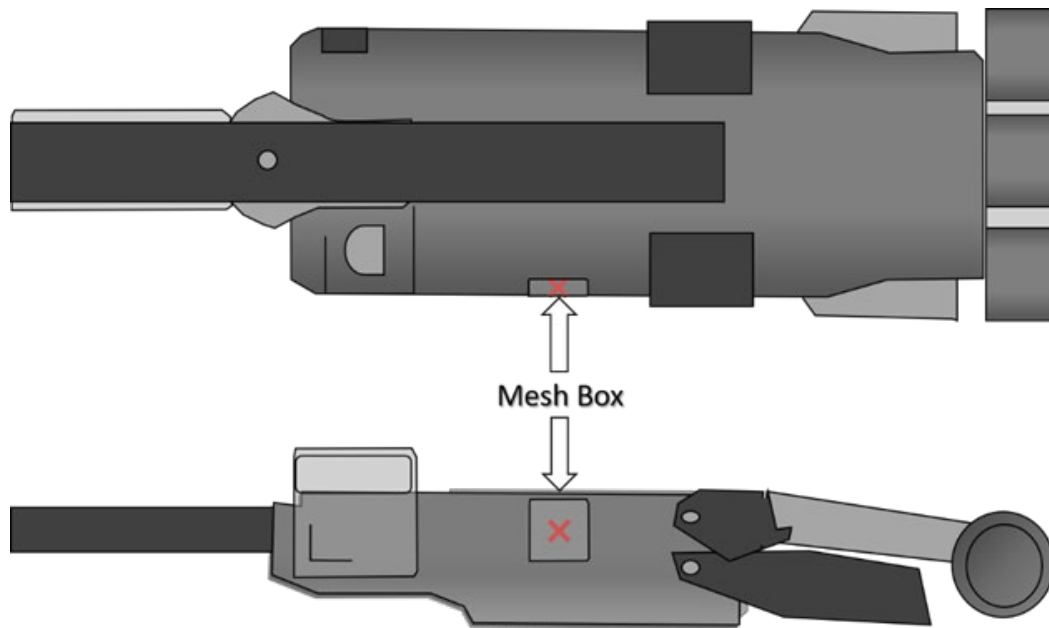

Figure 11. Approximate location of the mounted ICP sensor on the mesh box of the continuous miner for vibration measurements.
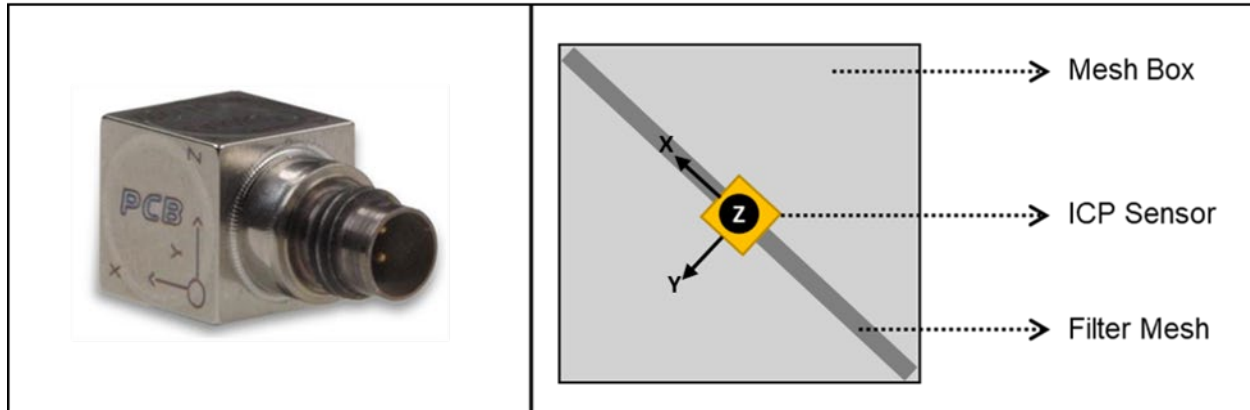
.

Figure 12. 356A15 triaxial ICP accelerometer (left panel) and schematic representation of ICP sensor location and position on the mesh box (right panel).

To temporarily install the vibration sensor, the team used adhesive mounting to secure the accelerometer to the continuous miner. First, we scrubbed the mesh box with coarse sandpaper, ensuring removing any particles and dirt from the surface and preparing a smooth, flat mounting surface. Next, we placed a quick-bonding gel (super glue) on the underside of the mounting base and firmly pressed it on the assembly to displace any extra adhesive remaining under the base, as depicted in Figure 13. We then mounted the triaxial ICP accelerometer on the base. The triaxial accelerometer allowed us to simultaneously record the vibration data in all three directions. It is worth noting that previous studies, including the measurements obtained by Fuchs (1979), recorded the vibration characteristics of the continuous miner only in one direction.
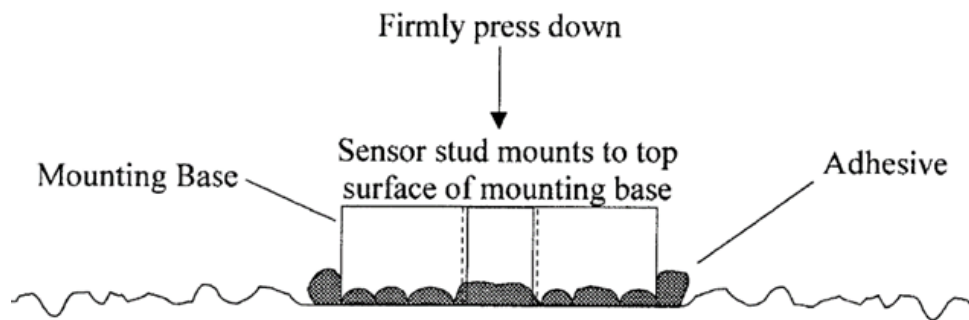
Figure 13. Installation of mounting base on the surface of mesh box using quick-bonding gel.

After mounting the accelerometer, we connected the ICP sensor to a data acquisition system (CoCO-80X) using a 20-ft four-conductor cable. The CoCo-80X is a new generation of handheld data recorders, dynamic signal analyzers, and vibration data collectors from Crystal Instruments. This battery-powered data acquisition system is equipped with up to 8 software-enabled input channels. For this study, three channels were used to record the time-domain frequency and acceleration level of the mesh panel in three X, Y, and Z directions. While recording, CoCO-80 X allowed us to monitor the recorded data and calculated averages in real-time. The measurement included vibration data in the frequency range of zero to 6,300 Hz. The equipment used to obtain the vibration data is schematically shown in Figure 14.
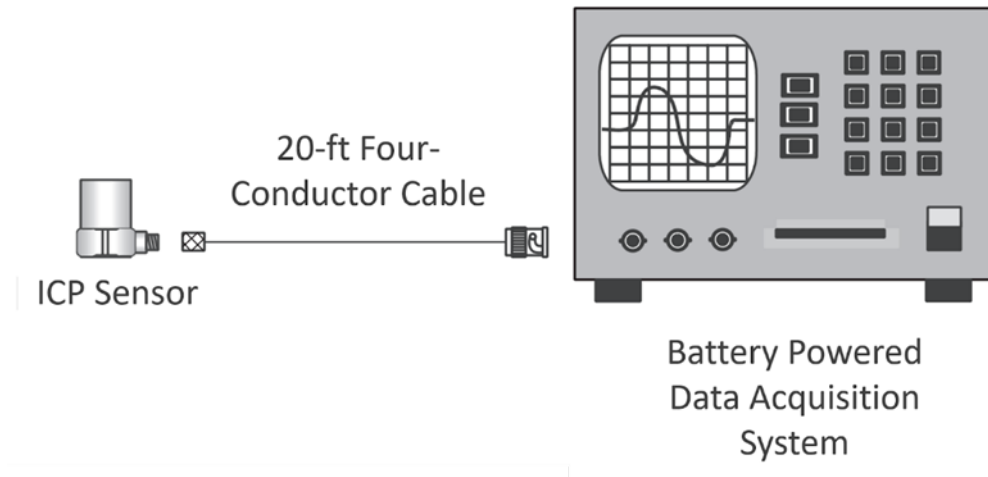
Figure 14. Schematic representation of ICP sensor system used for in-mine vibration measurements of filter mesh.

Following the equipment setup, we obtained time-domain acceleration data under various operating modes in either loaded or unloaded conditions and with the scrubber fan on or off. For this study, an operating mode is defined as when the machine is performing one or more of its potential functions (i.e., cutter head on/off and conveyor on/off). In addition, the loaded vs unloaded condition signifies whether or not the miner is interacting with the rock/coal. This combination of operating conditions, loading status, and fan status was tested in full factorial so that the relative contribution of each equipment subsystem to the mesh vibration could be adequately isolated and determined. Table 1 shows the full experimental matrix for data collection. These test IDs will be used identify test results in later sections of this report.

Table 1. Summary of continuous miner operating conditions and modes under which vibration data was collected.

Test ID	Operating Condition		Operating Mode		Fan Mode		Duration (Sec)
	Unloaded	Loaded	Cutter Head	Conveyor	On	Off	
UOF1	×		×			×	120
UOF2	×		×		×		120
UOF3	×		×		×		120
UOO1	×		×	×		×	120
UOO2	×		×	×	×		120
UOO3	×		×	×	×		120
UFO1	×			×		×	180
UFO2	×			×	×		180
UFO3	×			×	×		180
LOF1		×	×			×	120
LOF2		×	×		×		100
LOF3		×	×		×		90
LOO1		×	×	×		×	30
LOO2		×	×	×	×		30
LOO3		×	×	×	×		30

During testing, the real-time vibration data was collected for 30-180 seconds for each combination of operational conditions. The specific length of time for data collection was determined by visually observing the time-averaged vibration data in real time during the test. As the test progressed, the vibration data stabilized to a steady state, at which point the data collection was suspended and the file was saved onto the data acquisition system. It should be noted that these test durations greatly exceed those of the Fuchs (1979) study, where vibrational data was only recorded for 5 to 10 seconds. In addition, we systematically repeated some test conditions to further investigate the reproducibility of the results.

3.1.3.2.   Vibration Metrics

Following data collection, the project team conducted systematic and comprehensive post-processing analyses on the recorded vibration time-domain acceleration data. An example of the raw time domain data is shown in Figure 15. When analyzing acceleration data in the time domain, the results limited to a few parameters that quantify the strength of a vibration profile: amplitude, peak-to-peak value, and RMS (root-mean-square). The amplitude and peak-to-peak do not consider the time duration and thus the energy in the event. Additionally, the RMS value is directly related to the vibration profile's energy content and, therefore, its destructive capability. Identification of the most appropriate vibration frequencies for energy harvesting necessitates further detailed analyses to fully understand the natural vibrational characteristics of the machine, particularly at the location of the mesh panel.

Vibration is an oscillating motion about equilibrium, so most vibration analyses seek to determine the frequency in Hertz (Hz). To determine the vibration frequencies of the collected raw data, the team performed *spectrum analysis* to obtain a clearer picture of the vibration frequency. We utilized *Fourier analysis* or *spectrum analysis* to deconstruct vibration signals into their individual components (frequency and acceleration). The result is acceleration as a function of frequency, which provides an opportunity for detailed analysis in the frequency domain (or spectrum) to gain a deeper understanding of the vibration profile. Therefore, to fully understand the vibrational characteristics of the continuous miner, we first followed the *fast Fourier transform (FFT)* approach and determined frequencies and their corresponding acceleration levels. An example of the result FFT data is shown in Figure 16.
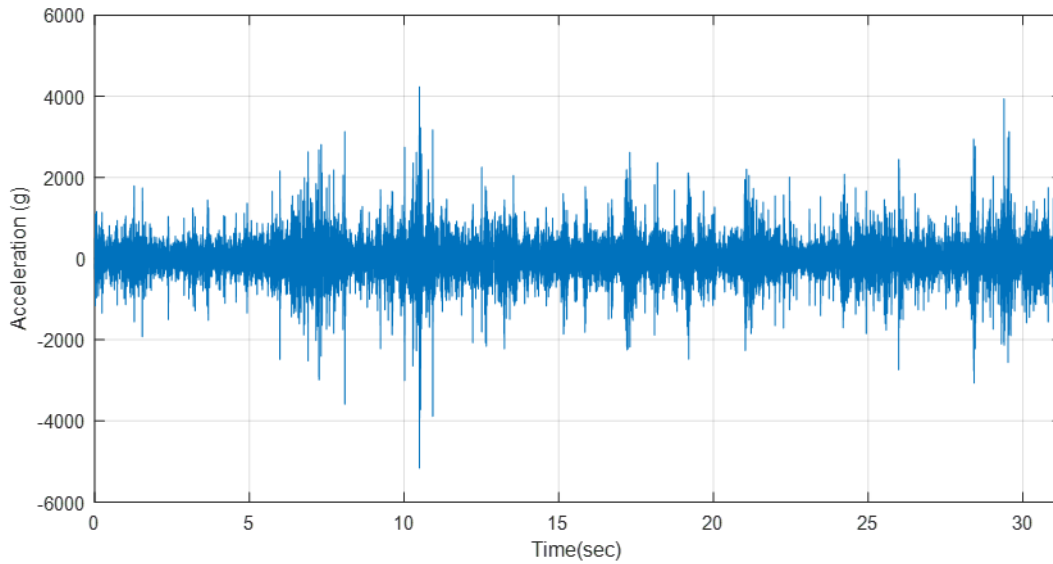

Figure 15. Example of recorded time domain acceleration data on X coordinate when continuous miner is under loaded condition and the conveyor is in On mode. The RMS value is 293.22 g.
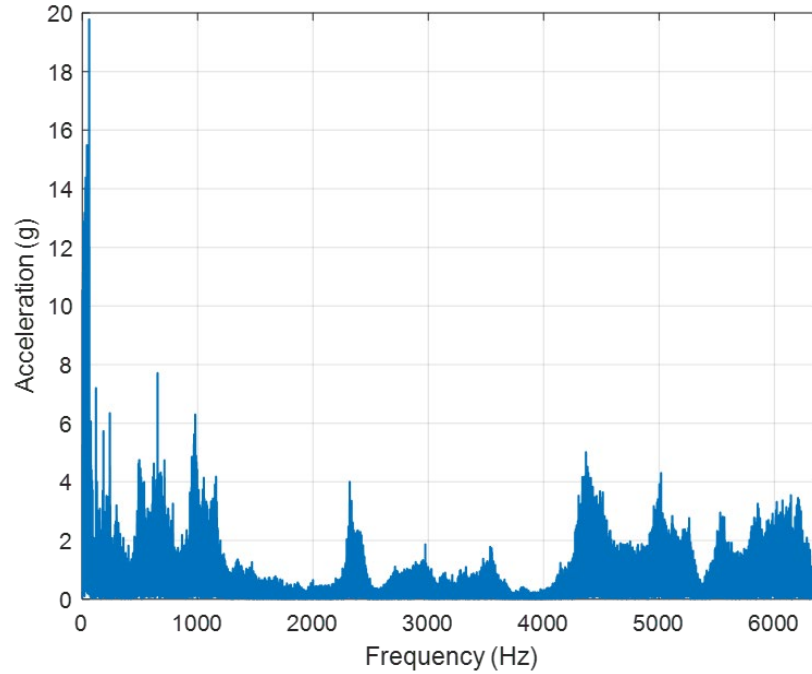
Figure 16. Example of FFT of recorded time domain acceleration data when continuous miner is under loaded condition and the conveyor is in the operating mode.

Most vibrations in the real world are "random" vibrations because they show many frequencies simultaneously. FFTs are excellent tools for analyzing vibration when there are a finite number of dominant frequency components. In addition, power spectral densities (PSD) are used to adequately characterize real-world vibration signals. The critical aspect of a PSD that makes it more valuable than an FFT for random vibration analysis is that the acceleration value is normalized to the frequency bin width with units of g^2/Hz. By normalizing the result, the dependency on frequency bin width will be eliminated; so that we can compare vibration levels in signals of different lengths. Figure 17 shows an example PSD from the in-mine dataset. As indicated, vibration frequencies below 60 Hz provide the maximum power. The power may then remain consistent for frequencies between 60 and 1000 Hz and dramatically drop above 1,000 Hz vibration frequencies.
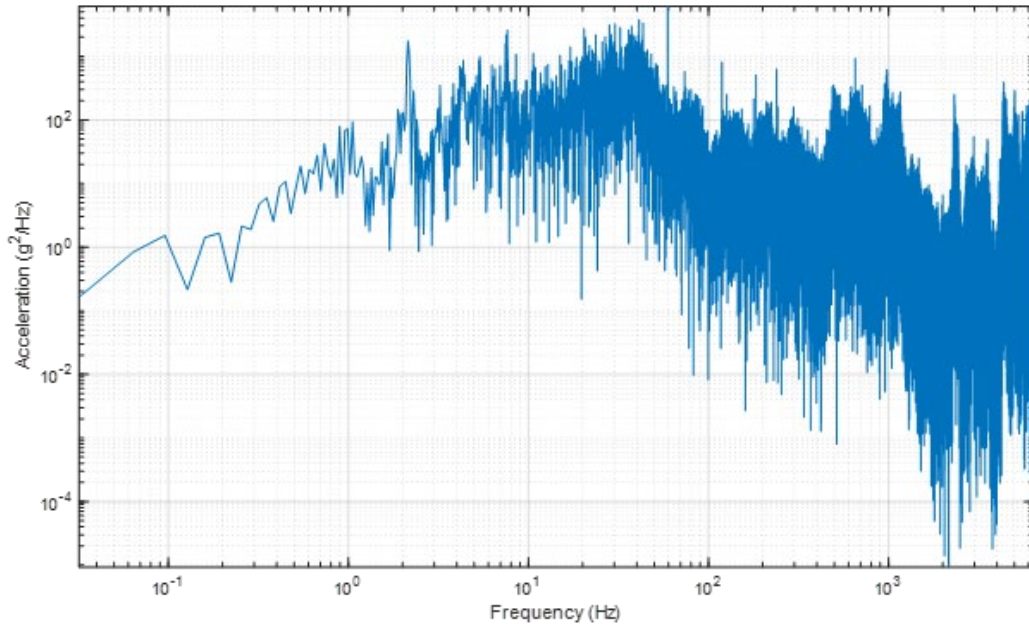
Figure 17.Example of PSD of recorded time domain acceleration data when continuous miner is under loaded condition and the conveyor is in On mode.

An effective energy harvesting system requires a relatively consistent vibration frequency and acceleration over time to be used as a vibration input for the system. The results obtained from time and frequency domain analyses were thus collectivity used to investigate the consistency of vibration source over time. While random high-power vibration frequency and amplitudes may be recorded during the in-mine vibration testing, only consistent frequency levels may be employed for energy harvesting. A spectrogram takes a series of FFTs and overlaps them to illustrate how the spectrum (frequency domain) changes with time. Since in-mine vibration measurements were completed under very different operating conditions, spectrograms can be an excellent tool to illustrate precisely how that spectrum of the vibration changes. Figure 18 shows two- and three-dimensional spectrograms that can be used to identify stable vibration spectrums. For example, under the operational conditions shown in Figure 18, consistent high acceleration frequencies may be identified at very low-frequency ranges below 100 Hz (as shown with dark red homogenous red color). Additionally, consistent low acceleration vibration spectrums may be obtained at high-frequency levels of 2,000 and 4,000 Hz (as shown with green color). Nevertheless, these high-frequency vibration spectrums may provide a minimum power of nearly one g^2/Hz, as depicted in the PSD plot of Figure 17.
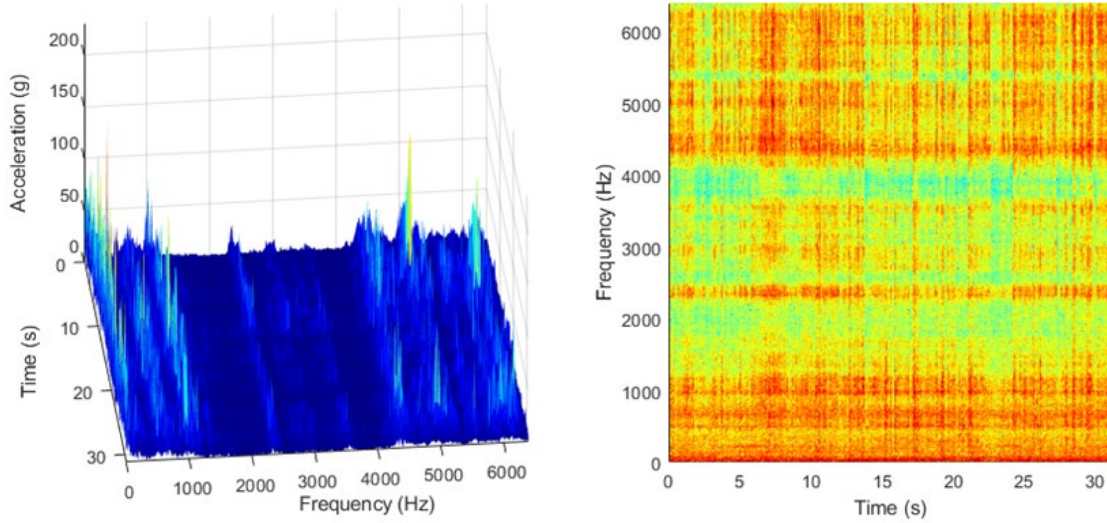
Figure 18. Example of spectrograms of vibration data at the panel X coordinate when continuous miner is under loaded condition and the conveyor is in On mode.

3.1.3.3.   Data Analysis

All post-processing vibration data analyses were conducted in MATLAB on a Dell Studio PC with Intel(R)Xeon(R) CPU E5–1607 processor running at 3.00 GHz and 16.0 GB of RAM under a 64-bit Windows operating system. While the computation time may be different for distinct scenarios according to the measurement time duration, the approximate time for analysis was often less than 10 seconds.

For each condition, the vibration data analysis began by creating two-dimensional spectrograms depicting the consistency of vibration frequencies over the measurement time. We anticipate the resonant frequency of the full-scale mesh filter to be much smaller than 1,000 Hz. As such, given the infeasibility of using vibration frequencies greater than mesh resonant frequency level for energy harvesting, we investigated spectrograms for frequencies below this threshold. After identifying uniform frequency levels, we studied FFT results to determine the acceleration ranges associated with these frequency levels. This procedure was repeated for all testing conditions and coordinates, and the results were evaluated to:

1. Determine the most appropriate vibration spectrums for the mechanical energy harvesting system.
2. Compare the vibrational characteristics of continuous miners with respect to each coordinate.
3. Investigate the reproducibility of the vibration results.
4. Identify the contribution of individual subsystems (i.e., cutter head, conveyor, and fan) to the overall vibrational characteristics of the continuous miner.

Despite detailed vibration measurements at various operating conditions and modes, the vibration data analysis focused more on the loaded conditions when the continuous miner is in contact with coal/rock, thereby generating the maximum amount of dust particles. Additionally, the scrubber fan is continuously operating in real case scenarios. Therefore, we devoted special attention to the measurement cases where the scrubber fan was on.

3.1.4. Field Data Collection: Results and Discussion

3.1.4.1. Vibrational Characteristic of Filter Mesh

Figure 19 shows when the continuous miner operates under loaded mode with running conveyor and cutter head, vibration spectrums with frequencies below 100 Hz (low-frequency range) are relatively consistent over time (see PSD at the top panel). These low-frequency vibration spectrums are associated with a wide range of acceleration levels from 1 to 20 g. The most apparent accelerations are below 5 g (see FFT at the top panel). As shown in the PSD of the top panel in Figure 19, the highest power levels are associated with these vibration spectrums. Also, mid-frequency range vibration spectrums (400 – 450 Hz) are relatively consistent over time (see homogenous yellow color). This vibration spectrum is associated with smaller acceleration values below 1 g. The PSD plot also shows that the power level may be several orders of magnitude smaller in mid-range frequency levels than in low-range frequency spectrums.
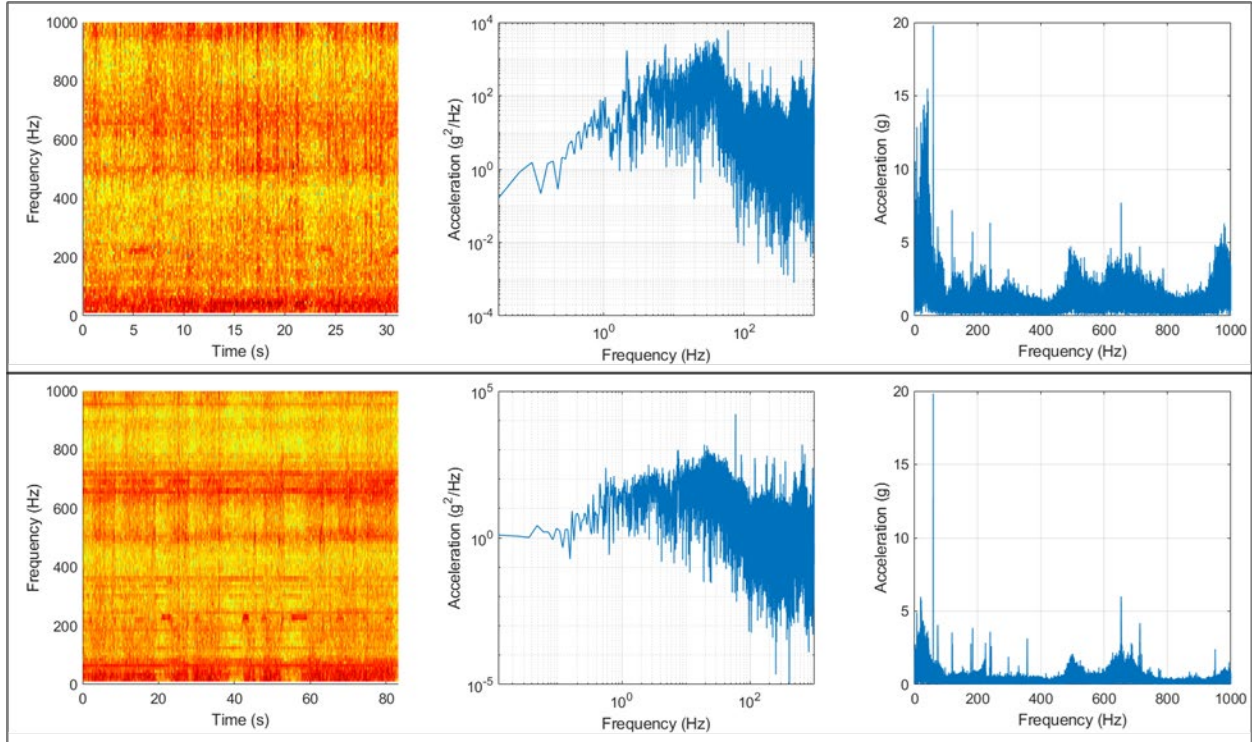
Figure 19. Spectrogram, PSD, and FFT of LOO3 (top panel) and LOF3 (bottom panel) in the X direction.

On the other hand, when the conveyor does not operate, the acceleration levels are dramatically dropped at all frequency ranges (see bottom panel FFT of Figure 20). However, both the low- and mid-frequency range vibrations remain consistent at nearly 90 seconds of measurement. Similar to the LOO operation mode, low-frequency vibrations are associated with high acceleration levels. Under the LOF operation mode, vibrations with higher frequency levels of 660 and 720 Hz are relatively stable at acceleration levels of 2-6 g and 1-4 g, respectively. Additionally, stable high frequency-low acceleration vibration spectrums (>720 Hz) were introduced under LOF operation mode.
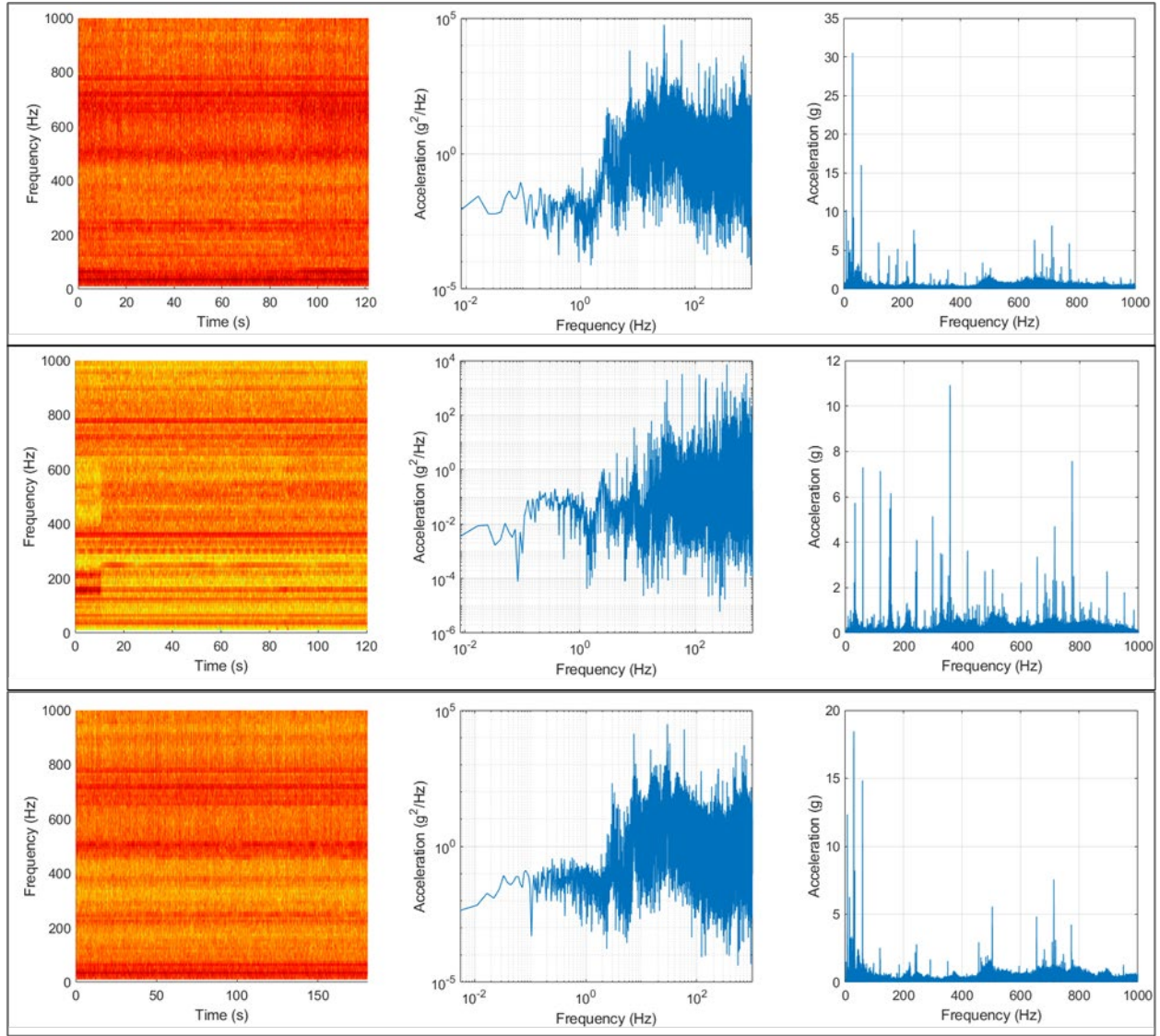
Figure 20. Spectrogram, PSD, and FFT of UOO3 (top panel), UOF3 (middle panel), and UFO3 (bottom panel) in the X direction.

Under unloaded operation conditions, as shown in Figure 20 several stable vibration spectrums are observed. Interestingly, low-range vibration frequency spectrums (<100 Hz) are consistent at higher acceleration levels. For example, as shown with the harmonious red color in Figure 20 (top and bottom panels), low-range vibration frequencies with high acceleration values are dominant. When the conveyor is off, both high and low acceleration values remain consistent at the same frequency levels, as shown by distinct red and yellow color bars in the middle pane of Figure 20.

When the conveyor is in the operation mode for both UOO and UFO, vibration frequencies at 500, 720, and 780 Hz are consistently observed at acceleration values close to 1 g. Similarly, at UOF, high-range vibration frequencies (720 and 780 Hz) are steadily associated with acceleration levels below 1 g. At UOF operation mode, several steady vibration spectrums at the mid-range frequency and high/low acceleration are observed. Some examples are vibrations at 260 Hz and 380 Hz at 1 g.

Similar to the X coordinate of the mesh panel, the team performed detailed vibration data analyses at Y and Z coordinates (see Figure 21 and Figure 22). The comparison between Figure 19 and Figure 20 with Figure 21 and Figure 22 illustrates the independency of mesh vibration behavior in different coordinates. Additionally, these comparisons show that generally under loaded operation modes, as expected, random vibration behavior of the mesh panel may be intensified. However, even under loaded conditions, several consistent vibration spectrums may be introduced, which can be later used for mechanical vibration energy harvesting.

Table 2 summarizes the collective results of performed analyses in X, Y, and Z conditions identifying relatively consistent vibrational frequency and associated acceleration levels at different coordinates.
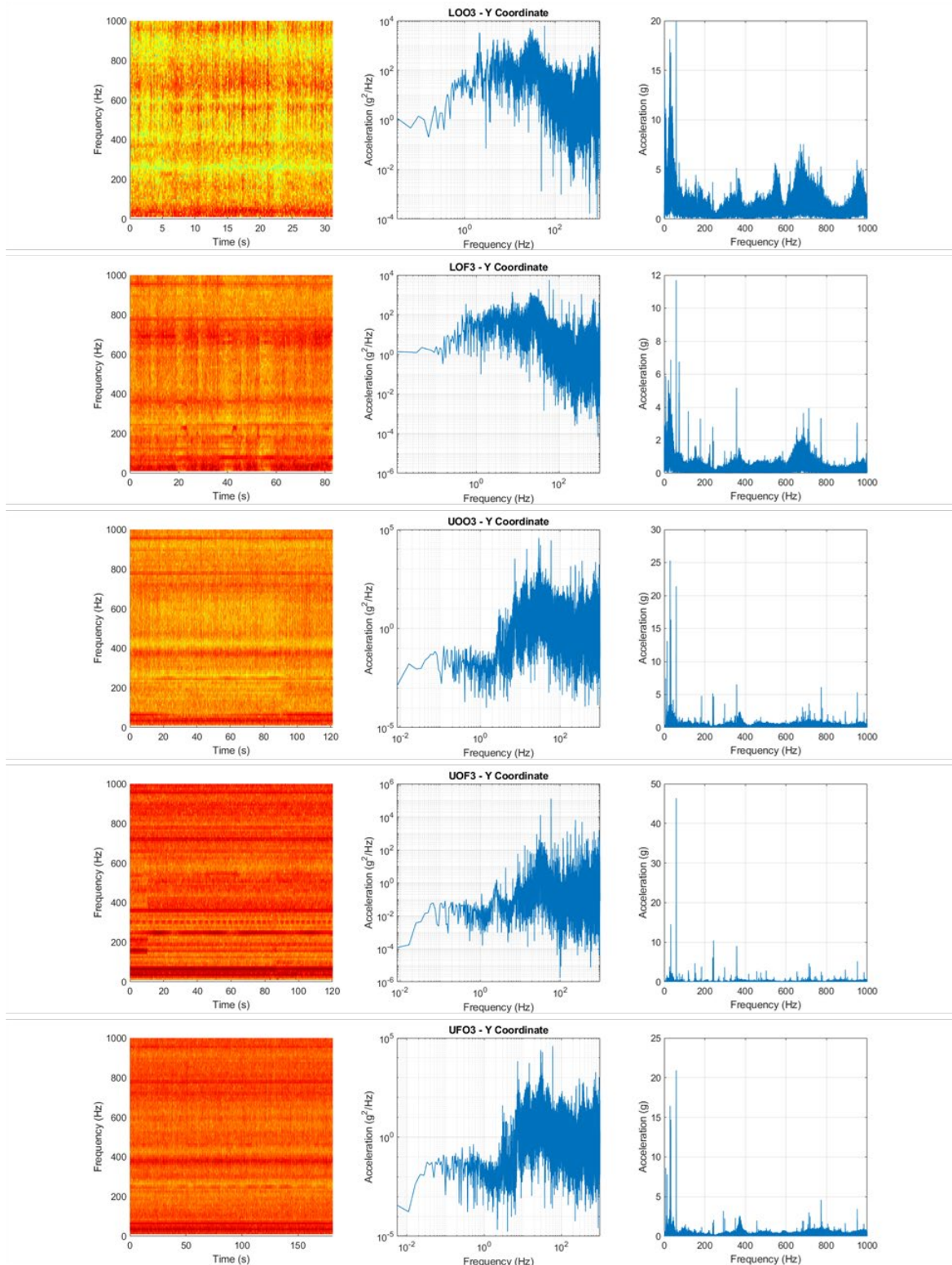
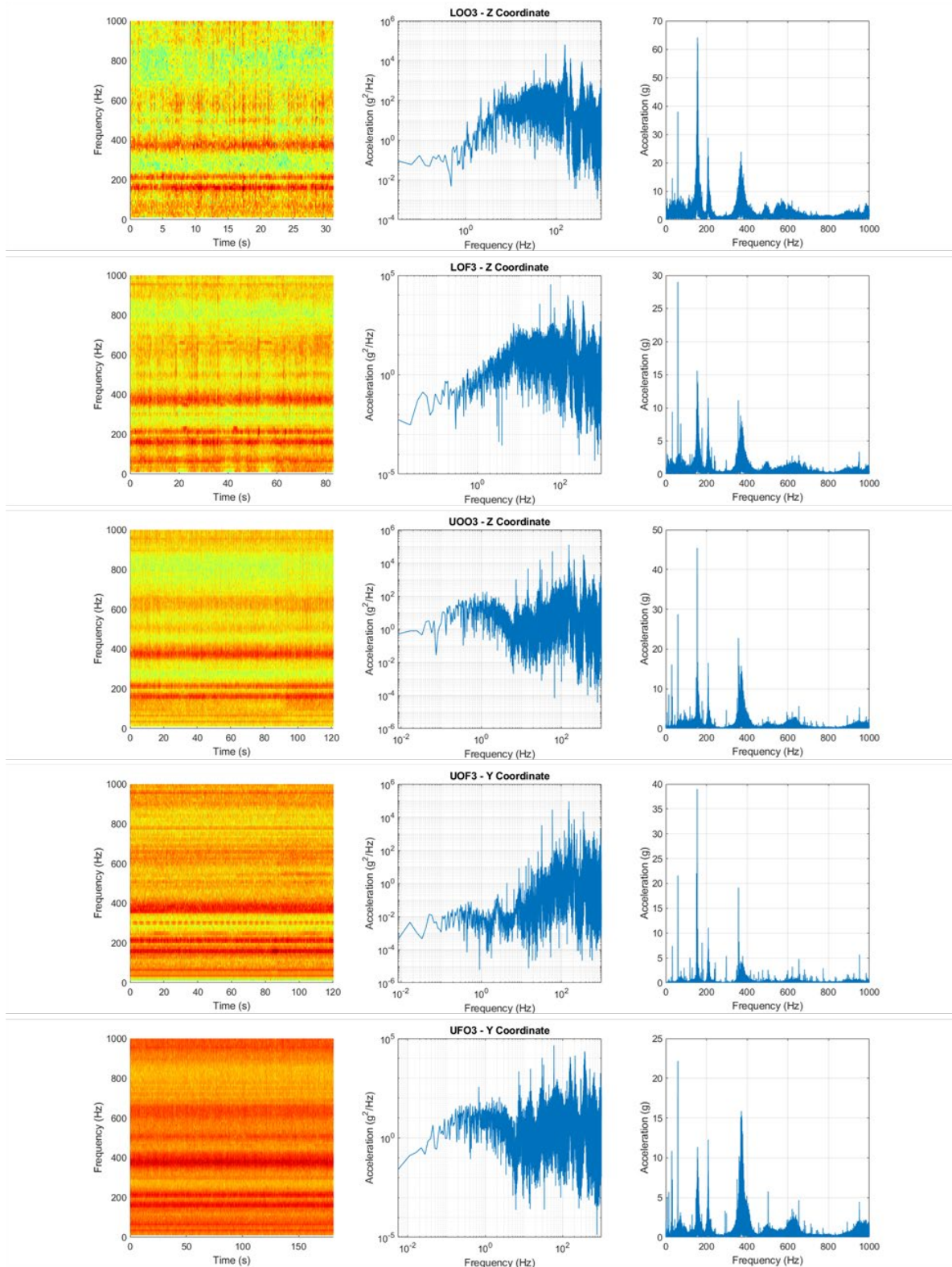*Figure 21. Spectrogram, PSD, and FFT of CM vibration in the Y direction.*

Figure 22. Spectrogram, PSD, and FFT of CM vibration in the Z direction.

Table 2. Optimal vibrational frequency and acceleration introduced by continuous miner that can be used as input vibration for mechanical vibration energy harvesting system.

Filter Mesh Coordinate	Frequency (Hz)	Acceleration (g)
X	<100	1-3
	700-800	1-2
Y	<100	1-3
	250-280	0.5-1
	360-380	1-2
	770-790	1-2
	950-970	1-2
Z	160-180	1-10
	210-230	1-10
	370-390	1-12

3.1.4.2. *Contribution of Subsystems to the Mesh Vibration*

Given the proximity of filter panel location to conveyor and fan, the team expected these two sub-systems to be the sources of the primary vibrations. To fully understand the contribution of scrubber fan, conveyor, and cutter head, the team has drawn detailed comparisons on vibration measurement under unloaded operating conditions.

Figure 23 compares the vibrational characteristics of the filter mesh UFO1 and UFO3 operational conditions. According to these results, the scrubber fan has minimal contribution to the vibration of the continuous miner. The PSD and FFT calculations show that the scrubber fan only introduces high-frequency vibration to the overall vibration spectrum.
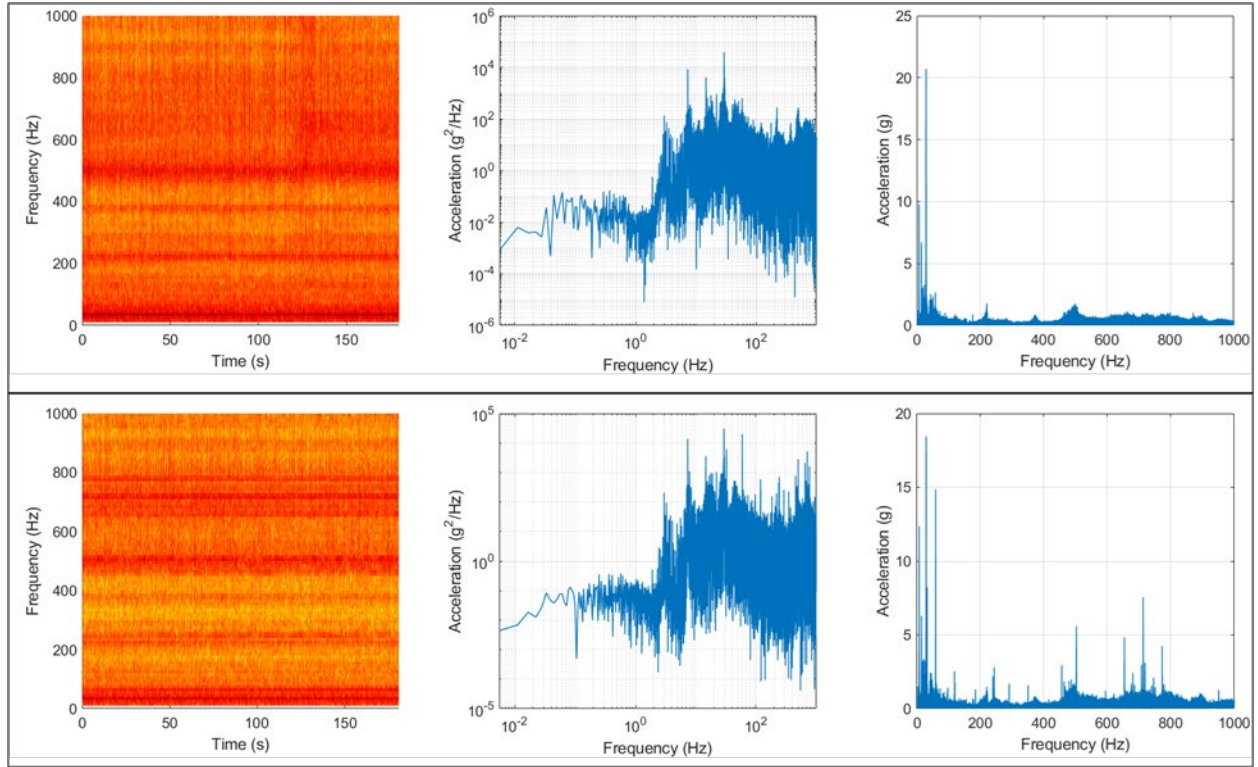
Figure 23. Spectrogram, PSD, and FFT of UFO1 (top panel) and UFO3 (bottom panel) in the X direction.

Additionally, when in operation, the cutter head slightly increases vibration frequencies and acceleration at the lower and mid-range of vibration frequencies. The spectrogram in Figure 24 indicates the presence of consistent high-power vibrations at the low- and mid-range of vibration frequencies.

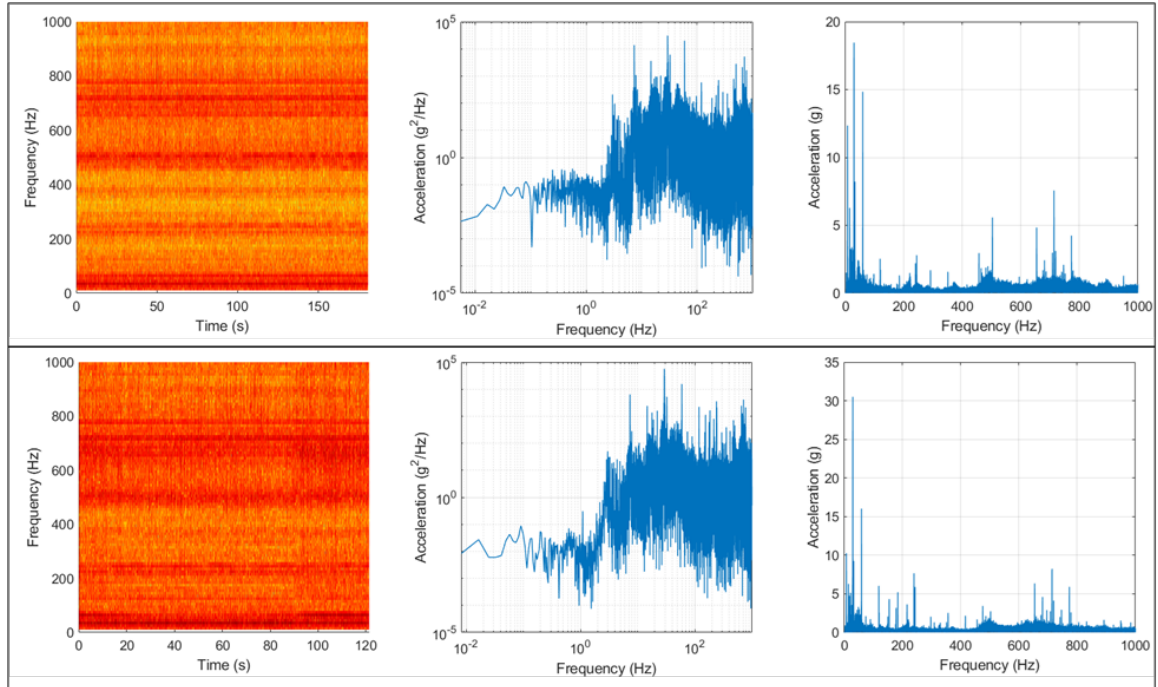*Figure 24. Spectrogram, PSD, and FFT of UFO3 (top panel) and UOO3 (bottom panel) in the X direction.*

On the other hand, as depicted in Figure 25, the conveyor is the primary source of vibration in the continuous miner at the filer panel location. Once the conveyor runs, vibrations at a broad range of frequency levels are introduced.
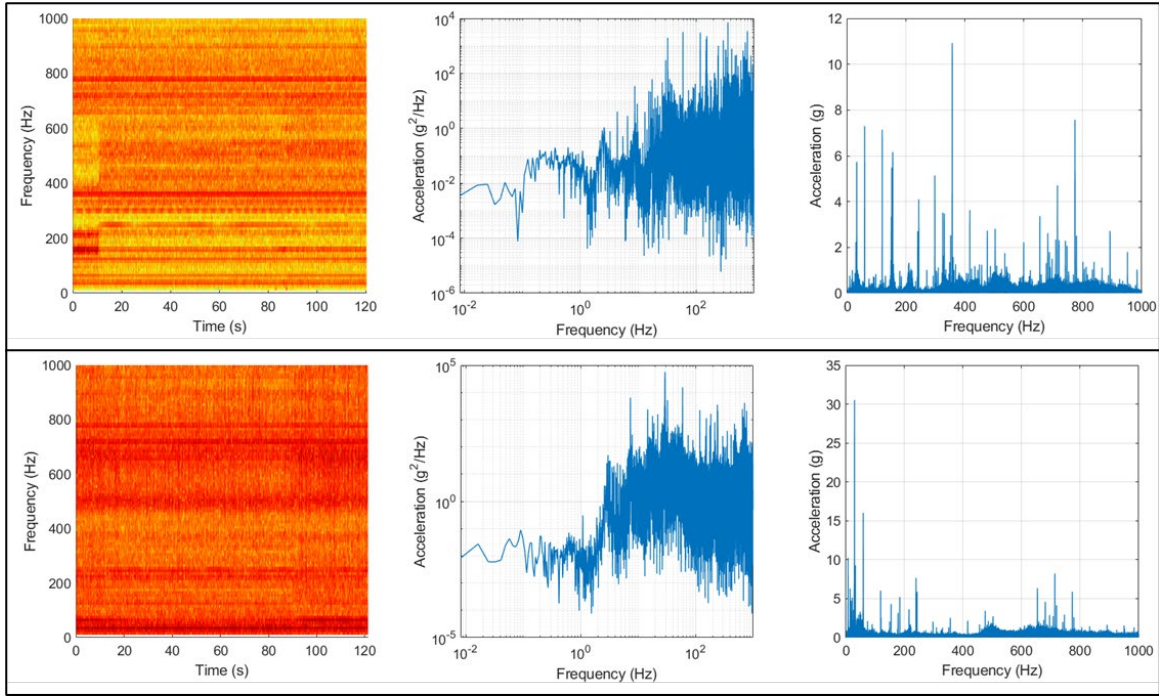
Figure 25. Spectrogram, PSD, and FFT of UOF3 (top panel) and UOO3 (bottom panel) in the X direction.

3.1.4.3. *Measurement Reproducibility*

As discussed in the previous section, the team repeated in-mine vibration measurements for most continuous miner operating conditions and modes to investigate the reproducibility of the results. Figure 26 shows that the normalized PSD data are almost identical under unloaded conditions. Under unloaded operating conditions, similar spectrograms may be obtained demonstrating the reliability of the measurement procedure completed.

Interestingly, even under loaded conditions, similar vibration measurements were recorded under identical operating conditions (Figure 27). Although noisy vibrations, as a result of cutter head interaction with coal/rock, are evident, the normalized PSD data and FFT results show similar frequency-acceleration trends. Altogether, these results demonstrate the high degree of repeatability of in-mine vibration measurements.

Figure 26. Spectrogram, PSD, and FFT of UOO2 and UOO3 in the X direction.

Figure 27. Spectrogram, PSD, and FFT of LOO2 and LOO3 in the X direction.
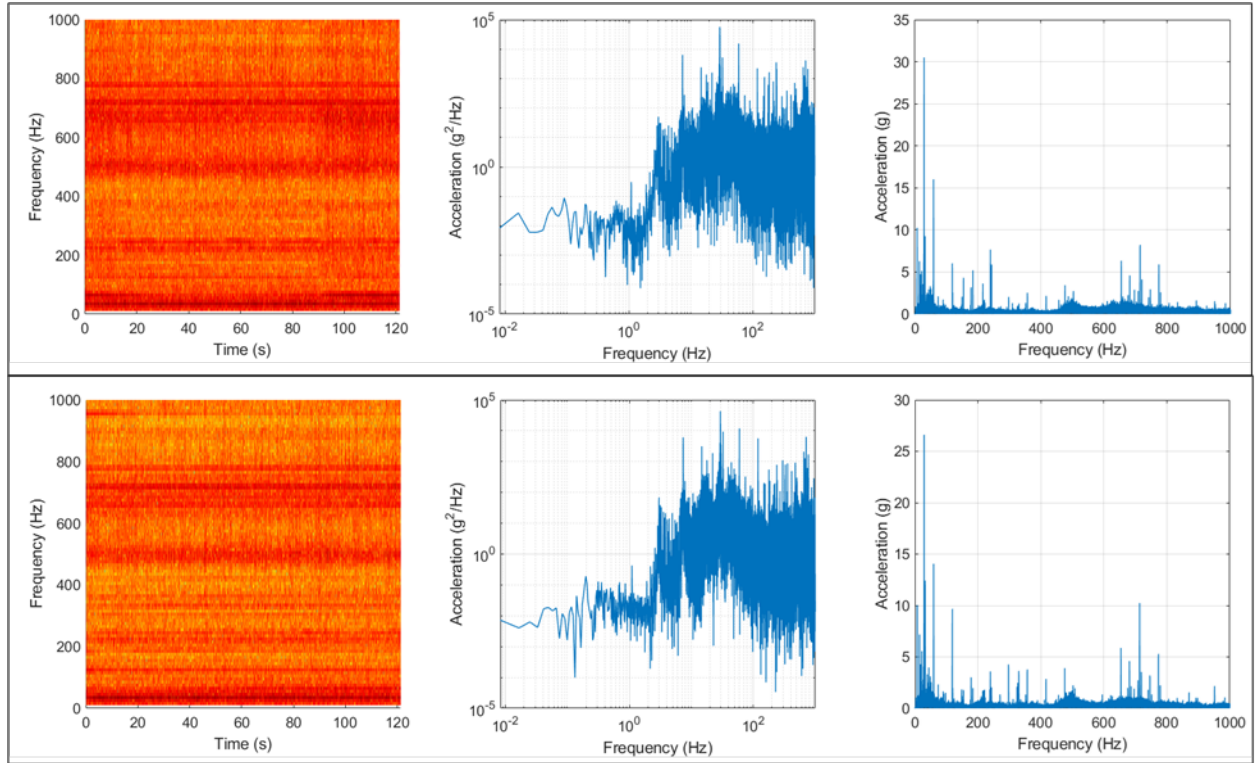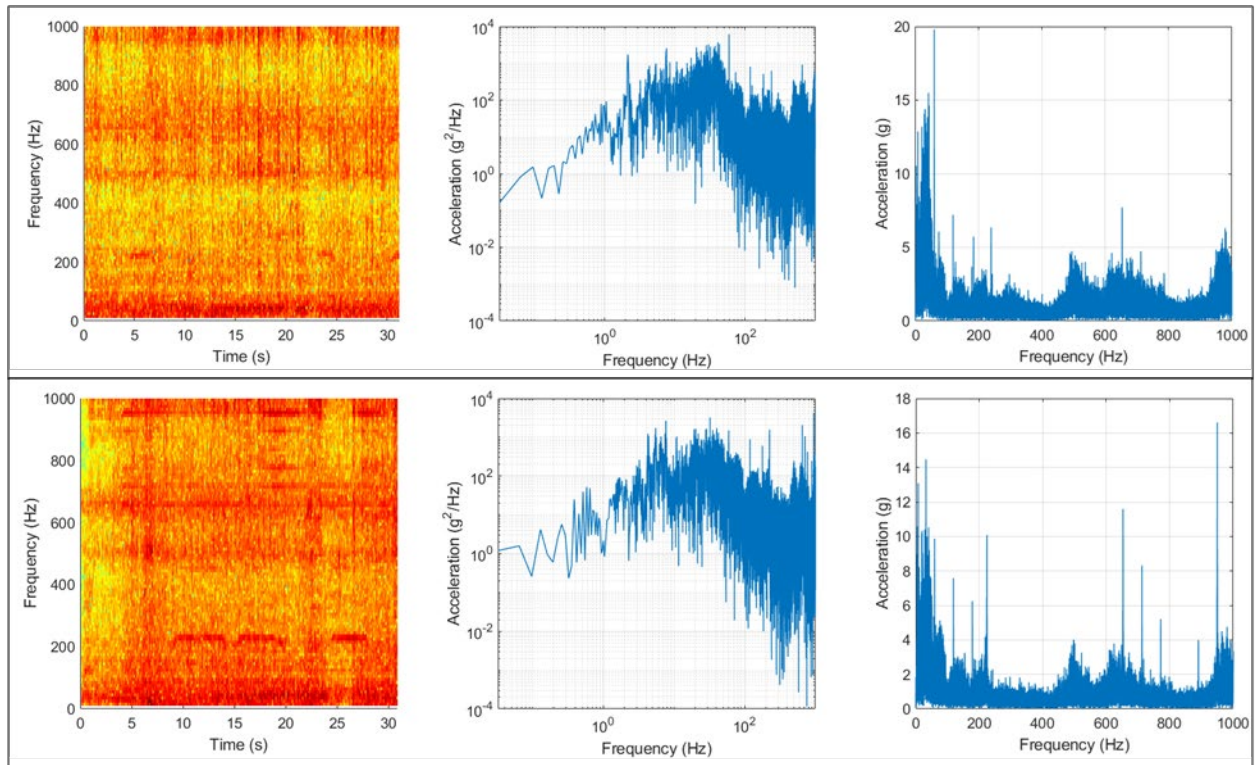
31

3.2. System Modeling

3.2.1. Parameter Characterization Modeling

3.2.1.1. Study Objectives

While static screening systems are commonly used in most air or hydraulic filters, studies on fibrous filters have suggested that filtration efficiency can be improved by filter vibration (Kim et al., 2006; Yang et al., 2015). Additionally, several studies have investigated the role of harmonic vibrations in minimizing the fouling (clogging) of membrane filters (Coster et al., 2011; Bilad et al., 2013; Genkin et al., 2006). Unfortunately, for mesh-screen type filters used in the flooded-bed scrubbers, a similar assessment is not available in the literature.

In this task, preliminary Computational Fluid Dynamics (CFD) simulations were performed to assess the effects of mesh vibration on the particle-mesh interaction using COMSOL Multiphysics®. CFD simulation has been frequently applied to understand the complex behavior of the dust-laden airflow in the longwall mining environment (e.g., Ren et al, 2014). More recently, researchers have employed numerical simulations to optimize the capture efficiency of dust scrubbers (Wedding et al., 2015; Arya, 2018; Arya and Novak, 2019, Kumar, 2015) and to calculate the collection efficiency of a novel vortecone scrubber, which is a potential substitution for flooded-bed mesh scrubber (Arya and Novak, 2019).To investigate the geometric and vibrational system parameters and limit the extent of empirical studies, computational fluid dynamics (CFD) simulations were performed in COMSOL® to evaluate the behavior of the vibrating mesh screen. Despite the previous simulations of the flow in the continuous miners, none of them assessed the flow inside the flooded-bed scrubber. Therefore, the results of this work also facilitate an understanding of the flow behavior in the flooded-bed scrubber channel. These findings will, in turn, inform the project team on the appropriate design for the vibrating mesh dust scrubber and reduce the extent and scope of empirical testing needed for system optimization.

Based on the mechanism of the flooded-bed scrubber described earlier, the dust removal efficiency depends on two key factors. One is the wetting condition of the mesh screen, as the dust particle is captured by the water on the mesh surface. The other is the strength of the interaction between the dust particle and mesh wires, in other words, the possibility of the dust particle coming into contact with the droplets on the mesh wires. Therefore, we will numerically investigate these two factors separately due to the complexity of the problem. We present the numerical models for dust-laden air two-phase flow and nozzle spray (i.e., air-water two-phase flow) to assess the strength of dust particle-mesh interaction and mesh wetting conditions. We also propose a simplified three-phase flow model consisting of both dust particle and spray droplet to further compare the behavior of the vibrating and static mesh screen. Additionally, parametric studies on the operating conditions are carried out to identify the critical parameters on the performance of the vibrating mesh screen.

3.2.1.2. Dust-Laden Air Two-Phase Flow Model

Modeling Approach: In this section, a numerical model for dust-laden air two-phase flow was formulated to systematically investigate the impact of mesh vibration on the interaction between the dust particles and the mesh screen. The underlying assumption of the model is that the mesh screen is thoroughly wetted. Even though the nozzle spray system is not incorporated into the simulated scrubber environment, the particle-mesh interaction is translated to particle-water droplet adhesion. As a result, the dust particles are assumed to be captured once they collide with the mesh screen surface. The strength of the interaction is quantified by the number of dust particles collected by the mesh wire throughout a specific time interval.

A simplified two-dimensional scrubber channel domain shown in Figure 28. The left boundary is the inlet of the airflow with a horizontal velocity of 4 m/s and the right boundary is the outlet. A mesh screen composed of circular wires is located in the middle of the simulation domain with a taper angle of 40°. For brevity, we considered only one layer of mesh in the vibrating screen and represent the net opening of the screen by a parameter named mesh aperture, which denotes the smallest distance between two adjacent wires (see Figure 28). The channel length is twice of the channel height and the corresponding third dimension in 3D (i.e., width) was assumed. Detailed dimensions of the scrubber channel, and mesh screen can be found in Table 3. The mesh vibrates vertically with a harmonic sinusoidal profile. The non-slippery boundary was applied to the mesh wire surface, and the slip boundary condition was applied to the upper and lower channel boundaries, assuming the channel is large enough to neglect the influence of the wall. Therefore, the mesh wire diameter, d, was used as the characteristic dimension to quantify the Reynolds number. The fluid domain was discretized by triangular elements with prism elements added around the wire boundaries. The Arbitrary Lagrangian-Eulerian method was used to deal with the fluid domain deformation due to the mesh vibration. The generalized alpha method was used for matching the governing equations in time.
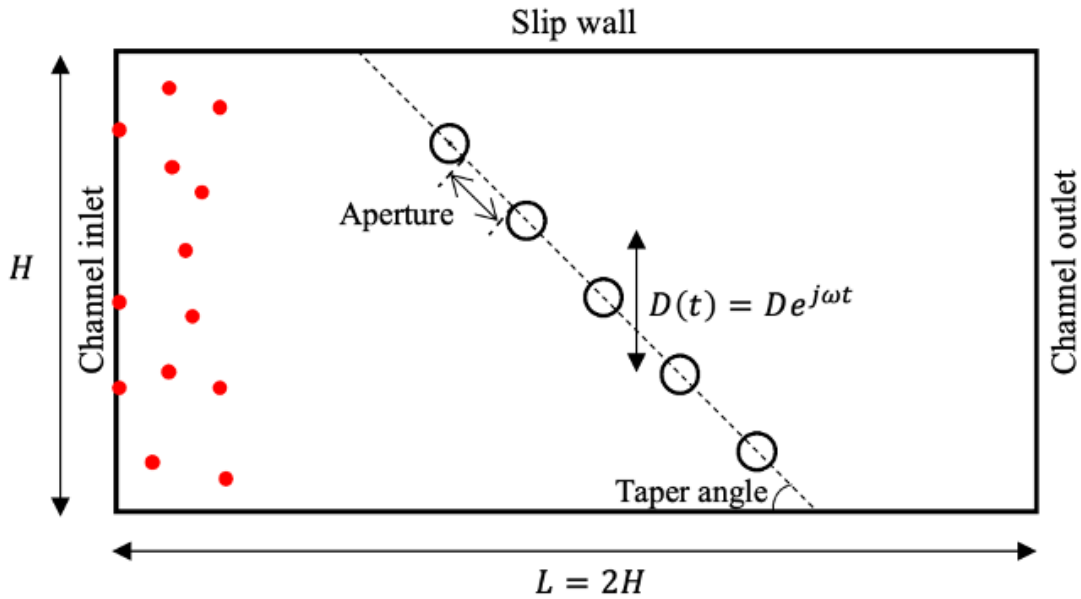

Figure 28. Dust particle and mesh interaction simulation domain schematic.

Table 3. Scrubber channel and mesh screen parameters.

Property	Value
Channel height, H	0.128 m (0.42 ft)
Channel width	H
Channel length, L	2H
Inlet airflow speed, U_{in}	4 m/s
Wire diameter, d	0.003048 m (0.12 inch)
Mesh screen taper angle	40°
Aperture, A_p	2d

The dust particles are released from the left boundary at an interval of 1e-4 seconds. Dust concentration was set to be 40 mg/m³. The particles are assumed to be already entrained in the airflow with the same initial velocity. The particle diameter was randomly distributed from 1 to 75 microns with an average of 38 microns, following the definition of float coal dust that specifies less than 75 microns in particle diameter. The number of particles per release was calculated as well as the volume fraction of the dust particle in the air, where the dust particle density is assumed to be 1200 kg/m³. The dust-laden flow can be treated as a sparse flow that considers only the force from flow to particles but not vice versa. This treatment is often referred to as one-way coupling. The dust particle-particle collision was neglected due to the low volume fraction. Each dust particle was treated as a dimensionless mass point with its trajectory solved by the Newtonian formulation (i.e., Newton's second law). Brownian force is neglected as it only affects particles smaller than 0.1 microns. Lift force acts on dust particles in the shear flow near the wire surface, along the direction of the gradient of the flow velocity. To determine the proper formulation of the lift force, we first calculated the mean particle Reynolds number. Therefore, the Saffman law, which computes the lift force of particles was used. The drag force experienced by the dust particles acts in the direction opposite to the relative motion of the particles with respect to the fluid. Given the small mean particle Reynolds number (<<1), the Stokes law was used. In COMOSL, a stick boundary condition was set for dust particles on the wire boundary, and a bounce condition was set on the channel wall boundaries. For each case setup, the number of collected dust particles in a 0.1 seconds simulation duration was obtained to quantify the strength of the dust particle-mesh interaction, which further reflects the dust collection efficiency of the scrubber.

Results: Here, we assess the effects of vibration conditions, dust concentration, and mesh aperture on the strength of dust particle-mesh interaction to evaluate the performance of vibrating mesh under different working conditions.

Effects of mesh vibration conditions. We first assessed the influence of the vibration frequency and amplitude on the dust particle-mesh interaction. The velocity of the harmonic vibrating wire was normalized by the incoming velocity of the dust particles. Simulations were performed at various displacement amplitudes and frequencies. Figure 29 shows the airflow velocity magnitude contour and dust particles as the mesh screen vibrates.
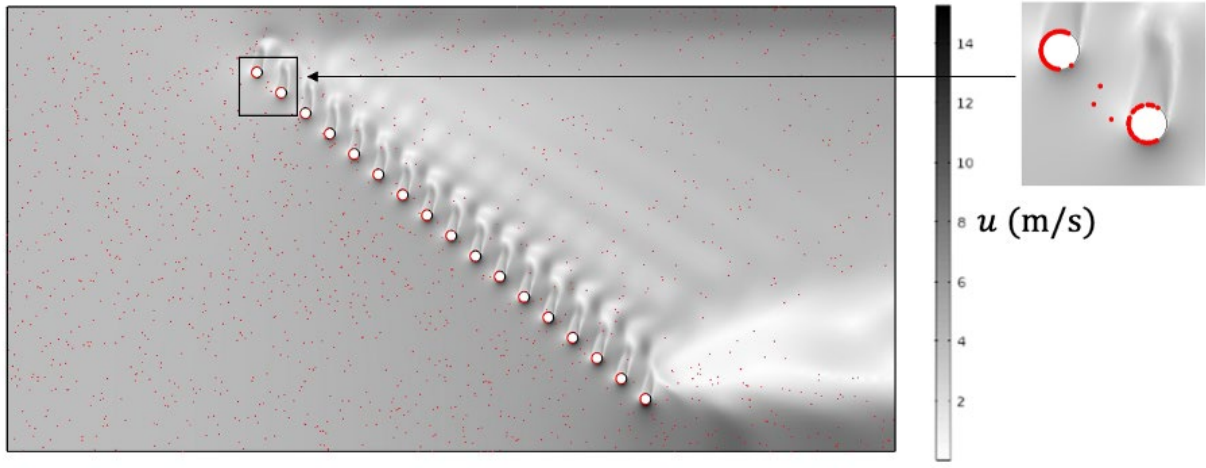
Figure 29. Airflow velocity contour (m/s) and dust particles (dust particle size is enlarged for better visualization).

The number of captured dust particles at different mesh vibration conditions along with the static mesh is plotted against normalized velocity amplitude (β) in Figure 30. The results suggest that the vibrating mesh allows stronger dust particle-mesh interaction than the static mesh, and the interaction becomes stronger as the vibration velocity increases, allowing for higher dust collection efficiency. Interestingly, the smaller vibration amplitude outperforms the larger amplitudes. To explain this observation, the Stokes number of the dust particles, which governs the behavior of particles in the ambient flow is calculated.

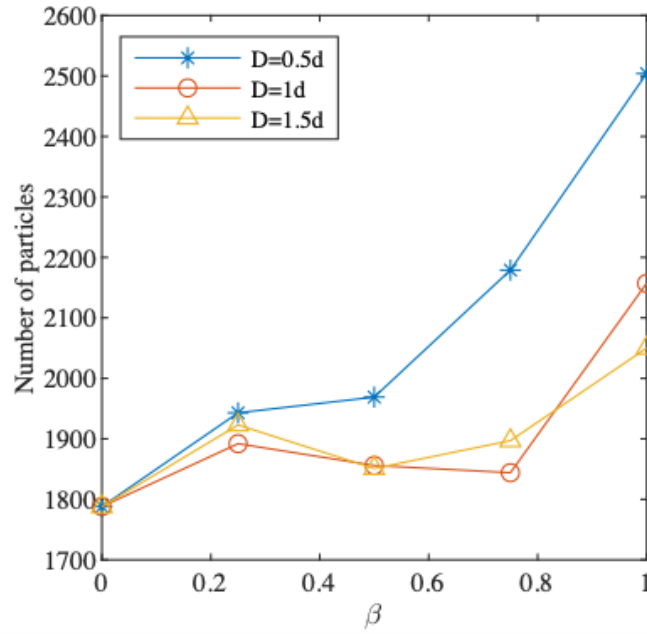*Figure 30. The effects of vibration conditions on the dust particle-mesh interaction.*

For larger Stokes number, particles do not follow the streamline of the flow perfectly but rather travel on straight paths. For a smaller Stokes number, the particles tend to follow the motion of the surrounding flow. Dust particles are more likely to travel along the streamline. As a result, vibrating mesh provides a favorable environment for particle-mesh interaction by actively intercepting the particles on the lateral side of the wires, which otherwise would flow past the static wire. The degraded performance of the larger amplitudes may be explained by the fact that a larger flow region is perturbed in front of the wire, allowing the dust particles to be deflected and escape through the gap between the wires.

Effects of dust concentration. During the continuous miner operation, coal dust concentration in the mine face may fluctuate through the cutting cycle. To effectively evaluate the performance sensitivity of vibrating mesh scrubbers to the dust concentration in the intake air, the dust concentration is simulated at a range of values from 40 mg/m^3 assessed in the previous section to 20 and 10 mg/m^3. The vibration amplitude is fixed and frequencies are sampled. For each dust concentration scenario, the number of captured dust particles at various values is normalized to ones obtained from the static mesh. As shown in Figure 31, similar increasing trends suggest that the advantage of the vibrating mesh over static mesh is not sensitive to the dust concentration. Therefore, the excellent performance of the vibrating mesh may be persistent throughout the dust cleaning cycle as the dust concentration in the air fluctuates.
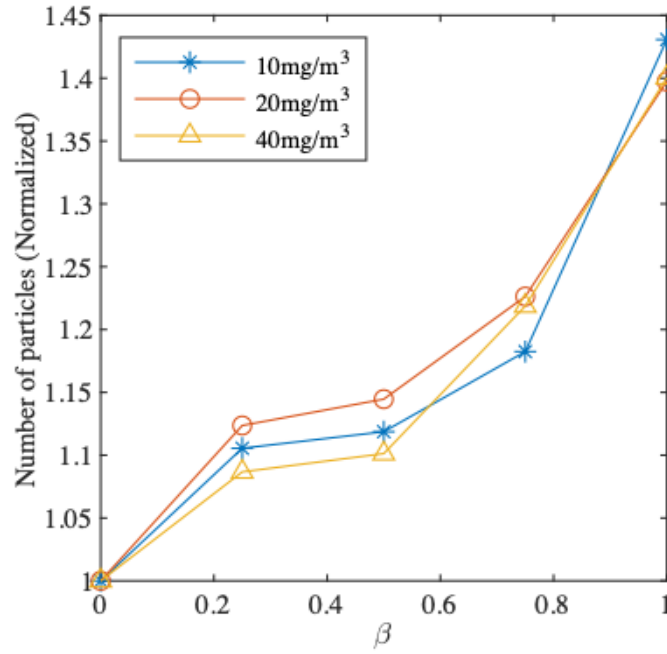
Figure 31. The effects of dust concentration on the dust particle-mesh interaction.
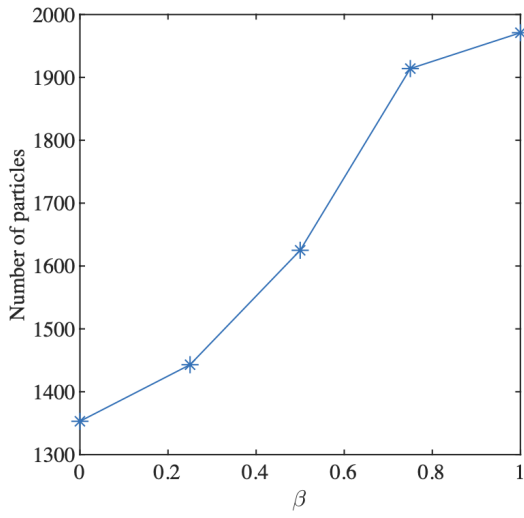
Effects of mesh aperture. The mesh aperture is closely related to clogging. With a small aperture, the agglomerates formed by the combination of water droplets and dust particles can easily block the opening of the mesh. Although a larger aperture effectively avoids this issue, fewer dust particles could be captured as fewer wires could be fitted into the mesh screen. Given the importance of mesh aperture parameter, the current work evaluated the performance of the vibrating mesh and the static mesh with various mesh apertures. In addition, the dust collection performance of screens with aperture is evaluated. Here, the vibration amplitude was fixed, and different frequencies were sampled. The number of collected dust particles is plotted in Figure 32. For the smaller aperture values, the vibrating mesh does not have an advantage over the static mesh, as shown in Figure 32a. This is because the net opening area of the mesh screen is so small that the static mesh can intercept almost all the dust particles, whereas the vibrating mesh allows some of the particles to pass through as openings may be created during a vibration cycle. However, using this small aperture can be impractical under certain circumstances as it increases the potential for clogging, which is a common issue associated with the static mesh scrubber. As for the larger apertures of (Figure 32b-d), the number of dust particles exhibits a linear relationship with the normalized vibration velocity. These data indicate that the vibrating mesh can ideally achieve equivalent dust particle-mesh interaction strength and hence the same collection efficiency with a larger aperture than the static mesh, thus mitigating the clogging problem.
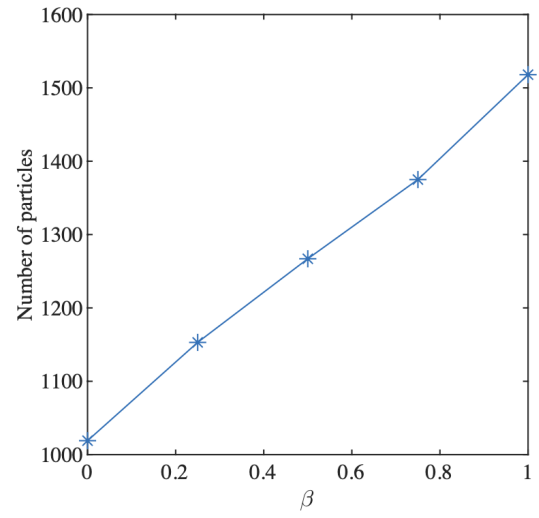
37
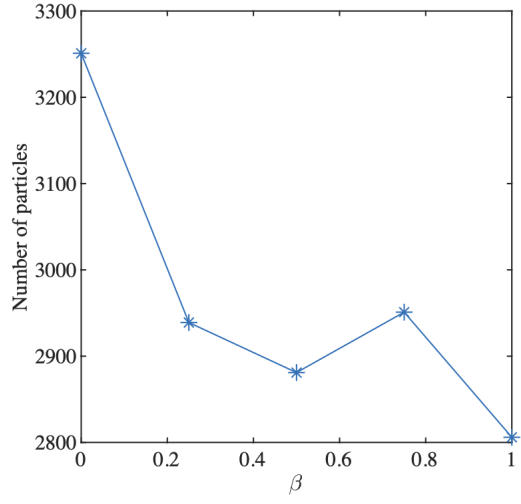
(a) $A_p = d$
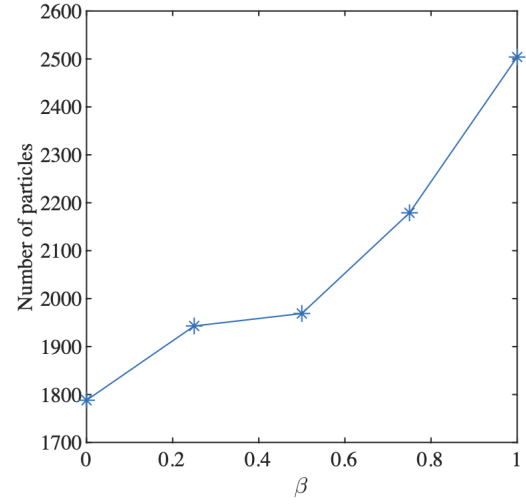
(b) $A_p = 2d$

(c) $A_p = 3d$

(d) $A_p = 4d$

Figure 32. The effects of mesh aperture on the dust particle-mesh interaction.

3.2.1.3.   Nozzle Spray Model (Air-Water Two-Phase Flow)

Modeling Approach: Apart from dust particle-mesh interaction, the mesh wetting condition (or total wetted area) may also significantly affect the scrubber collection efficiency, as mentioned in the previous section, larger wetted area leads to a higher probability for dust particles to be captured by the water droplets on the mesh screen, given the same degree of particle-mesh interaction. In this section, we focus on the simulation of the wetting condition of the mesh screen. The water spray nozzle is modeled to compare the wetted area of the mesh screen under different vibrating conditions. For simplicity, dust particles are not included, making the flow an air-water two-phase system.

Nozzle spray is a highly complicated event, which can be characterized by the breakup of liquid jets or sheets. Based on the distance from the nozzle orifice, the spray can be divided into a spray formation region and a spray region, as shown in Figure 33. In the spray formation region, the liquid jet (a.k.a. liquid core) exiting the nozzle disintegrates into large liquid bodies and ligaments (a.k.a. primary droplets) due to the instabilities that arise from the gas-liquid interface. Following this primary breakup, shear mechanisms transfer primary droplets into smaller and more uniform spherical droplets further downstream (spray region). Thus, the impact mechanism of the spray on the mesh screen depends on which spray region it is located. Due to the complex mechanism of the entire lifecycle of the nozzle spray, the current study models the spray formation region and the spray region separately. As such, simplified spray models are formulated assuming the nozzle has a full-cone profile. The objective is to compare the performance of the vibrating mesh and static mesh in each spray regime and identify important parameters that might affect the wetting condition of the mesh wires.
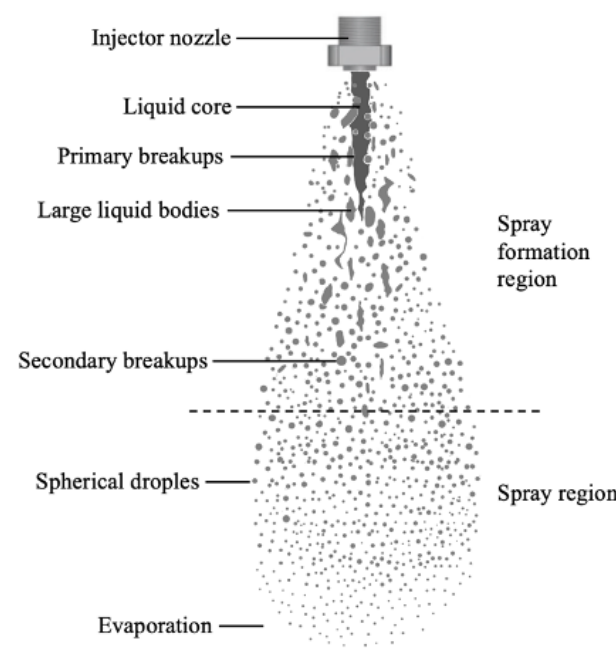

Figure 33. Nozzle spray flow schematic.

Since the mesh screen is most likely located in the spray region where spherical droplets have already been formed, we first considered the mesh wetted by droplet spray. The simulation domain is shown in Figure 34. The geometry is based on the channel in Figure 28, with the channel length extended to three times the channel height to accommodate the nozzle spray.
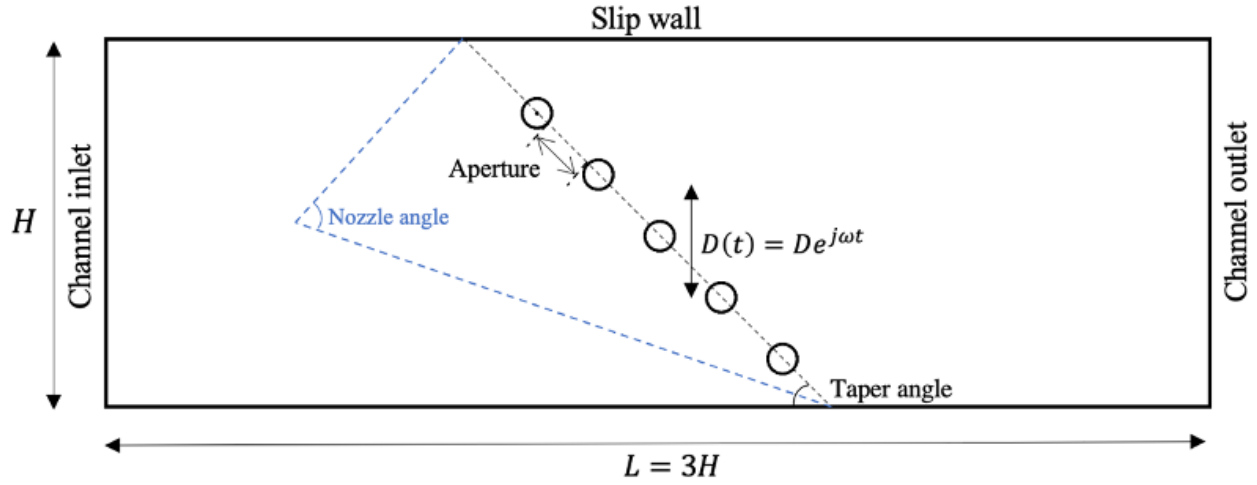
Figure 34. Droplet spray simulation domain schematic.

Table 4 summarizes the parameters associated with the simulation domain configuration and spray nozzle. The spherical water droplets were assumed to have a uniform size once released from the nozzle. The initial speed of the droplet was calculated as a function of volumetric flow rate of the nozzle, and the diameter of the orifice, assuming the flow is continuous and straight. The full-cone nozzle is represented by a point in the simulation domain with a spray angle of 60°. The nozzle was located on the centerline of the channel with a certain distance from the mesh and slightly tilted such that the droplet spray fully covers the span of the mesh screen, as shown in Figure 34. The droplets were ejected at an interval of 1e-4 seconds with the number of droplets determined as the ratio of the volume per ejection to the volume of the spherical droplet, assuming the droplet diameter to be 500 microns. The ejected droplets were consistently distributed across the nozzle angle.

Table 4. Droplet spray simulation domain and nozzle parameters.

Property	Value
Channel height, H	0.128 m (0.42 ft)
Channel width	H
Channel length, L	3H
Inlet airflow speed, U_{in}	4 m/s
Aperture, A_p	2d
Nozzle cone angle	60°
Nozzle flow rate, Q	1 gpm
Nozzle orifice diameter, d_o	0.003048 m (0.12 inch)
Droplet diameter	500 μm
Droplet release interval	1e-4 s
Number of droplets per release	24
Droplet velocity, V_d	34.6 m/s

As discussed in the previous section, an intuitive Lagrangian method, based on the Newton's second law, can be used to describe dust particle movement under the drag force imposed by the airflow. Similarly, the Lagrangian approach may be utilized to track individual water droplets as dimensionless particles. Nevertheless, due to the large volume fraction of water droplets, the effects of droplets on the surrounding airflow field may no longer be neglected. Therefore, a Euler-Lagrange method (i.e., Discrete Element Method) was employed to model a water droplet-air two-phase flow system. In the Eulerian framework, the laminar flow relationships are used to describe the continuous air phase as a Newtonian flow. The flow governing equations are spatially and temporally discretized by the same approach. Additionally, the contribution of the droplets to the flow was considered by adding a force equal to the drag force experienced by the droplet to the body force term in the fluid momentum equation. Newton's second law then calculates the motion of the droplets in the Lagrangian framework. The droplet particle Reynolds number can be calculated.

If we estimate the relative velocity by using the difference between the initial droplet velocity (34.6 m/s) and the ambient airflow velocity (4 m/s), the Reynolds number then becomes 1034.3. At such a high Reynolds number, the Stokes drag law is no longer valid. Alternatively, the standard drag correlations in COMSOL Particle Tracing Module are used to calculate the drag force on the droplet particle. Similarly, the Saffman law is not appropriate for calculating shear-induced lift force due to the large droplet particle Reynolds number. At a high particle Reynolds number, the lift coefficient is quite small, and further

decreases with a larger particle Reynolds number. Therefore, the lift force was neglected for droplet simulation. The inter-particle interaction was not modeled to relieve the computational burden. The droplets were assumed to be captured by the wire if the distance from the wire surface is smaller than the droplet radius. The wetted area was approximated by the total wetted arc length of the wire, assuming the center of the droplet rides on the circumference of the wire, Figure 35. The simulation lasts for 0.02 seconds, and the wetted area is calculated at the end of the simulation.
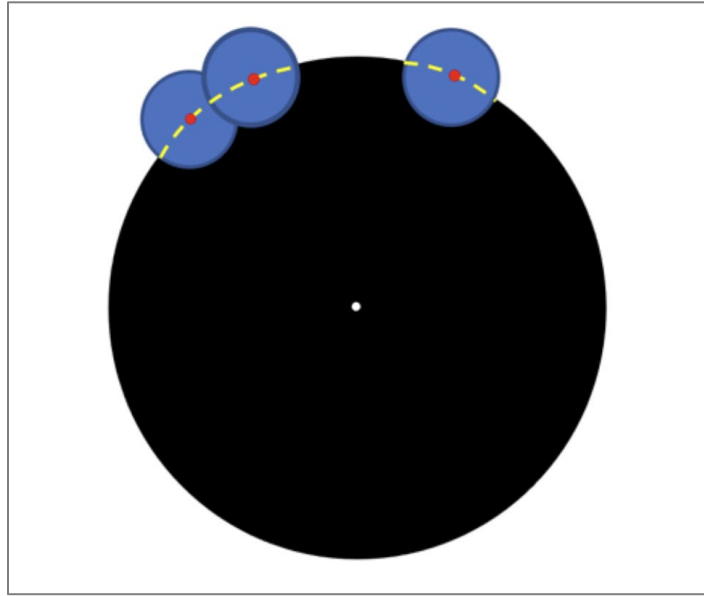

Figure 35. Illustration of the wetted area calculation. The black and blue solid circles represent mesh wire and droplet, and the yellow dotted line denotes the wetted area (arc length).

Results: Parametric studies on the effects of vibration conditions, nozzle flow rate, and mesh aperture on the mesh screen wetting condition were performed. Results are presented below.

Effects of vibration conditions. As listed in Table 3, the nozzle flow rate was set to be 1 gpm, and the mesh aperture was 2*d*. Here, we define another parameter to normalize the vibration velocity of the mesh screen by the droplet velocity. Displacement amplitudes are assessed with different frequencies. Four more data points for each amplitude with the corresponding frequencies to cover the frequency range were assessed for dust particle-mesh interaction. Figure 36 shows the velocity contour plot with water droplets for *D=d* simulation for demonstration. The calculated wetted area plotted in Figure 37 indicates that mesh vibration makes the wetted area larger than the static mesh and the wetted area becomes larger as the vibration velocity increases. Vibration allows the droplets to be coated on a wider range of the wire surface, leading to an increased wetted area. The difference between the different vibration amplitudes is minimal, Figure 37. Unlike the dust particle-mesh interaction results shown in Figure 30, the performance of the larger amplitudes (i.e., 1 and 1.5) is not compromised because the droplet has much higher inertia (larger Stokes number) than the dust particle. Hence, the droplet tends to continue along its trajectory rather than being deflected by the perturbation from the larger vibration amplitudes.
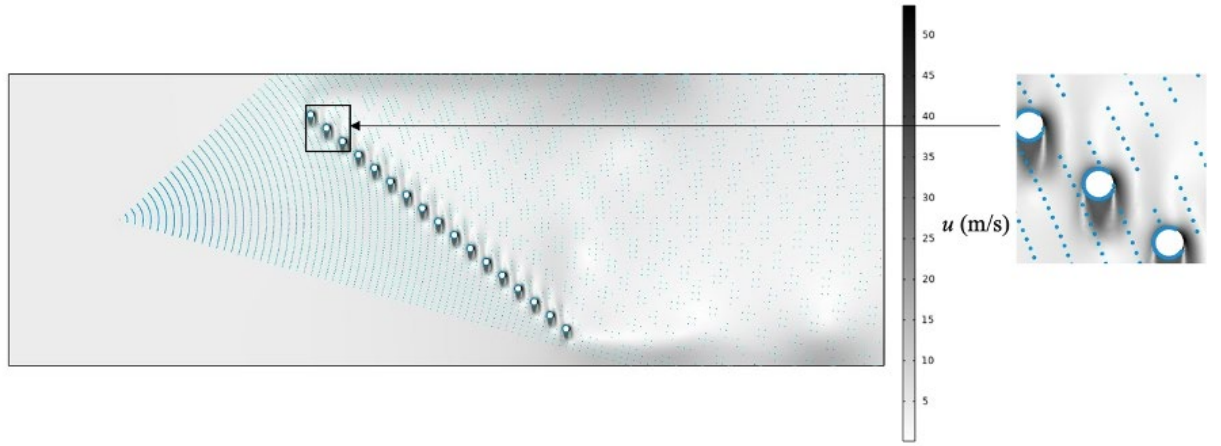
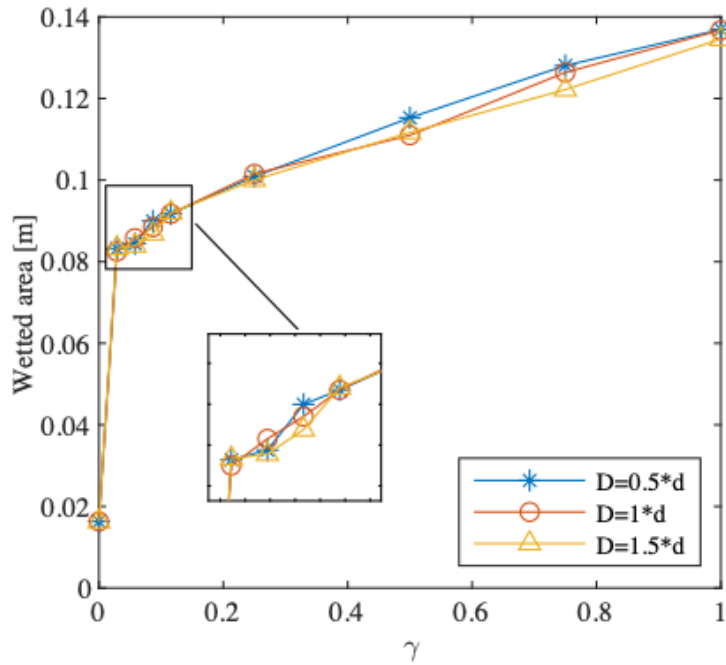*Figure 36. Velocity contour plot and droplet particles.*

Figure 37. The effects of vibrating conditions on the wetting condition (normalized vibration velocity was plotted against the wetted area).

Effects of nozzle flow rate. In this section, the 1 gpm nozzle flow rate assessed in the previous section was decreased to 0.5 and 0.25 gpm to compare the wetted area of the vibrating mesh and the static mesh under different nozzle operating conditions. The droplet velocity (i.e., nozzle flow speed) is fixed at 34.6 m/s by decreasing the orifice outlet diameter. The number of droplets released each time becomes half and a quarter of the 1 gpm case, which means the droplet density in the air is smaller. As observed in Figure 38, the difference between different vibration amplitudes becomes larger as the nozzle flow rate decreases. A larger displacement amplitude increases the total wetted area of the mesh screen when the nozzle flow rate is low. This result could be explained by the small droplet density in the air, in which case a larger vibration amplitude can collect droplets in larger proximity, thereby increasing the wetted area. Therefore, a larger vibration amplitude is more beneficial when the nozzle flow rate is low.

(a) 0.5 gpm   (b) 0.25 gpm
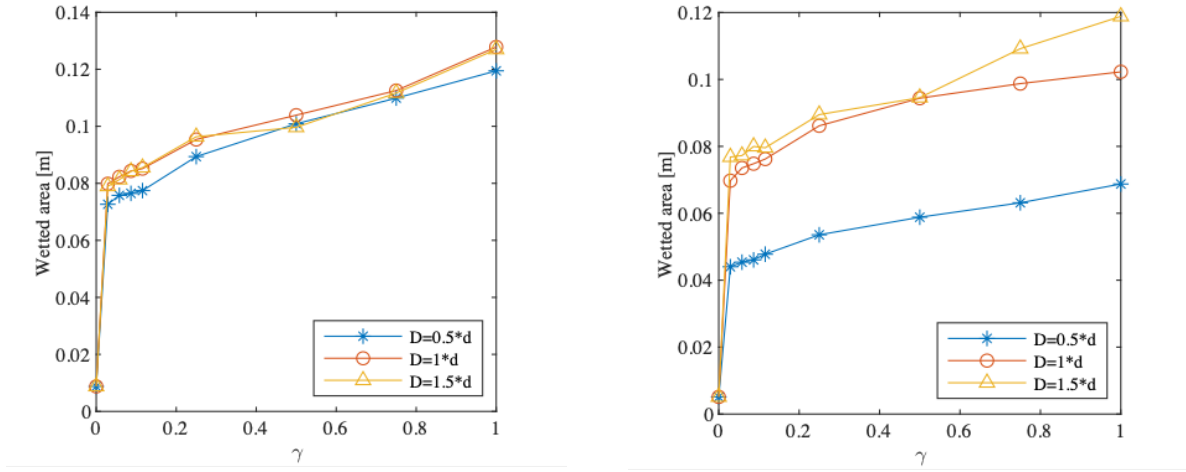
Figure 38. The effects of nozzle flow rate on the wetting condition (normalized vibration velocity plotted against the wetted area).

Effects of mesh aperture. We then determine the effects of mesh aperture on the wetting condition of the vibrating mesh. In addition to the results presented in the previous sections, the mesh wetted area was also assessed. The vibration amplitude was fixed at a standard value, and frequencies corresponding to normalized vibration velocity of the mesh equal to 0.25, 0.5, 0.75, and 1 are sampled. The nozzle flow rate was set to be 0.25 gpm. Unlike the dust particle-mesh interaction simulated earlier in this section (see Figure 32), the mesh aperture does not compromise the advantage of the vibrating mesh, as shown in Figure 39. Vibrating meshes have larger wetted area than their static counterparts with smaller aperture. Therefore, replacing the static mesh with the vibrating mesh with a larger mesh aperture to mitigate clogging still makes sense from the wetting condition perspective.
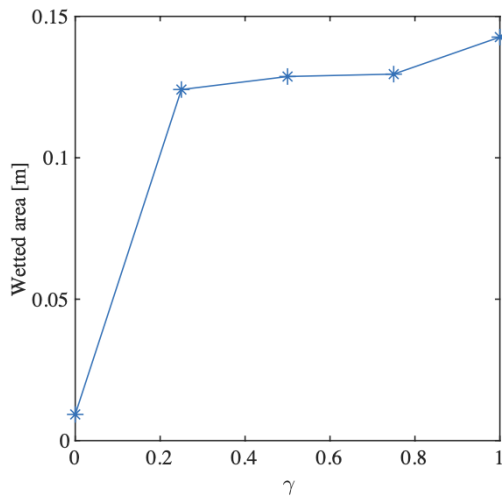
(a) $A_p = d$

(b) $A_p = 2d$

(c) $A_p = 3d$

(d) $A_p = 4d$

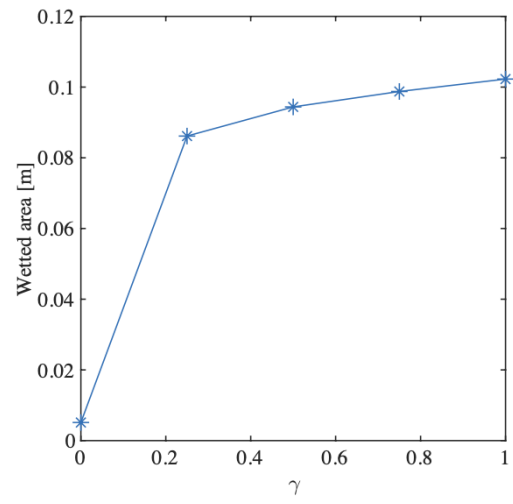*Figure 39. The effects of mesh aperture on the wetting condition (normalized vibration velocity plotted against the wetted area).*

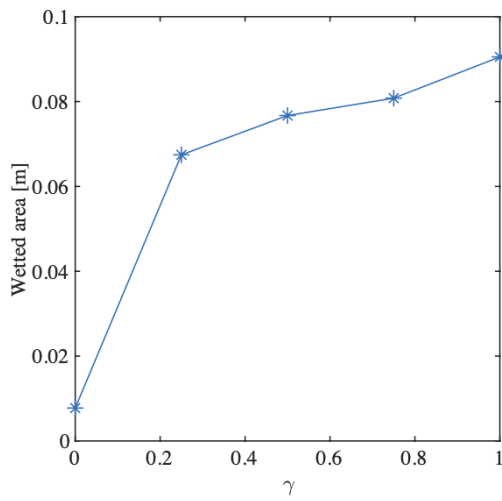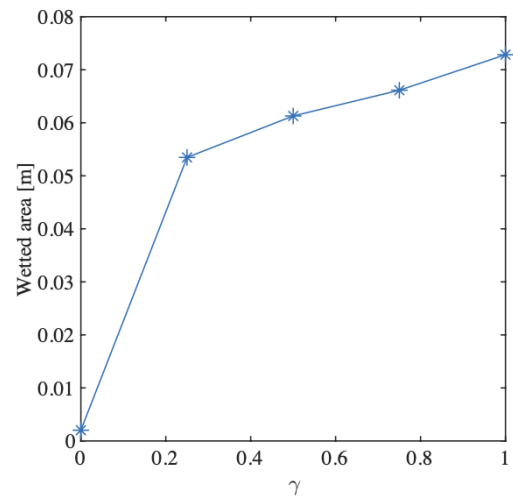### 3.2.1.4. Water Jet Model

Modeling Approach: In this study, a water jet model was constructed to further evaluate the mesh wetting conditions in the spray formation region. The large liquid bodies are simplified to a water jet with a diameter twice of the droplet (1 mm) and identical initial velocity (34.6 m/s). Three mesh wires are used to model the local effect of the spray impact, and the water jet is assumed to be normal to the mesh. Figure 40 shows the 2D simulation domain where a cylindrical nozzle with a rectangular cross-section pumps the water jet into the domain from its left boundary. The rest of the domain boundaries are set to be open.
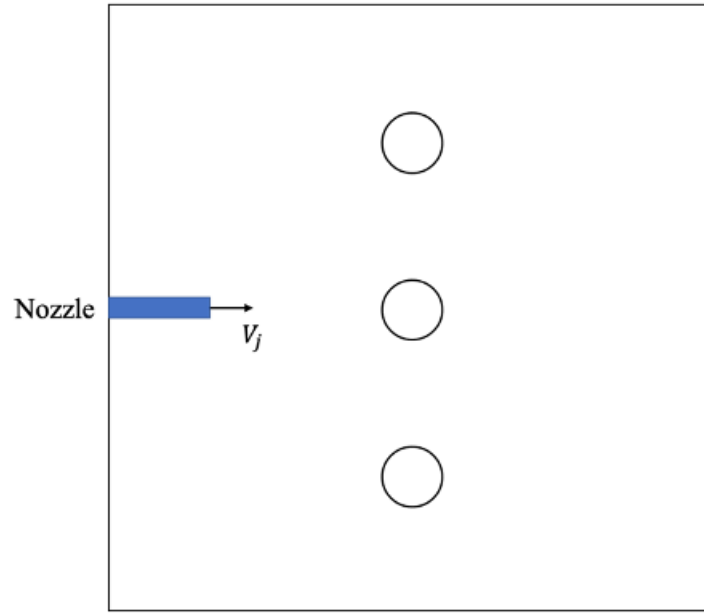
Figure 40. Water jet simulation domain schematic.

The flow is modeled as a separated two-phase flow (a.k.a. stratified two-phase flow) since a clear interface presents between the water jet and air, which are immiscible with each other. The Reynolds number of the water jet is calculated using the wire diameter. Because of the high Reynolds number of the water jet and the turbulent nature of the two-phase flow, the flow is treated as turbulence. The revised RANS model is employed to model the dynamics of the turbulent two-phase flow due to its robustness and excellent performance near the solid surface. The turbulent model is coupled with the phase-field method, which is used to track the evolution of each phase.

Results: For the water jet model, the effect of vibration conditions on the wetted area of the mesh screen was assessed. Since a large amplitude would leave the vibrating wire unimpacted by the spray during the vibration cycle, the displacement amplitude was set to be fixed. Rather, the vibration frequency was varied (larger was not assessed due to the demanding computational requirements). The mesh aperture was set to be fixed. To obtain an idea of the wetting condition, we integrate the volume fraction of water on the wire surface to represent the wetted area. The simulations were run for a duration of 3e-3 seconds. The wetted area was integrated in time and plotted in Figure 41 with respect to the average wetting

condition throughout the simulated water jet impact period. Overall, the wetted area is increased with the vibration velocity, see Figure 41. To visualize the flow pattern, the volume fraction of water for different values at 1e-3, 2e-3, and 3e-3 seconds is plotted in Figure 42, Figure 43, and Figure 44. According to these results, the diverged flow passing the wire is drawn towards the centerline of the wire and ends up merging as the vibration velocity is increased. Further increasing the vibration velocity, the merged jet flow wraps the wire and creates a larger wetted area. This flow phenomenon could be explained by the pressure drop behind the wire due to vibration. The jet flow is driven towards the backside of the wire by the pressure gradient, which becomes stronger as the vibration velocity increases.
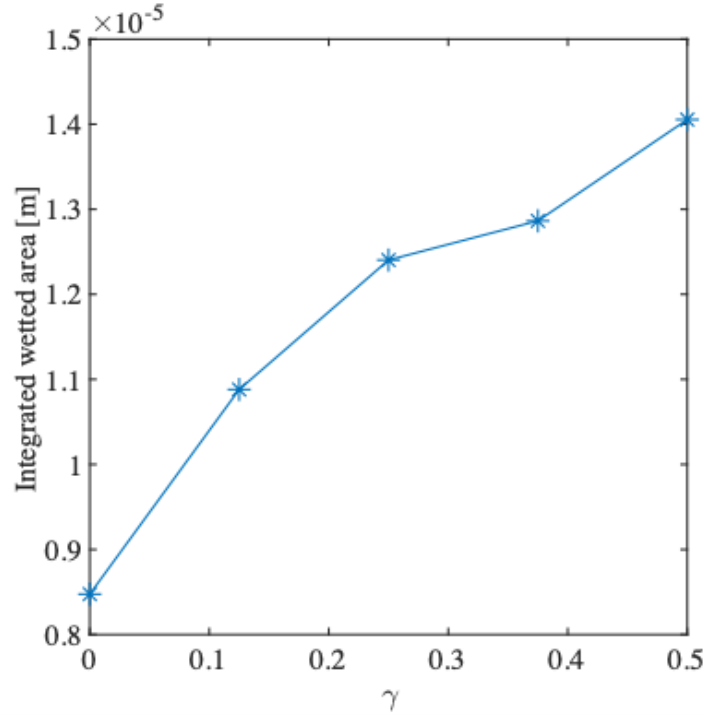
Figure 41. The effects of vibration velocity on the wetted area (normalized vibration velocity plotted against the integrated wetted area).

(a) $\gamma = 0$ (b) $\gamma = 0.125$ (c) $\gamma = 0.25$ (d) $\gamma = 0.375$ (e) $\gamma = 0.5$
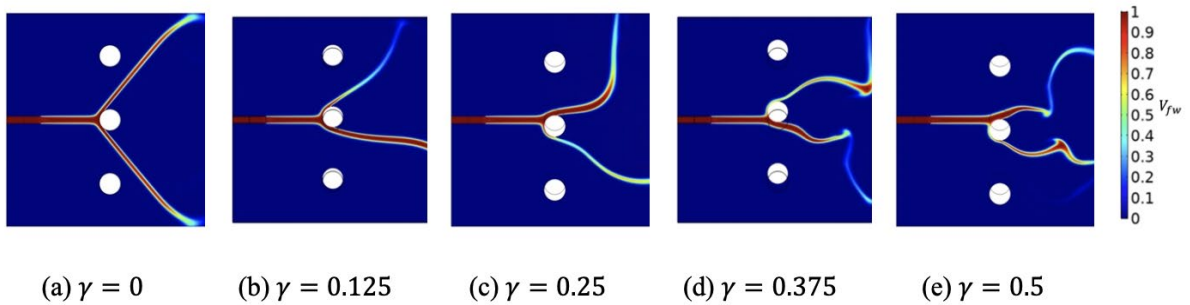
Figure 42. Volume fraction of water at 1e-3 seconds.

(a) $\gamma = 0$ (b) $\gamma = 0.125$ (c) $\gamma = 0.25$ (d) $\gamma = 0.375$ (e) $\gamma = 0.5$
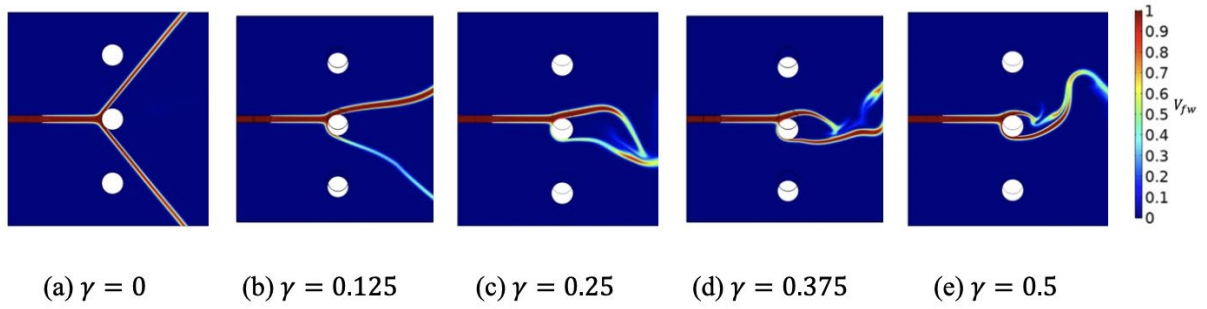
Figure 43. Volume fraction of water at 2e-3s.

(a) $\gamma = 0$ (b) $\gamma = 0.125$ (c) $\gamma = 0.25$ (d) $\gamma = 0.375$ (e) $\gamma = 0.5$
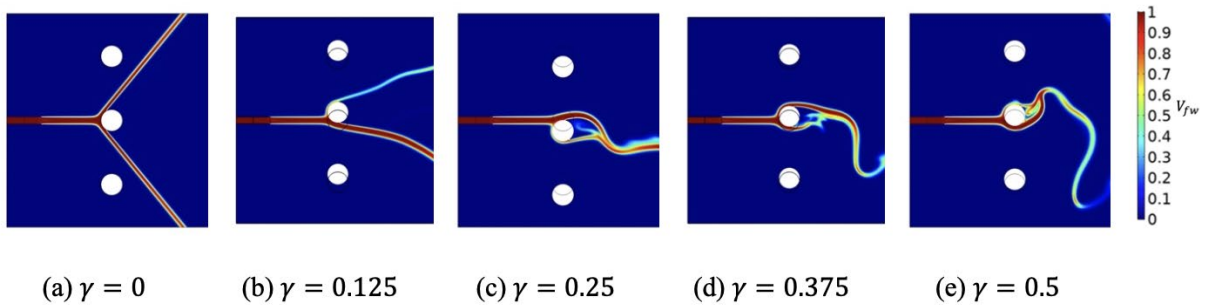
Figure 44. Volume fraction of water at 3e-3 seconds.

3.2.1.5. Three-Phase Flow Model

Modeling Approach: Following the model development and simulation of two-phase flow systems, a simplified three-phase flow model was formulated, incorporating both the dust particles and droplet models as described above, to evaluate the performance of the vibrating mesh screen in a more realistic setup. Figure 45 and Table 5 show the simulation domain, dust particles, and water droplets parameters.
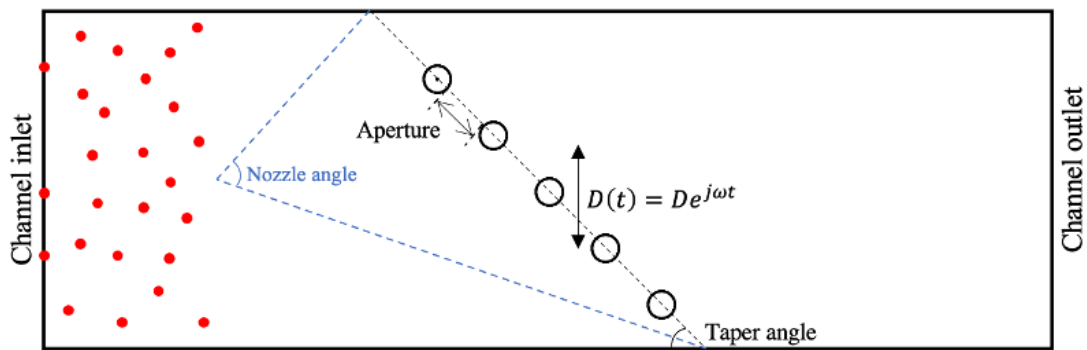
Figure 45. Three-phase flow model schematic.

48

Table 5. Three-phase flow simulation domain, dust, and droplet parameters.

Property	Value
Aperture, A_p	2d
Wire diameter, d	0.003048 m (0.12 inch)
Mesh screen taper angle	40°
Number of wires	17
Inlet airflow speed, U_{in}	4 m/s
Dust concentration, C_o	40 mg/m^3
Nozzle cone angle	60°
Nozzle flow rate, Q	1 gpm
Nozzle orifice diameter, d_o	0.003048 m (0.12 inch)
Droplet diameter	500 μm
Droplet release interval	1e-4 s
Number of droplets per release	24
Droplet velocity, V_d	34.6 m/s

Given the COMSOL limitations in modeling dust particle and water droplet interaction, we first simulated their motion together without considering the interaction. Nevertheless, the dust particles are still affected by the air perturbation caused by the droplets. Then, the interaction was considered in the post-processing stage, where the dust particle and droplet position are exported along with their corresponding particle size information at each time step. In an external MATLAB code, the collision between the dust particles and droplets was assessed. If the distance between the center of a dust particle and a droplet is smaller than the combination of their radius, the dust particle collides with the droplet. The dust particle sticks to the droplet once captured, assuming the adhesion force is strong enough, and the motion of the droplet is assumed to be unaffected by the attached dust particle due to their vastly different size and weight. Dust particle-water droplet collision may occur in the air or on the mesh screen. Following a particle-droplet cohesion, the horizontal coordinates of the droplet in the subsequent simulation time step are used to distinguish between cohesion locations. The dust particle is assumed to be captured on the mesh if the horizontal coordinates of the droplet remain unchanged. On the contrary, different horizontal coordinates indicate cohesion in the air.

For the three-phase system simulation, the dust particles are released from the left boundary of the simulation domain for a duration of 0.029 seconds. The simulation lasts for 0.087 seconds, which allows

the released dust particles to pass through the mesh screen. Dust particle and droplet parameters are consistent with those in Table 5. We experimented with two different nozzle operating schemes. The first scheme turns on the nozzle as soon as the dust particles enter the domain and keeps it on throughout the simulation. The second scheme only keeps the nozzle on for 0.02 seconds to saturate the mesh before the dust particles are released such that there will be no interaction between the droplets and dust particles in the air.

Results: Prior results using simplified models have demonstrated that vibrating mesh possesses an advantage over static mesh in terms of dust-particle interaction and mesh wetting condition. To augment these findings from, this section presents simulation results of a more complex three-phase flow model. The vibrating mesh with various velocity magnitudes was compared with the static mesh. We only assessed the performance of the vibrating mesh with the amplitude given its advantage for dust particle-mesh interaction compared to larger amplitudes. We found that over 99% of the dust particles could be intercepted by the nozzle spray and do not reach the mesh if operation scheme one is executed at such high nozzle flow rate. For operating scheme two, all the dust particles are captured by the mesh screen. The collection efficiency (ratio between the number of captured dust particles and total particles) is plotted in Figure 46. The efficiency increases sharply as the mesh starts to vibrate and keeps increasing as the vibration frequency becomes higher. The trend essentially follows the prediction in Figure 30 and Figure 37, which suggests the importance of the dust particle-mesh interaction and the wetting condition on the dust collection efficiency. Interestingly, this result suggests that in an actual operation, the flooded-bed scrubber could operate between scheme one and two (i.e., the nozzle is turned on intermittently). Therefore, dust particles would be captured both in the air directly by the water spray and by the mesh screen, which makes the collection efficiency higher than what is shown in Figure 46. By replacing the static mesh with vibrating mesh, more dust particles could be captured by the droplets on the mesh screen so that less water is required to achieve the desired dust collection efficiency (e.g., 90%). Alternatively, a larger mesh aperture (e.g., 10- or 20-layer mesh rather than 30-layer mesh) may be used by the vibrating mesh to mitigate the clogging issue without compromising the collection efficiency.
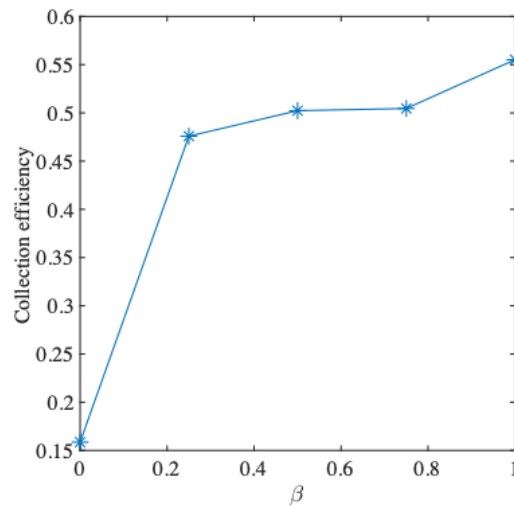

Figure 46. The effects of vibration velocity on the dust collection efficiency.

3.2.1.6.   Summary and Design Implications

CFD simulations were performed to compare the dust collection efficiency between the vibrating and static mesh and evaluate the influence of key design parameters on dust and water droplet behavior. We employed a dust-laden air model to assess the interaction between dust particles and mesh screen and two nozzle spray models to simulate the mesh wetting condition in spray formation region and spray region under various scrubber operating conditions. To further evaluate the performance of the vibrating mesh in a more realistic setup, we developed a simplified three-phase flow model combining the dust-laden air and droplet spray two-phase models. From the cumulative results of the modeling study, the following conclusions were obtained:

1. For the dust particle-mesh interaction, simulation results suggest that the mesh screen vibration can enhance the interaction and higher vibration velocity leads to a stronger interaction. Under the same vibration velocity, a smaller vibration amplitude is more efficient than the larger amplitudes assessed. A further investigation found that vibration allows the vibrating mesh to achieve an equivalent degree of interaction to the static mesh with a larger mesh aperture, thus effectively mitigating the clogging problem. Simulations also suggested that the advantage of the vibrating mesh is barely affected by the dust concentration which tends to fluctuate throughout the cleaning cycle.

2. For the mesh wetting condition simulation facilitated by the droplet spray model, a larger wetted area was found for the meshes with higher vibration velocity while vibration amplitude and mesh aperture make little difference. As for the spray formation region, the vibration was found to curl the flow passing the mesh wire to its centerline due to the low-pressure region generated behind the wire, allowing the flow to wrap around the vibrating mesh wire and create a larger wetted area. The better performance found for vibrating mesh in terms of the two decisive factors on the dust collection efficiency, namely dust particle-mesh interaction and wetting condition, theoretically proves its advantage over the static mesh.

3. Using the three-phase flow model, the water spray itself was found to have a strong dust collection capacity if the nozzle is kept on continuously. Nevertheless, operating the nozzle intermittently along with the mesh screen can ideally achieve the same dust collection efficiency with reduced water consumption. It was demonstrated that the mesh vibration can improve the collection efficiency of the mesh screen. As a result, less water consumption is required for the vibrating mesh screen compared to the static mesh screen. If the mesh clogging is a more critical concern, the vibrating mesh may achieve the same collection efficiency with a larger mesh aperture, mitigating agglomerates accumulation that leads to clogging.

3.2.2. Multi-Physics Modeling System Modeling for Energy Harvesting

3.2.2.1. Modeling Objectives

The parameter characterization CFD model described in Section 3.2.1 provides a detailed framework for a complete three-phase flow model that mimics the dust scrubber section in the continuous miner. It gives a very close approximation of the experimental test setup and provides both qualitative and semi-quantitative information on how various design parameters will influence performance. The simulations performed on this model give a multivariable analysis of dust collection efficiency for different condition such as, dust concentration, water nozzle flow rate, mesh aperture etc. Extending from these results, additional CFD modeling was performed to quantifying and comparing mesh performance for different frequencies that exist in the operational frequency range of the continuous miner. Additionally, we seek to compare the performances of the mesh screen for different axes of vibration and find an optimal frequency range that can be harvested from the continuous miner's ambient vibrations and imparted on the mesh screen. As such, additional multi-physics modeling was conducted to simultaneously evaluate the parameters relevant to both energy harvesting and dust capture.

The same simulation model was used to investigate the scrubber performance for the frequency range of 0-1000 Hz. This frequency range was selected based on the findings from the in-mine vibration measurement study described in Section 3.1. With our energy harvesting approach, one of the operational frequencies is imparted on the mesh screen and is utilized as the vibrating frequency in the scrubber section. In this section, we utilize our three-phase model framework and investigate the change in dust collection efficiency within the operating frequency range of the continuous miner. This approach does not require the multivariable analysis that was performed earlier, but uses the established simulation model to quantify mesh screen efficiency for the vibration frequencies of interest. The model was modified accordingly, and the complete details of the new model are following.

For the initial modeling, a two-phase numerical model was developed. In the model, dust laden air is flown through a chamber fitted with the mesh filter. The interaction between the dust particles and the mesh screen was observed as we introduced vibration on the mesh screen. Vibration was stimulated in two separate orthogonal directions: X (parallel to the mesh screen), and Y (perpendicular to the mesh screen) unlike the earlier CFD studies. A harmonic sinusoidal profile was provided to the mesh screen as its vibrational displacement in the two directions. The vibrational frequency was swept from 0 Hz to 1000 Hz in both X, and Y coordinates individually and the effect of frequency was independently explored for the two directions. Data from this study was used, first, to evaluate the effects of inducing vibrations on the mesh screen, and second, identifying the optimal vibration characteristics i.e. frequencies and the vibration directionality, that can be induced on the mesh screen for better interaction of dust particles and mesh screen.

3.2.2.2. Dust Particle-Mesh Interaction

In our simulation model, we considered dust particles as individual points in space with specific position, mass, and physical properties. We introduced the dust particles into the air chamber and simulated their entrainment in the air flow with a mesh screen included in the simulation domain to capture any dust particles that encountered it. To isolate impact of vibration, we initially excluded the nozzle spray typically used to wet the mesh surface in a real continuous miner. Instead, we assumed that the mesh surface is completely wet, causing dust particles that came into contact with it to adhere. We used

particle-mesh adhesion to implicitly estimate droplet-particle interactions, assuming that dust particles become trapped upon contacting the mesh screen.

In the next stage of our simulation model, we incorporate a nozzle spray into the model to wet the mesh screen, enabling us to more accurately model droplet-mesh interactions within the scrubber environment, as seen in Figure 47. Using the updated model, we calculate the wetted area of the mesh and assess the number of dust particles that adhere to it as a result of the nozzle spray.
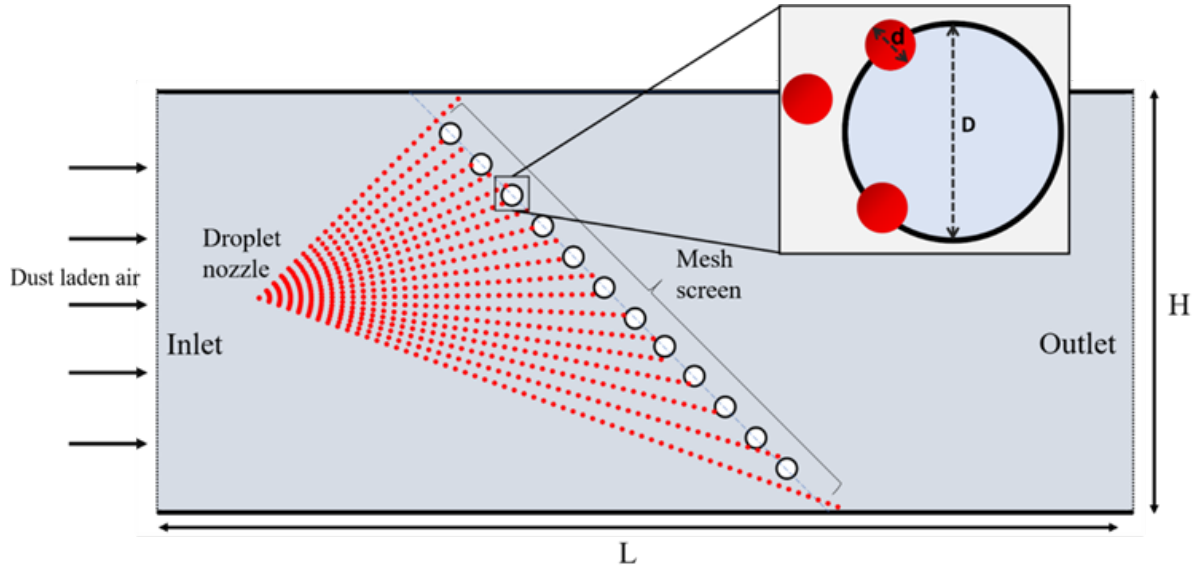

Figure 47. The CFD simulation domain snapshot.

The 2-D simulation was performed using a scrubber channel, with the domain mesh illustrated in Figure 48. The left boundary is the airflow inlet with only a horizontal velocity component of 4 m/s. The right boundary is the outlet with ambient pressure. The mesh screen is represented with the array of small circular wires in the middle of the channel domain which is tilted at an angle of 45°. The mesh is composed of a single layer of circular wires of diameter, d. The gap between the adjacent wires represents the net opening for the dust particles to pass through. It is parametrized by a metric called *Aperture*. The benchmark mesh screen was composed of 17 wires of d diameter each with an aperture of *2d* mm. The channel length is twice the channel height. The geometric details of the channel domain and the mesh screen are presented in Table 6. A no-slip boundary condition was applied on the mesh screen surface for the air flow, while a slip boundary condition is applied to the top and bottom boundaries of the channel to ensure that the effects of the wall are negligible.
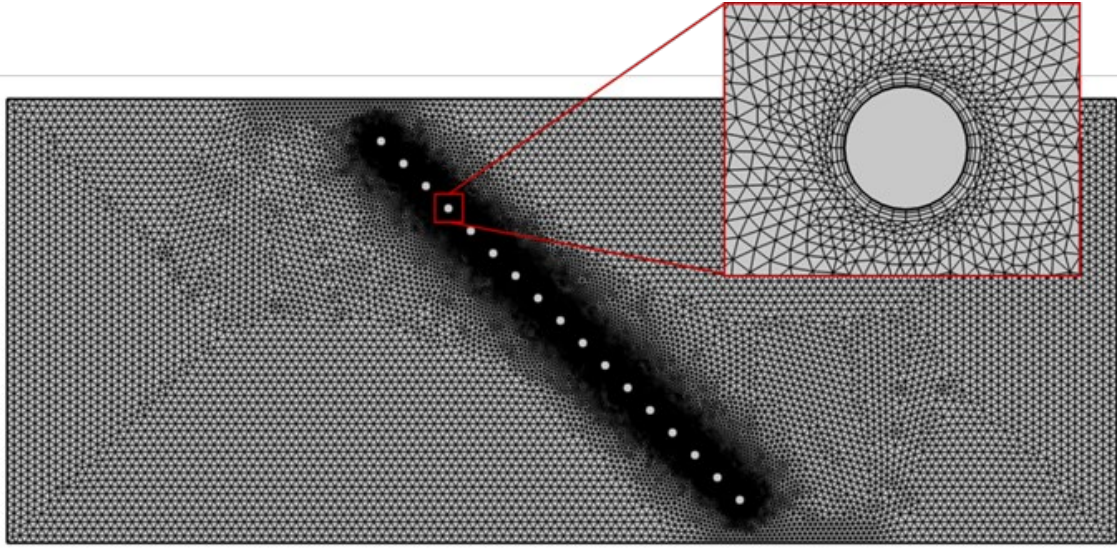
Figure 48. The domain mesh with triangular elements and boundary layers around the curve.

Table 6. Simulation Parameters.

Parameter	Value
Channel length 'L'	0.84 ft
Channel height 'H'	0.42 ft
Air inlet speed 4 m/s	4 m/s
Mesh inclination angle	45°
Wire diameter	0.01 ft
Number of wires	17
Aperture	0.02 ft

The concentration of dust in the scrubber domain was determined by the release characteristics of the dust particles. We assumed that the dust particles were entrained in the airflow and released from the left boundary with the same initial velocity every 1e-4 seconds. The particles have a diameter ranging from 1 to 75 microns, with an average of 25 microns. The dust concentration in the domain is set at 40 mg/m^3, and the dust particle density is estimated to be 1200 kg/m^3. Using these specified values, we calculated the volume fraction and quantity of dust particles released per unit time. Since the dust-laden flow is such that the dust does not exert force on the airflow but is itself affected by it, we treated it as a sparse flow or one-way coupled flow. Due to the low volume fraction of dust particles in the airflow, we have ignored the dust particle-particle collisions to save computational costs. We model each dust particle as a point

mass of a specific size and calculate its trajectory using the Newtonian formulation. Brownian motion is negligible due to the large size of the particles. The lift force acting on the particles was determined using Saffman's law and applies to particles in shear flow near the mesh surface, acting in the direction of the flow velocity gradient. To obtain an accurate lift force calculation, we computed the mean Reynolds number. In addition, the drag force experienced by the dust particles acts in the opposite direction to their relative velocity with respect to the fluid. Given the low relative velocity of the dust particles and the airflow, we appropriately used Stoke's law to calculate the resulting drag force.

The fluid domain was discretized by triangular elements, but the wire-mesh's curvature required additional refinement. To account for this, boundary layers were added which transition into the unstructured triangular elements as shown in Figure 48. The vibrating mesh screen was accounted for by using a deforming domain handled by arbitrary Lagrangian-Eulerian method. Time marching of the governing equations was done by the generalized alpha method. For the dust particles, a stick boundary condition was applied on the mesh wire surface and a bounce condition was applied on the rest of the channel boundaries. Simulations were run for a duration of 0.1s, and the resulting data was used to determine the number of dust particles collected by the mesh. By comparing the number of dust particles collected by the vibrating mesh to the benchmark static mesh, we quantified the strength of the particle-mesh interaction.

3.2.2.3.   Droplet-Mesh Interaction

Next, we incorporated a spherical droplet spray that wets the mesh surface. The nozzle was modeled as a cone shape with a 60° angle and positioned to ensure full coverage of the mesh screen. We assumed a continuous and straight flow, and calculated the initial velocity of the droplet particles based on flow rate and the nozzle orifice diameter. The simulation domain was similar to that shown in Figure 47, but with additional length to fully capture the droplet spray-wetting. This setup accommodated the required y-direction space to cover the entire mesh screen, which is not feasible with the dimensions listed in Table 6. The simulation parameters of the model are detailed in Table 7. We used normal mathematical relations to calculate the release characteristics of the droplets, and distribute consistently across the nozzle angle.

Table 7. Simulation parameters.

Parameter	Value
Channel length 'L'	1.26 ft
Channel height 'H'	0.42 ft
Droplet speed 4 m/s	34.6 m/s
Nozzle spread angle	60°
Droplet diameter	500 μm

Individual droplets can be tracked as dimensionless particles using a Lagrangian technique based on Newton's second law. However, owing to their large volume fraction, the effects of droplets on the surrounding airflow can no longer be ignored in this case. To model a water droplet-air two-phase flow

system, the Discrete Element Method was used. In the Eulerian framework, the laminar flow relationships are used to describe the continuous air phase as a Newtonian flow. Additionally, the contribution of the droplets to the flow was considered by adding a force equal to the drag force experienced by the droplet to the body force term in the fluid momentum equation. Newton's second law then calculates the motion of the droplets in the Lagrangian framework.

Because the difference between the initial velocity of the droplets (34.6 m/s) and the ambient airflow (4 m/s) is very high, Stokes drag law which was used in the previous section could no longer be used. So, the standard drag correlations in COMSOL Particle Tracing Module were used to calculate the drag force on the droplet particle. Because of the large droplet particle Reynolds number, Saffman's law for lift is also invalid, and the lift force is ignored in droplet modeling. Droplet-droplet interaction was not modeled in order to reduce computational load. For the water droplets, a stick boundary condition was added to the mesh surface. The total wetted arc length of the wire was then used to approximate the wetted area, and the center of the droplet was assumed to be riding on the circumference of the mesh wire. The simulation lasts 0.02 seconds, and the total wetted area is calculated at the end.

Then we combined both the two-phase flow systems: dust-air and droplet-air, to formulate a simplified three-phase flow model. This includes the dust particles described in the earlier section with the water droplet spray for a more realistic evaluation of the performance of the vibrating mesh screen.

The interaction between the water droplets and the dust particles cannot be modeled in COMSOL. So, we first simulate the two systems, dust-air, and droplet-air, independently neglecting the dust-droplet interaction. The interaction between the droplets and the dust particles is considered in post-processing in an external MATLAB code. The position coordinates and the corresponding size information of the dust particles and the droplets were exported to MATLAB and the interaction was assessed. The droplets wet the mesh wire and capture the dust particles that collide with the droplet that rides the mesh wire. The distance between the center of the droplets and the dust particles was calculated and if that distance was smaller than their added radius, the dust particle was considered captured. Once captured the dust particle is assumed to not affect the motion of the droplet.

For this three-phase model, the droplets were released for a duration of 0.02 seconds and the simulation for dust particles lasted for 0.1s allowing them to pass through the mesh screen. The droplet spray would saturate the mesh screen and the dust particles then pass through the wetted mesh and get captured only at the area wetted by droplet spray.

3.2.2.4.   *Vibration Efficiency Analysis*

Figure 49 shows the efficiency of dust collection over the mesh screen at the end of the simulation. Efficiency is calculated from the number of dust particles captured at the surface of the wetted mesh and the number of particles released into the domain per unit time, as follows:

$$\mu = N_{captured}/N_{released}$$

μ = collection efficiency
$N_{captured}$ = number of dust particles captured at the wetted mesh screen per unit time
$N_{released}$ = number of dust particles released into the domain per unit time
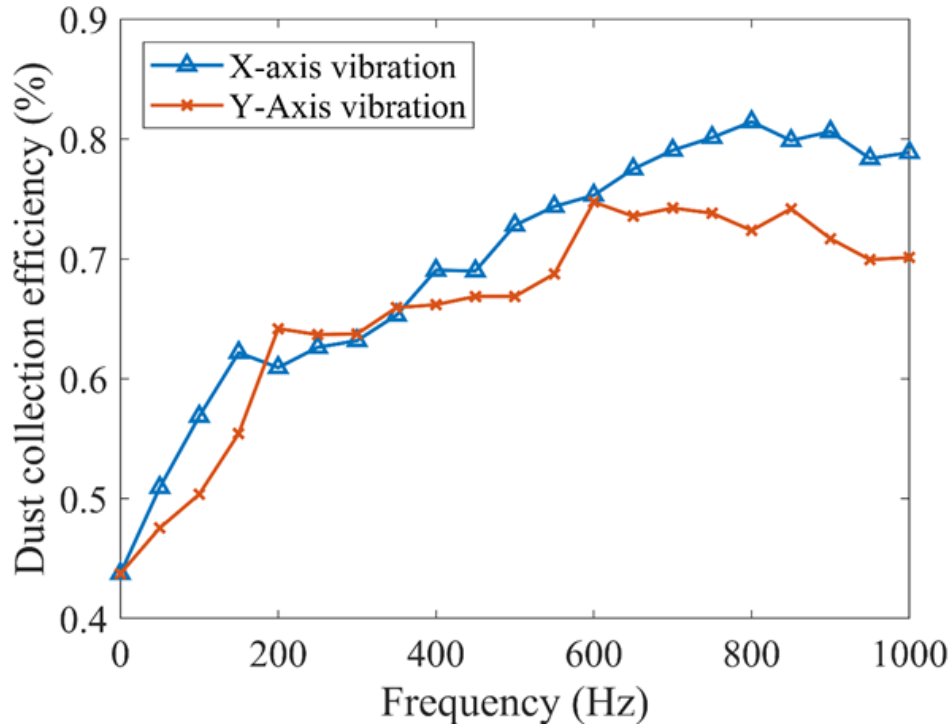
Figure 49. Collection of dust against vibration frequency.

One of the aims of this study was to investigate whether introducing vibrations on the mesh scrubber screen would enhance the particle-mesh interaction and, subsequently, the dust collection efficiency of the system. The efficiency of the vibrating mesh screen was assessed for vibrations ranging from 0 Hz to 1000 Hz in both X and Y directions. The dust laden flow depicting dust particle-mesh interaction, and the nozzle wetting the mesh screen are shown in Figure 50 and Figure 51. The simulation results align with the initial hypothesis. The findings indicated that the vibration in X-direction, even at a frequency of 50 Hz, results in a sharp increase in dust collection efficiency at the mesh screen. The dust collection efficiency increased as the vibration frequency increased as depicted in Figure 49. However, at frequencies over 600 Hz, the increase in dust collection efficiency was observed to be smaller. It is important to note that in machines, vibrating parts operating at high frequencies have a greater risk of wear. Therefore, when designing the energy harvesting system, it is necessary to weigh the benefits of an increase in vibration frequency against the accelerated wear of the machine. Similar trend was observed in Y-direction vibrations. However, it was observed (Figure 49) that dust collection was slightly more significant for vibration in X-direction compared to Y-direction for most frequencies, and the overall impact of vibrations was stronger when it was encouraged in X-direction.
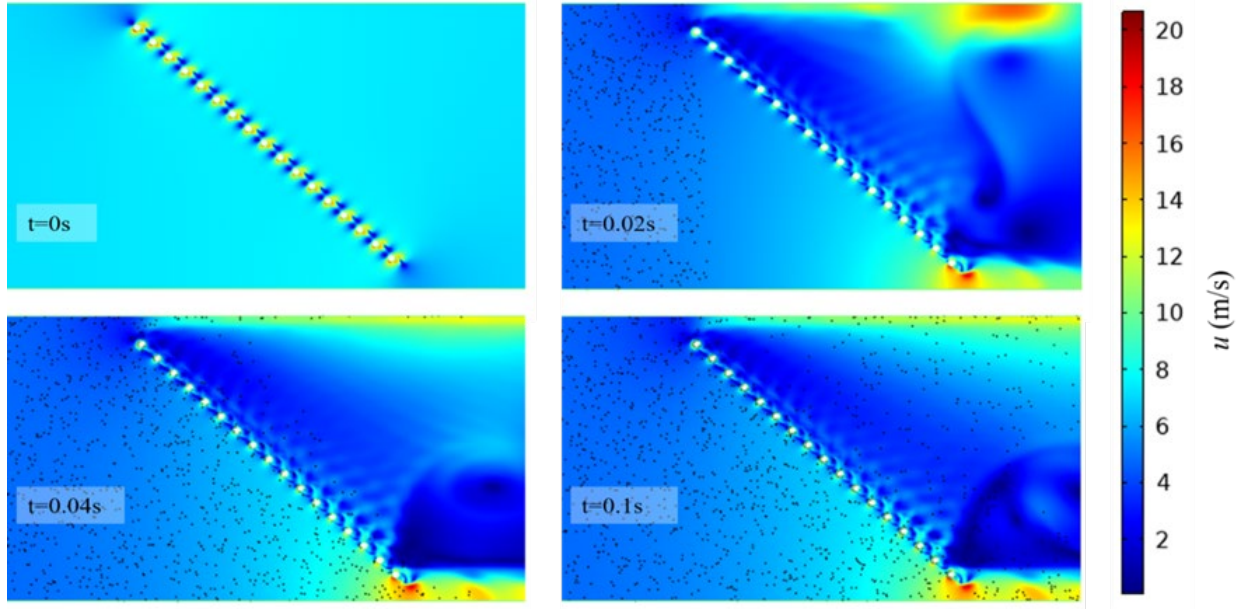
Figure 50. Velocity contour of dust-laden flow passing through the mesh screen. The air velocity is shown (in m/s) along with dust particle trajectory at different times, where t represents time.
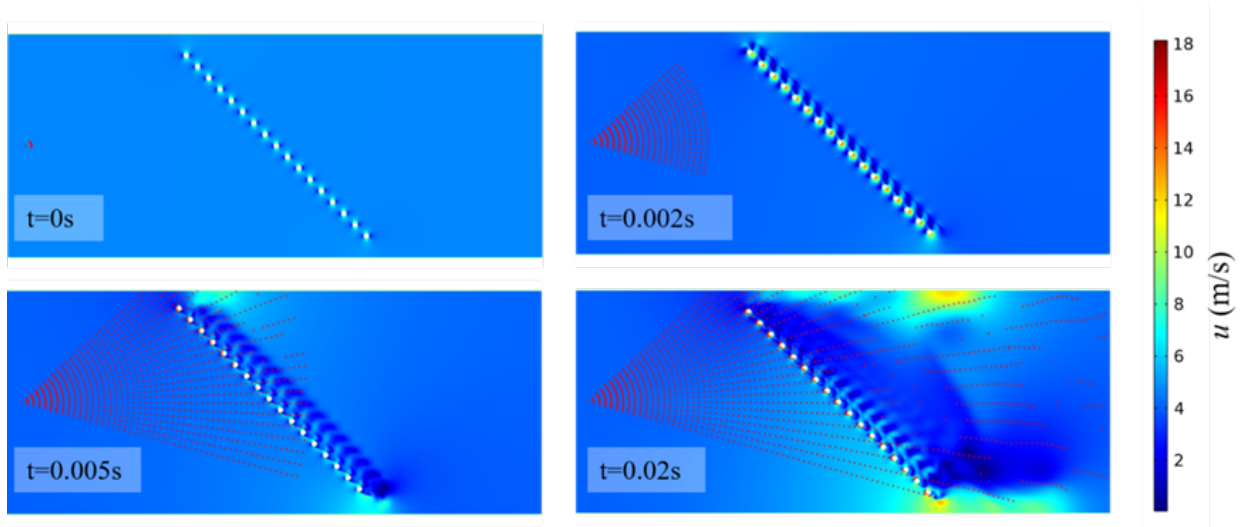

Figure 51. Velocity contour of nozzle wetting the mesh screen. air velocity is shown (in m/s) along with water droplet trajectory at different times.

3.2.2.5.   *Energy Harvesting Evaluation*

The results of these findings serve as the basis to select the optimal range of frequencies that the mesh can be practically vibrated. As we noticed that the dust collection efficiency of the mesh scrubber system increased with the introduction of vibrations, we modeled a system that vibrates the mesh screen harvesting energy from the operational vibrations of the continuous miner. An elastic base composed of springs is designed to be used for the mesh to move in a particular direction. This base would take the

shaking of the continuous miner as the source of vibrations and transmit that to the mesh screen. The mesh screen vibrates independently of the continuous miner vibration frequency. An important role here is the stiffness of the elastic base of the mesh scrubber which determines the frequency of the output vibrations. The mesh-spring-miner system is simplified in Figure 52.
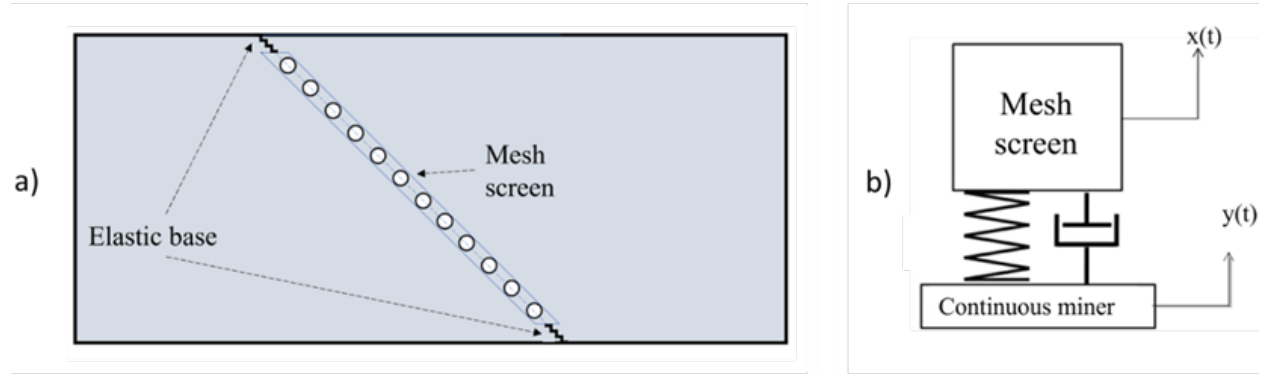

Figure 52. Simplified system model. (a) A schematic of the scrubber. (b) An equivalent lumped-parameter damped mass-spring model of the scrubber. Here x(t) and y(t) are the mesh screen and miner displacements, respectively.

In the continuous miner, as described earlier, there are several different subsystems which altogether produce a spectrum of frequencies. These vibrations are experienced at the housing (base) of the mesh screen. The elastic foundation of the mesh screen is designed in such a way that the mesh resonates at a particular frequency from all the available frequencies imparted on the mesh base. This resonant frequency is the natural frequency of the elastic system designed. The energy transmitted to the mesh is the highest when the driving frequency is equal to the system natural frequency. Consequently, if the natural frequency of the system falls into the spectrum of the frequencies available to the mesh from the continuous miner, resonance occurs and the mesh screen will culminate in primarily vibrating at its natural frequency. At this frequency, the transmissibility of force from the source (continuous miner) to the mesh screen is the highest and the natural frequency of the system is amplified. Using this model, the response of a benchmark mesh screen of 3.52 kg is computed using MATLAB using the in-mine vibration data described in Section 3.1 as input. The relationship of natural frequency, mass, and stiffness of the system is given as: $f_n=1/2\pi \sqrt{(k/m)}$, where f_n is the natural frequency (Hz), k and m are stiffness and mass of the system, respectively.

Figure 53 shows two signals that were recorded during mining operations in both time and frequency domains, which are used as the input signals to compute the response of the mesh screen with elastic base. The results shown in Figure 54 and Figure 55 illustrate the effect of stiffnesses of the base on the mesh screen vibration as it is subjected to the input excitation shown in Figure 53. The incurring of vibration also ensues losses in the system, so for simplicity, we have assumed a 5% damping ratio in the system.
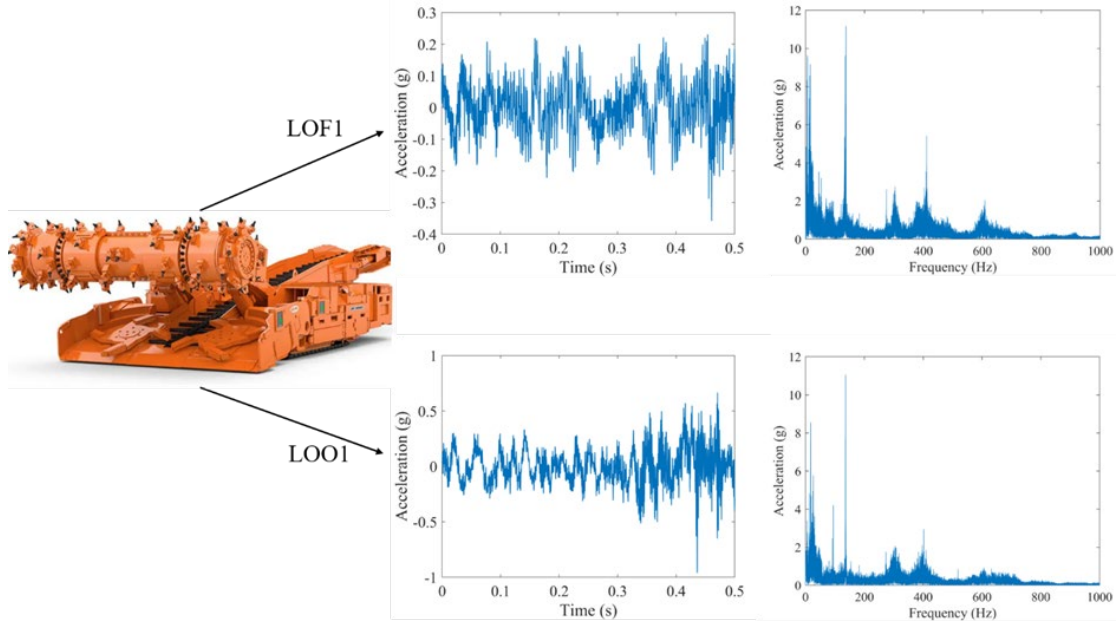
59

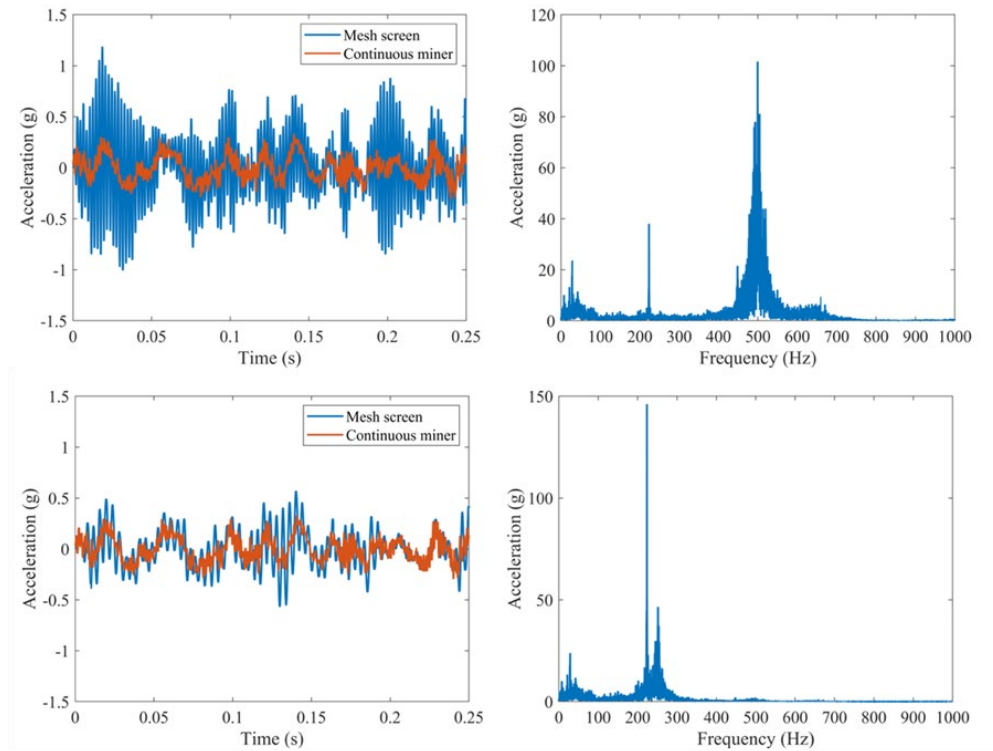*Figure 53. Two examples of operational signals in time and frequency domains: LOF1 (top) and LOO1 (bottom).*

Figure 54. Time-domain signal, and frequency spectrum of the response of the mesh screen when the input is LOO1. (a) corresponds to stiffness of k=3.48x107 N/m and (b) corresponds to k=8.7x106 N/m.
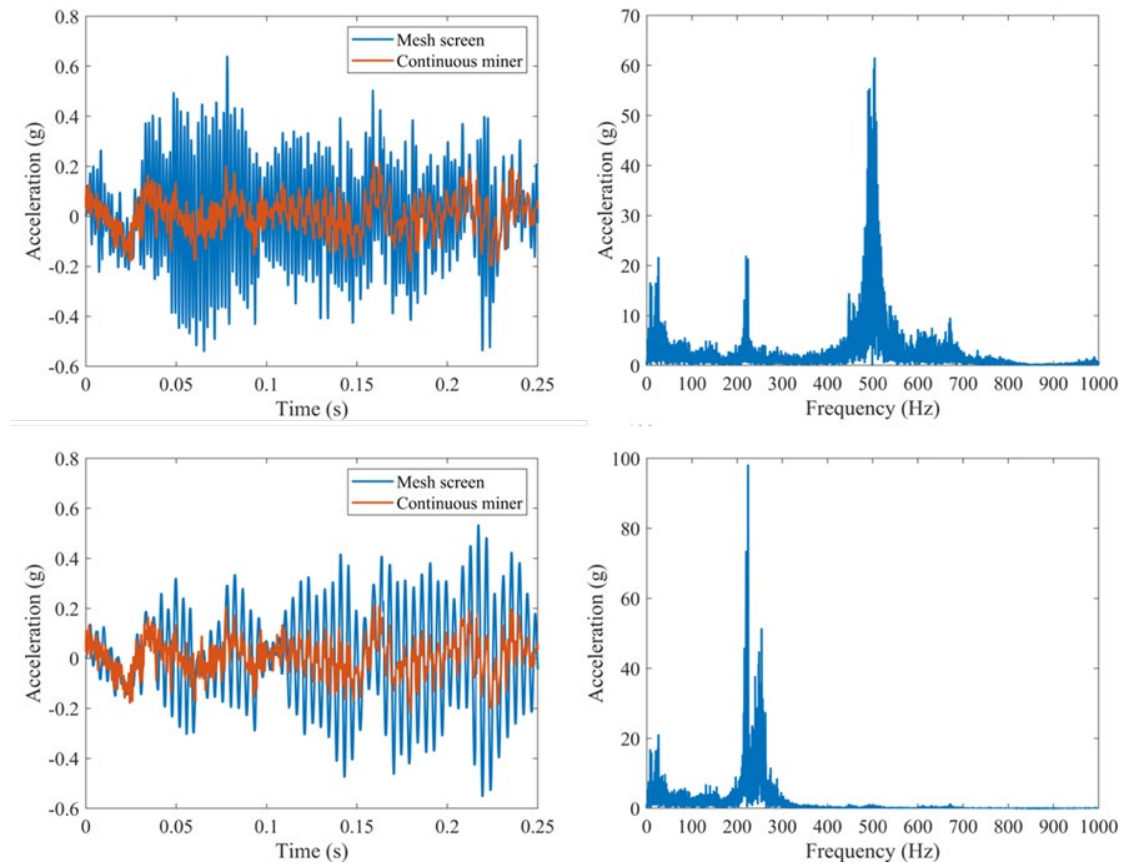
Figure 55. Time-domain signal, and frequency spectrum of the response of the mesh screen to the CM vibrations when the input is LOF1. (a) corresponds to stiffness of k = 3.48x107 N/m and (b) corresponds to k = 8.7x106 N/m.

A system with a stiffness of $k = 8.7 \times 10^6$ N/m has a natural frequency of 250 Hz, which is in resonance with the frequency spectrum of the signals L001 and L0F1. As a result, the natural frequency is amplified, and the mesh vibrates primarily at 250 Hz, as depicted in Figure 54 and Figure 55. Similarly, a system with a stiffness of 3.48×10^7 N/m has a natural frequency of 500 Hz, which is amplified due to the elastic base, allowing the mesh to vibrate at that frequency. This relationship between the stiffness of the elastic base and the natural frequency of the mesh scrubber system is given by $k = 4\pi^2 f_n^2 m$ and can be utilized to design an elastic base that induces any desired dominant frequency on the mesh screen without the need for an external source. It gives the stiffness to design the elastic base for the mesh screen that vibrates at our desired frequency. The peaks observed in Figure 54 and Figure 55 at the natural frequencies of the elastic base system confirm that the scrubber mesh predominantly vibrates at the system natural frequency, despite experiencing input vibrations of a wide range of frequencies, as shown in Figure 53. This result suggests that it is possible to design a system with a specific natural frequency that aligns with the range of frequencies encountered while the continuous miner is in operation. As a result, this system will induce vibrations in the mesh screen primarily at the desired frequency. Therefore, the presence of the elastic base will result in the mesh vibrating at the natural frequency of the system for all signals, including LOO, LOF, UFO, UOO, and UOF.

61

3.3. Laboratory Investigation of Hydrophobic Mesh Coatings

3.3.1. Experimental Setup

The objective of this task was to evaluate the effect of mesh vibration as well as different surface coatings on draining a particle-laden liquid collected on a mesh to avoid clogging. In this subtask, our experimental apparatus consists of a stainless-steel mesh, a 3D-printed frame for holding the mesh, a crank slider mechanism for vibrating the mesh, and a DC power supply for controlling the vibration. In the center of the model is a bracket which is used to hold the wire mesh as indicated by yellow in Figure 56a. This bracket is held loosely in place by the top and bottom rails (indicated by blue) which allow it to slide on one axis. On the right of the model is a DC electric motor which is used in conjunction with a camshaft (indicated by red) in order to induce vibration of the bracket. One full revolution of the camshaft causes one linear oscillation of the bracket. To keep the bracket in contact with the camshaft, a wire spring is held inside of the "holder for metal spring" on the left of the model (indicated by red). Finally, all components are held together on top of the base structure shown in green. The final apparatus is shown in Figure 56b.
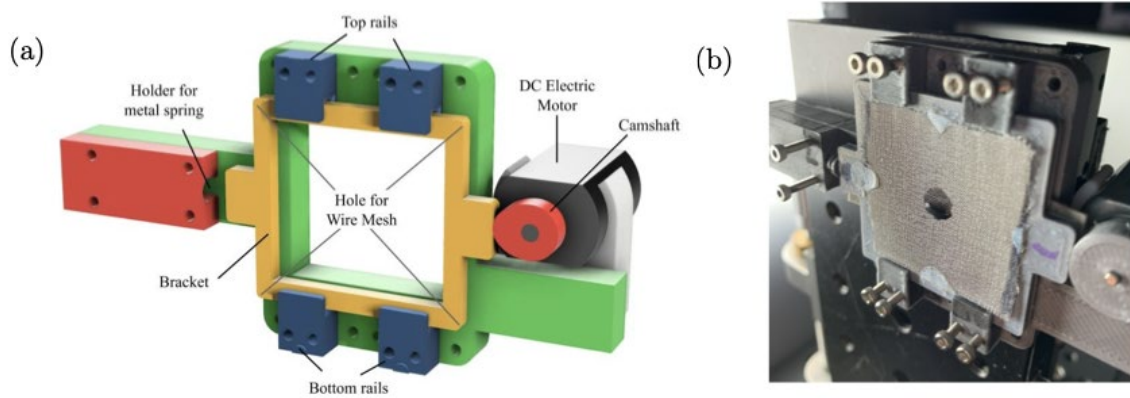

Figure 56. (a) A CAD render of the current experimental setup used to vibrate the wire mesh. (b) The experimental setup built from the CAD design.

After construction and shakedown of the experimental apparatus, we tested three different hydrophobic surface coatings in addition to the bare surface: NeverWet, Naisol, and Cytonix. In addition, we tested two different mesh sizes (80 mesh and 120 mesh) and three different frequencies for vibration (50 Hz, 100 Hz, and 150 Hz). The choice of the frequency range was based on the resonance frequency of the water drops. These values are also in close agreement with the peak acceleration frequencies found in the continuous miner system vibrational analysis.

3.3.2. Experimental Procedure

As mentioned above, we first coated the same dimensions of 80, or 120 mesh with three different coatings (NeverWet, Naisol, and Cytonix) as shown in Figure 57. Next, we made a mixture of water and fine coal dust particles with 10% solids by weight. In order to enhance the wettability of the drops, we added three different concentrations of Triton: 0.1 millimole, 0.5 millimole, and 1 millimole. After coating the surface

and making the mixture, we deposited a 20 μL drop of the mixture onto the desired mesh that was installed on the 3D-printed part. We then induced vibrations on the mesh by imposing a designated voltage through the DC power supply. The drop's behavior under vibration was recorded using a high-speed camera. We measured the limits of the drop wettability on each coating by extracting the two contact angles (the advancing angle and receding angle) at the two sides of the droplet when the drop exhibited sliding behavior under vibration. We noted that the drops did not stay on the surface for some combinations of surface coating and surfactant solution.
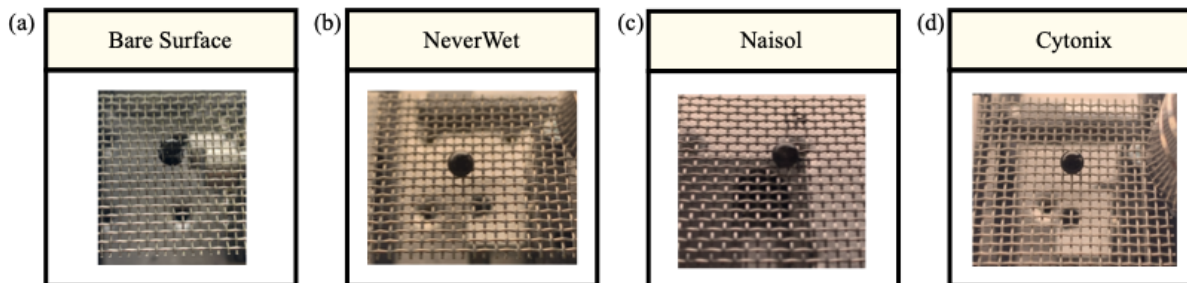

Figure 57. Four different surfaces are tested in the experiments: (a) the bare stainless-steel surface (b) the NeverWet coated surface, (c) Naisol-coated surface, and (d) Cytonix-coated surface.

3.3.3. Results and Discussion

3.3.3.1. Effect of Wettability of Hydrophobic Coatings

The goal of experiments in this subtask was to identify the optimum surface wettability to collect particles and drain particle-laden drops from the mesh. In order to collect more particles, the drops should stay on the mesh for a longer period, therefore the surface should be hydrophilic. However, to enhance the rate of drop drainage, the surface should be hydrophobic. Due to the two competing effects, we tested different coatings that provide different wettability of the surface.

In addition, we can control the surface wettability by changing the concentration of the surfactant in the liquid drop. The contact angle can be used to quantify this change; however, the contact angle is not a single value, but instead a range of values. We can measure both the advancing and receding contact angles to find this range. The advancing contact angle is defined as the maximum contact angle of a drop at a given surface, and the receding contact angle is the minimum contact angle. The difference between the advancing and receding contact angles of the drop is a measure of surface wettability. A higher difference corresponds to more sticky surfaces while a lower value refers to less sticky surfaces. Figure 58 shows time-evolution snapshots of a particle-laden drop under vibration on a non-coated surface versus a Naisol-coated surface, which is hydrophobic. As indicated in Figure 58, the hydrophobic coating results in a sliding drop in contrast with a sticking drop on the bare surface under the same conditions.
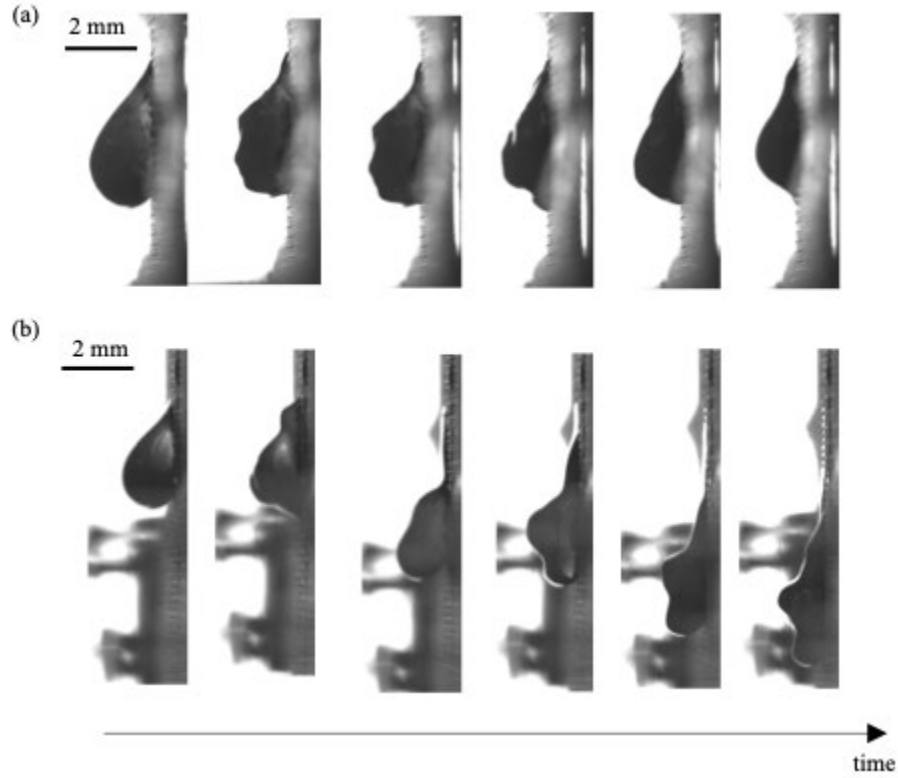
Figure 58. Time evolution snapshots of a 20 µL drop mixed with 10% weight fraction of coal particles and 0.1 millimole of Triton as surfactant under 100 Hz vibrations on (a) 80 mesh bare surface, and (b) 80 mesh Naisol-coated surface.

To find the best hydrophobic coating, we tested 3 different coatings and compared their surface wettability as presented in Figure 59. The difference between the maximum advancing contact angle and minimum receding contact angle which is denoted by $\Delta\Theta$ is proportional to surface wettability. Therefore, higher $\Delta\Theta$ corresponds to more hydrophilic surfaces while lower $\Delta\Theta$ refers to more hydrophobic surfaces. Among the four different surfaces that were tested, the Naisol-coated surface provided the best balance between a hydrophilic surface for particle collection and a hydrophobic surface for particle-laden drop drainage.

Coating	0.1mM Trition			1mM Trition		
	θ_r	θ_a	$\Delta\theta$	θ_r	θ_a	$\Delta\theta$
Bare Surface	18°	140°	122°	43°	142°	99°
NeverWet	133.63°	152.97°	19.34°	126°	159°	33°
Cytonix	131°	155°	24°	116°	155°	39°
Naisol	37.15°	88.99°	51.84°★	23°	117°	94°

$$\Delta\theta = \theta_a - \theta_r$$

Figure 59. Surface wettability for the bare surface and three different hydrophobic coatings. The desirable surface wettability is achieved by using Naisol coating.

64

3.3.3.2. Effect of Vibration

Here we investigate the effect of vibration on particle-laden drop drainage rate, by testing droplets behavior under three different frequencies: 50 Hz, 100 Hz, and 150Hz. In all cases, the drop sliding speed increases with increasing vibration frequency. It is noteworthy that for cases where the droplet is still sticky under low frequency vibration, increasing vibration frequency increases the chance of sliding by exerting higher inertia forces on the particle-laden drop. For instance, the particle-laden drop in the experiments does not slide under 100 Hz vibration on the bare surface, but it slides under 150 Hz vibration as indicated in Figure 60.
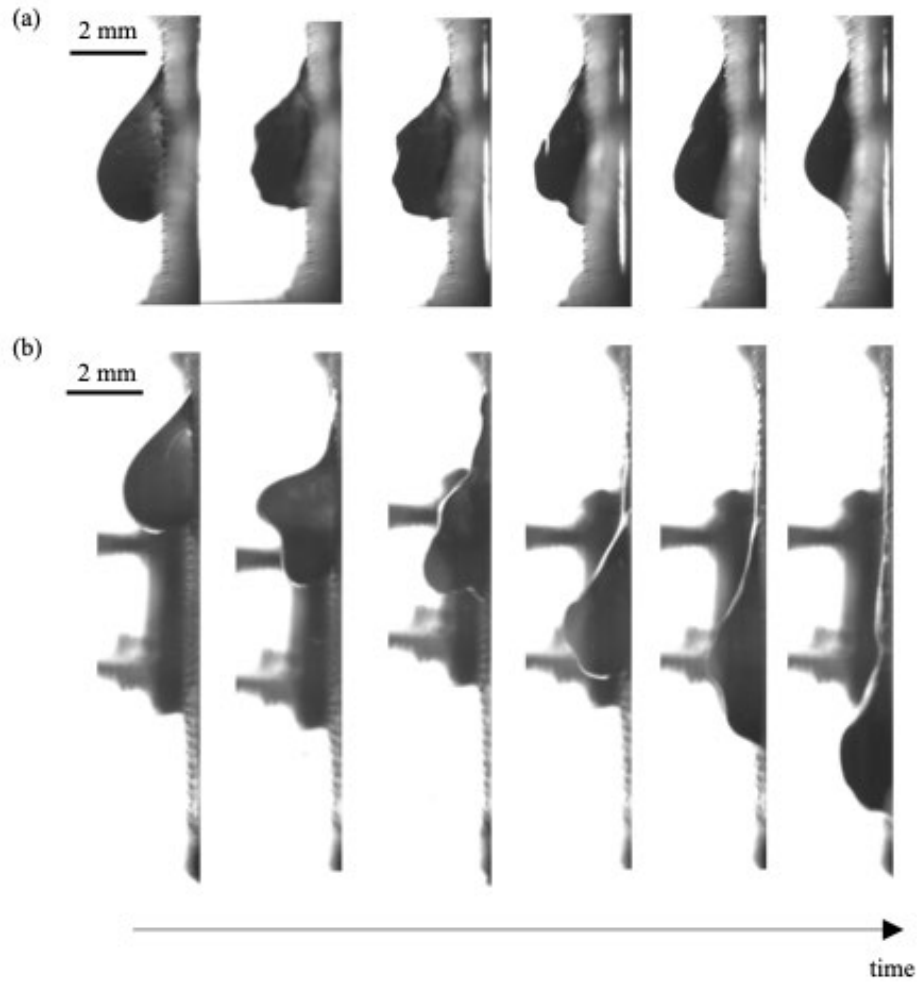

Figure 60. Time evolution snapshots of a 20 µL drop mixed with 10% weight fraction of coal particles and 0.1 millimole of Triton as surfactant on the 80 mesh bare surface under (a) 100 Hz vibration, and (b) 150 Hz vibration.

3.3.3.3. Effect of Mesh Type

Here, we investigate the effect of the mesh size on particle-laden drop by testing 80 mesh and 120 mesh. Our experiments show that drops slide faster and more frequently on 120 mesh compared with 80 mesh as indicated in Figure 61.
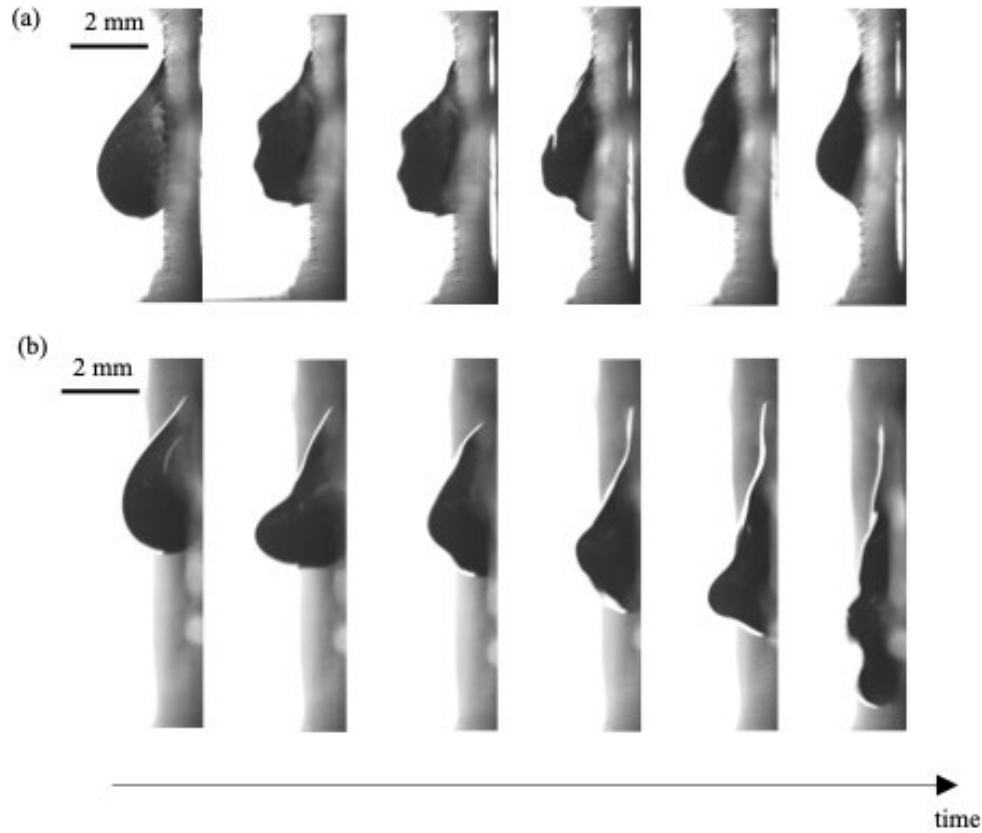

Figure 61. Time evolution snapshots of a 20 µL drop mixed with 10% weight fraction of coal particles and 0.1 millimole of Triton as surfactant under 100 Hz vibration on the bare surface of (a) 80 mesh, and (b) 120 mesh.

3.3.3.4. Concluding Remarks and Design Implications

Based on our experimental findings covered in this section, we summarize the best combination of parameters that leads to the highest rate of particle collection as well as particle-laden drop drainage to ensure maximized particle collection while avoiding clogging. In addition to the experiments presented in this section, we also tested three different concentrations of Triton as surfactant: 0.1 millimole, 0.5 millimole, and 1 millimole. Our experiments indicated that drops never stick to any surface with 0.5 millimole and 1 millimole Triton which is not desirable for particle collection purpose. Therefore, 0.1 millimole Triton is preferred. In conclusion, Naisol coating combined with 0.1 millimole Triton concentration gives the best balance for wettability of the surface. 120 mesh is preferred to 80 mesh and 150 Hz frequency is more effective than 50 Hz and 100 Hz.

3.4. Laboratory Investigation on Mesh Clogging

3.4.1. Introduction

The original patent of a flooded bed scrubber system (US 4,787,920) described a filter design as a series of nylon or plastic brushes arranged in rows within a frame that was overlaid with mesh. In modern practices, the fibrous filters consist of 10-30 layers of fine steel wool held into place by stainless-steel meshes (Colinet et al., 2013). Improvements on these filter screens are ongoing (Kumar et al, 2022; Schafrik, 2022), but little has been done to understand the clogging mechanism of these filters.

Past studies have focused on studying the pressure drop across filters under different operation parameters, such as water spray volume and airflow rate. Results showed that both impacted significantly the pressure drop across the filter due to the wetting of the filters. The characteristics of respirable coal mine dust varies due to the geographic location of coal mines as well as and source of coal dust particles. The coal rich seams of materials vary greatly in comparison to the rock heavy adjacent walls creating a variation in coal mine dust composition and grade (Pan, 20212; Colinet, 1990). Past research has focused on studying effects of wetting agents on the settling velocity of coal particles (Wang et al, 2019) and the influence on filter cake structures within closed systems (Yao et al, 2014). No work has been done, though, to evaluate the effects of filter surfaces as well as dust particle hydrophobicity property on the clogging of dust particles within a flooded-bed scrubber system. In this subtask, the mechanism of filter clogging within the flooded-bed scrubber were investigated using a laboratory-scale setup, and the setup was also used to evaluate how mesh vibration influences the clogging mechanism.

3.4.2. Materials and Methods

3.4.2.1. Test Apparatus

The laboratory scale clogging study was completed using the system shown in Figure 62. The system operates by simulating the contacting of fully wetted particles onto the flooded bed scrubber filter system in a controlled environment. In order to deliver a constant flow of slurry the group utilized a peristaltic pump that delivers 0.675 L/min of 1.6 wt% slurry through a full cone nozzle. The nozzle was chosen due to its similarity to nozzles being used in current flooded bed scrubber systems but also, due to its ability to provide even spraying and wetting of the filter pack. The mixing tank chosen was to hold 15 gallons of slurry and was under constant agitation to ensure a homogeneity. To draw airflow through the filter, a 1 hp shop vac was utilized as it could handle wet and dry mixtures but also pulled sufficient airflow through the filter (rated 50 CFM). The static pressure drop across the filter pack was monitored in real-time by a pressure transducer (510i, Testo). After the slurry passed through the filter pack it was stored in a 16-gallon drum.
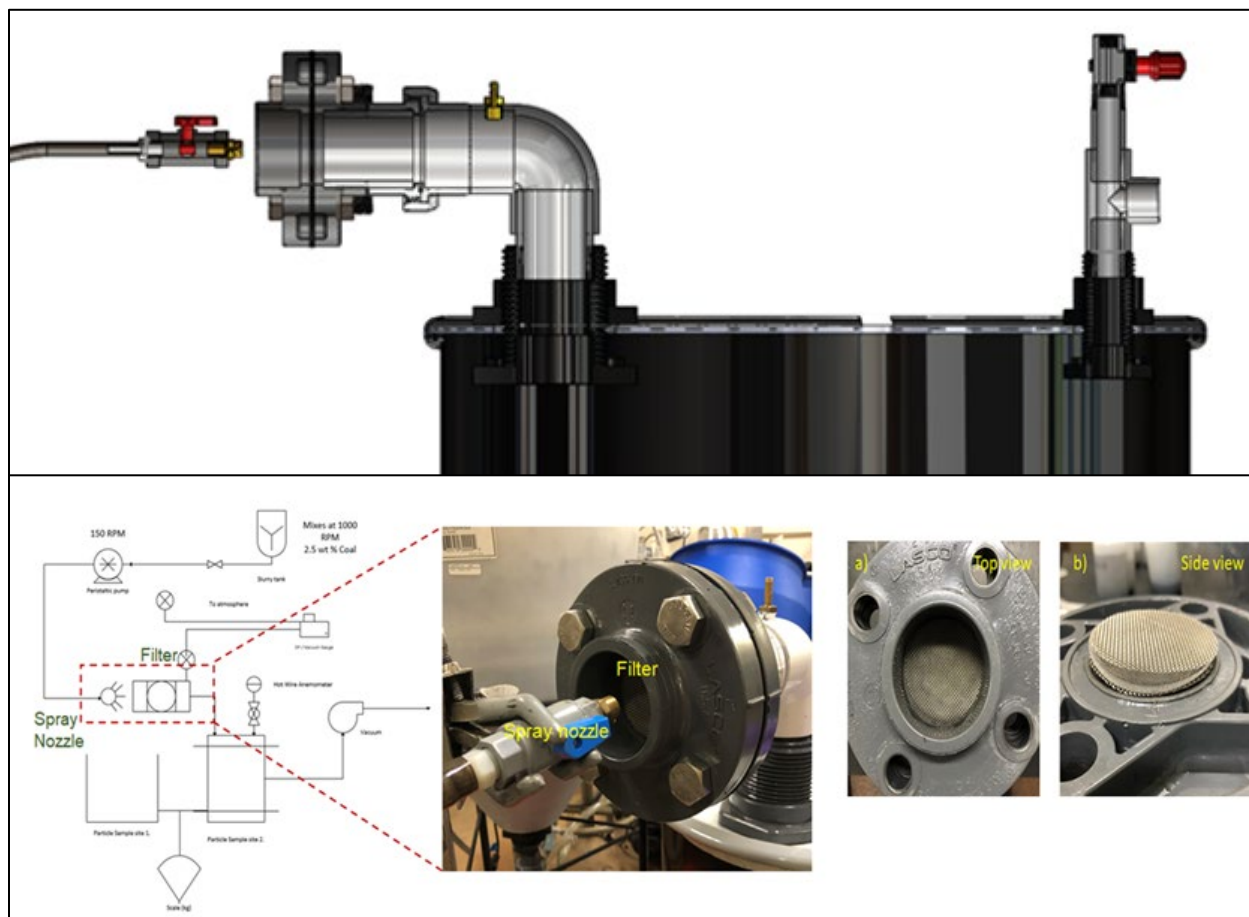
Figure 62. 3D drawing and experimental configuration of a laboratory setup to study the clogging of dust particles across the filter.

After the initial static trials, a vibrational modification was added onto the unit. Figure 63 shows the design of this apparatus. The modification was constructed using a flex hosing that allows the filter housing to move. The springs chosen were 3" long with two springs being used per socket of the supporting flange. The spring rate of those springs was 23lbs/in. In order to supply vibration, an ABU-06 pneumatic vibrational unit was placed on top of the filter as seen above.
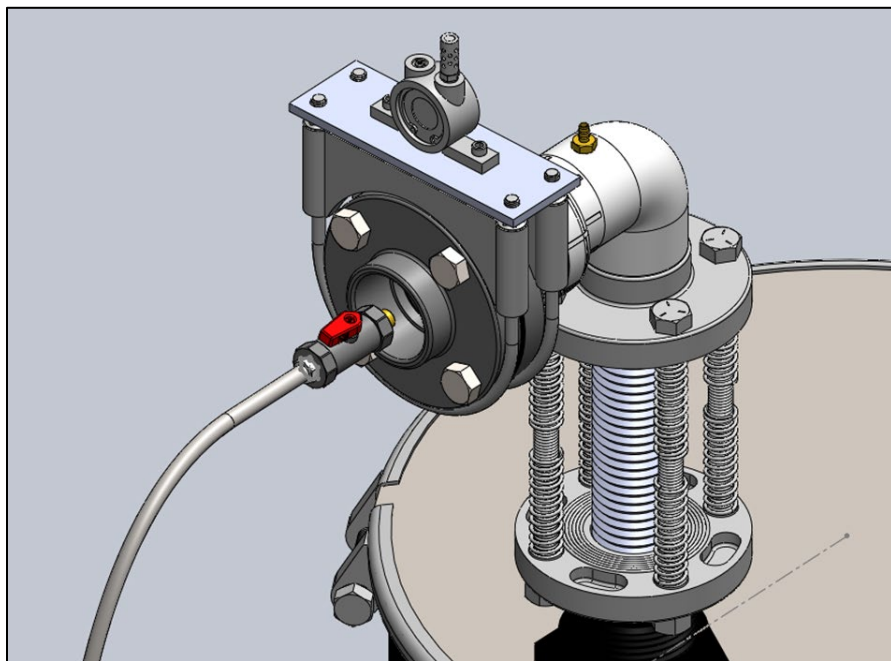
Figure 63. 3D drawing of a modified experimental set up with a vibrating system.

3.4.2.2. Materials

Fine bituminous coal sample were obtained by a coal mine in West Virginia. The fine coal powder sample, as received, was wet ball milled for 15 minutes. The D_{50} (where 50% of the materials by volume has a certain size or smaller) and D_{80} (where 80% of the materials by volume has a certain size or smaller) sizes of ground coal samples were 11.0 and 31.1 microns, respectively. In addition to raw coal, naturally hydrophobic fine graphite powders were obtained from Sigma Aldrich to be used as comparative fine dust materials for this study. The top size of the graphite sample was 44 microns, and the D_{50} and D_{80} sizes of fine graphite samples were 11 and 15 microns, respectively. Lastly, granite mineral samples were obtained from a domestic source. The samples were wet ball milled for 45 minutes in deionized water. The D_{50} and D_{80} sizes of the ground graphite were 11 μm and 15.6 μm respectively and are naturally hydrophilic. The samples were washed with DI water to remove any soluble organic residue, and the slurry was filtered. The filtered solids were dried in an oven at a temperature of 100° C overnight. The feed slurry was prepared by mixing the solids with DI water to prepare a 1.6 wt% slurry.

The filters obtained for the study were both 316 stainless steel pads and woven filters (100 & 200 mesh). The contact angle of the bare steel was 92.6° ± 1.45°, which is considered hydrophobic. In order to fully observe the effects of filter surface modification, the filters were modified to become hydrophilic and super hydrophobic. The hydrophilic surface modification was completed by reacting the iron of the steel in a low oxygen environment furnace at 750° C to produce a blued steel oxide magnetite (Fe_3O_4). The contact angle produced from this heat treatment was 37.1° ± 1°. Super hydrophobic surface modification was completed by thinly coating the filters with a commercial polymer agent. The filter was coated three times in a thinned solution and dried 24 hours before use. The contact angle measured from this modification was 156.6° ± 0.88°.

3.4.2.3. Test Procedure

In order to quantify the hydrophobicity of the filters used in testing, a goniometer was utilized (Figure 64). Steel strips were prepared in order to replicate the surface conditions of the filters used in the study. The strips were placed onto the stage and the camera was used to collect high-definition images of the sample. The receding, resting and advancing angle was taken for each sample. In order to accurately capture the super hydrophobic surface contact angle, the high-speed camera took a video that was then analyzed. The images were taken at three random sites along the surfaces.
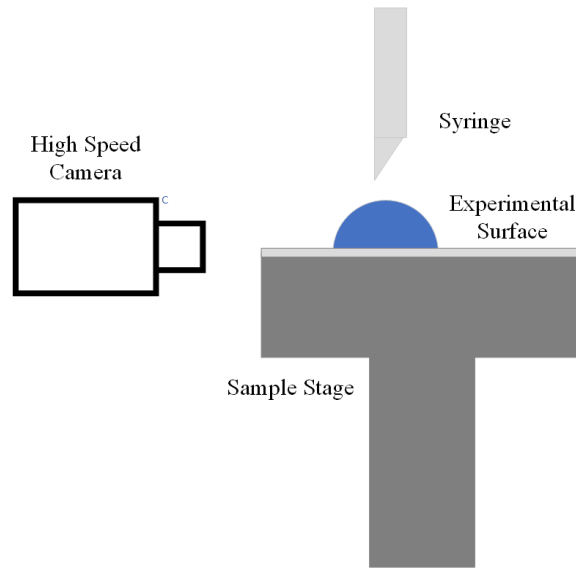

Figure 64. A schematic drawing of an experimental setup for contact angle measurements.

Two experimental protocols were developed to better understand the clogging of dust particles through a filter pack, including a) continuous trials and b) intermittent trials. Continuous trials were performed with both the coal and graphite samples. The mixing tank was filled with distilled water and feed materials. The slurry was mixed prior to spraying into a filter assembly before the start of the trial. The nozzle was cleaned in an ultrasonic cleaner for 15 minutes, and the slurry was recirculated for 5 minutes. The tubing was then reconnected to a nozzle. The air was drawn through a filter assembly by a 1 HP wet/dry vacuum (Shop-Vac, rated at 50 CFM). The velocity of the air passing through the filter panel was in the range of 5.8 to 6.5 m/s. The slurry spray rate was 0.675 L/min, and solid concentration of the slurry was 1.6%. The slurry spray ran up to 90 minutes until the filter was completely clogged and the slurry was rejected by the filter pack and collected at the front of the bucket. After each experiment, the filter pack was dissembled, and the total weight of the dust particles trapped between the wire meshes was determined. In addition, the weight of solid particles trapped on individual woven packs or wire meshes was determined.

The second protocol was intermittent trials. The intermittent trials were performed to better understand the clogging mechanism by investigating how dust particles accumulated within the filter layers over the time. These intermittent trials were performed by varying spray times from 2 minutes to 60 minutes. Filter packs were divided into different sections. For wire meshes, the first two layers of fine wire meshes, including a front supporting coarse mesh layer, were classified as the front layer. The intermediate four layers of fine wire meshes were classified as the intermediate layers, and the back two layers of fine wire meshes and one coarse supporting mesh were classified as the back layer. For the fibrous woven filter

pack assembled by layering two steel woven wool pads, the filter pack was split into the back and front sections, with each consisting of one wool pad. The intermittent trials were performed in the same manner as the continuous trials with the pressure drop monitored by a differential pressure transducer. The filter pack was then dried at 100° C overnight in a conventional forced air oven. The filter was weighed and then taken apart by each layer, and the clogged dust particles on each layer were weighed. Photos were taken of each individual wire mesh.

The intermittent testing was then repeated with the vibrational modification unit, with 100 mesh filters tested with graphite material. These tests were used not only to validate the results of the bench and pilot scale scrubber systems but also provided insight into the interaction of fully wetted particles. In these tests, the vibrational force was controlled via a needle valve where the pressure of the air corresponded to the frequency and force of the vibration. The pressures used to evaluate the impacts of vibrational forces were 40 psig and 60 psig.

3.4.3. Results and Discussion

3.4.3.1. Single- and Two-Phase Pressure Drop Tests

To accurately depict the filter as a system for a comparison, initial trials were conducted with water and air (i.e. no particles). Results from this preliminary testing are shown in Figure 65. The spike in pressure drop across the filter is caused by water wets the filter, reducing the permeability of the filter assembly.
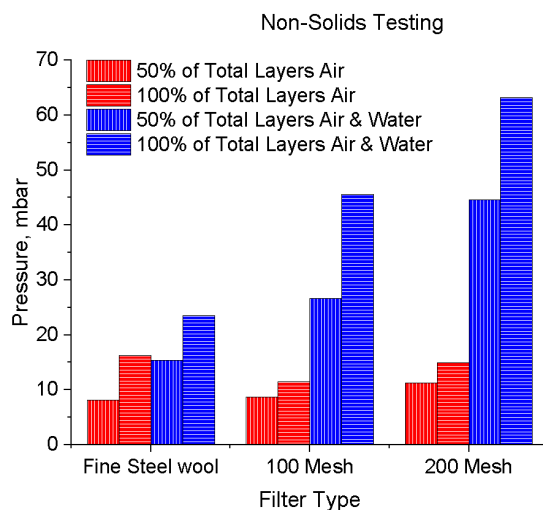

Figure 65. Non-solid characterization of filter performance based on pore size and type.

As expected, these findings showed that both the number of layers and pore size greatly affected the initial spike in pressure drop across the filter. The smallest pore size (200 mesh) exhibited the largest increase in the pressure drop. In this case, the pressure increased by 45 and 63 mbar when tested with four- and eight-layer filter packs, respectively. By comparison, the pressure drop on the fine steel wool packs due to the water spray was relatively small. We saw an increase of 7-9 mbar on average with a water spray, suggesting the area of void occupied by water was considerably minimal compared to the total void within the filter pack. This may be attributed to the larger pore volume and small wire thickness with steel wools compared to the mesh wires or even the tortuosity of the filter.

71

3.4.3.2.   *Influence of Mesh Configuration*

Stop trials were performed with a spray of a slurry containing 2-5% solid by weight of fine graphite powders. The graphite particles were hydrophobic to mimic coal rich seams of particles. Results from these tests are presented in Figure 66. and show a linear relation in the rise of pressure drop to the total accumulation of materials within the filters. In all cases, the data show an initial spike in pressure drop across the filter consisting of steel wool pads, after that the increase in pressure drop was minimal as spray continued. As shown, the total of dust particles trapped in the steel wool filter after 20 minutes of slurry spray was approximately 1.8 grams, after 45 minutes and 90 minutes of graphite slurry spray, the total accumulated weight of trapped dust particles were determined to be 3.5 grams and 5.2 grams, respectively. However, the increase in the pressure drop across the filter was rather marginal compared to the woven mesh filters. This result clearly suggests that the larger void fraction within steel wool extends the service life of the scrubber filters and further studies should be conducted to investigate the effects of tortuosity.
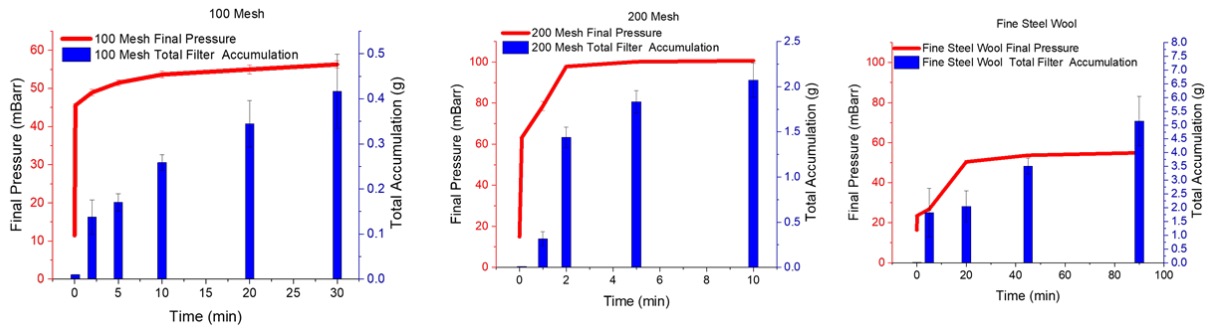

Figure 66. Stop trial data for 100 Mesh, 200 Mesh and fine steel wool.

To better understand the clogging mechanism, filter packs with different mesh configurations were disassembled and characterized. Figure 67, Figure 68, and Figure 69 shows photos of individual mesh layers with 8 layers of 100-mesh wire, 8 layers of 200-mesh wire meshes, and 4 layers of steel wools, respectively. Graphite particles trapped at the front three layers were classified as the front layer, the middle four layers were considered as the intermediate layers, and back three wire meshes are classified as the back layers. The photos show that more graphite particles were trapped at the front layers of the filter consisting of 200-mesh wire meshes. For 100-mesh wire meshes, the amount of clogged dust particles was considerably less.
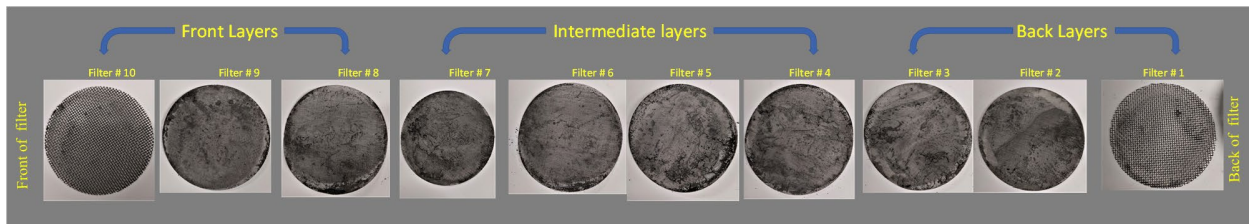

Figure 67. Filter accumulation across a 100 mesh filter after 5min of being sprayed with graphite slurry.
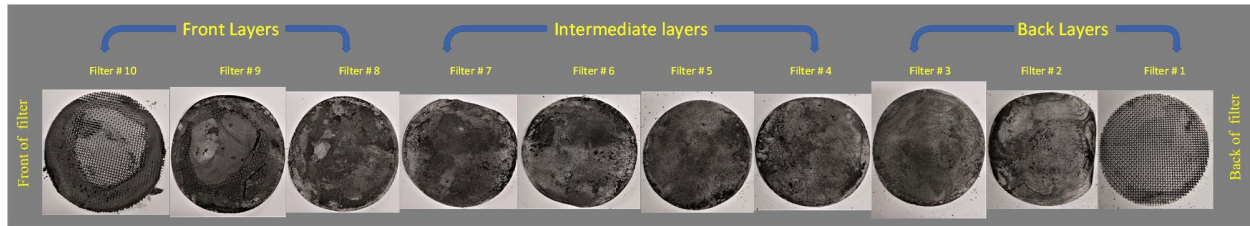
Figure 68. filter accumulation across a 200 mesh filter after 5min of being sprayed with graphite slurry.
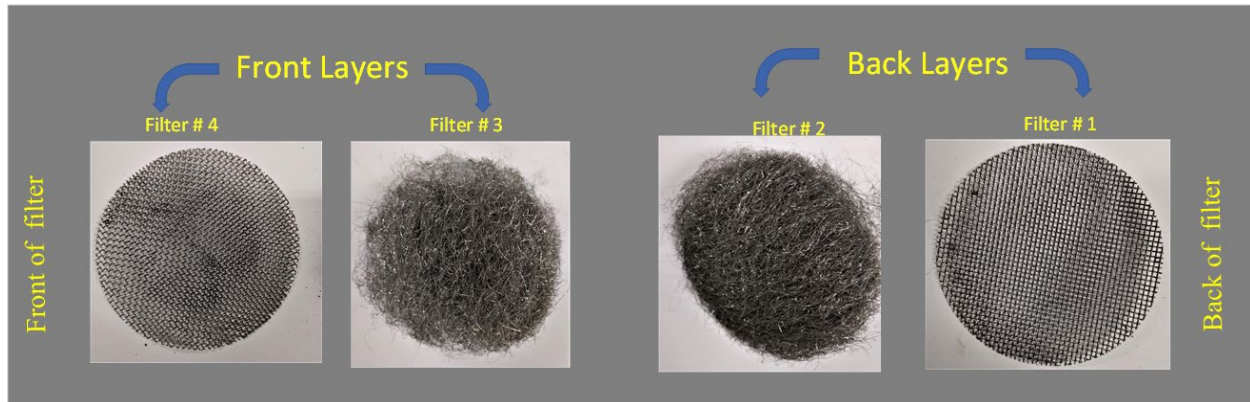

Figure 69. Filter accumulation across a fine steel wool filter after 5min of being sprayed with graphite.

Figure 70 shows the total weight of accumulated dust particles trapped at each layer of the 100 mesh filter pack. Quantitative result showed that the accumulated weight of trapped dust particles increases linearly proportional to the time of the slurry spray. Results showed that the accumulated mass of the trapped dust particles collected at the front three layers was slightly more than those collected at the back side of the filter pack.

Figure 71 shows the total accumulation of the trapped graphite particles between the filter pack consisting eight layers of 200-mesh wire meshes with two supporting 20-mesh coarse meshes. Results showed that there was an increase in the total weight of trapped graphite particles at both intermediate and back layers of the wire meshes within the filter assembly. However, at the front side of the filter pack, the increase in the total weight of graphite particles increased sharply within 10 minutes of a spray of graphite slurry. After 10 minutes of a spray of graphite slurries, the filter pack was completely clogged as the pressure drop across the filter was above 90 mbar, which effectively blocked all the pore within the filter assembly.

On the contrary, data from the filter assembly consisting of fine steel wool shows the total accumulation of the graphite particles continued to increase with increasing the spray time (Figure 72). Overall mass accumulation was also notably higher than that of the woven mesh filter packs. Over 90 minutes of a spray of graphite slurry, the total accumulation of trapped dust particles increased proportionally to the spray time. The total accumulation at the front side of the filter pad was more than those being collected at the back side of the filter pad.
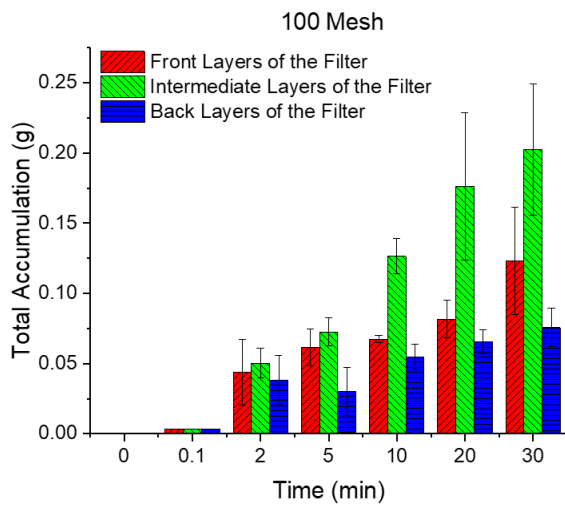
Figure 70. Stop trial data showing particle accumulation within the filter (100 mesh).
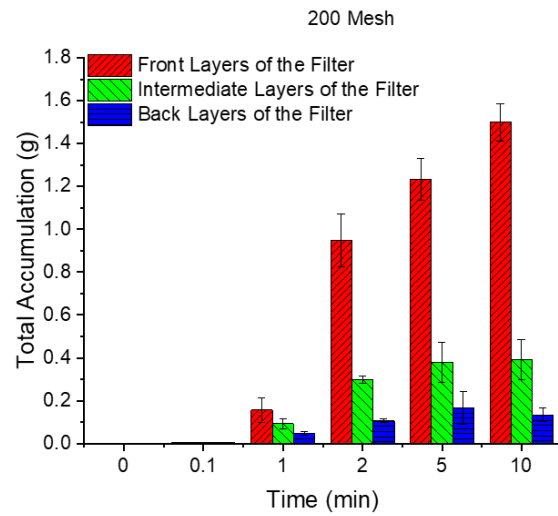

Figure 71. Stop trial data showing particle accumulation within the filter (200 mesh).
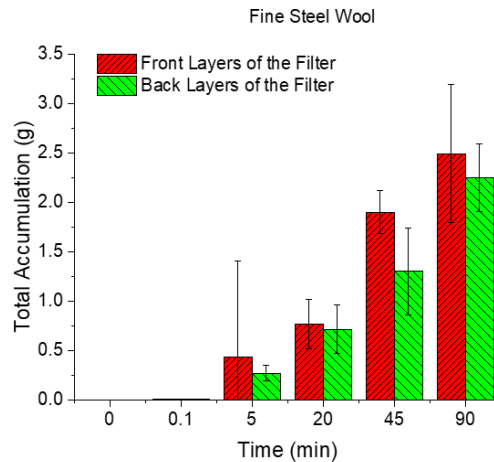

Figure 72. Stop trial data showing particle accumulation within the filter (Steel Wool).

Figure 73 shows the particle size distribution (PSD) of trapped graphite particles from the various mesh configuration. These results show that clogged graphite particles were found to be finer than those in the feed. In particular, the PSD of the graphite particles clogged between 200-mesh wire meshes filter pack was similar to those in the feed. However, for dust particles that were clogged between 100-mesh wire meshes as well as fine steel wool pads, graphite particles trapped between the filters were much finer than those in the feed, suggesting that more finer graphite particles were trapped between the wire meshes or steel wool, while allowing larger particles to penetrate through. It is possible that the hydrophobic interaction was present between mesh wires and hydrophobic graphite particles, and velocity of air

74

passing through the filter pad was significant enough to remove coarse graphite particles but not fine graphite particles.
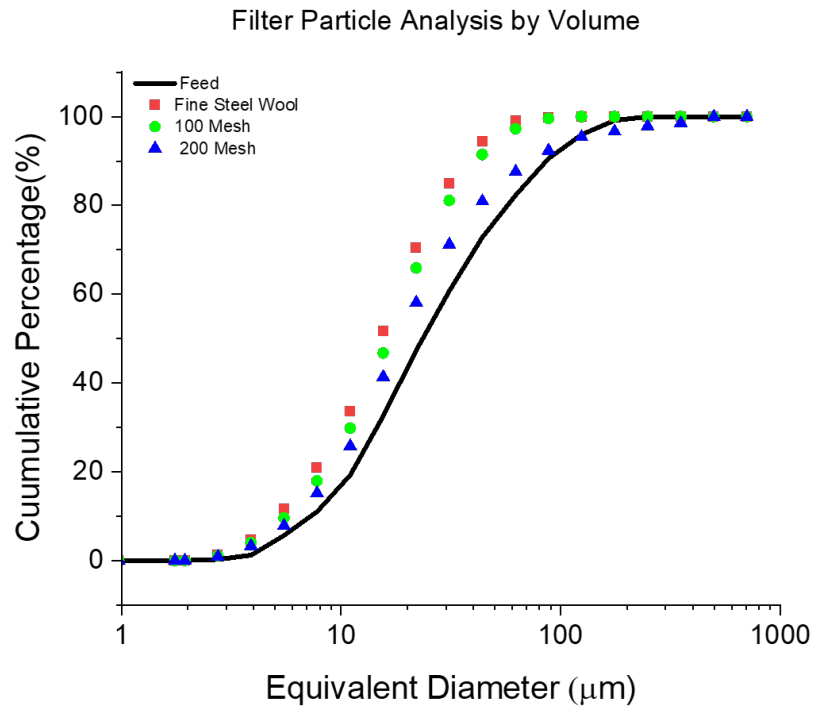

Figure 73. Particle size distribution of different filter types with graphite slurry.

3.4.3.3.   Influence of Particle Hydrophobicity

Figure 74 shows the stop trial data for both naturally hydrophobic (graphite) and naturally hydrophilic (granite) particles. For this trial, the filter pack was assembled by packing eight layers of untreated 100-mesh wire meshes and 2 layers of 20-mesh supporting layers together. The result showed that the total accumulation of clogged particles increased with increasing spray times for both cases; however, overall accumulation was much higher for the graphite as compared to the granite. As shown above, clogging of dust particles resulted in an increase in the pressure drop across the filter. After 30 minutes of a slurry spray, the total accumulation of dust particles within the filter reached 0.38 grams for the graphite and 0.06 grams for the granite. Clearly, granite particles are less likely to be clogged between meshes compared to graphite particles.
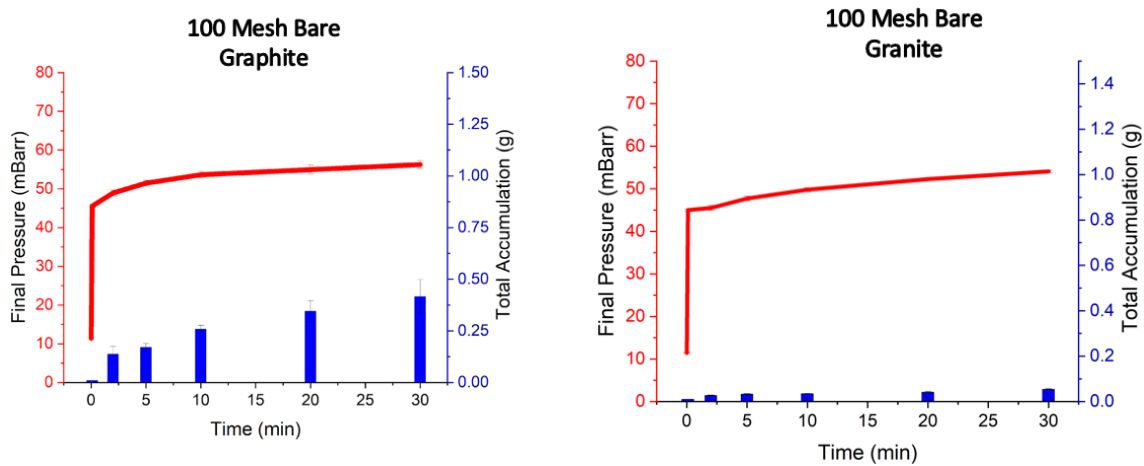

Figure 74. Pressure drop developed across the filter pack vs. spray time across the filter assembled by 8 layers of un treated 100-mesh wire meshes with two supporting 20-mesh wire meshes.

Figure 75 shows similar data for the super hydrophobic treated mesh. When compared with bare stainless-steel wire meshes, the total account of accumulated graphite particles was significantly higher. After 30 minutes of a spray, the total accumulation reached 0.75 grams, which is significantly higher that of accumulated between bare stainless-steel mesh wires (0.38 grams). Despite the fact that the total accumulation of granite particles within the filter is very minimal, the pressure drop continues to increase. This phenomenon is likely due to the interaction of granite solid with the carrier fluid water. Since granite is more hydrophilic, it has a greater attraction and affinity for water. Because of this the particles of granite are found within water droplets. Due to this, the air has to permeate through water and granite particles. This result is in contrast to the graphite particles which are hydrophobic and would be found on both the edges and inside of the droplet, thus creating a more direct path for the air to permeate through.
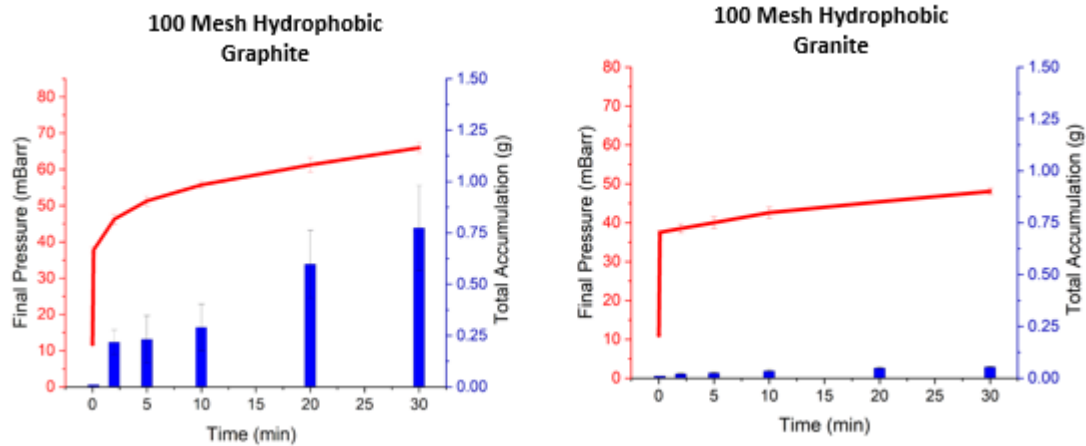
Figure 75. Pressure drop developed across the filter pack vs. spray time across the filter assembled by 8 layers of hydrophobic 100-mesh wire meshes with two supporting 20-mesh wire meshes.

The results of the stop trials also showed that the accumulation pattern changed. Figure 76 and Figure 77 compare the total accumulation of graphite particles between the wire meshes with and without the surface treatment. For both the untreated and hydrophilic-treated wire meshes, most of the graphite particles were clogged at intermediate and back layers. For hydrophobic wire meshes, most of the graphite particles are clogged at the front layers of the filter packs. A general conclusion is that as the hydrophobicity of the filter medium increases, graphite particles are likely being accumulated at the front layers of the filter pack.
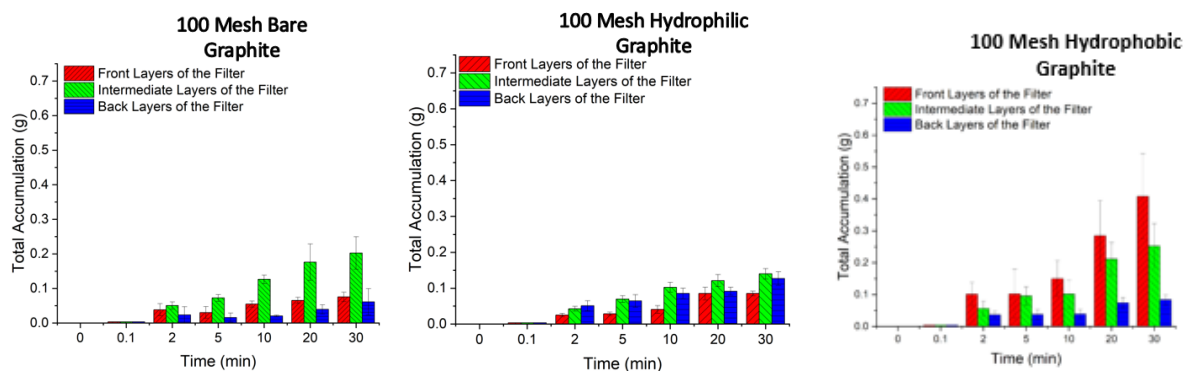

Figure 76. The effect of surface hydrophobicity of the filter medium on total accumulation of dust particles at front, intermediate and back layers of the filter pack with graphite.
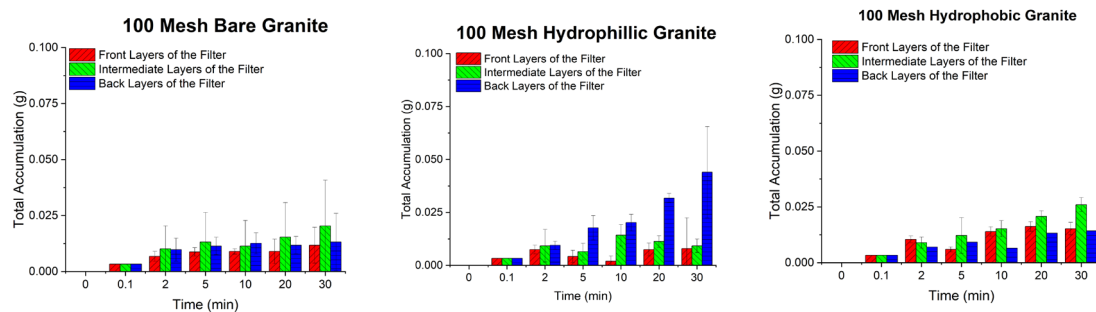
Figure 77. The effect of surface hydrophobicity of the filter medium on total accumulation of dust particles at front, intermediate and back layers of the filter pack with granite.

Another phenomenon observed through the strop trials was the accumulation of graphite particles at the front of the filter pack (Figure 78). This finding is attributed to the fact that the carrier fluid is being rejected by the hydrophobic filter. As seen below, a large amount of solid material was accumulating in front of the filter as the hydrophobic testing was taking place. As the hydrophobic filter is repelling the water particles the granite is traveling with the water and sedimentation is occurring in front of the filter.

Figure 78. A photo of a filter assembly after a spray of granite slurry on a filter pack with 8 layers of hydrophobic 100-mesh wire messes.

3.4.3.4.   *Vibrational Results*

In addition to the static stop trials, additional tests were conducted using the modified vibration-enhanced unit described in the methods section above. Here vibration is supplied by an ABU-0 pneumatic vibrational unit, and as such, the vibrational intensity is signified by the pneumatic supply pressure (psi). Figure 79 shows the overall continuous results of this trial using the 100 mesh filter pack and the graphite slurry, while Figure 80 shows the stop trial accumulation data. Lastly, Figure 81 shows the accumulation distribution between various portions of the filter pack.

Figure 79. Laboratory-scale vibrational studies with a graphite slurry.
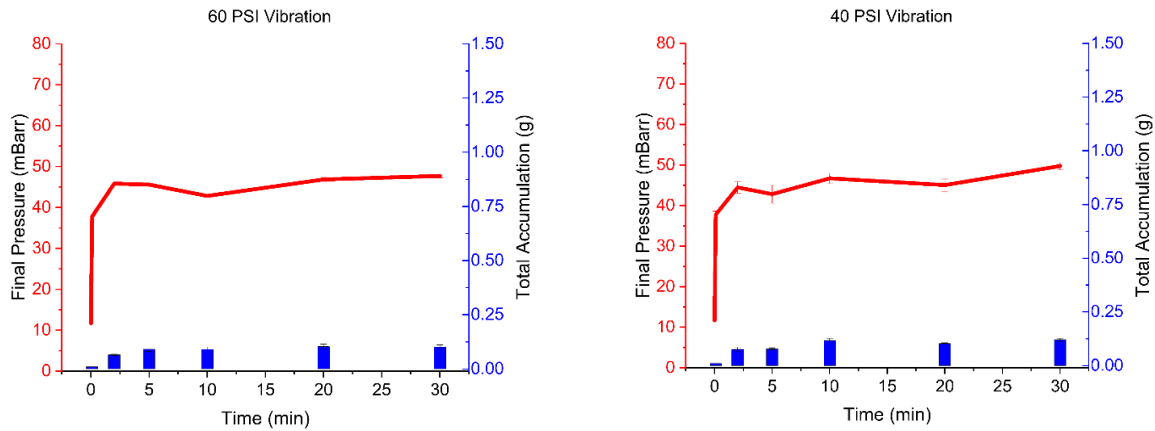
Figure 80. Laboratory-scale intermittent trials with different vibrational forces applied.

79
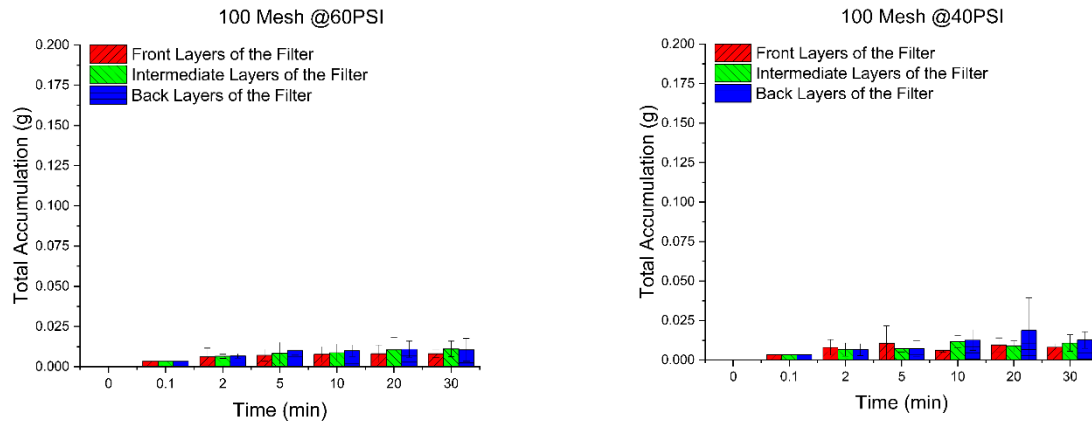
Figure 81. The effect of vibratory forces on the filter medium on total accumulation of dust particles at front, intermediate and back layers of the filter pack with graphite.
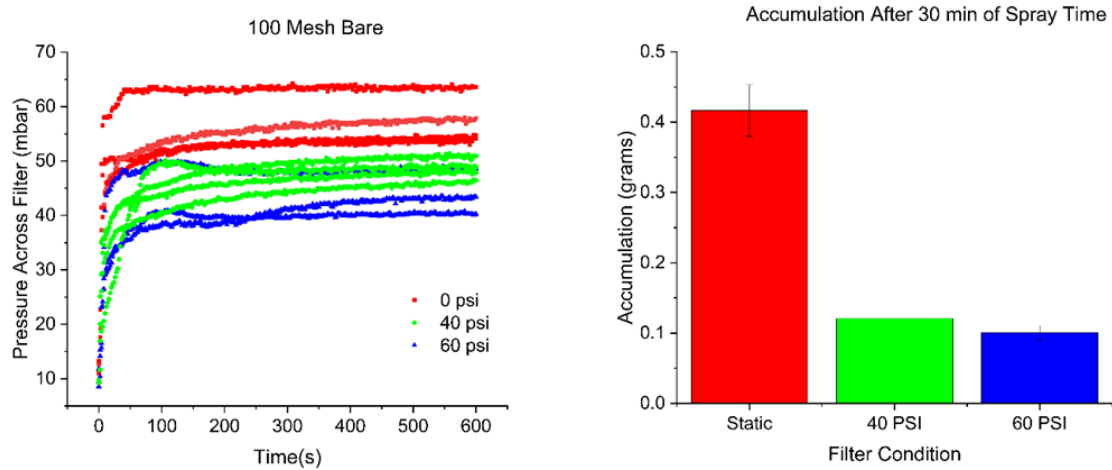
Overall, the data confirm the results from other modeling and experimental studies, namely that applied vibration can significantly inhibit clogging when compared to that of a static mesh. In these tests, the total amount of material accumulated in the filter greatly decreased from 0.416 grams of material to 0.100 grams of material with the application of vibration. This decrease is in total amount of solids accumulating within the filter is nearly ¼ of a static filter. In addition, the stop trials showed that there were slight swings in mass accumulation but also the addition of vibrational forces led to a greater amount of solid material ending up near the rear of the filter.

3.5. Vibrational Translation

3.5.1. Approach

To investigate the energy harvesting/vibrational translation system, we designed a bench-top model that is scaled down approximately 10 times smaller compared to the real mesh structure in the mining environment. For the laboratory setup, the frame holding a mesh is 9 cm wide, 5 cm tall, and 1.25 cm thick. The frame was made of aluminum with a total mass of 92.3 grams. The frame holds an 80-mesh screen made of steel by M5 bolts on the top corners of the frame. The frame was then connected to a transducer with a system of four parallel springs and a bed frame made of aluminum. Figure 82 shows the bench-scale experimental schematics along with two photos of the designed frame before and after connecting to the transducer.
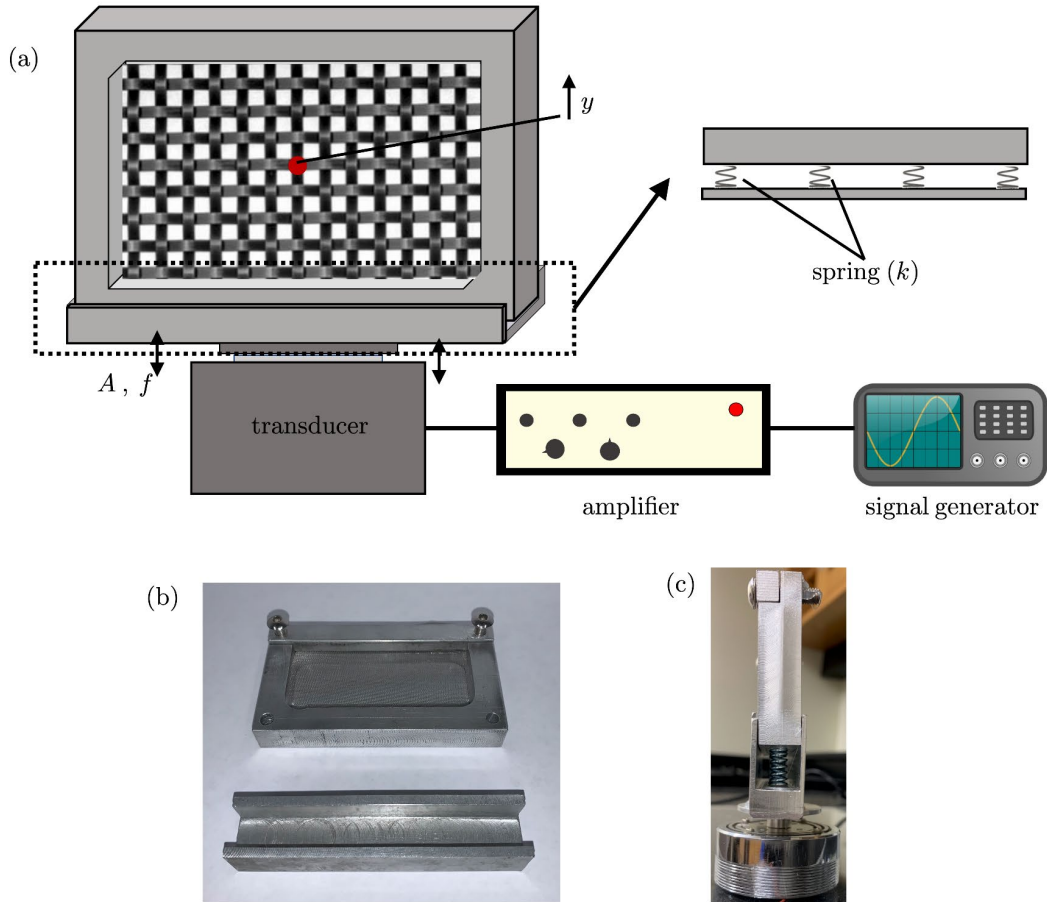

Figure 82. Experimental schematics. (a) overall system; (b) snapshot of the designed frame; (c) the assembled frame connected to the transducer through a system of 4 parallel springs.

81

To apply vibrations, we connected the transducer to a signal generator through a high-power amplifier. The signal generator produces signals of a certain frequency, f, and certain amplitude, A. The amplifier provides a gain to amplify the amplitude of vibrations to make visualizations possible. The experiments were then recorded with a high-speed camera (Photron) with a frame rate of 2000 frames per second and a Macro lens (Nikkor 105mm) and two extension tubes (Kenko 36mm). Two reflective markers are placed on the mesh and used for the purpose of image processing.

Next, we measured the spring constant of the springs used in the design. We hung different masses and measured the spring stretch as shown in Figure 83. By measuring the slope of force vs. displacement for the spring, the spring constant was calculated k_4=3850 N/m. It is noteworthy that we have also used three springs with k_1-k_3~300-800 N/m, but we decided to use stronger springs as it will become apparent in the results section.

We also calibrated the amplifier by finding the linear relation between the amplifier gain and the amplitude of the mesh vibrations. Figure 84. shows the relation for f=50 Hz which looks similar in other frequencies as well.
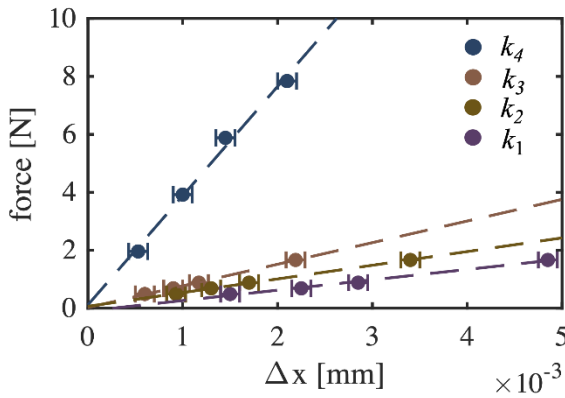

Figure 83. Force vs. displacement for the springs used in the bench-scale model.
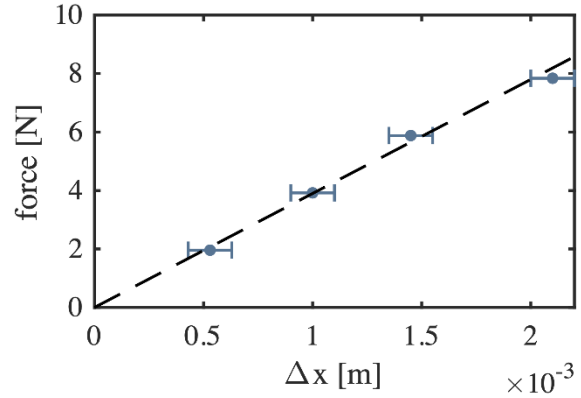
Figure 84. The Amplitude, A, vs. the amplifier gain for f=50 Hz.

The goal of these bench-scale experiments was to characterize the vibration frequency regimes where more energy can be harvested from the system. Hence, we evaluated different frequencies of base vibration ranging from 10-100 Hz. In addition, we test three different input gains which will generate different amplitudes, and for each set of parameters we repeat the experiments three times. Ultimately, we track two separate points marked by a reflective marker on the mesh in each test. We then extracted the vertical position of each tracked point, y, and apply a Fast Fourier Transform (FFT) on the vertical position of the marked points. The FFT data will reveal the most dominant frequencies of oscillations where the local maximums appear in the FFT data.

We first calculated the approximate natural frequency of the system. Considering a system of 4 parallel springs with k=3,850 N/m for each and a total mass of 92.3 grams, the natural frequency of the system, f_N, yields 65 Hz. Hence, we divide our results into two parts: $f<f_N$, and $f>f_N$. The former represents cases

where the applied frequency by the transducer, f, is lower than the natural frequency of the system while the latter shows cases the frequency of transducer is larger than the natural frequency.

3.5.2.   Results and Discussion

Figure 85 shows the results for the frequencies that are larger than the natural frequency (b-c) or close to the natural frequency (a). As shown in subset (i) of Figure 85, under these vibration frequencies, the mesh exhibits a single mode vibration. The FFT results demonstrated in subset (ii) in Figure 85 proves this observation that the mesh structure oscillates with the same frequency as the base oscillations. Hence, the effect of spring system in this limit is negligible.
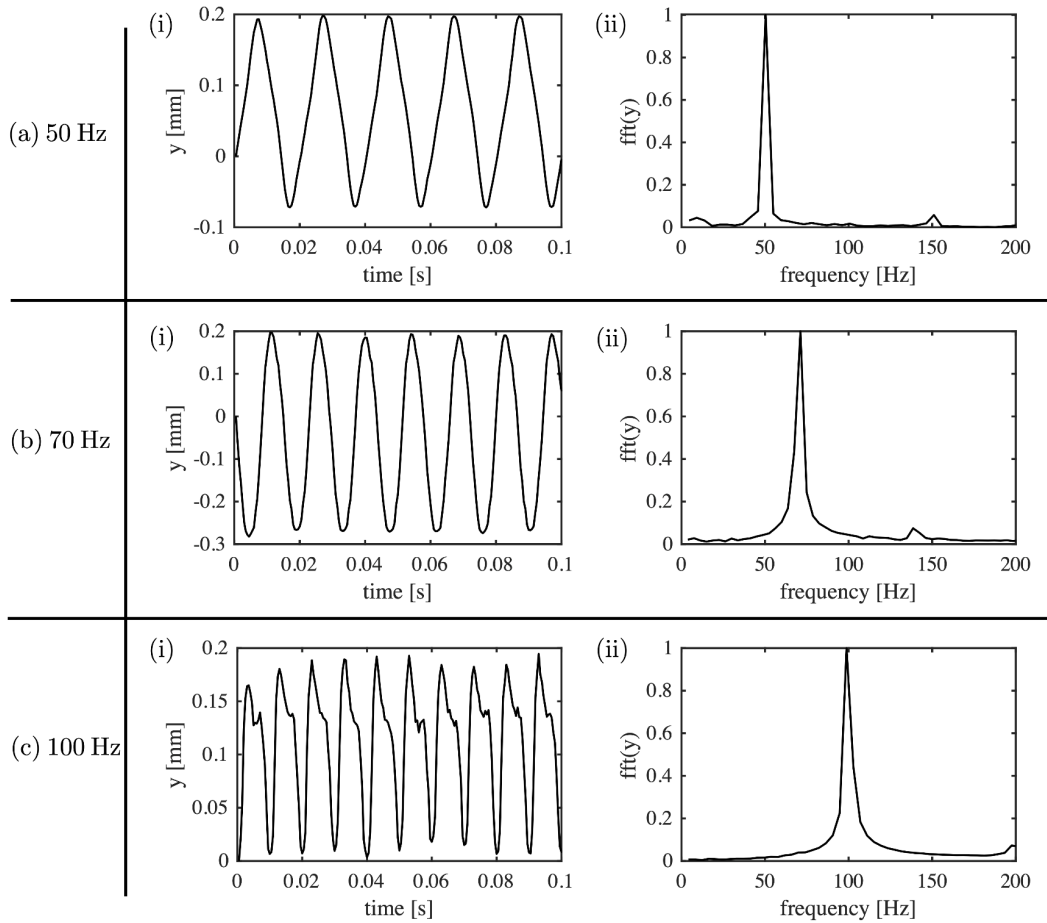
Figure 85. Results for varying vibration frequencies of (a) f=50 Hz, (b) f=70 Hz, and (c) f=100 Hz. (i) shows the average oscillations for a certain amplitude in each frequency. (ii) shows the average Fast Fourier Transform results across all trials of the same frequency.

On the other hand, Figure 86 shows that the spring system has a strong effect on the vibration modes when the vibrations have lower frequencies than the natural frequency. The subset (i) in Figure 86 suggests that there is a bimodal behavior shown by the system for the frequency range of 10-25 Hz. In

fact, the FFT data presented in subset (ii) of Figure 86 proves this hypothesis as two strong peaks are observed in the FFT data: one near the base frequency, f, and one near the natural frequency, f_N.
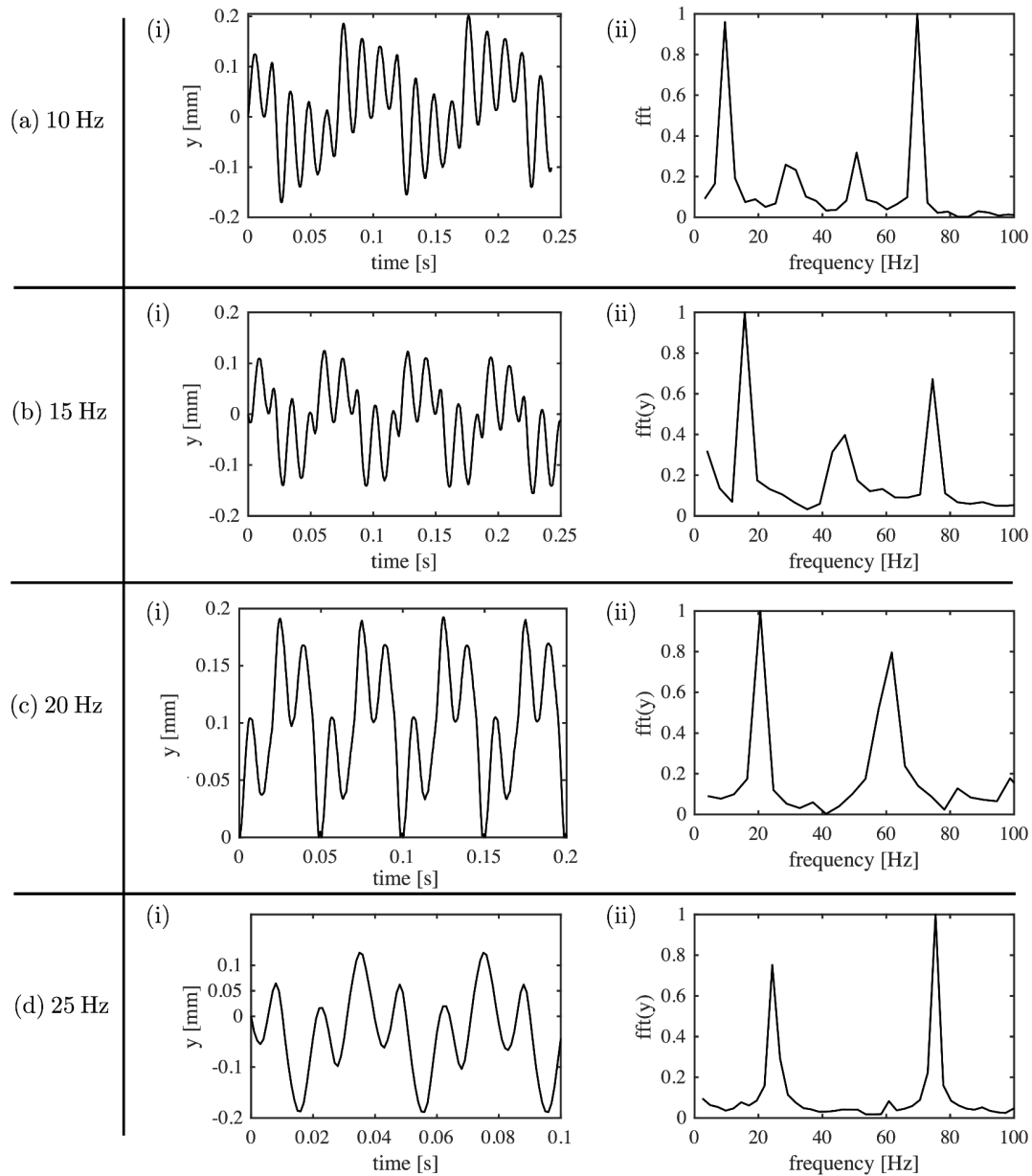
Figure 86. Results for varying vibration frequencies of (a) f=10 Hz, (b) f=15 Hz, (c) f=20 Hz, and (d) f=25 Hz. For each frequency, (i) shows the average oscillations for a certain amplitude, and (ii) shows the average Fast Fourier Transform results across all trials of the same frequency.

Figure 87 shows the dominant frequencies from the image processing presented in Figure 84 and Figure 86 as a function of the base frequency. These results show that it is possible to excite the natural

frequency of the system in frequencies lower than the natural frequency of the system. Hence, in order to harvest more energy to the vibration system, it is recommended to choose a spring constant that provides a natural frequency larger than the range of viable frequencies in-mine.

Figure 87. The dominant frequency vs. the base frequency for vibrational translation tests.

4. Technology Evaluation

4.1. Overview

Technology evaluation was conducted through two test campaigns: (1) a bench-scale scale system; and (2) a full-scale prototype system. Each are described in separate sections below. Initially, the bench-scale system was evaluated to determine the optimal range of operating conditions (vibrational frequency, amplitude, water flow rates, etc.) through detailed parametric testing. Moreover, the smaller stature of the system allowed more detailed internal system ana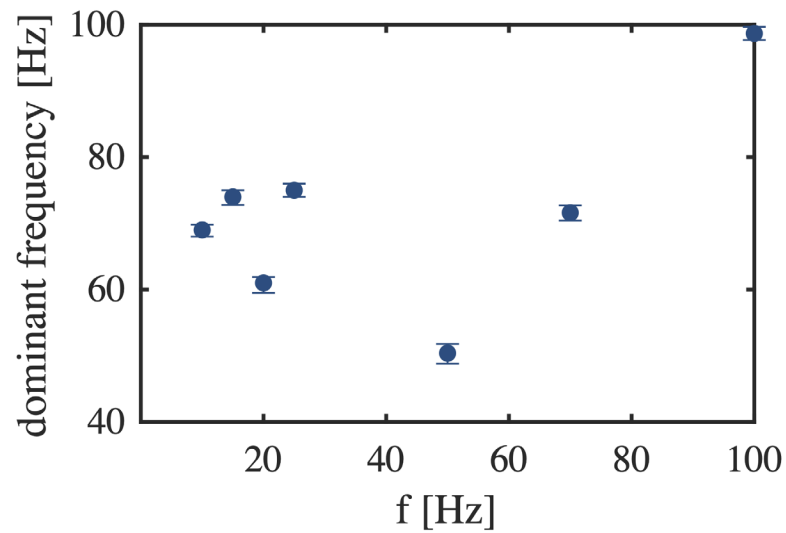lysis, particularly with the respect of particle deportment and fate through the system. Alternatively, the prototype system was tested at realistic operational conditions (air flow rate, dust concentration) in a high-fidelity simulated environment. While the same level of internal detail was not recorded during testing, the prototype testing was instead used to validate the smaller scale findings and stress test the system. Moreover, the prototype system implemented and tested an initial design of the vibrational translation system described in prior section.

4.2. Bench-Scale Testing

4.2.1. Design and Construction

The bench-scale scrubber was modified and refurbished in accordance with findings from the initial proof-of-concept tests (AFC-518-25) and initial system shakedown. These updates principally include the addition of: a new assembly for the mesh shaker and ancillary vibrational equipment, a new curve vane demister, and additional sampling ports. The chamber maintains the original 0.152 m × 0.152 m internal cross-section, with the scrubber section consisting of four detachable units and a shaker unit mounted on the mesh screen holder. These detachable units include: (1) the upwind section where the coal dust is fed into the system and from where the pre-mesh screen samples are collected, (2) the mesh screen unit, (3) the demister unit, and (4) the post-demister section where final downwind samples are collected. Figure 88 shows the fully assembled unit attached to the fan and dust collection unit.

The mesh screen and demister housing sections are 0.36 m in length, and they have grated blackwater sumps underneath to collect wastewater for confirming the water flow rate measurements and supplying the required outlet for wastewater from the mesh screen and demister units' floor. The longer sections provide the place for the sampling ports and allow the dust-laden air to travel from one unit to another and share a common length of 1.22 m. Altogether, the full system spans nearly 3.8 m in total length.
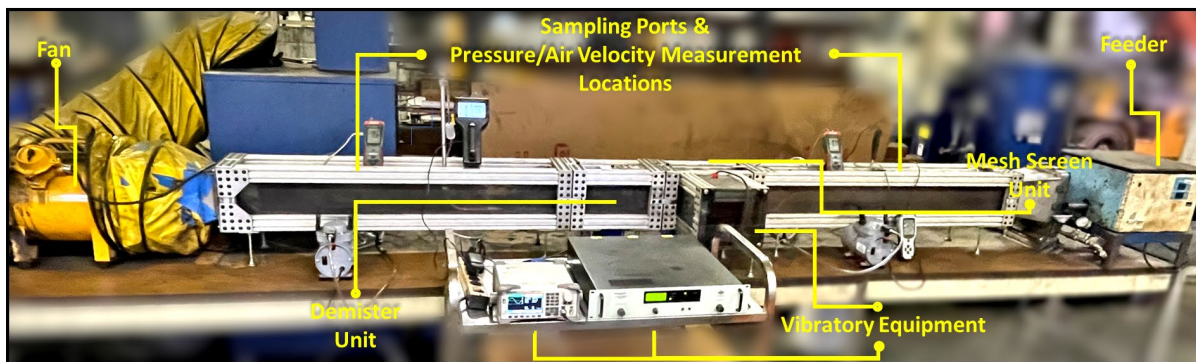

Figure 88. Refurbished bench-scale scrubber system.

The framework of the scrubber consists of 80/20 extruded aluminum framing with walls made from clear polycarbonate. The sections were made modular in nature and shared a new common mode of fastening. This fastening, shown in Figure 89a, includes 6.35-mm inner alignment dowels and outer slide-locking alignment bars that are fastened with wing nuts for ease of assembly/disassembly during testing. In this modular configuration, sections can be separated and realigned quickly and in a matter that is both airtight and watertight. Another update included the addition of flat neoprene rubber seals between each section (Figure 89b) and barbed neoprene rubber seals (Figure 89c) running the length of each section around each joint containing the polycarbonate sheeting. This additional chamber sealing provided the airtight and watertight seal necessary for verifying that no unmetered air entered or left the chamber during testing. Figure 89d shows the entirety of these changes shown on one of the four main assembly joints.
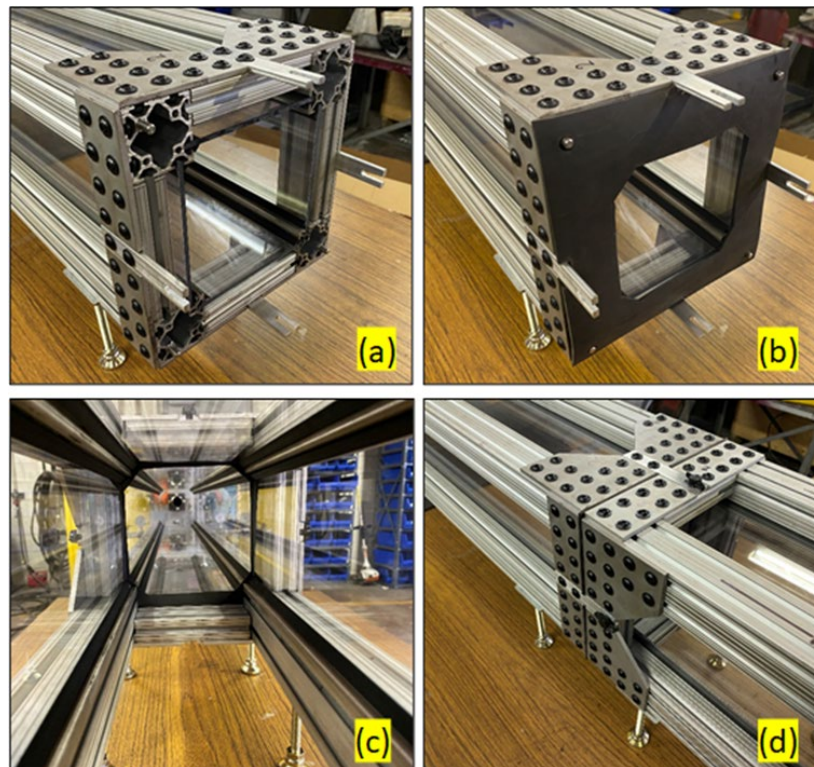
Figure 89. Refurbished tunnel structure: (a) alignment dowels and bars; (b) inter-chamber neoprene seals; (c) barbed rubber wall-joint seals; (d) chamber sections fully fastened.

The system also includes other notable components including: an innovative dust feeding system, an air-handling puller fan, an assortment of air sampling ports down the length of the tunnel, and an exciter that is mounted to the mesh screen.

Tunnel airflow is regulated by a nominal 2,700 cfm portable ventilation fan. The fan was selected to more accurately represent the airflow rates and velocities, in scale, of an industrial flooded bed scrubber. The fan is positioned at the end of the tertiary downward section of the chamber with its output fed into an industrial dust collection system shown in Figure 90. The dust collection system ensures that no extraneous dust particles are entering the laboratory work area.

To properly size the exhaust fan for the laboratory-scale unit, the team sought to scale down the tunnel cross-sectional area while maintaining a constant linear air velocity equal to that of a full-scale scrubber

unit. The constant air velocity was selected as the scaling parameter, given that velocity dictates particle settling/suspension in the tunnel section. Data from NIOSH shows that typical measured volumetric flow rates in mine scrubbers are approximately 6,300 cfm (Colinet et al., 2013). Moreover, geometric data provided by Komatsu shows that typical scrubbers have a cross-sectional area of 1.38 x 1.38 ft, though this value can vary significantly between models. Together, these values suggest that typical air velocities are on the order of 3,308 ft/min. Scaling this air velocity to the 6 x 6 in cross-section of the laboratory tunnel produced a target airflow rate of 827 cfm.

Figure 90. Exhaust fan and dust collector assembly.

After selecting and installing the fan, the actual airflow rate in the tunnel was measured using both a manual anemometer and a pitot tube. The results indicate that the airflow rate in the tunnel was slightly exceeding the target velocity of 827 cfm.

During testing, coal dust particles are injected into the scrubber by an innovative feeding system composed of a volumetric screw feeder and a Trost jet mill, as shown in Figure 91. Characterization of the volumetric screw feeder was found to be linear in nature and thus extremely predictable, which in turn allows us to independently control dust concentration as an independent variable.

To reduce the size of coal particles and create fresh dust surfaces, a laboratory-scale Trost jet mill (Figure 92) was employed. The jet mill employs high-velocity jets of compressed gas to impart energy to particles for size reduction. This device contains no moving parts in the grinding chamber, and the energy for size reduction is solely brought by the carrier gas. The primary grinding action is by particle-particle attrition, and as such, no contamination is introduced during the grinding process. The compressed air, typically 50 to 55-psi, sweeps the original feed particles around the grinding chamber. The particle interactions reduce the size of particles until the particles are fine enough to leave through the centrifugal classifier located in the grinding chamber.
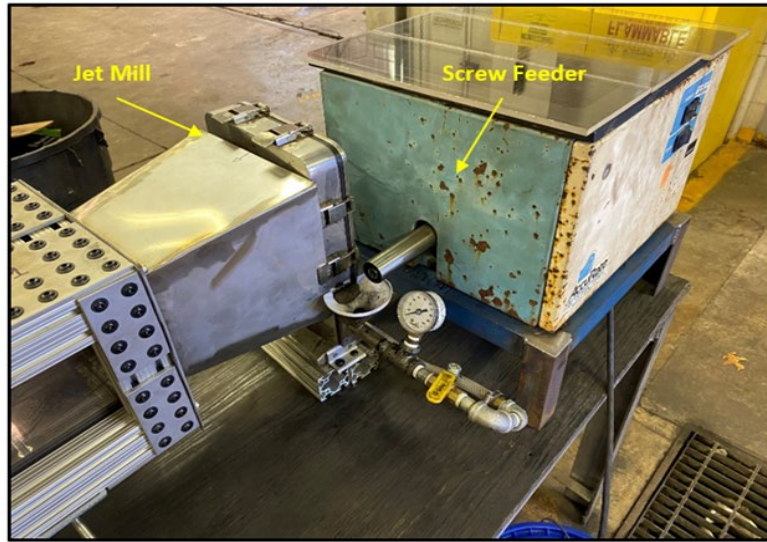
Figure 91. Scrubber particulate feed system.
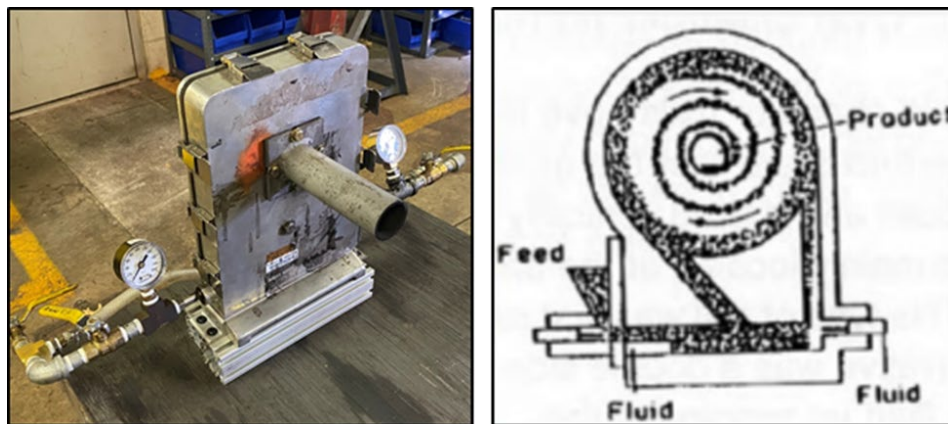
Figure 92. Trost jet mill used to feed the scrubber.

The original feed and jet mill product were analyzed for particle size distribution using a Microtrac S3500 laser particle size analyzer. Data from this evaluation are shown in Figure 93. Based on the particle size analysis data, the top size of the original feed is approximately 300 microns, with approximately 59% coarser than 20 microns. A further parametric study of the jet mill also indicates it produces particles typically finer than 5 microns when operated at 55 psi jet pressure, and nearly 54% of the product is within the respirable range of below 5 microns. The ash and moisture content of the coal dust feed were determined by content analyses. In the analyzed sample, there is a low moisture content of 1.2% and a dry ash content of 16.2%.
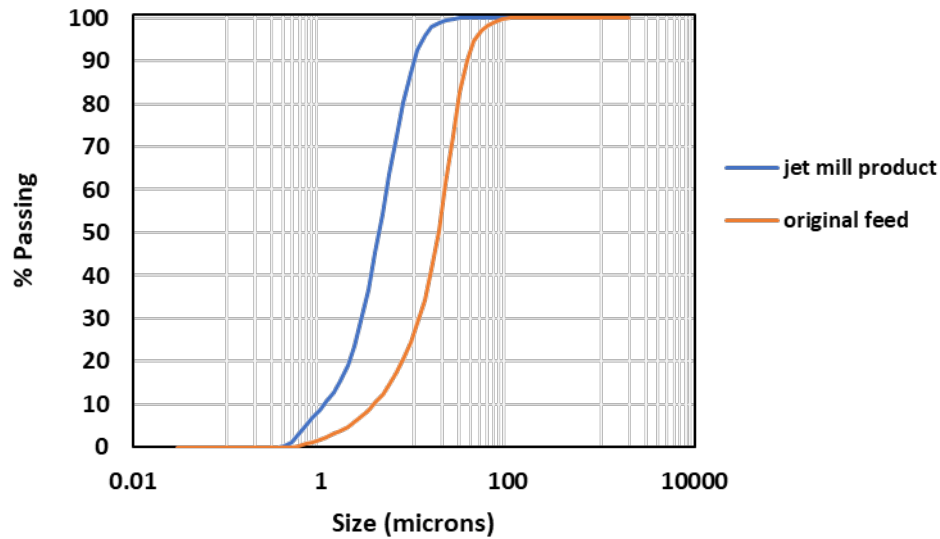
Figure 93. Particle size distribution analyses of the original dust sample and jet mill product.

During testing, dust samples are collected using 37-mm air sampling cassettes preloaded with Teflon filters. The first of the sampling locations, tasked with collecting pre-filtration data, is located within the preliminary upwind section, 0.2-m upstream from the secondary upwind section which contains the filter assembly. The second sampling port, tasked with collecting post-demister data, is located within the downwind section, 0.9-m upstream from the demister assembly. All sampling locations were placed in the long airflow sections to allow for more consistent air particulate mixing from the entrance and filter assembly sections of the scrubber. The team also sample the mesh screen itself, mesh screen unit blackwater sump and the demister unit blackwater sump to further analyze the particle size distribution along the scrubber system and determine overall particle deportment/partitioning. The sampling ports themselves consist of identical long radius 90° bends of 1/8" inner diameter copper tubing that are placed parallel to the incoming airstream at the centerline velocity of the chamber shown in Figure 94. Particulate matter capture testing was performed at all sampling locations with the chamber void of the filter and demister assembly to confirm that the sampling locations were collecting similar amounts of particulate at their respective locations. Air velocity sampling was also performed with the chamber fully dressed to confirm that similar mass flow rates of coal rich air was entering all cassettes to aid in accurately gauging capture efficiency.
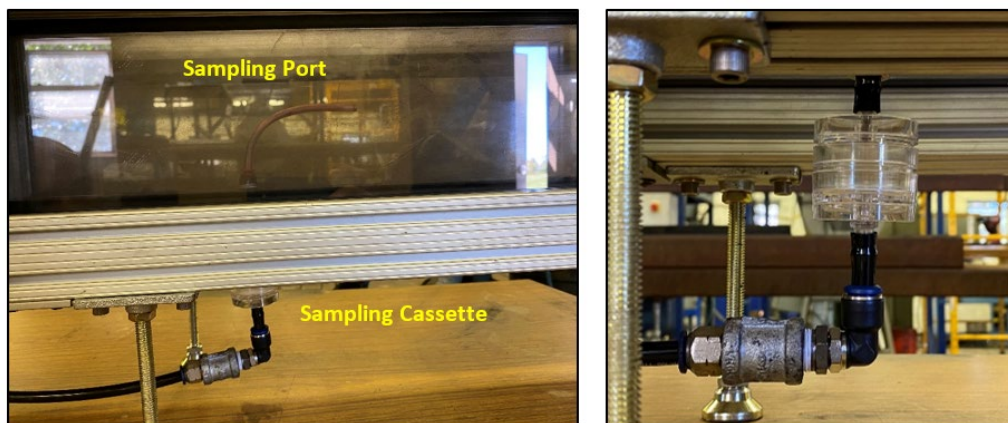
Figure 94. Gravimetric sampling system.

To control the egress of water into the scrubber unit, a system of gate valves along with flowmeter is teed off of the laboratory building's water supply. Mass flow rate and pressure of the incoming water is set up and checked before testing using a timing system and container of specified fluid volume. As with the introduction of air into the system, the amount and pressure of water was also scaled down with a cross-sectional-area scaling factor calculated from the information obtained from an operational scrubber unit.

The nozzle is housed within the preliminary upwards section utilizing a bulkhead fitting and directed towards the middle section of the filter assembly. Due to its higher wettability efficiency a brass 60° spray angle full cone nozzle which is capable of spraying at a rate of 0.25 gpm at 55 psi was employed in the test runs.

The filter mesh utilized in the scrubber unit was a small portion of an industrial-grade, steel-woven, scrubber mesh. The panel is approximately 6-mm in thickness and contains 20 layers of wire screen. The wire that the screen is composed of is 0.09-mm in diameter and is evenly spaced at 7 wires per centimeter of the screen. The panel is installed in the filter section of the scrubber, shown in Figure 95, at a downward sloping angle of 45° with a face area totaling 0.074 m^2. The mesh screen housing includes two additively manufactured parts to hold the screen steady while it shakes including a quick-change stainless-steel mount for the upper part of the screen and a lower mesh mount (Figure 96). The additive parts were also optimized for water collection and mesh sealing. As installed, the filter assembly can be easily interchanged to integrate design modifications (e.g. hydrophobic/hydrophilic treatment, modifications to mesh layering) as dictated by the experimental design.
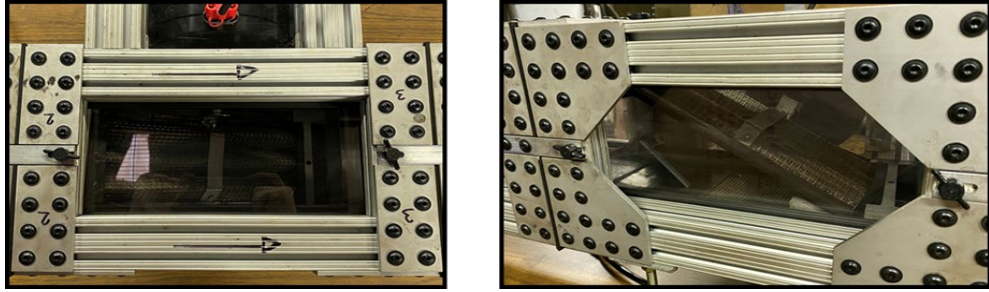
Figure 95. Top and longitudinal view of the filter assembly.
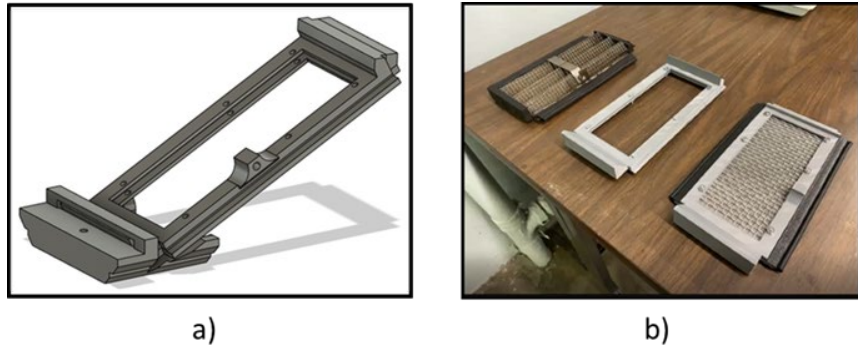
Figure 96. The mesh frame-adapter assembly a) Illustrated in a CAD drawing, b) Additively manufactured frames

An extra unit containing the shaker was designed and mounted to the system in such a way that it can be attached to the mesh screen unit from the side (Figure 97). This unit completely protects the shaker from water and coal dust exposure and allows the mesh screen to be connected to the aluminum rod end of the shaker.
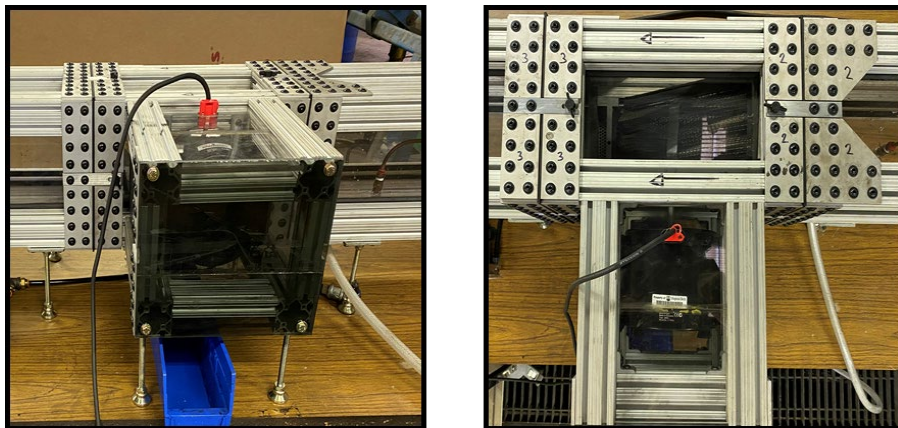
Figure 97. Top and longitudinal view of the shaker assembly.

92

The mesh screen itself was connected to an electromechanical shaker (Brüel and Kjær Type 4809) by an actuating rod and clamping mechanism (Figure 98). The square waves were generated by a SDG1000X function waveform generator and applied to the shaker through a Brüel and Kjær Type 2718 power amplifier for base excitation over a range of frequencies. The vibration equipment, as shown in Figure 99, are located around the mesh screen section.

Figure 98. Clamping mechanism between the shaker's actuator rod and mesh screen.
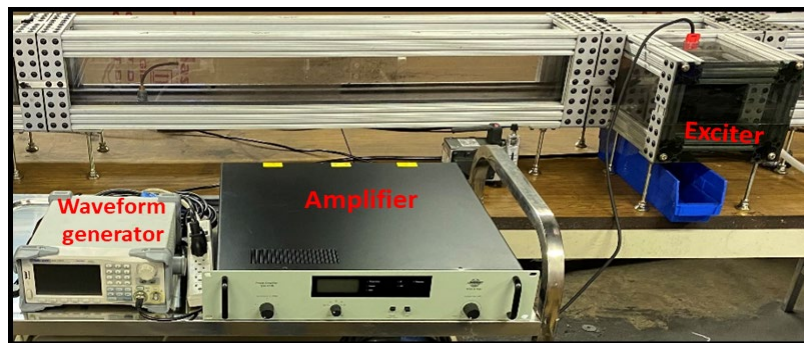
Figure 99. Vibration equipment utilized in the test set-up.

A demisting assembly added to the system to create a more accurate representation of a full-size scrubber assembly. An in-house and purpose-built demister assembly (curved vane demister) was designed, 3-D printed, and additively manufactured (Figure 100). This unit was then tested and shown to increase airflow and water collection into the bottom sump that actively pulls excess water from clean charge air while maintaining sufficient flow rates through the chamber.
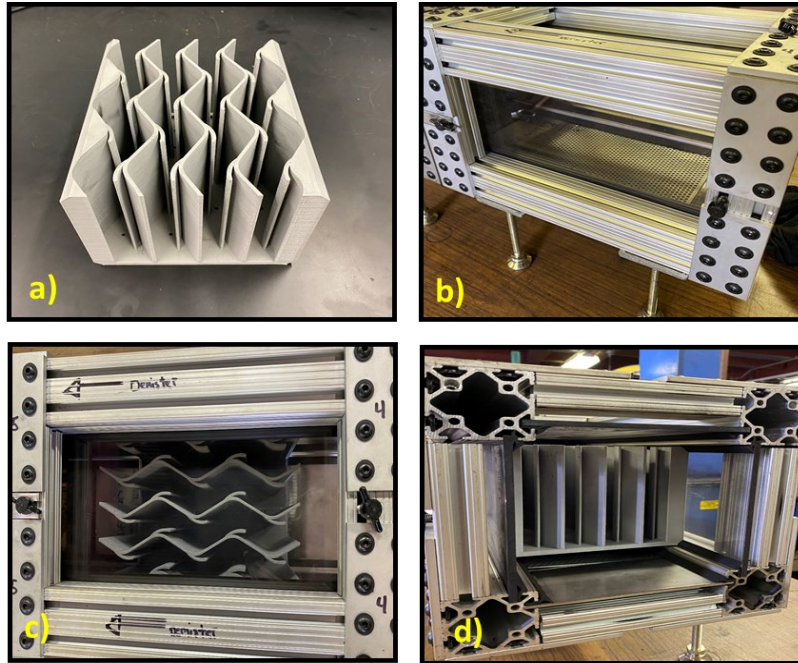
Figure 100. Demister assembly: (a) additively manufactured curved-vane demister; (b) bottom of the demister (water collection equipment); (c-d) Top and front view of the shaker assembly.

4.2.2. Materials and Methods

During each trial, several parameters were kept constant in order to minimize random error and ensure that the experiments were conducted in a steady, stable manner. The fixed test parameters are listed in Table 8.

Table 8. Fixed operating parameters for each trial.

Property	Value
Dust feed rate	14.0 to 22.7 g/min
Downwind airflow velocity	10 m/s
Sampling method	Gravimetric Sampling
Sampling duration	5 min
Sampling pump flow rate	5 lpm
Jet mill pressure	55 psi
Signal generator gain	20 Vpp

Given the system factors, gravimetric measurement is considered to be the most reliable and least likely to lead to bias. For reliable quantification of gravimetric filters, and for reducing the impact of weighing error, a minimum mass accumulation in the downwind cassette of 1 mg is required. As such, the following was used to calculate the time required for accumulating enough mass in the downwind sampling cassette for analysis:

$$t = m/[Qpump * Cfeed * (1 - \eta)]$$

where m is the mass accumulation in downwind sampling cassette, $Qpump$ is the sampling pump flow rate, $Cfeed$ is dust feeding concentration, η is the scrubber efficiency.

Before each trial, various portions of the system, including the mesh screen, demister, sampling ports, and black water sumps, were thoroughly cleaned with compressed air to ensure experimental integrity, and maintain a consistent airflow rate. In order to determine the dust mass differential collected in the specified time interval, sampling cassettes with the appropriate filters were weighed before and after each test. All experiments were conducted with the same cleaning procedure in order to compare the efficiency of all operational modes effectively.

Gravimetric samples collected during these tests were used to determine the dust collection efficiency:

$$Collection\ Efficiency\ (\%) = \left(1 - \frac{weight\ of\ downwind\ sample}{weight\ of\ upwind\ \ sample}\right) * 100$$

Using these general procedures, four test campaigns were conducted: (1) Vibrational Parameter Optimization; (2) Size-by-Size Performance Results; (3) Evaluation of Mesh Density; and (4) Evaluation of Mesh Surface Treatment. Additional protocols and distinctives for each campaign are discussed with the results below.

4.2.3. Results and Discussion

4.2.3.1. Vibrational Parameter Optimization

To investigate and evaluate the operational sensitivity of the bench-scale flooded bed dust scrubber, a three-factor, three-level Box-Behnken Design (BBD) was employed and the experimental data were statistically analyzed. Experimental factors for this study are given in Table 9. Following this analysis, 3-D plots were developed to show the relationship between operating factors and collection efficiency as well as pressure drop and particle accumulation in the mesh.

Table 9. Experimental factors and range values for vibrational parameter tests.

Factors	Level		
	Low (-1)	Medium (0)	High (+1)
Water flow rate (lpm)	6	7.5	9
Amplitude (dB)	20	30	40
Frequency (Hz)	130	2565	5000

In addition to the experimental variables, repeated trials at the center point demonstrate the importance of controlling constant operational parameters in the propagated pure error in the experimental program. Although all three repetitive runs were performed under the same levels of water flow rate, amplitude, and vibration frequency, it is thought that improper control of airflow rate in each trial resulted in different collection efficiency values.

The software used to create the BBD program provides the necessary experimental design as well as statistical tools obtained from the test results and their relationships with the operational parameters to construct the statistical model with the lowest error as well as the highest reliability. Among these statistical tools, lack of fit, the coefficient of determination (R^2), and the adjusted coefficient of determination (R^2_{adj}) were particularly examined and considered adequate as they are some of the most critical statistics showing the reliability of the statistical analysis. Based on these analyses, optimal conditions were determined to maximize the bench-scale flooded bed dust scrubber dust collection efficiency.

The statistical analysis results of the experimental program based on a limited number of experimental studies do not necessarily indicate that the models have superior predictive capacity; however, the analysis results provide a rigorous tool to gain insight into the combinatory effects of operational parameters. The information obtained from this analysis can be used to guide modeling studies later on.

The experimental test results shown in Table 10 describe the scrubber collection efficiency as a function of three operational parameters: the water flow rate, the vibration frequency generated by the waveform generator, and the amplitude of that signal. The results of the experimental setup created with 12 different combinations of these 3 parameters emphasize the importance of the mentioned operational factors in determining the collection performance of the mesh screen. It can be seen from the surface plots slight

changes in the level of the variable may significantly affect the collection efficiency. For instance, while the efficiency was 96.22% in the 11th run, after the level of the variables changed slightly, the efficiency of the system decreased to nearly 18% in the 3rd run.

Table 10. Summarized collection efficiency results for bench-scale scrubber optimization experiments.

Experiment	Variables			Collection Efficiency (%)
	Water Flow Rate (lpm)	Amplitude (dB)	Frequency (Hz)	
1	7.5	40	130	97.25%
2	7.5	20	130	95.27%
3	6	30	130	68.45%
4	9	30	130	97.15%
5	6	20	2565	84.71%
6	9	20	2565	93.31%
7	6	40	2565	84.36%
8	9	40	2565	94.21%
9	9	30	5000	89.97%
10	6	30	5000	30.38%
11	7.5	40	5000	96.22%
13	7.5	20	5000	93.39%
C1	7.5	30	2565	90.48%
C2	7.5	30	2565	93.93%
C3	7.5	30	2565	80.42%

As shown in the surface plots and in the collection efficiency results in Table 10, Figure 101, and Figure 102, the collection efficiency usually increases as the water flow rate increases. Also, it can be inferred from the surface plots that the collection efficiency generally increases with the increase in amplitude, therefore, this value is also in a linear relationship with the performance of the mesh screen collection ability. However, this relationship is not as steep as it is in the water flow rate-collection efficiency relationship, as it can be deduced from the fitted line plots (Figure 101). Unlike the mentioned two variables, as it will be seen at these plots, no linear relationship and proportionality between frequency and collection efficiency have been determined. For example, as shown in panel B and C of Figure 102, an increase in the frequency may result in either improving or reducing the flooded bed dust scrubber performance efficiency based on the level of water flow rate and amplitude.

The results of these tests were also subjected to particle size analysis. As shown in Table 10, the results obtained from the particle size analysis are mostly in agreement with the overall collection efficiency values in the range of 5 μm to 15 μm and larger particle sizes. It is thought that the reason for the inconsistency at below 5 μm could be that the ultrafine particles more likely adhere to the filter and do not easily separate when scraping the filter.

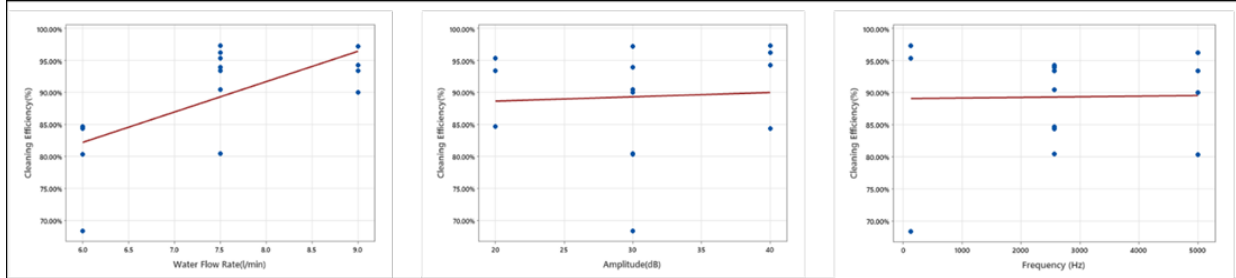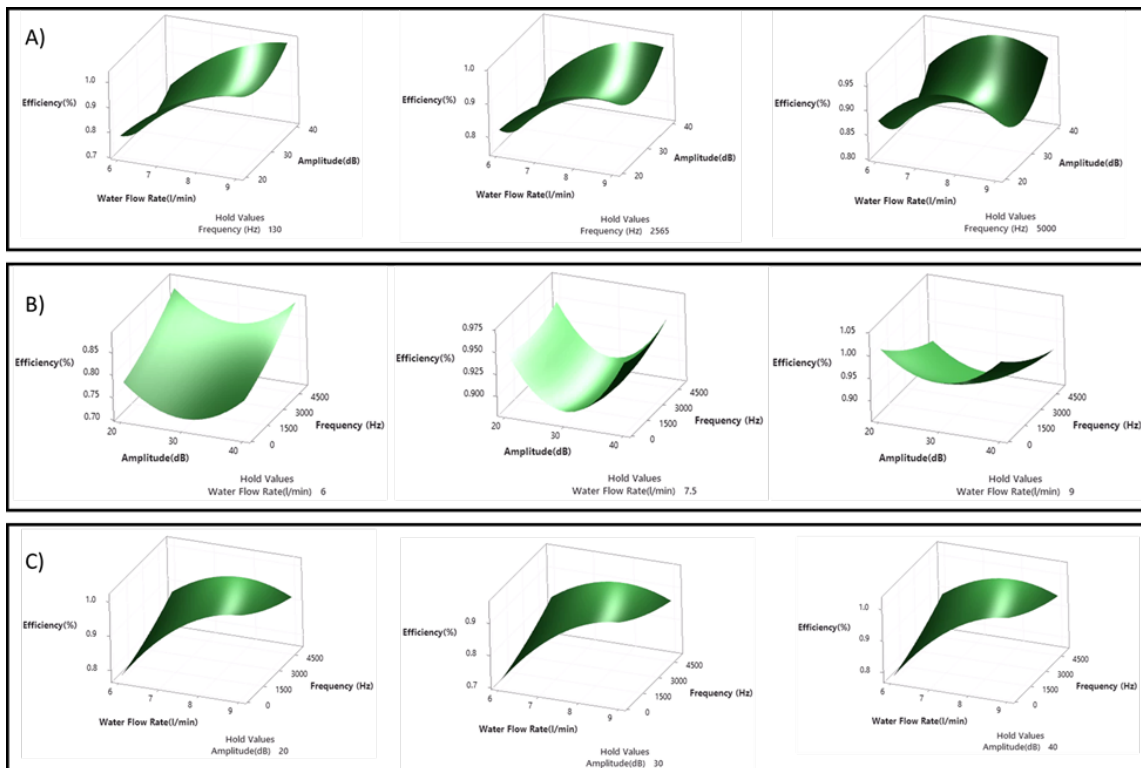*Figure 101. Regression analysis of bench-scale scrubber tests: fitted line plots.*

Figure 102. Surface plots of (A) Collection Efficiency vs Amplitude – Water Flow Rate at different vibration frequency values; (B) Collection Efficiency vs Frequency – Water Flow Rate at different levels of amplitude; and (C) Collection Efficiency vs Amplitude – Frequency at different levels of water flow rate.

98

As explained above, the collection efficiency usually increases with an increase in the water flow rate and amplitude. However, no linear relationship between frequency and collection efficiency was observed. Nevertheless, the performance of the mesh screen's collection efficiency increases much more when around 130hz vibration frequency applied. Therefore, low frequency, high water flow rate, and high amplitude will be the most optimal application for increasing the collection efficiency.

The optimum collection efficiency was identified through interpolation using the RSM plots and regression model generated from the experimental program (water flow rate (+1 or 9 L/min); amplitude (+1 or 40 dB); and vibration frequency (-1 or 130 Hz)). This result was compared to that of the other scrubber operational modes, including dry testing and no-vibration testing. Data from this comparison are shown as a function of size class and overall in Table 11 and Figure 103. The vibration imparts considerable improvement in overall collection efficiency in both wet (98% versus 90%) and dry (77% versus 72%) conditions. The results were most pronounced in the intermediate size class (5 x 15 microns); however, improvements were also observed in the finest size class in the wet condition.

Table 11. Summarized collection efficiency data for various scrubber operational modes.

Experiment	Variables			Collection Efficiency (%)			
	Water Flow Rate (lpm)	Amp. (dB)	Freq. (Hz)	-5 μm	5x15 μm	+15 μm	Overall
Optimal Trial*	9	40	130	97.68	97.36	97.62	97.86
Wet-No Vibration	9	0	0	93.02	76.54	96.57	89.68
Dry-With Vibration	0	30	130	68.77	78.87	85.17	76.62
Dry-No Vibration	0	0	0	72.84	71.15	87.96	72.15

Optimum results were predicted using the RSM plots and regression equation obtained from the BBD test results
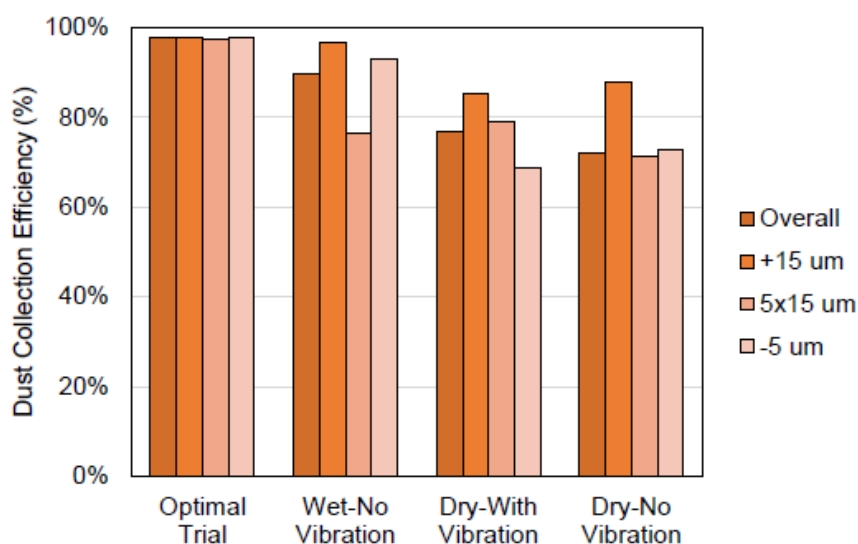

Figure 103. Collection efficiency by particle size class for various operational modes.

Finally, the upwind and downwind tunnel section were both subjected to pressure drop measurement to determine and quantify the self-cleaning potential of the vibrating mesh system. In addition, after testing, the mass accumulation of dust in the filter was measured and recorded. Data from these trials are shown Table 12 and Figure 104 for the various operational conditions as well at the optimal trial determined from BBD. As shown, the vibration imparts a significant improvement to clogging mitigation in both the wet and dry conditions. For the wet mesh trials, a 56% reduction in pressure drop and a 43% reduction in filter accumulation we are achieved as a result of the induced vibration. Even greater reductions were observed in the dry mesh trials, further supporting the original thesis that induced vibration can provide a cleaning mechanism that will prolong the mesh filter operational time.

Table 12. Summarized clogging data for various scrubber operational modes.

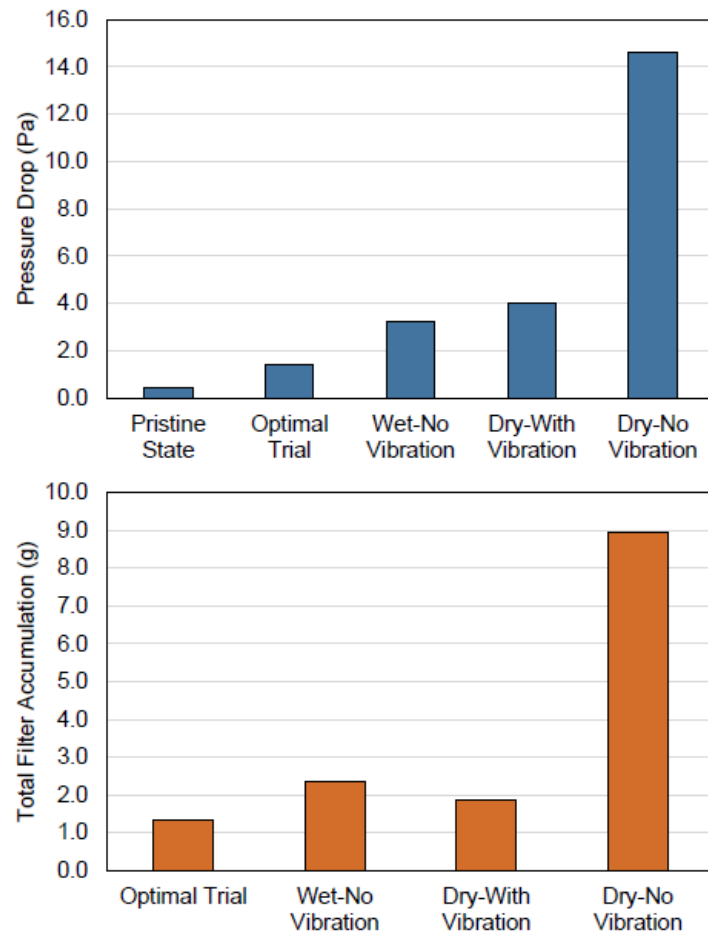| Experiment	Variables			Pressure Drop (Pa)	Total Filter Accumulation (g)
	Water Flow Rate (lpm)	Amp. (dB)	Freq. (Hz)		
Pristine State	N/A	N/A	N/A	0.45	N/A
Optimal Trial	9	40	130	1.42	1.35
Wet-No Vibration	9	0	0	3.24	2.36
Dry-With Vibration	0	40	130	3.99	1.86
Dry-No Vibration	0	0	0	14.62	8.96

Figure 104. Pressure drop data across mesh screen (top), total accumulation between wire meshes (bottom) for bench-scale scrubber tests

4.2.3.2.   Size-by-Size Performance Results

Using the optimized parameter values identified in the previous section, a series of follow-on trials were conducted to investigate the size-by-size deportment of particles through the system. In this study, representative samples were taken at predetermined locations across the system. The coded sampling locations along the chamber are illustrated in Figure 105.
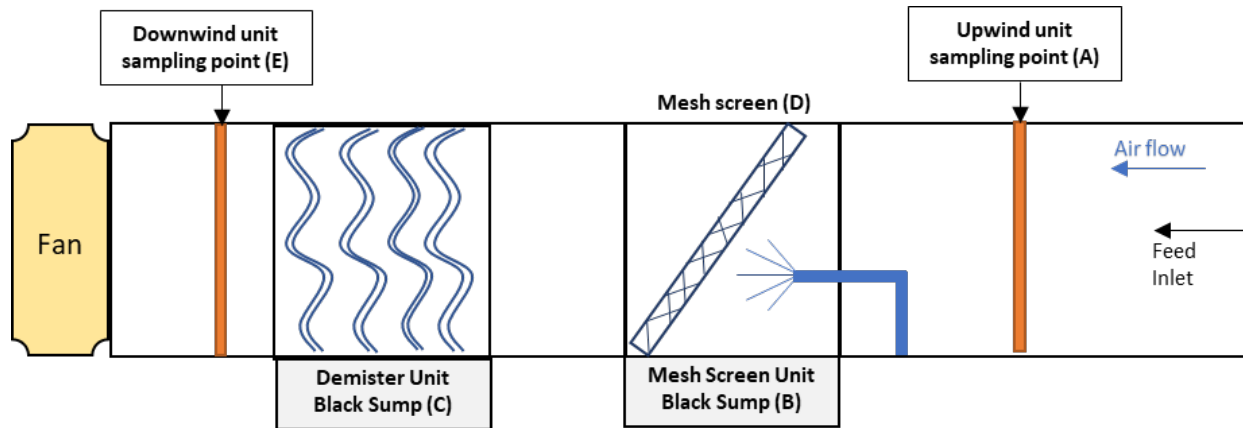

Figure 105. Visual illustration of sampling locations.

After collecting samples from these locations, the coal dust particles from the Teflon filters as well as coal dust & water mixture from the mesh screen itself, mesh screen section blackwater sump and demister section blackwater sump were analyzed with Microtrac laser particle size analyzer to determine the particle size distribution of each sample.

Table 13 to Table 16 and Figure 106 and Figure 107 show the size-by-size results of this study for both vibration free and vibration enhanced operation in both dry and wet modes. The particle amounts sampled at the predetermined locations are listed in the results as both a percentage of stream (i.e. the size distribution of the sample stream) and a percentage of feed (i.e. mass recovery to the stream).

In the dry operational conditions (Table 13 and Table 14), over half of the feed mass accumulated on the floor of the duct between the mesh screen and demister and was thus not found in the various sampling endpoints. While this result does hinder the interpretation of the material balance, the data does provide evidence that intermediate sized particles (10 x 2.5 microns) are being preferentially recovered in the mesh screen, as indicated by the higher % of feed recovery for this size class as compared to the other classes. In addition, the dry data indicates that the vibration leads to lower accumulation in the mesh screen, as the total % of feed recovered to this stream was reduced from 7.59% to 4.51% with the addition of vibration.

Table 13. Summarized size-by-size material balance data for dry and vibration-free operational mode.

Size (µm)	Feed (A)		Sump (Screen Unit) (B)		Sump (Demister Unit) (C)		Mesh Screen (D)		Ejected Air (E)		U/S – D/S Collection Efficiency (%)
	% of stream	Mass (g)	% of stream	% of feed	% of stream	% of feed	% of stream	% of feed	% of stream	% of feed	
+10	35.04	39.77	NA	NA	NA	NA	28.28	6.12	28.27	29.7	70.29
10 x 2.5	37.23	42.26	NA	NA	NA	NA	54.78	11.1	35.59	35.2	64.80
-2.5	27.73	31.47	NA	NA	NA	NA	16.94	4.64	36.14	47.9	52.01
Total	100.00	113.5	NA	NA	NA	NA	100.00	7.59	100.00	36.8	63.18

Table 14. Summarized size-by-size material balance data for dry and vibration operational mode.

Size (µm)	Feed (A)		Sump (Screen Unit) (B)		Sump (Demister Unit) (C)		Mesh Screen (D)		Ejected Air (E)		U/S – D/S Collection Efficiency (%)
	% of stream	Mass (g)	% of stream	% of feed	% of stream	% of feed	% of stream	% of feed	% of stream	% of feed	
+10	46.08	52.30	NA	NA	NA	NA	33.98	1.53	45.89	14.8	67.83
10 x 2.5	43.51	49.38	NA	NA	NA	NA	47.92	2.16	38.33	12.3	71.54
-2.5	10.41	11.82	NA	NA	NA	NA	18.10	0.82	15.78	5.10	51.03
Total	100.00	113.5	NA	NA	NA	NA	100.00	4.51	100.00	32.3	67.70

Data from the wet testing (Table 15 and Table 16) provide better accounting of the mass and as such provide better insight on particle deportment. As expected, the majority of the feed mass ultimately reports to the demister sump (53% for vibration free; 59% for vibration enhanced) however, a notable portion is also retained in the screen sump (23% for vibration free; 25% for vibration enhanced). Moreover, the data shows that the vibration enhanced unit has a higher collection efficiency (92.6% versus 87.2%) and lower accumulation in the mesh screen (2.9% versus 3.2%) when compared to the static mesh. As in the dry tests, the intermediate particles (10 x 2.5 microns) were preferentially recovered to the mesh screen; however, this trend was not as prominent as that found during the dry testing.

Table 15. Summarized size-by-size material balance data for wet and vibration-free operational mode.

Size (µm)	Feed (A)		Sump (Screen Unit) (B)		Sump (Demister Unit) (C)		Mesh Screen (D)		Ejected Air (E)		U/S – D/S Collection Efficiency (%)
	% of stream	Mass (g)	% of stream	% of feed	% of stream	% of feed	% of stream	% of feed	% of stream	% of feed	
+10	17.59	19.96	16.77	3.78	15.51	8.27	40.75	1.29	6.45	0.83	95.30
10 x 2.5	54.79	62.19	56.81	12.8	56.75	30.2	57.14	1.81	54.55	7.00	87.23
-2.5	27.62	31.35	26.42	5.95	27.74	14.7	2.11	0.07	39.00	5.00	81.88
Total	100.00	113.5	100.00	22.5	100.00	53.3	100.00	3.17	100.00	12.8	87.17

Table 16. Summarized size-by-size material balance data for wet and vibration operational mode.

Size (µm)	Feed (A)		Sump (Screen Unit) (B)		Sump (Demister Unit) (C)		Mesh Screen (D)		Ejected Air (E)		U/S – D/S Collection Efficiency (%)
	% of stream	Mass (g)	% of stream	% of feed	% of stream	% of feed	% of stream	% of feed	% of stream	% of feed	
+10	30.33	34.42	36.60	9.12	29.81	17.5	14.12	0.40	21.67	1.61	94.73
10 x 2.5	48.94	55.55	45.09	11.2	52.71	31.0	60.05	1.72	39.02	2.87	94.11
-2.5	20.73	23.53	18.31	4.56	17.48	10.3	25.83	0.74	39.31	2.90	86.00
Total	100.00	113.5	100.00	24.9	100.00	58.9	100.00	2.86	100.00	7.38	92.62

As shown in Figure 106, vibration improves overall collection efficiency in both wet (93% versus 87%) and dry (68% versus 63%) conditions. Similarly, the data shows that the presence of vibration generally has a positive effect on the collection efficiency of the system in finer size classes. While almost the same results are obtained in dry conditions for particles below 2.5 micron (52% versus 51%), a significant improvement in collection efficiency is observed in this size class under wet conditions (86% versus 82%). In the coarse size class, very slight decreases in collection efficiency were observed. While these decreases were more pronounced in dry conditions (70% under vibration versus 68% with no vibration), the difference was less significant in wet conditions (95% in both conditions).
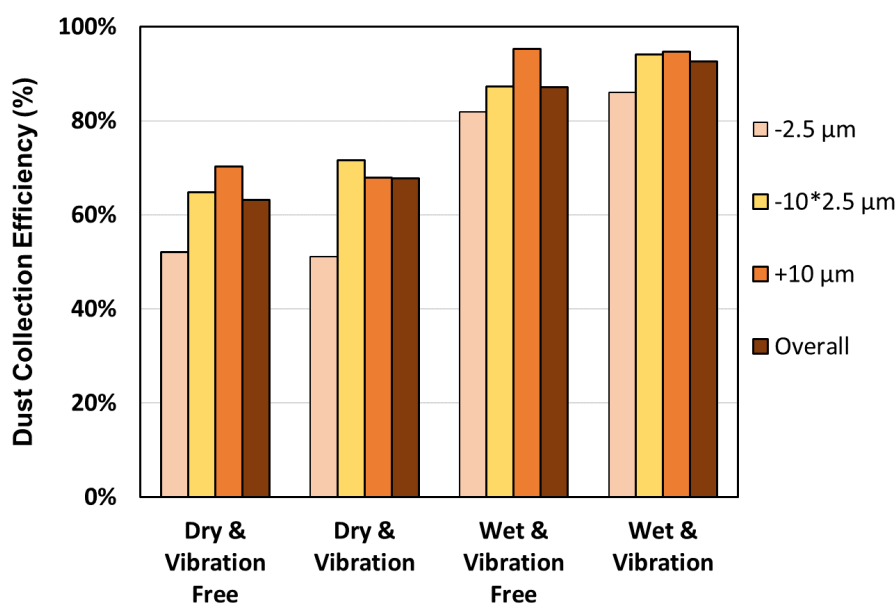
Figure 106. Collection efficiency by particle size class for various operational modes.

To further assess the data, Figure 107 shows the Gaudin-Schumann size distribution curves of the various product streams for the evaluated operational conditions. By comparing curves for the different conditions, the variations in particle size characteristics can be assessed and the distribution profiles can be understood better. When the operational conditions change from dry and vibration-free condition to wet and vibration condition, the sharpness of the curves are usually increasing. This is most prominent in the mesh screen section. It has a slope of 1.03 for the dry & vibration-free condition while it has a slope of 1.46 for the wet and vibration condition. This means in the wet vibration condition the mesh screen has a narrower particle size distribution.

The d_{80} values obtained from the curves also show the significant change in mean particle size between the dry and vibration free conditions (d_{80} = 24.5 microns) versus that of the wet with vibration condition (d_{80} = 9.7 microns) (Figure 107). The decrease in this value shows that adding water to the system and vibrating the mesh screen at the same time will increase the possibility of finer dust particles getting captured by water droplets due to the increased surface wettability and improve the efficiency of the screening activity. It is also important to note that more amount of dust particles that were introduced to the stream were eliminated in the upwind section of the mesh screen. The blackwater sump located in the upwind section of the mesh screen is largely collecting the particles that are shed from the mesh screen surface. While the percentage of feed in the mesh screen section black water sump under the wet & vibration-free condition is 23%, the same parameter for the wet & vibration condition increased to 25%.
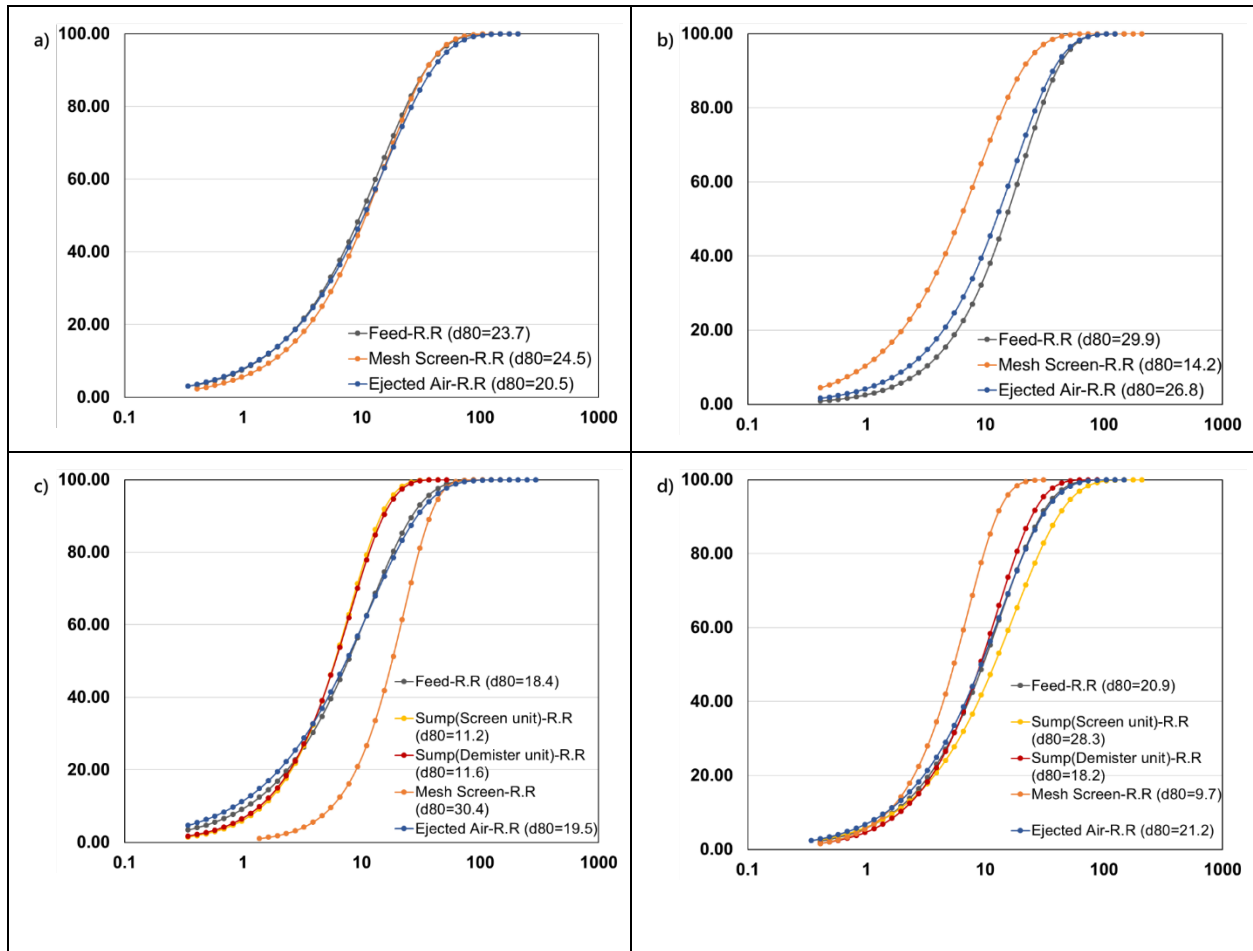
Figure 107. Size distributions of a) Dry & vibration-free mode b) Dry & vibration mode c) Wet & vibration-free mode d) Wet & vibration mode.

Mass accumulation on the mesh screen and pressure drop across the mesh screen are two important indicators of the mesh screen's self-cleaning ability when vibration is applied. These data are given and illustrated in Table 17 and Figure 108. When vibration was induced, pressure drop across the mesh screen decreased by 23% and filter accumulation decreased by 9.7% in the wet environment compared to vibration-free test. In the dry condition, when the vibration was applied, a 43% decrease in pressure drop and a 41% decrease in mass accumulation were observed. The reductions supporting the proposed vibration enhanced mesh screen design can provide the mesh screen with a self-cleaning mechanism and enable the mesh screen to operate longer.

Table 17. Summarized clogging data for various scrubber operational modes.

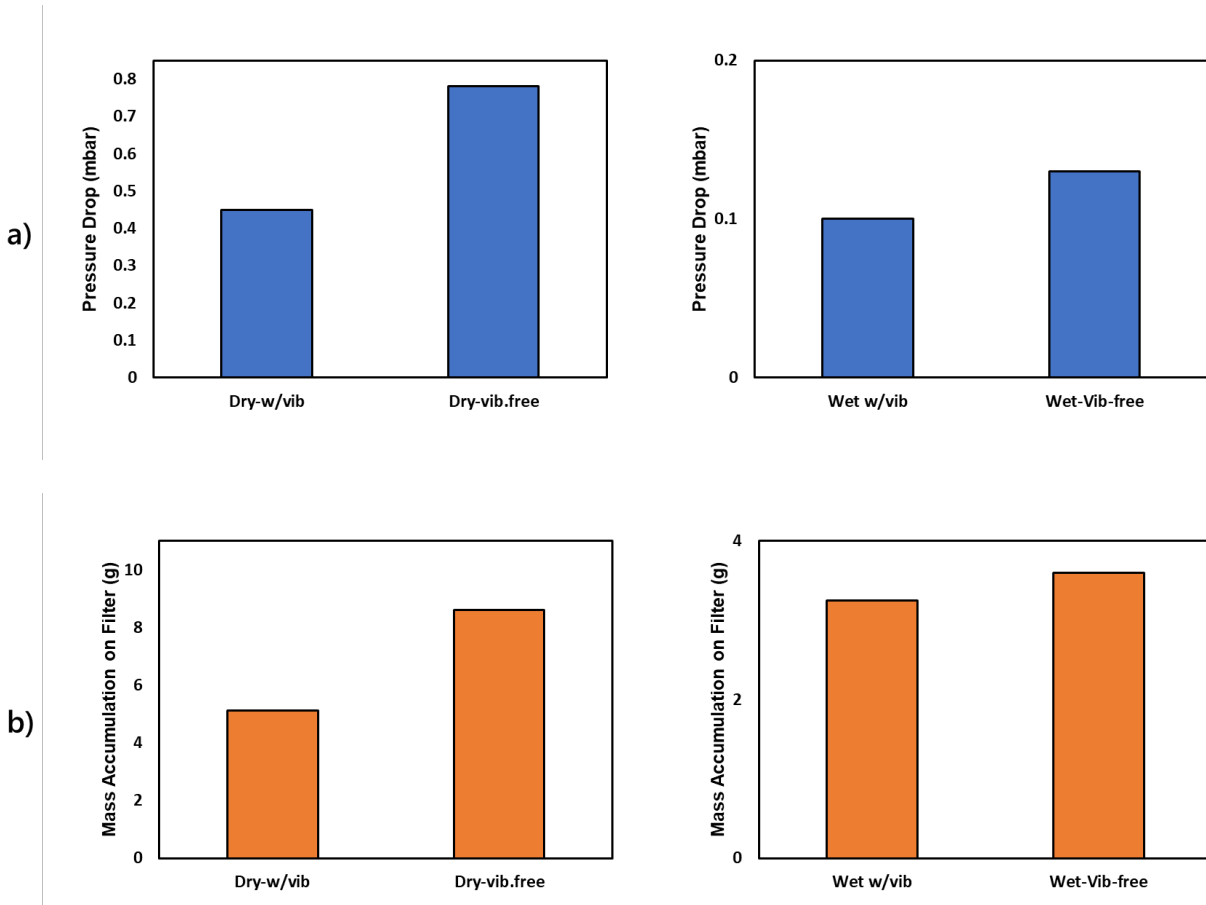| Operational Mode	Increase in Pressure Drop (mbar)	Total Mass Retained on Filter (g)
Dry & Vibration-Free	0.78	8.61
Dry & Vibration	0.45	5.11
Wet & Vibration-Free	0.13	3.6
Wet & Vibration	0.1	3.25

Figure 108. a) Pressure drop data across mesh screen in dry and wet operational conditions, b) Total accumulation between wire meshes in dry and wet operational conditions.

4.2.3.3. Influence of Mesh Density

Additional tests were conducted to evaluate the combined influence of mesh density and induced vibration on system efficiency. In this trial, three separate mesh densities, namely 30 layers, 20 layers, and 10 layers of woven stainless steel, were evaluated in both vibration enhanced and vibration free settings. All layering tests were conducted for 5 minutes of run time, and pressure drop was measured continuously throughout the test. Dust-laden air samples were collected upwind and downwind of the filter assembly to determine the dust collection efficiency. All tests were performed at an initial airspeed of approximately 9.5 m/s, and post-run air velocity measurements were taken to determine loss in air flow.

Dust collection efficiency data from these tests is shown in Figure 109. The data obtained from the dust collection efficiency calculations showed that regardless of what filter package were used when the mesh screen is enhanced with the vibration, better results are obtained in both wet and dry conditions compared to the tests conducted in static condition. These differences are sometimes negligibly small for some operational conditions. However, an improvement of about 3.5% was obtained in the collection efficiency with the 30-layer screen in the wet vibration-enhanced operational condition compared to the same screen type under the wet vibration-free condition. The 30-layer wet vibration-enhanced operational condition was the most efficient run (92%). This is followed by the 30layer-wet vibration-free state with 89% efficiency. When we evaluate each operational condition in itself, we will see that the lowest efficiency of that operational condition is always taking place with a 10-layer screen. The maximum achieved efficiency with the 10-layer screen was under the wet vibration-enhanced operational condition (80%) and the lowest was about 77% under the dry vibration-free condition.
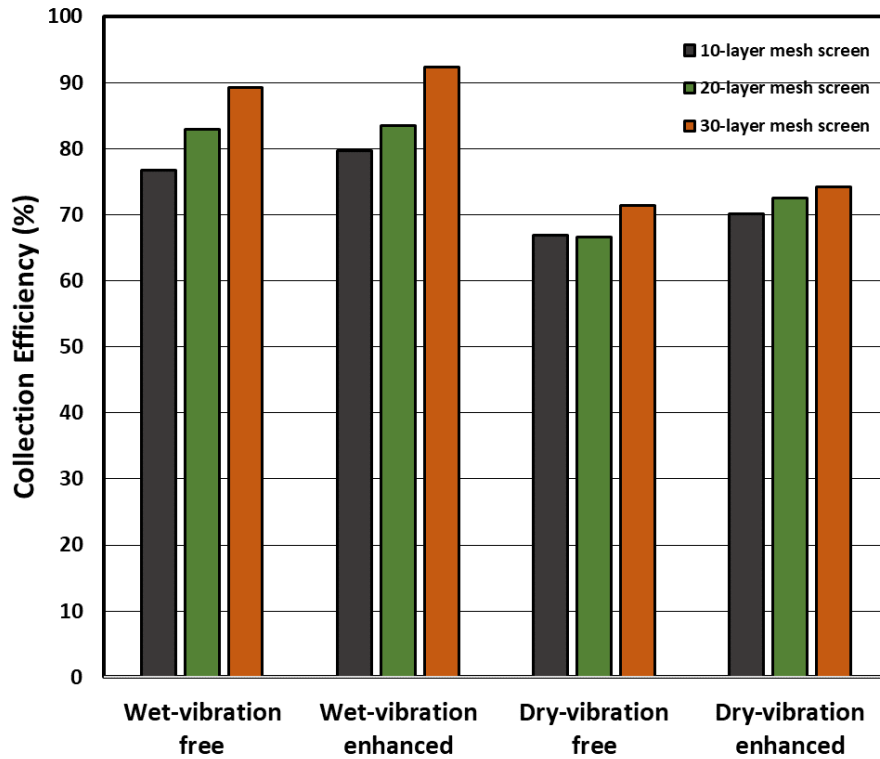
Figure 109. Collection efficiency by different mesh screen packages with various filter layering under various operational modes.

While collection efficiency is one evaluation metric, it must be considered alongside other metrics of performance. As such, throughout the same tests, the pre-test and post-test conditions of the downstream airflow were monitored. The difference of these two values shows how much airflow loss occurs through the test duration. The greater the detected loss in airflow implies greater mesh clogging and thus lower the overall system efficiency. Data from this analysis is shown in Figure 110. The highest airflow loss occurred in the test with a dry and vibration-free operational condition with 30-layer screen (3.5 m/s). The conditions with the least air loss were the tests with a 10-layer screen in each operational condition. The lowest airflow loss occurred when a 10-layer mesh screen was used under the wet vibration-enhanced operational condition (0.81 m/s).
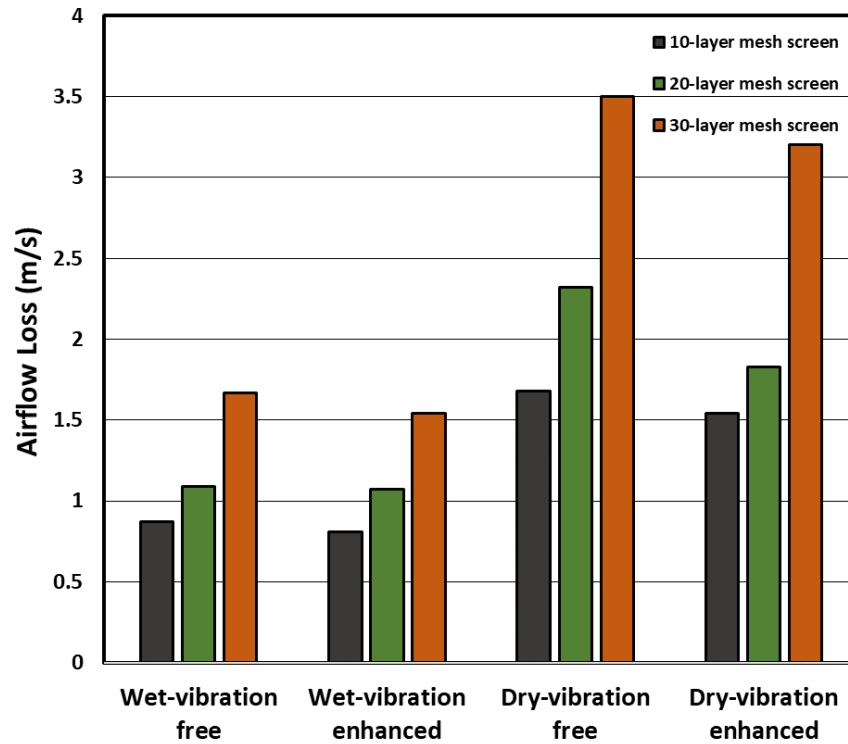
Figure 110. Downwind section airflow loss on mesh screen with different filter layering under various operational modes.

As a supportive indicator to the airflow loss parameter, the pressure difference data read digitally from the downstream and upstream directions of the system continuously throughout each run (Figure 111). This data shows that the pressure in the wet condition tests always starts higher than the dry condition test, likely due to the water layer that coats the mesh and reduces mesh porosity. However, when the pressure change is monitored throughout the test, the data shows that the pressure changes in the tests performed under wet conditions is much less than the increase in pressure changes under dry conditions. Because the initial pressure created by the water sprayed on the screen causes the initial pressure in the tests performed in wet conditions to start from high. The data show that the pressure difference in dry condition reaches much higher values (avg. 20% increase) than in wet condition (avg. 3.13% increase). The pressure drop increase throughout the test explains the partial clogging of the mesh screen. In the wet condition, no significant differences were observed in the vibrating and non-vibrating conditions. In addition, in each operational condition, the minimum increase in pressure difference was obtained in the tests performed with the 10-layer filter assembly under wet vibration-enhanced operational condition (2.2% increase), and the maximum pressure difference is obtained in the tests performed with the 30-layer filter assembly (22.4% increase).
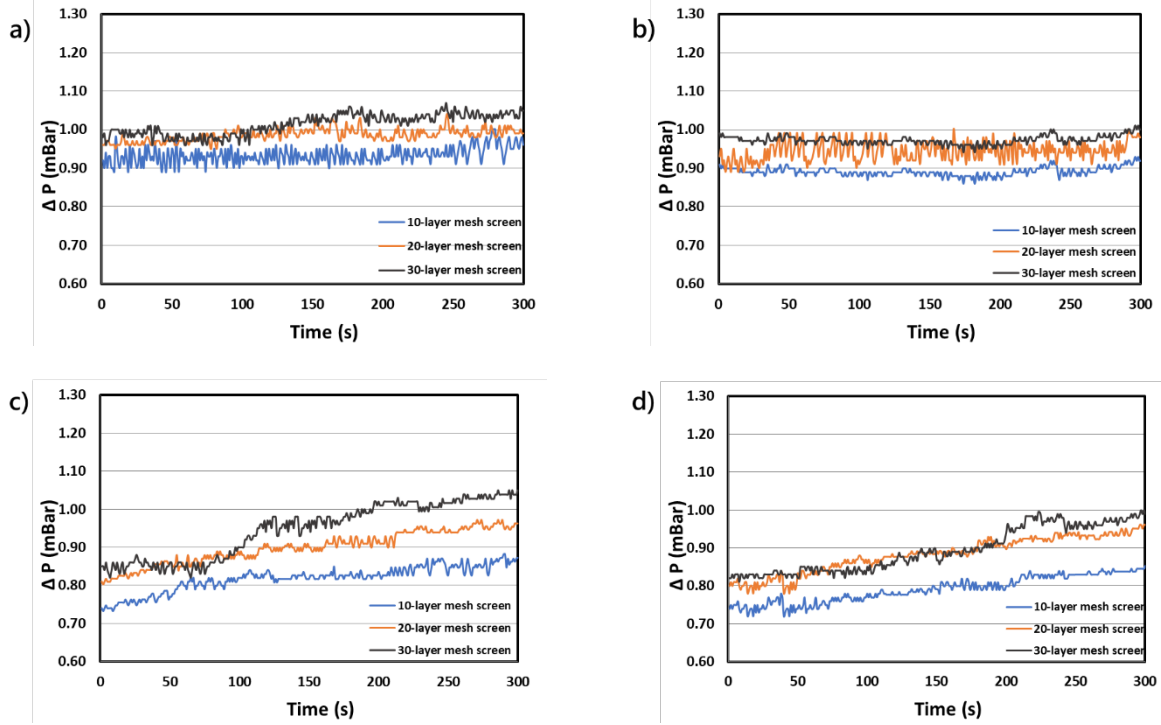
Figure 111. Δp across mesh screen with different screen packages of a) Wet & vibration-free mode b) Wet & vibration mode c) Dry & vibration-free mode d) Dry & vibration mode.

In addition to these data, in order to further support the assessment of system efficiency, after each test, the filter assembly of that test was passed through an ultrasonic bath. The mass of material obtained from this procedure is indicative of the amount of dust accumulated on the filter during the test. This parameter is one of the most important parameters showing the clogging of the filter. As shown in Figure 112, the operational condition in which the largest mass of particles accumulated on the filter during the test was the test with a 30-layer filter assembly under dry vibration-free condition (7.2 g). The operational condition where the least dust accumulation occurred on the mesh screen surface was the test with a vibrating 10-layer filter assembly under wet condition (2.9 g).
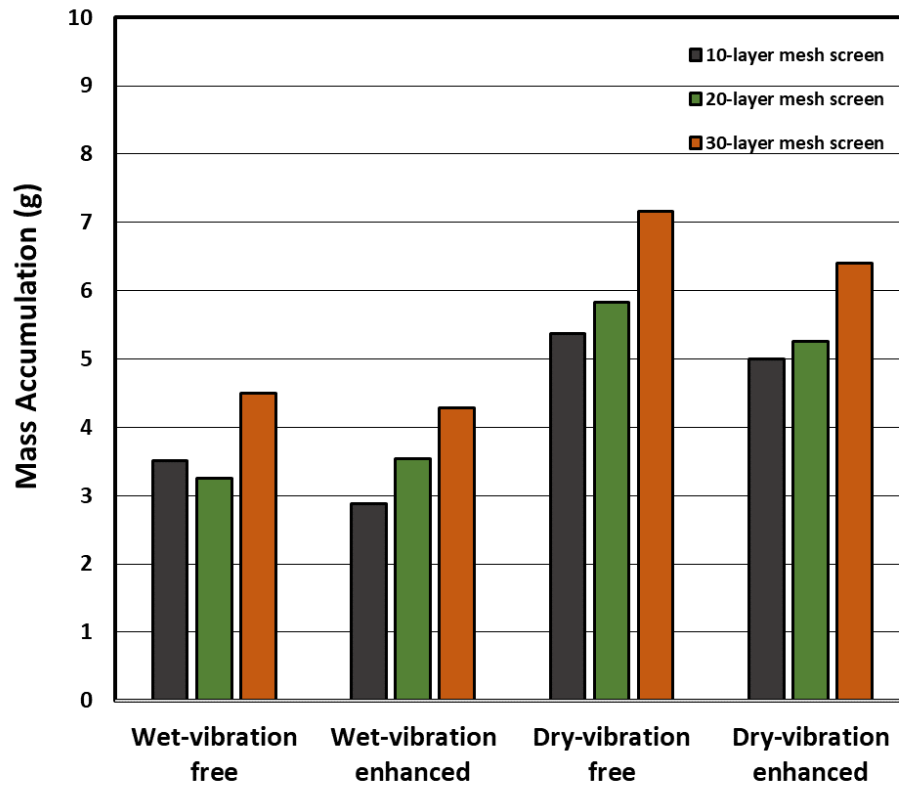
Figure 112. Mass Accumulation on mesh screen with different layering under various operational modes.

Although vibrating the mesh screen has been promising in many cases, it can be inferred from the combined data that there are a few situations where the static state is more advantageous. For example, while the air loss in the wet vibrating condition decreased by 7.78 % compared to the vibration-free condition in the tests performed with the 30-layer mesh screen, the airflow loss in the wet test using the 20-layer vibrating filter increased by 1.87 % compared to the vibration-free condition. Similarly, a decrease of 4.77% is observed in the vibrating 30-layer screen under the wet condition compared to the vibration-free condition, while an increase of 9.14% is observed in the amount of dust accumulated on the filter surface with the vibrating 20-layer mesh screen compared to the vibration-free condition. When all these data are combined, the performance of the 10-layer screen is remarkable in terms of air loss and dust accumulation on the filter. However, when the system efficiency is also considered, significant decreases are observed in the 10-layer screen compared to the higher-layer filter packages in each operational situation. The reason for its less overall efficiency is that the dust-laden air passes the 10-layer filter screen without getting captured by water droplets more easily than others. Since less dense screens cause an increase in the amount of material that can move downstream of the system, they are negatively affecting the system efficiency.

When all the test results are considered together, the data show that the lowest air velocity and pressure loss and the lowest amount of mass accumulated on the screen is the test performed under the wet vibrating operational condition performed with a 20-layer filter.

4.2.3.4. Influence of Mesh Surface Treatment

As described in Section 3.4, the surface of the filter panels can be coated in different ways to increase wettability and enhance particle-liquid adhesion. Following the protocols explained above, super hydrophobic filter coatings were obtained using a commercial polymer agent using the application instructions provided by the vender. Alternatively, the hydrophilic filters were obtained by heating them in a high-temperature low-oxygen environment furnace at 750° C for 20 minutes, allowing the formation of a blue magnetite layer on the surface of the stainless-steel filter.

Data from these tests are shown in Figure 113 to Figure 116 and include measured of both dust collection efficiency and clogging mitigation. First, Figure 113 shows the dust collection efficiency for the specified operational conditions. Across all conditions, the hydrophilic surfaces imparted the highest collection efficiency, with the differences being more pronounced for the vibration free conditions as opposed to the vibration enhanced conditions. These results compare well to those of Section 3.4 that indicated the advantages of a hydrophilic treated mesh.
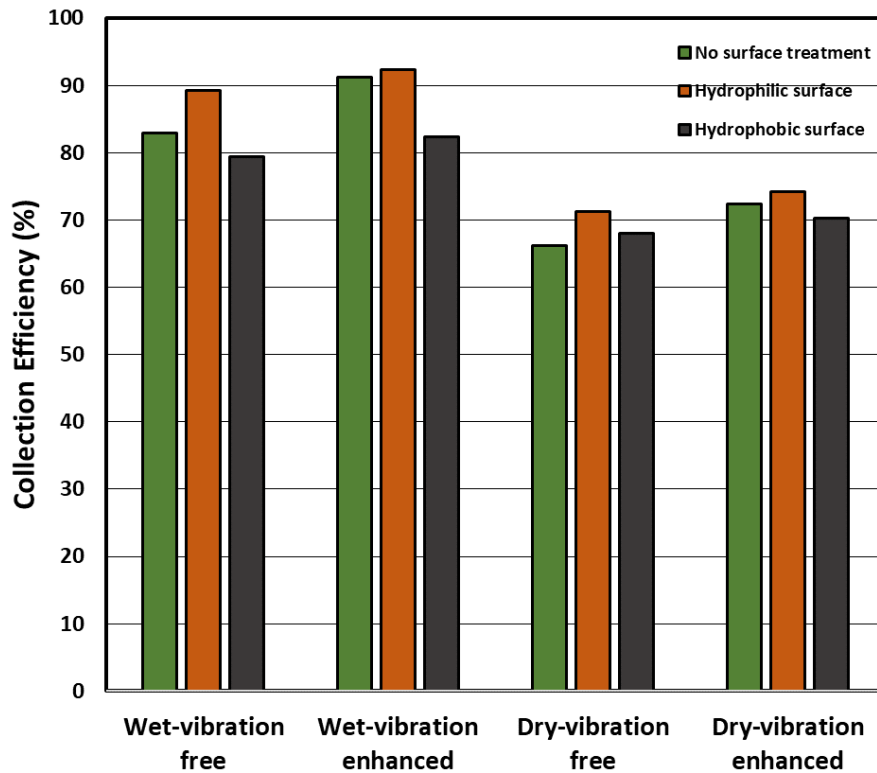

Figure 113. Collection efficiency by different mesh screens with various surface treatments under various operational modes.

Airflow loss data for the tested operational conditions are shown in Figure 114. As anticipated, the dry conditions showed the highest airflow loss, and in all cases, the hydrophilic mesh outperformed the other two. Overall, this data follows the same trend as that of collection efficiency with the difference between the various treatments being more pronounced in the vibration free cases.
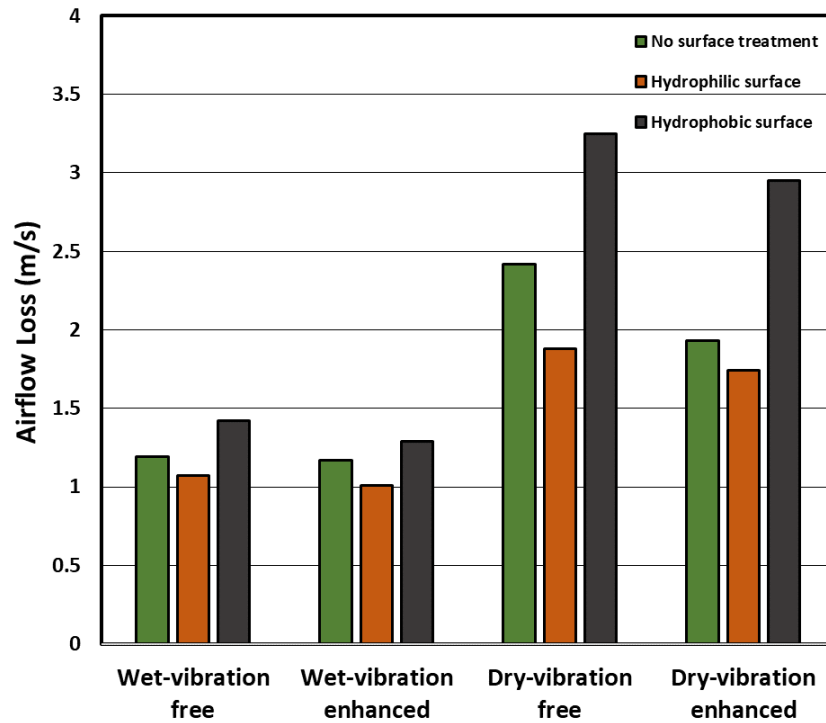

Figure 114. Downwind section airflow loss on mesh screen with different surface treatment applications under various operational modes.

Similarly, Figure 115 shows the real time pressure drop data through the test duration. For the wet-condition tests, the pressure drop was similar for all three surface treatments; however, significant deviations were observed in the dry tests. Generally, the hydrophilic and bear meshes performed similarly, with the hydrophobic mesh exhibiting a significantly higher pressure drop.
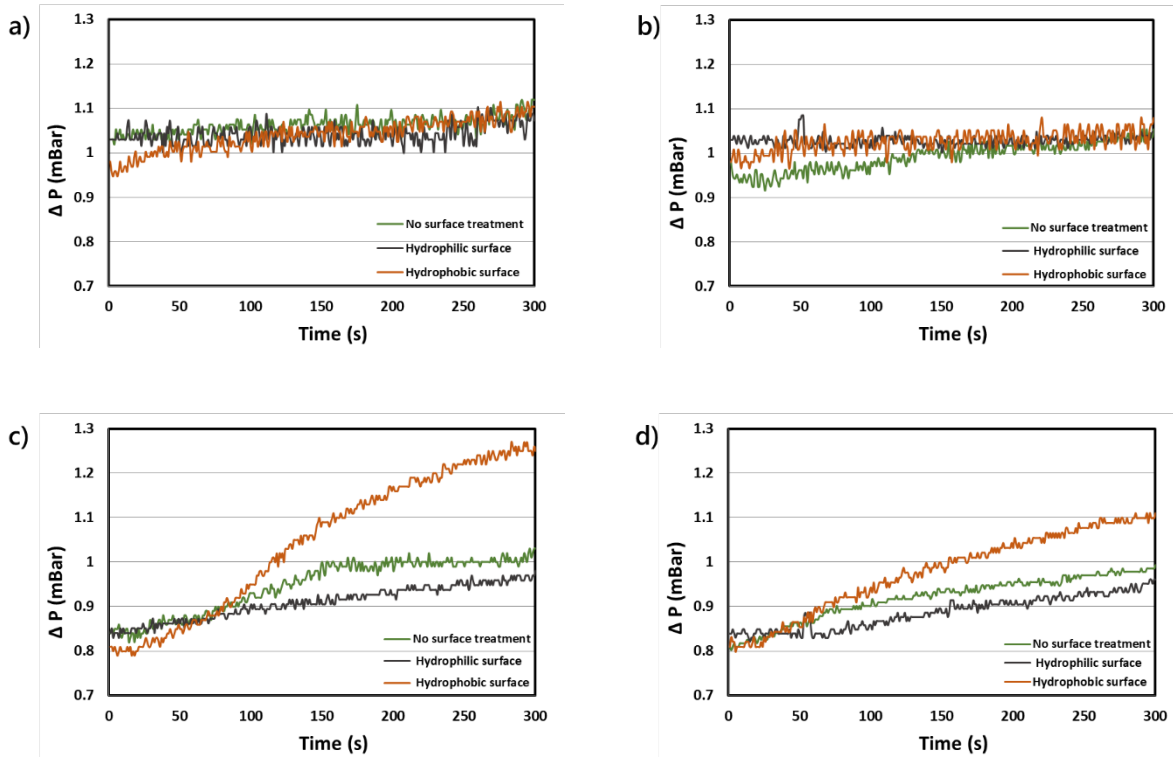
Figure 115. Δp across mesh screen with different surface treatments of a) Wet & vibration-free mode b) Wet & vibration mode c) Dry & vibration-free mode d) Dry & vibration mode.

Lastly, the mass of particle accumulation on the filter, which is another parameter that indicates the clogging process of the mesh screen and shows the self-cleaning capacity of the filter, was examined. Data from this analysis is shown in Figure 116, and closely follows the trends of airflow loss shown in Figure 114.
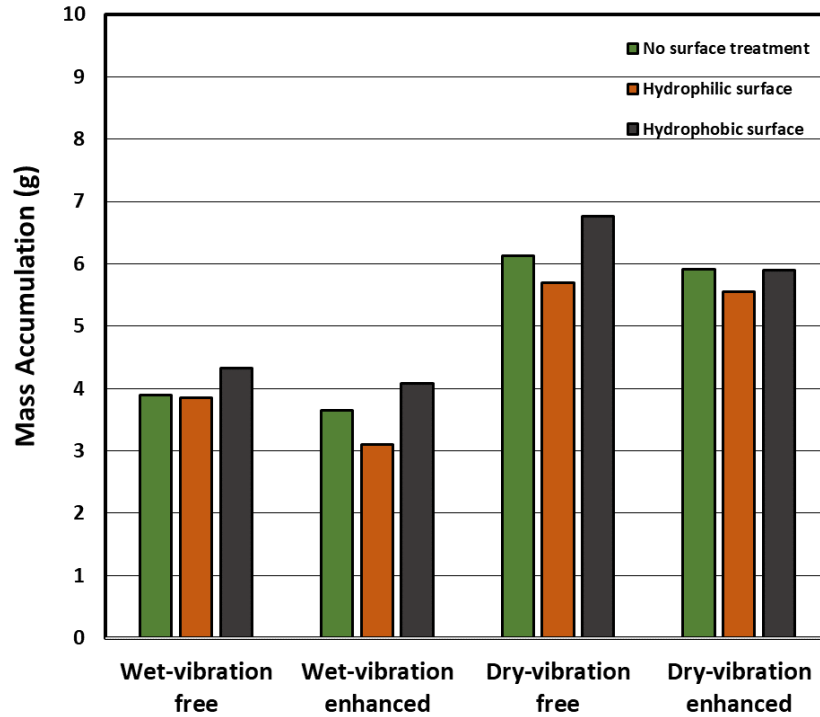
Figure 116. Mass accumulation on mesh screen with different surface treatments under various operational modes.

When the tests carried out under various operational conditions with different surface modifications are examined together, hydrophobic surface modifications tended to reduce system efficiency relative to the baseline, while hydrophilic treatment tended to improve conditions. This results closely aligns with that of the laboratory testing and validates the approach employed in that section. In explaining the findings, when water contacts hydrophilic surfaces, it forms a film, whereas when it contacts hydrophobic surfaces, it beads up. Since water droplets are highly mobile, if the surface becomes hydrophobic, the area covered by water droplets is significantly reduced of the total mesh wire surface area. Besides, hydrophilic coating is increasing the amount of liquid surface area on mesh, which increases chances of dust particles getting captured by the water droplets.

4.3. Prototype Testing

4.3.1. Design and Construction

4.3.1.1. Overall System

Initial design of the system prototype began with the intent to construct and manufacture a robust system capable of demonstrating the feasibility of vibratory mesh assemblies in full-scale, including the vibration translation system. Findings and lessons learned from previous laboratory and small-scale testing were used during the preliminary design process to ensure attainability of adequate airflow, waste-water egress, and mesh excitation. In addition, the unit was designed to be tested at the NIOSH dust gallery where testing of similar dust scrubber technologies is ongoing.

The full-scale unit, shown in Figure 117 and Figure 118, consists of a stand and shaker assembly, exterior tunnel structure, and interior vibratory mesh assembly; all of which adopted the modular structure found at the NIOSH facility.

Figure 117. Full-Scale Vibratory Prototype CAD model.

Figure 118. Full Scale Vibratory Prototype.

This prototype design and construction focused exclusively on the novel mesh section of the scrubber. Use of an existing particulate feeding system, water management system, demister assembly, and exhaust puller fan, analogous in nature to equipment found on a traditional flooded bed scrubber, has been provided by NIOSH for testing. Our unit has been designed and manufactured as a direct replacement of NIOSH's static-mesh scrubber section, eliminating the need for any on-site modification to their scrubber unit.

4.3.1.2.   Stand and Shaker Assembly

The stand assembly houses the scrubber mesh section and shaker and was constructed identical in nature to those found at the NIOSH facility. It was fabricated using an 8020-aluminum structure and bracketry. As shown in Figure 119, the shaker is securely mounted offset to the tunnel mounting location. The shaker utilized for this iteration of the project is a Modal Shop 2110E. This shaker can provide 110 lbf pk of sine force, a frequency range up to 6500 Hz, and a stroke distance of 1.0 inches; these specifications make this shaker an ideal option as it meets the operational parameters necessary for testing.

Figure 119. Stand and shaker.

4.3.1.3. Tunnel Structure

The exterior structure of the unit was developed to modularly adapt to NIOSH's existing flooded bed dust scrubber for testing purposes. The system at NIOSH consists of individual chamber sections with interior dimensions of 15.50 x 27.00 inches and employs a static mesh with the dimensions of 15.75 x 25.25 inches. Inability to package our vibratory mesh assembly within the confines of the NIOSH scrubber dimensions prompted a tapered chamber design. This taper, shown in Figure 120 and Figure 121, opens the interior of the chamber to a width of 32.25 inches, a total increase in width of 5.25 inches or a 2.625-inch increase in width from the chamber centerline.
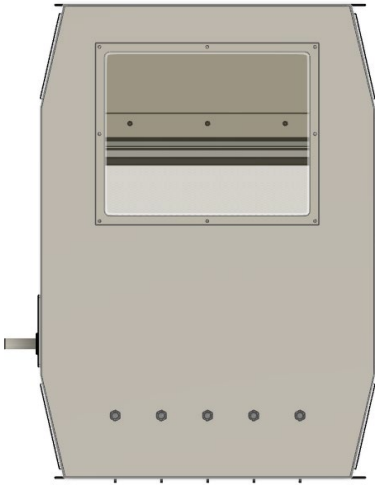

Figure 120. Chamber view showing taper, Top-view.

Figure 121. Plasma Cut Chamber Top Panel.

This outward taper will inherently decrease the velocity of air through this section of the chamber, but only marginally. As static and dynamic testing will be performed with the same mesh and chamber section in place, the potential effects of this change in geometry on airspeed will be negated through baseline control testing.

The structure itself is composed of eight individually plasma cut flat panels assembled and fabricated into a single structure using exterior fillet-welded corner joints. The material chosen for chamber construction was 0.125-inch 5052-H32 aluminum sheet. The assembly was fabricated using the Gas Tungsten Arc Welding (GTAW) process with 4042 filler material. While the NIOSH unit is constructed of carbon steel, aluminum was selected for this unit to minimize the mass of the finished assembly. A 5052 series aluminum was chosen, in lieu of a 6000 series alloy, for its cracking resistance when formed and bent, superior corrosion resistance, and weldability.

The chamber structure contains six separate viewing windows for later testing use and data collection. Visual monitoring, implementing a high-speed camera, will be applied to trace and characterize particulates flowing through the mesh, similar to previously performed testing. These windows are

constructed out of 0.25-inch-thick polycarbonate and are located on all four of the tapered panels, the mesh egress panel, and the top panel of the chamber. The mesh egress window will be used for both viewing purposes, upstream and downstream of the mesh, and for the installation of the vibratory mesh assembly into the unit.

This hollow structure is substantially reinforced using thick edge-flanges and an interior air-block plate. The edge flanges, shown in Figure 122, are equal in exterior dimension to the NIOSH unit and both designs share an identical hole pattern for ease of installation. They are constructed of 1.50-inch height x 0.125-inch thickness 90° aluminum angle. The addition of the air-block plate and its accompanying panel mounts, shown in Figure 122 and Figure 123, triangulate the interior of the structure and mechanically fasten the walls, ceiling, and floor of the chamber. This plate also provides chamber sealing for around the mesh and acts as a solid mounting surface for the vibratory mesh assembly. The plate is mounted within the structure on a 50° layback angle, similar to the setup found in small-scale testing.

Figure 122. Chamber with air-block plate CAD model.

Figure 123. Chamber with air-block plate Prototype.

4.3.1.4. Vibratory Mesh Assembly

While preliminary small-scale testing utilized a directly driven mesh, the full-scale prototype system focuses on harvesting and transferring machine-generated vibrations to the mesh. This necessary transference of vibration is noteworthy due to the potential ease of installation of this novel system onto existing mining equipment without requiring modifications. The implementation of machine-driven transference is applied through the vibratory mesh assembly. This assembly, shown in Figure 124 and Figure 125 consists of two separate sub-structures constrained using linear roller bearings.
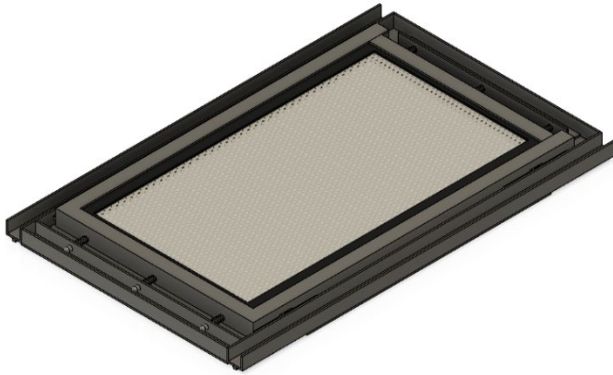

Figure 124. VMA CAD model.

Figure 125. VMA Prototype.

The driven panel, shown in Figure 126 and Figure 127, acts as the base of the vibratory mesh assembly of which all components are fastened. This panel attaches directly to the air-block plate through the use of four separate linear bearing carriages and rails and acts as the mounting interface between the chamber and shaker. These bearings allow for lateral movement of the assembly within the chamber with a maximum stroke of 1.00 inches. Another set of bearings and carriages are affixed to the upward portion of the driven panel for mounting of the mesh assembly.

Figure 126. Driven panel attached to air-block plate.

Figure 127. Air-block plate prototype.

The mesh panel assembly, shown in Figure 128, consists of the filter mesh, its accompanying mounting frame, and dampening springs. The mounting frame surrounds the mesh and is mechanically fastened to the driven panel through the secondary set of linear bearings. This dual-bearing design allows for independent range of motion from the chamber to the driven panel and from the driven panel to the mesh panel. A set of compression springs, mounted to the driven panel, act as hard mounts from the driven panel to the mesh panel. This set of springs maintains the range of motion of the assembly, within the stroke range of the driven panel, using the coil-bind of the spring as a hard-stop. Additionally, the springs will indirectly translate lateral driven movement, from the driven panel to the mesh panel, simulating machine harvested vibration.

The completed interior assembly, including the air-block plate and vibratory mesh assembly, provides adequate sealing with minimal bypass of coal-laden upstream air. Figure 129 shows the upstream section of the completed assembly. The design provides airflow over the full surface area of the mesh through the entire stroke of the shaker. As the assembly contains two positions of linear motion, low friction sealing surfaces were necessary to mitigate strain on the shaker. A slippery polyethylene, UHMW, was chosen for the sealing surfaces and was designed and installed between both linear assemblies.
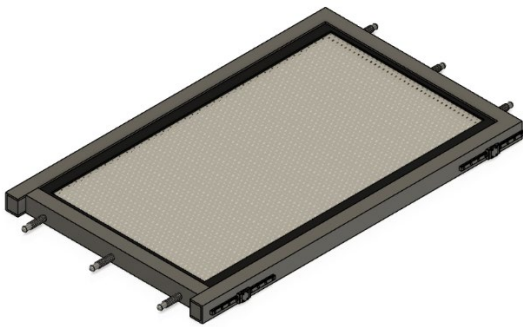

Figure 128. Mesh panel assembly.

Figure 129. Interior upstream assembly prototype.

Lastly, Figure 130 shows the opposing, downstream, side of the interior assembly. The vibratory mesh assembly and air-block plate are shown installed into the chamber body. This figure clearly displays the viewing windows surrounding the mesh that will aid in visual data collection during the testing phase at the NIOSH facility.

Figure 130. Interior downstream assembly prototype.

4.3.2.   Materials and Methods

4.3.2.1.   Test setup and Procedures

Testing of the prototype system was conducted at the NIOSH Dust Gallery using the systems and infrastructure in place. The experimental investigation studies the influence of various operating parameters (e.g., vibrational frequency, amplitude, mesh housing design, and mesh design) on dust capture and self-cleaning potential. The primary experimental trials were conducted with the standard fine coal dust blend that is used in the NIOSH dust gallery. The apparatus for testing included the standalone dust scrubber configuration, that includes several tunnel sections as well as a discharge fan, demister, water management system, and residual dust collection system (Figure 131). The Virginia Tech team supplied a single custom-built tunnel section that contains the vibrating mesh configuration (Figure 132) and a vibratory unit (Figure 133). The vibratory kit includes a dual-purpose platform shaker with power amplifier and a cooling package. The electrodynamic exciter is capable of imparting 489 N (110 lbf) pk sine force and 25.4 mm (1") pk-pk stroke.

Figure 131. Standalone dust scrubber unit at the NIOSH Dust Gallery.

Figure 132. a) Custom-built mesh housing section b) The vibrating mesh configuration supplied by the Virginia Tech team.
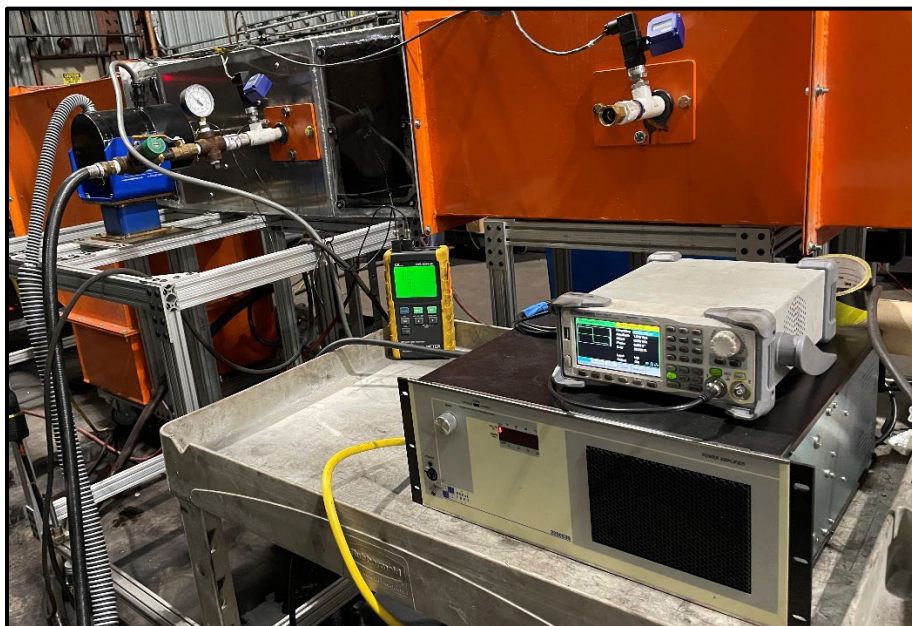

Figure 133. Shaker kit employed in the test.

The existing system was pretested to determine the operational and cleaning procedure for the filter and duct. Subsequent tests followed standard protocols and procedures for the dust scrubber system that have been developed by NIOSH. During each test, the fan, water sprays, mesh shaker, and dust feeding system (sequentially in that order) were initiated. Gravimetric sampling measurements were utilized using sample collection cassettes & vacuum pumps through the duration of the test (Figure 134). Pressure drops across mesh screen and demister and air velocity were measured using pressure gauge and pitot tube before introducing dust as well as throughout the duration of the test (Figure 135). The spent filters were cleaned using garden hose, the water sump was emptied when needed, and the system was prepared for a new run between tests (pre-test pressure drop was utilized as an indicator of cleanliness).

Figure 134. Upstream sampling configuration of the experiment.

Figure 135. Pressure monitoring station.

Similar to the bench-scale trials, the first block of experiments was designed using response surface methodology to empirically quantify the correlation between several independent variables and a response variable. To develop response surfaces, a 3-factor Box-Behnken-Design (BBD) was employed, and the experimental data was statistically analyzed. Surface plots were generated after data analysis. As dictated by the experimental program, 15 runs were conducted. 12 of the runs were performed using different combinations of the independent variables, and 3 repeated runs were performed at the test center point. Table 18 shows the factors associated with the independent variables. The experimental program was developed using Minitab software in order to set up a reliable regression model with the least amount of error at the end of the experiment. Analyzing the experimental results from 12 different combinations of the three independent variables and 3 repeated trials with only mid-level factors illustrates the significance of the operational factors in determining mesh screen dust collection performance.

Table 18. Experimental factors and range values for full-scale scrubber test.

Factors	Level		
	Low (-1)	Medium (0)	High (+1)
Spring rate (lbs/in)	10	103	-- (solid)
Amplifier gain (Vpp)	1	2	3
Frequency (Hz)	10	70	130

The constant parameters in the experimental setup are defined in Table 19. The duration of the test, dust feed rate/concentration in the duct, water flow rate, water spray nozzle pressure and the initial airflow rate were mainly determined by the capability of the facility's equipment capability. Test duration was determined as 25 minutes when the gravimetric sampling is employed to allow sampling cassettes to collect sufficient amount of dust concentration to evaluate the system efficiency.

Table 19. Fixed operating parameters for full-scale scrubber test.

Property	Unit	Values
Dust feed rate	g/min	250
Nozzle pressure	PSI	37
Dust composition	--	Grounded fine coal dust
Test duration (for gravimetric sampling)	Min	25
Fan speed	Hz	60
Mesh layering	--	30-layer

After the initial experimental program, three additional runs were conducted using the mid-values of the vibrational parameters, and different mesh screens with various layering, and three more runs were conducted with the same mesh screen layering configurations but with no vibration. The six additional tests were performed to compare vibrating and non-vibrating conditions under different mesh screen layering (Table 20). These tests were performed using the same fixed operating parameters as shown in Table 19.

Table 20. Post experimental program testing.

Run	Vibration conditions	Mesh layering
1	Vibration-free	10-layer
2	Vibrating mesh	10-layer
3	Vibration-free	20-layer
4	Vibrating mesh	20-layer
5	Vibration-free	30-layer
6	Vibrating mesh	30-layer

4.3.2.2. High Speed Video Analysis

During the latter stage of the testing campaign, highspeed video analysis was conducted in conjunction with the performance evaluation. The purpose of this effort was to characterize the particle-laden fluid flows in a mesh. One high-speed camera (Photron Nova S6), one LED light, as well as the attendant auxiliary equipment were utilized in the study. As shown in Figure 136, the camera was installed next to the wet scrubber with an added clear plastic window that allowed us to observe through it easily. Additionally, having a clear top window enabled us to place an LED light above it so we could illuminate the mesh better during our experiments.
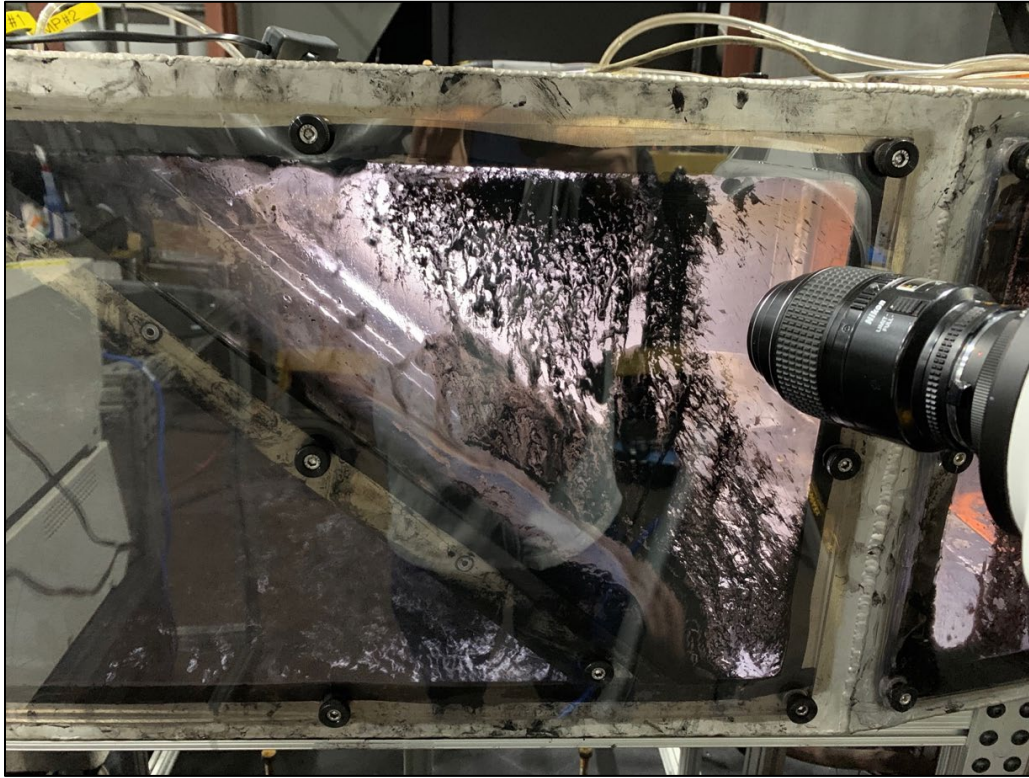
Figure 136. Experimental setup of a wet scrubber with a high-speed camera. (See the video https://youtube.com/shorts/v87fcB_IWcU)

The high-speed camera was placed close enough by the side window which let us capture coal-laden water droplets coming off from the mesh quickly and accurately without any obstruction or difficulty thanks to two windows allowing observation as well as illumination at the same time. This setup gave us full control over our observations while also providing detailed images of particles flying off from meshes which would be impossible otherwise without such precise placement and use of tools available on site like cameras, lights etc.

4.3.3.   Results and Discussion

4.3.3.1.   Vibrational Parameter Optimization

The tests carried out in the dust gallery of the NIOSH facility consist of two primary campaigns. In the first part, the experimental design was applied and 15 tests were carried out with different variations of the previously determined variables shown above. Throughout the test, data was collected via gravimetric sampling, real time dust concentration monitoring with DustTrak, real time optical particle size analysis with APS, analog air velocity monitoring, analog pressure drop across the screen and demister, and analog velocity pressure monitoring of the downstream air. Response surface plots were created with the obtained results and are shown in Figure 137 through Figure 139. Each figure shows the effect of two different variables on response by keeping one of the three variables used during the experiment constant.
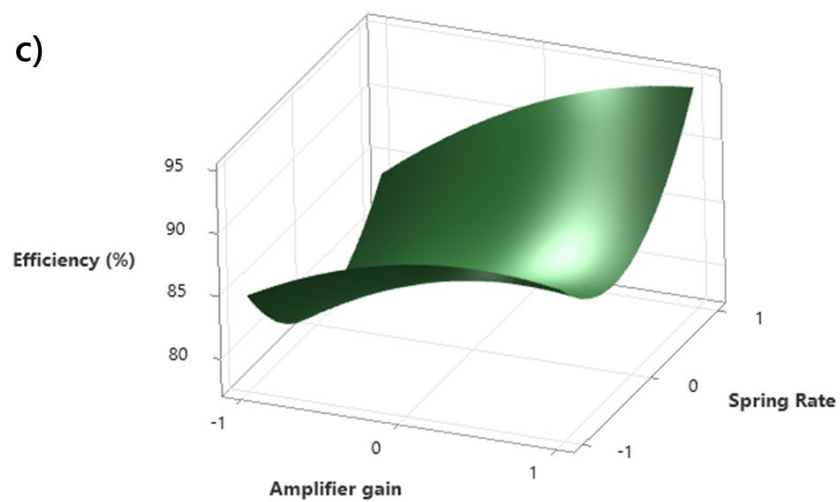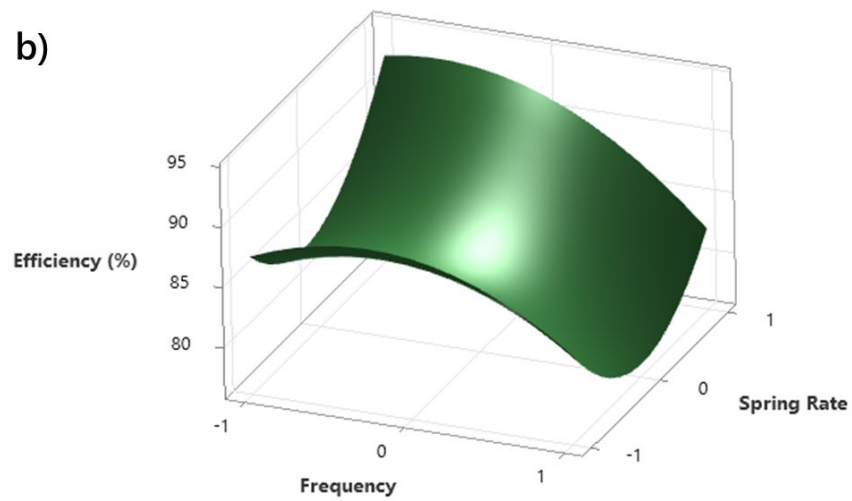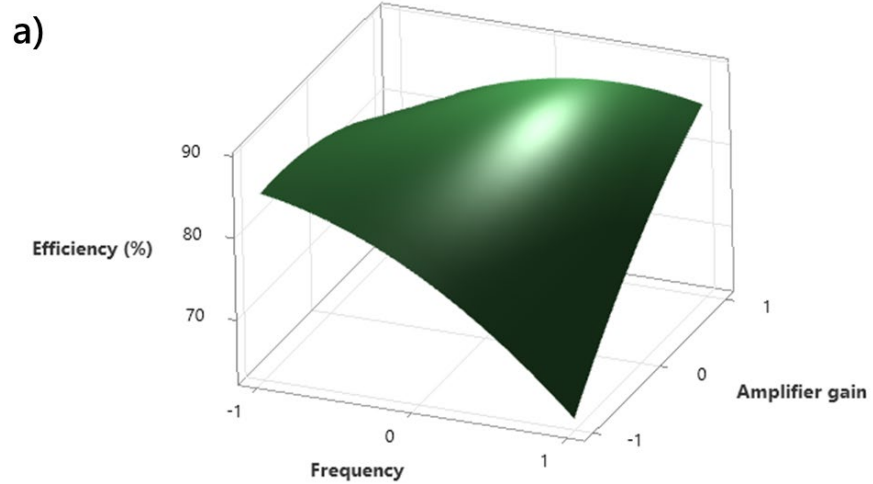
Figure 137. Surface Plots of Collection Efficiency (%) vs a) Amplifier gain and frequency, b) Spring rate and frequency, c) Spring rate and amplifier gain.
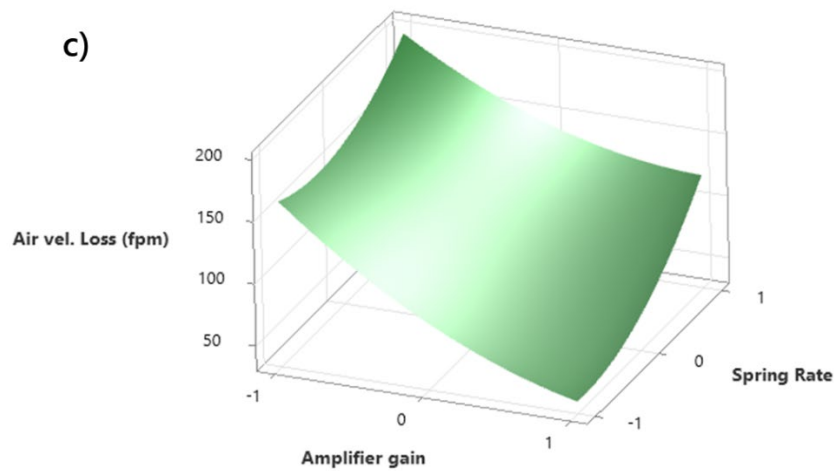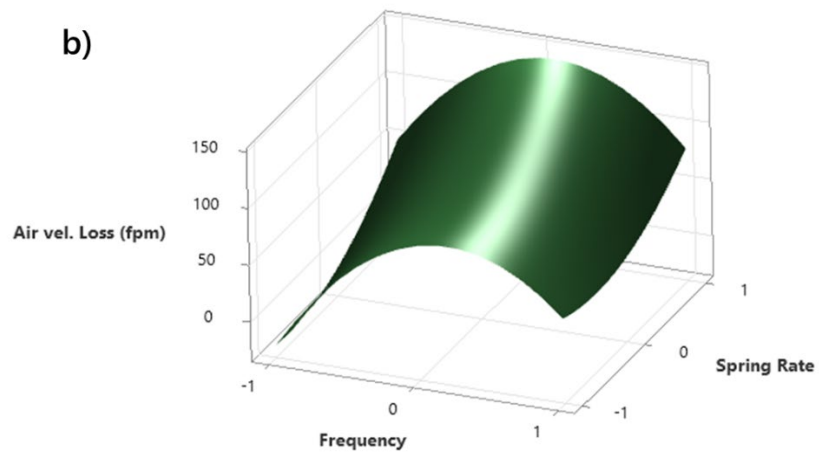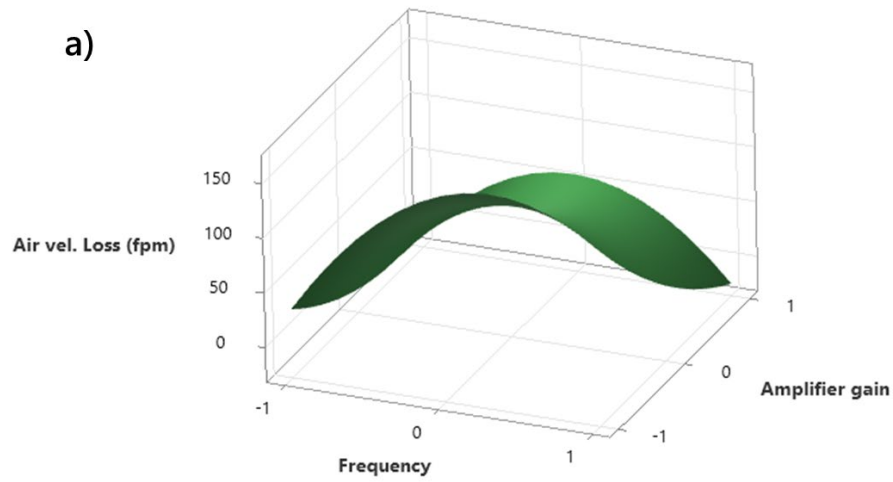
Figure 138. Surface Plots of Upstream Airflow Loss (fpm) vs a) Amplifier gain and frequency, b) Spring rate and frequency, c) Spring rate and amplifier gain.
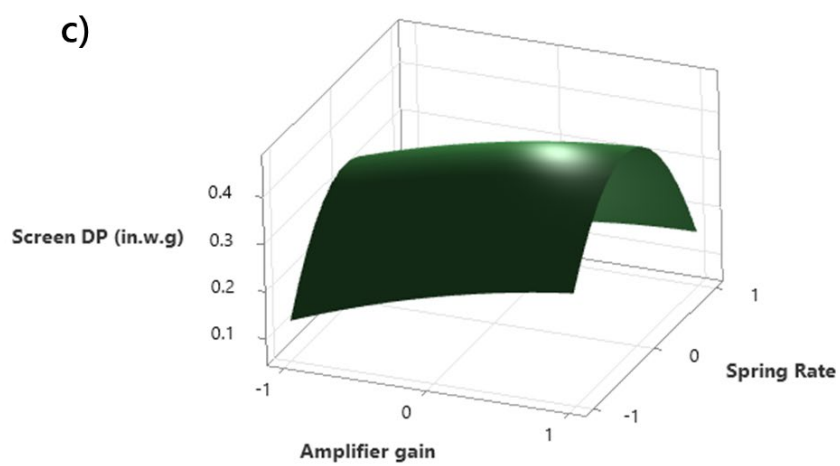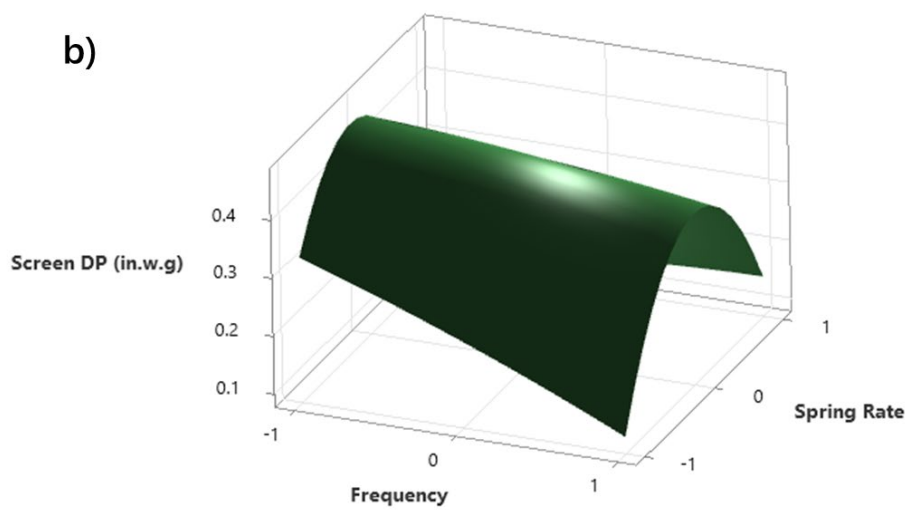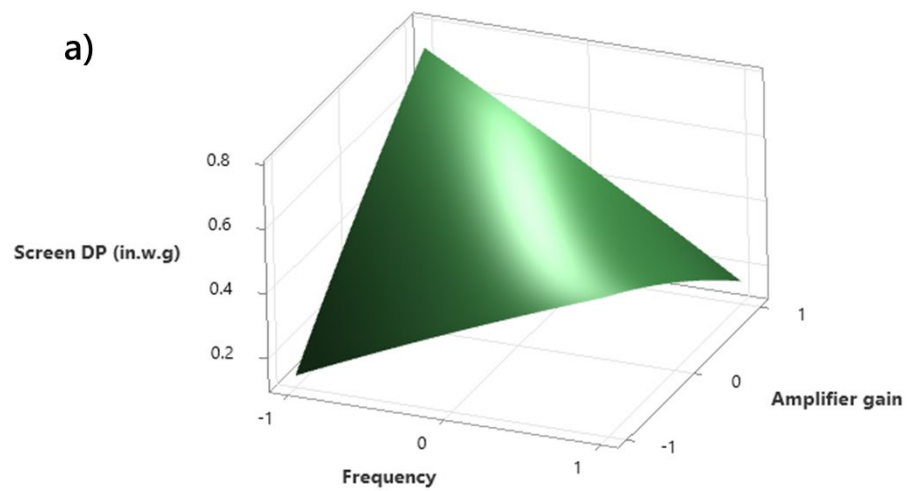
Figure 139. Surface plots of pressure drop across the mesh screen (in.w.g) vs a) Amplifier gain and frequency, b) Spring rate and frequency, c) Spring rate and amplifier gain.

The collection efficiency surface (Figure 137) was plotted from the data obtained with the gravimetric sampling. Dust concentration data were obtained in real time with DustTrak and APS; however, they were not used in the analysis due to their inconsistency and calibration issues that were noted during testing. In Figure 137a, the effect of the interaction of the amplifier gain with the frequency on the efficiency is examined. The highest efficiencies (over 85%) were obtained when the frequency values were at medium and above, and at the same time the amplifier gain values were at the highest. The effect of the interaction of the spring constant with the frequency on the efficiency shown examined in Figure 137b. The highest efficiency values (over 92%) were obtained when the spring constant is at the highest and the frequency is close to the medium value. However, it is worth noting that the collection efficiencies approaching 90% under the conditions where the spring constant is at its lowest and the frequency is close to the medium values. As observed in Figure 137a and Figure 137c, the spring constant does not impart a significant difference in efficiency, especially under low amplifier gain conditions. In addition, higher efficiency was always achieved under test conditions with the highest application gain.

When taken together, the highest efficiency values were obtained when the frequency is at its medium value (70 Hz), the amplifier gain is at the highest (3 Vpp), and the spring constant is also at the highest (solid spacer). It should be noted, though that the effect of the spring constant used on the prototype screen will not exhibit the same behavior as the spring constant to be used in the real mine unit. We believe that the spring constant will need to be reoptimized in an operational prototype, and it is likely that a lower spring constant value will produce the desired results. Our laboratory tests have shown that this lower spring constant configuration can move the screen independently and consistently from the outer frame. The slow-motion video of this movement can be found at the following link: (https://youtu.be/LRqoMVhpKoM)

In Figure 138, the effects of the binary interactions of the variables used in the test on the air velocity lost during the test were examined. In
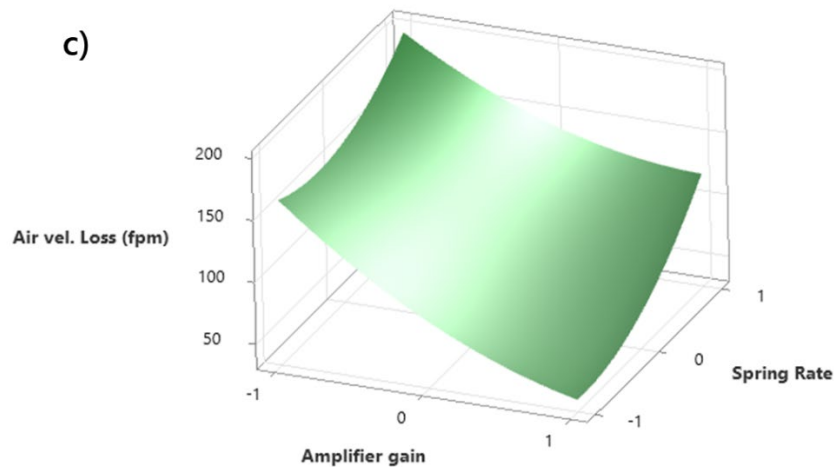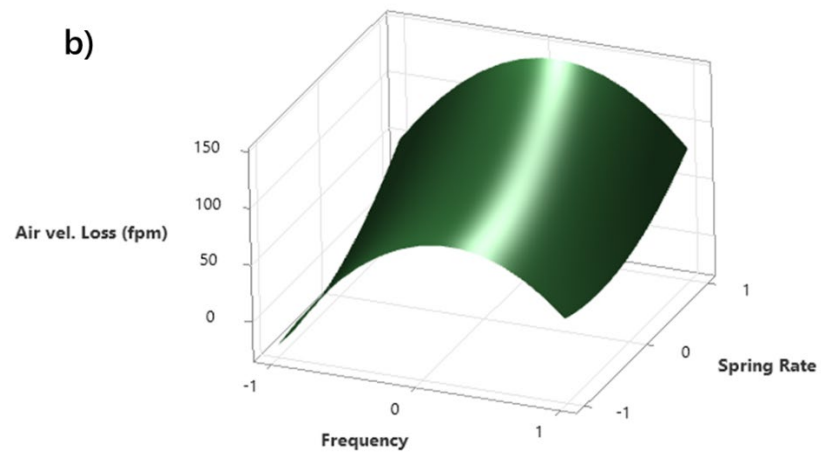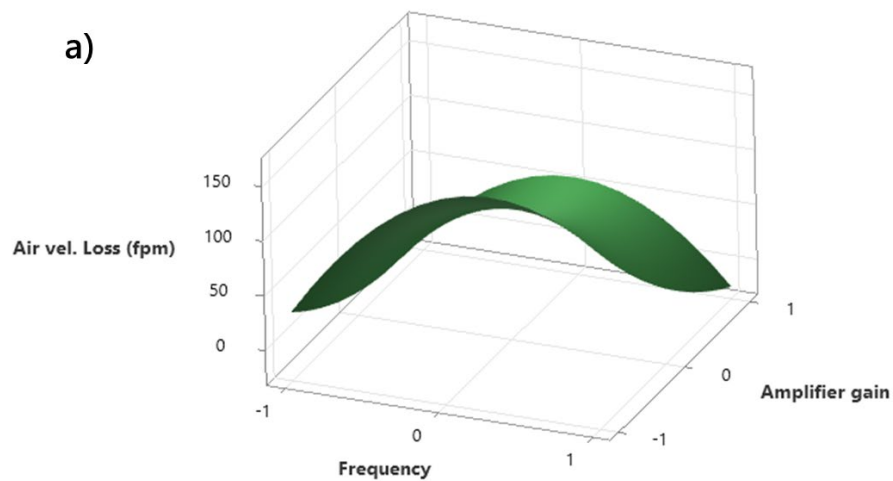

a)

b)

c)
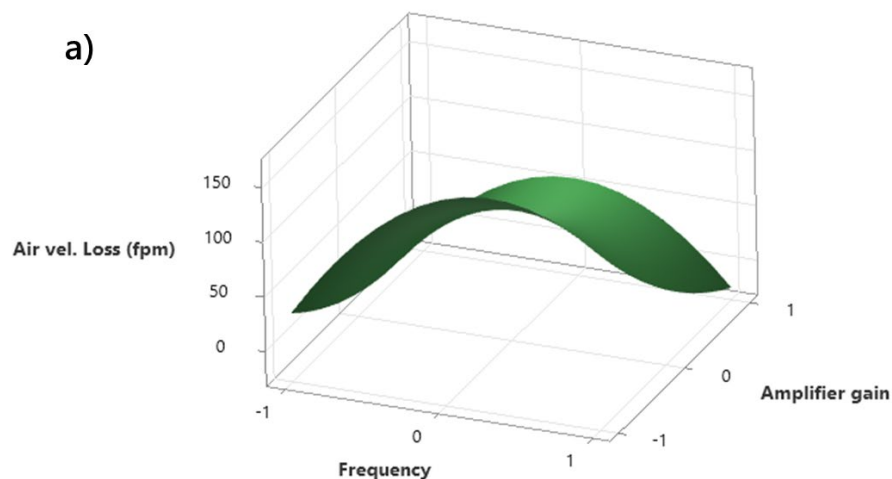
Figure 138a, where the effect of amplifier gain and frequency pair on air velocity loss is examined, it can be seen that the air velocity loss is most pronounced when the amplifier gain value is at its least (1 Vpp) and the frequency values are close to the medium values (70 Hz). As shown in
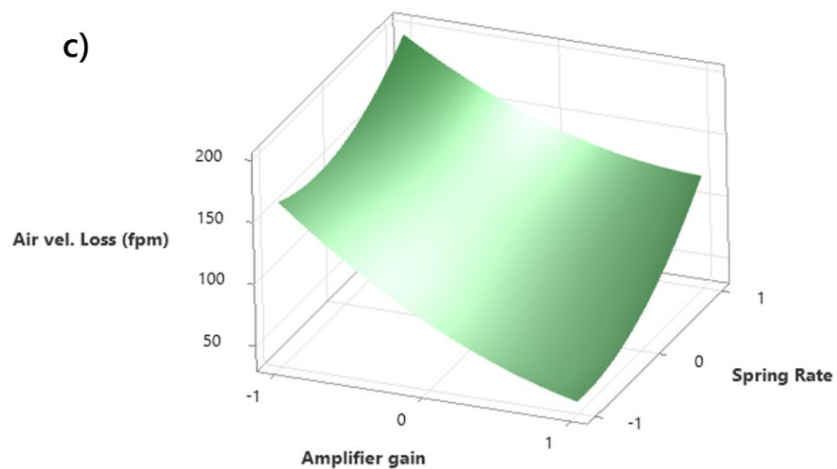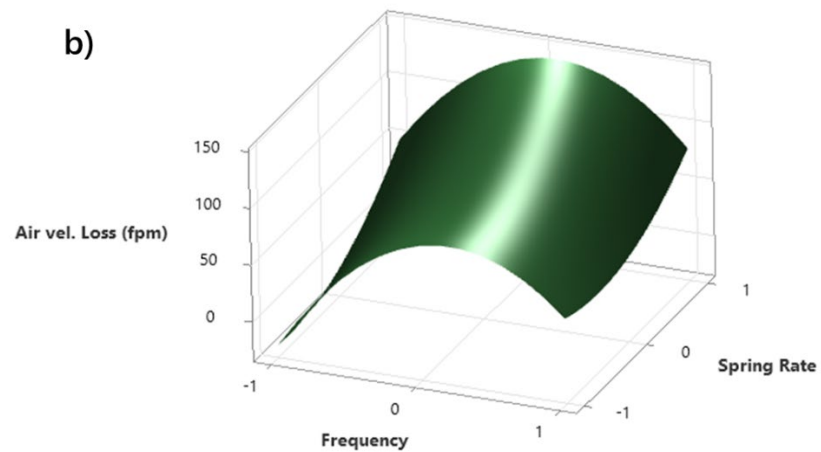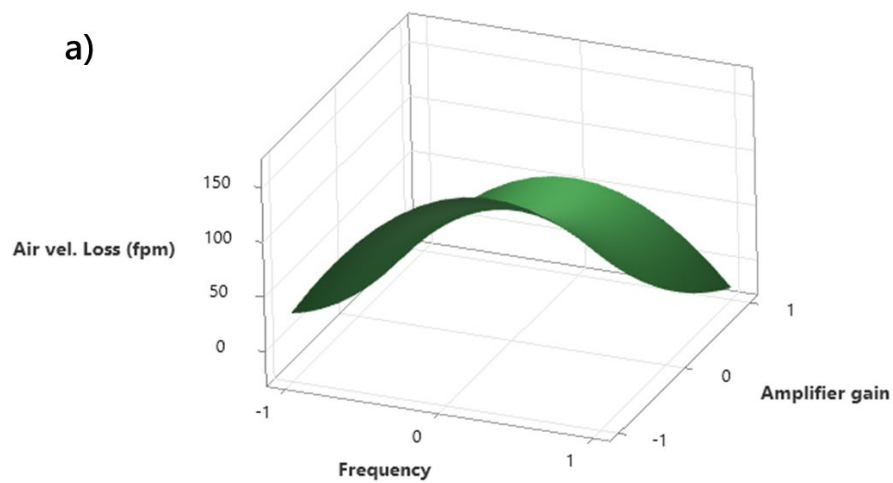

a)

b)

c)

Figure 138b, the air velocity loss reaches its highest (over 140 fpm) values where the spring constant is at its highest and the frequency is at its medium values. Lastly, it can be seen in

a)

b)

c)
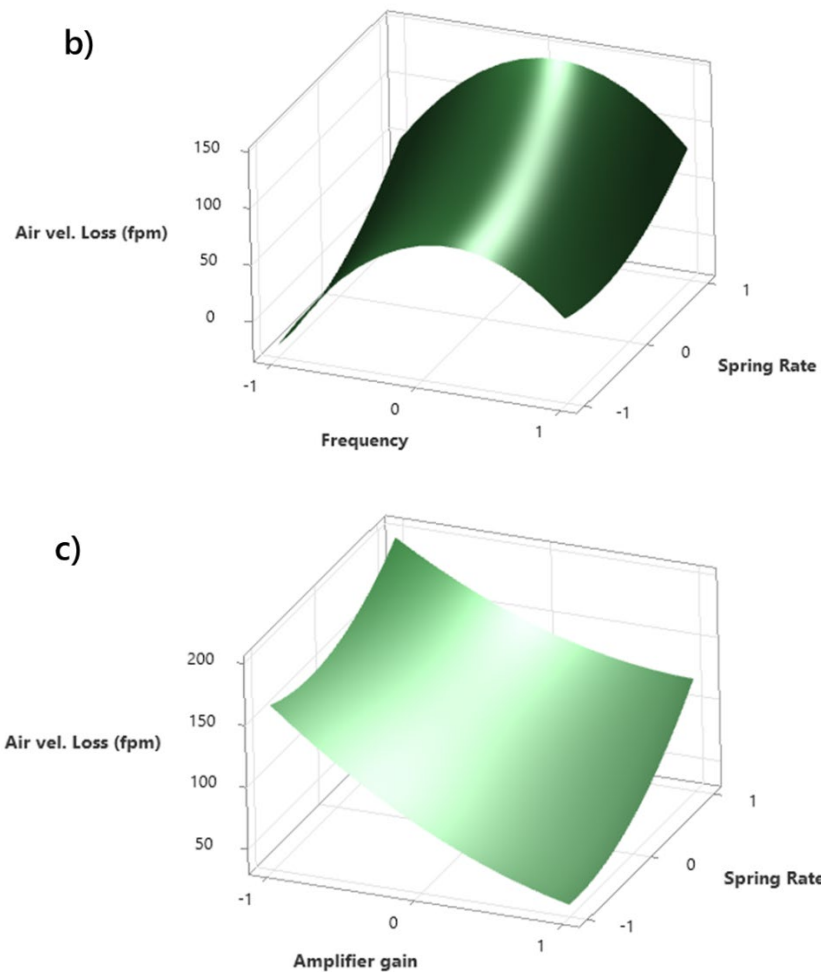
Figure 138c that the amplifier gain is inversely proportional to the spring constant, but in an almost exact linear relationship. Accordingly, it has been observed that the air velocity loss is the most significant (over 175 fpm) when the amplifier gain is at its least and the spring constant is at its highest. When taken together, the data show that the air velocity loss can be optimized when the amplifier gain values are at the highest, the spring constant value is at the lowest and the frequency is between medium and highest values. In addition to all these, when the air velocity pressure data in the downstream was examined, no significant change was found in any condition. Air velocity pressure drop at downstream close to fan were generally negligible throughout the test.

Lastly, Figure 139 shows the effect of the binary interactions of the variables used in the experimental design on the pressure drops across the screen. As shown in Figure 139a, the interaction of frequency and amplifier gain does not have any significant effect on the increase in pressure drops across the screen. For example, in cases where there is high frequency and high amplifier gain, the lowest screen pressure drop is observed, whereas the lowest pressure drop values are also obtained at the lowest frequency value and the lowest amplifier gain. Therefore, it can be said that these two do not have a consistent effect on the related response. In addition, as shown in the Figure 139b, the most significant increases in the pressure drop across the screen (over 0.4 in.w.g) are observed in cases where the frequency value is between its medium and low and the spring constant is close to its medium value. Similarly, Figure 139c shows that when the amplifier gain value is between its medium and high and the spring constant is close to its medium value, the most significant increases in pressure drop across the screen are observed (over 0.4 in.w.g).

In addition, when the pressure drop data across the demister is examined, the data show that there is almost no increase in pressure drop in most conditions. There are even increases in the total pressure difference due to the location where the demister outlet is closest to the fan. The data show that the variables used in the experiment design do not have any significant effect on the pressure differences across the demister.

When taken together, the data indicate that the pressure drop is optimized when the spring constant is at its medium, the frequency value is between the medium and low range, and the amplifier gain is between its medium and high range.

4.3.3.2.   Influence of Mesh Density and Vibration

The second part of the tests carried out at the NIOSH facility with the full-size prototype consists of six tests with mesh screens with different steel mesh layers. These tests include vibrating and non-vibrating conditions of those mesh screen variations. The response parameters examined are the same with those examined in part 1 tests including the collection efficiency, the change in the air velocity at the system inlet during the test, and the pressure drops on the screen during the test (Figure 140, Figure 141, and Figure 142).

As shown in Figure 140, collection efficiency in the vibrating condition decreased only in the test with the 20-layer screen, however, the collection efficiency increased in the tests with the 10-layer and 30-layer screens. The effect of the difference between vibrating and non-vibrating conditions on the collection efficiency was most evident in the test with a 30-layer filter (32% increase). The collection efficiency was highest (94%) when tested with a 20-layer screen in vibration-free conditions. In addition, the test with the lowest efficiency was the test performed with a 30-layer screen in vibration-free conditions (68%). Comparing the 3 different screen types, although the highest efficiency was obtained in the vibration-free test with the 20-layer screen, it is worth noting that vibration increased the dust collection efficiency of the system in both tests using 10-layer (from 87% to 89%) and 30-layer (from 68% to 90%) screens.
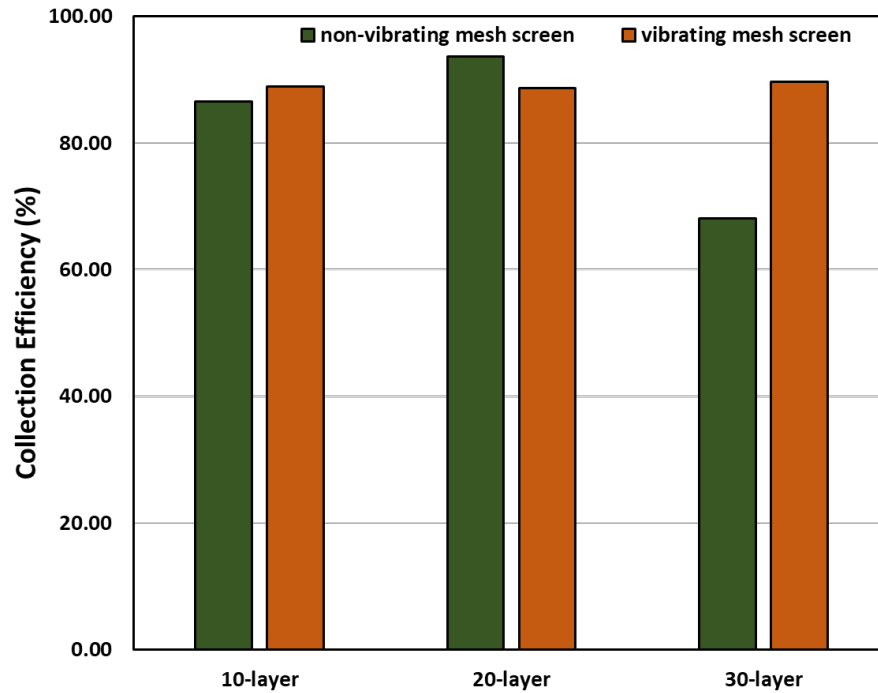
Figure 140. Collection efficiency by different mesh screen packages with various filter layering under vibrating and non-vibrating operational modes.

In Figure 141, the initial and final air velocity changes of the tests carried out in vibrating and non-vibrating conditions with screens with different steel mesh layer densities are given. Accordingly, in the 10-layer and 30-layer tests, significant air velocity losses were observed in the system (over 100 fpm), while no significant air velocity loss was observed in the tests performed with the 20-layer screen. It should be noted that the air velocity loss was greater in the tests with the vibrating 10-layer screen, and much greater in the tests with the non-vibrating 30-layer screen. These results are inconsistent and suggest that further testing and analysis of the measurement system may be needed to discern the implications of the findings.
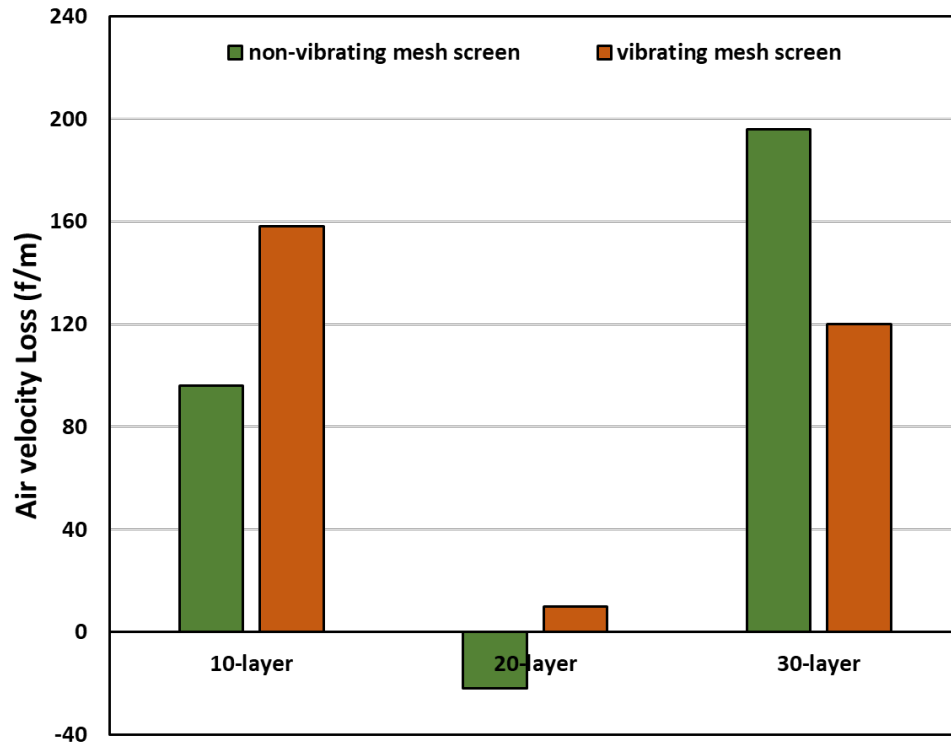
Figure 141. Upstream section airflow loss by different mesh screen packages with various filter layering under vibrating and non-vibrating operational modes.

Figure 142 shows the difference in the pressure drop detected across the screen during the tests performed. In tests with the 10-layer screen, the pressure drop decreases both in vibrating and non-vibrating conditions. It is considered that this may be due to the high air velocity upstream of the 10-layer screen. On the other hand, in the tests performed with 20- and 30-layer screens pressure drop increased throughout the tests. Less pressure drop increases were detected in the tests performed under vibrating conditions with both screen types. This finding is supporting that the presence of vibration increases the self-cleaning capacity of the screen compared to the vibration-free state.
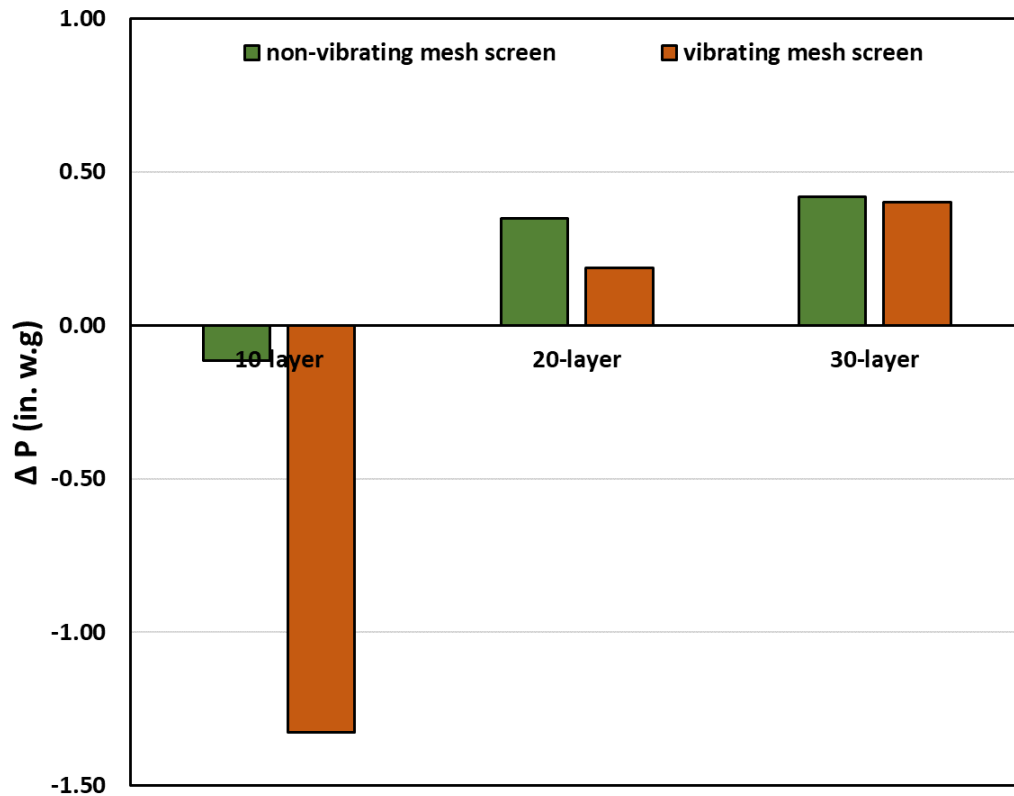
Figure 142. Pressure drops across the mesh screen by different mesh screen packages with various filter layering under vibrating and non-vibrating operational modes.

When the findings of the first and second parts of the experiments with the full-size prototype are combined, it can be said that the vibration-enhanced systems using 20 or less dense layered screens will positively affect the overall efficiency of the flooded bed dust scrubber. However, the tests performed in the NIOSH facility with the 10-layer mesh screen showed that regardless of vibrating condition there could be some waterflow passing the demister and going through the fan. This could damage the fan and affect the correct data generating process. In order to eliminate this issue in the tests with 10-layer screen, either water flow rate or airflow rate can be decreased. If the air and water flow rates are wanted to be kept at their current values, the design of the demister could be modified as a more sophisticated solution.

4.3.3.3. Highspeed Video Analysis

Figure 143 shows the analysis of the highspeed video collected from one of our tests. All videos are available on YouTube (https://youtu.be/z_ze04aldZY https://youtu.be/uFQNkU2AA-c https://youtube.com/shorts/dE5URSP1dJY?feature=share). In our experiment, we were able to observe both clean water droplets and coal-laden droplets coming off from the mesh. The frequency of coal-laden droplets was less than that of pure water ones. Additionally, the velocity of coal-laden droplets was slower than that of pure water due to their increased specific density caused by the presence of coal particles in them. As a result, this led to a lower angle trajectory for these heavier drops as they fell down under gravity more compared with clean water ones.

The size distribution of coal-laden droplets from the wet scrubber was observed to be slightly smaller than the water droplets. This phenomenon is explained by the concept of surface tension, which determines how much energy it takes for liquids to form into spherical shapes before they are expelled as droplets. In presence of coal particles in fluids, the surface tension gets lower and hence results in shorter capillary length and subsequently smaller ejected drop sizes. The lower surface tension does not have a significant impact on size distribution here since we saw slight decrease in drop sizes compared with pure water ones, which can also be explained by the surface tension change.
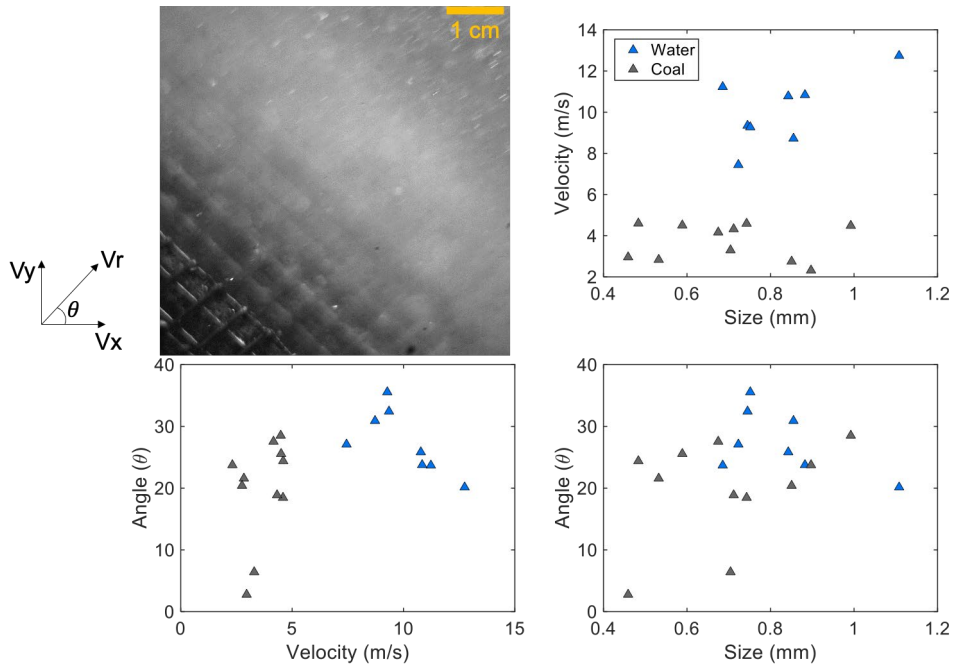

Figure 143. The left-top panel of the wet scrubber shows a snapshot of the droplets off. The right-top graph illustrates velocity versus size of droplets, with water droplets in light blue and coal-laden particles represented by gray color. The bottom two graphs a are ejection angle versus velocity (left) and ejection angle versus size (right).

Figure 144 shows the data collected from a series of experiments conducted to measure the speed of coal-laden droplets and water droplets. The legend represents different video names, with the last letter indicating whether it is a coal-laden or water droplet. As expected, our data showed that coal-laden particles had lower speeds than pure water particles under similar conditions; this explains why we saw so many dense concentrations of coal just after passing through the wet scrubber. The results suggest that having a drainage system directly after leaving the wet scrubber would be beneficial in collecting all these heavy particles before they can cause any damage to other parts of duct system downstream. This could help protect against corrosion and clogging due to large amounts of particulate matter being released into other areas where it may not be desired or safe for them to accumulate too heavily over time.
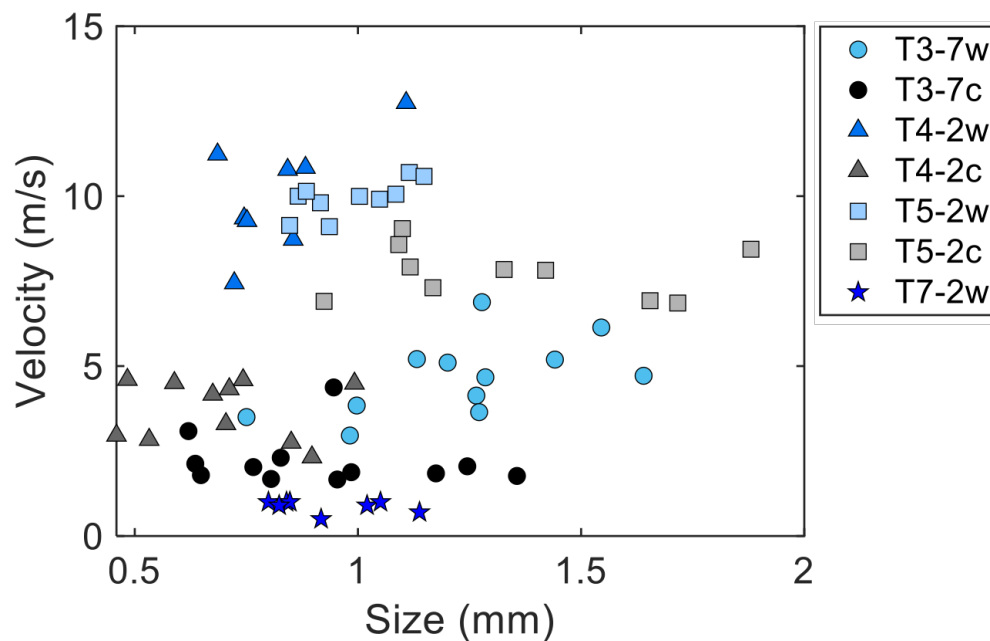

Figure 144. Velocity vs size of droplets from a wet scrubber. We have four high-speed videos at different conditions. The last letter represents either coal-laden droplets "c" or pure water droplets "w".

5. Technology Capability Assessment and Readiness Assessment

The results of the laboratory and prototype testing campaigns have confirmed that the vibrating mesh system can improve operational outcomes over that of a static mesh system, and fundamental modeling efforts have provided insight into particle clogging within porous mesh materials.   The final test prototype integrated several design features derived from the fundamental testing, notably including the use of a hydrophilic mesh and the use of a flexible housing to translate external vibration. Based on the work of this project, the vibrating mesh technology has matured to TRL 6, *prototype validated in a relevant environment*. To achieve TRL 7, *fully integrated prototype validated an operational system*, a mine worthy system must be designed and rigorously tested using either a retrofit or custom built add on to a continuous miner. Successful demonstration of a mine worthy unit would facilitate broader commercialization within the industry.

Based on the current study data, project constraints, and overall lessons learned, the project team recommends these post-project activities:

- Additional in-mine vibrational studies should be conducted to better understand the variability of the characteristic vibrational frequencies as a function of the following variables: continuous miner machine, mining height, geologic factors, operator factors, and others. The current project has provided a robust methodology for data collection and analysis that can be easily repeated in a longitudinal study.
- Additional modeling efforts should seek to improve the fidelity and predictive capacity of the multi-physics modeling. Due to computational constraints, the models used in this study were often simplified with respect to geometry, scale, time, phase, and other parameters. The development of properly validated surrogate models for specific mechanisms (e.g. mesh clogging) may support more detailed simulations, which will in turn hasten commercial design, scale-up, and deployment.
- The energy harvesting system should be evaluated in an operating mine environment. For the current project, most of the major design components were fully integrated into the test prototype; however, owing to practicality constraints, the vibration was still supplied by a unidirectional external source with a fixed frequency and amplitude. Nevertheless, this project has supplied the data and the approach needed to properly select the spring constant for the elastic housing, namely a spring constant such that the natural frequency is higher than the viable frequency range inside the mine. Data from our in mine survey and multi-physics modeling can be used a first approximation, which can in turn be adapted to site-specific criteria.
- Future testing of the dust scrubber should be conducted with a hydrophilic mesh that has been subject to the heat treatment process developed in this project.   Prolonged stress testing should be conducted to determine durability of this treatment.
- Based on high-speed visualizations, future iterations of the scrubber system should include a drainage system after the wet scrubber but prior to the demister to effectively remove heavier particles. This adaptation may reduce damage to downstream parts of the duct system and protect against corrosion and clogging.
- In the next phase of testing, several construction materials/design approaches for the elastic housing should be evaluated to determine the most operationally robust and cost-effective option.
- In the next phase of testing, results should not only focus on the factors local to the continuous miner (e.g. dust capture, pressure drop), but also on the global factors at the mining face and throughout the mine environment. While most scrubber testing is conducted with a standalone unit, more information is needed to determine how these results will be translated to overall dust mitigation system performance.

6. Publication Record and Dissemination Efforts

6.1. Published/Presented

1. Amini, S. H., Schaefer, M.*, Jung, S., Pan, L., Szczap, J.*, Shahab, S, Noble, A, Lu, Z., Shigo, M.*, Uluer, E.*, "Development and testing of a novel vibrating mesh dust scrubber technology", 2023 Society of Mining, Metallurgy & Exploration Annual Meeting and Exhibit, Denver, CO.

2. Amini, S. H., Sadeghi, O.*, Uluer, E.*, Pan, L., Shahab, S., Jung, S., Noble, A., "Novel vibrating mesh design for the wet flooded-bed scrubber: system design and bench-scale experiments", 2021 Society of Mining, Metallurgy & Exploration Annual Meeting and Exhibit, Virtual Conference.

3. Lu, Z.*, Rath, A.*, Amini, S. H., Noble, A., Shahab, S., "A computational fluid dynamics investigation of a novel flooded-bed dust scrubber with vibrating mesh", International Journal of Mining Science and Technology 32(3). 2022: 525-537.

4. Szczap, J. , Pan,L. "Prevention of Clogging of the Flooded-Bed Scrubbers with Filter Surface Modification",2023 Society of Mining, Metallurgy & Exploration Annual Meeting and Exhibit, Denver, CO.

6.2. Pending as of Report Date

1. Nawaz Janjua, A.*, Shaefer, M.*, Amini, S. H., Noble, A., Shahab, S., "Vibration Energy Harvesting in Underground Continuous Mining: Dynamic Characteristics and Experimental Research of Field Data", {Submitted to Applied Energy}

2. Szczap, J. ,Jung, S., Pan,L. "Understanding the Microscopic Mechanism of Clogging of both Fibrous and Mesh Filters in Flooded-bed Wet Scrubbers Using Experimental Approaches and Modeling"{Submitted to FUEL}

3. Szczap, J,Pan . "Understanding Interfacial Interactions in Filter Clogging of Flooded bed Scrubbers using Experimental Approach and Modelling" {Submitting to Powder Technology}

4. Uluer, M.E., Shigo, M., Amini, S. H., Noble, A., "An Exploratory Investigation on the Effectiveness of a Novel Vibration-Enhanced Flooded Bed Dust Scrubber" {Submitting to Mining, Metallurgy & Exploration}

5. Uluer, M.E., Noble, A., "Influence of Mesh Design and Surface Treatments on Particle Transport and Fate" {Submitting to Mining, Metallurgy & Exploration}

7. References

1. Arya, S. N. (2018). Investigation of the effectiveness of an integrated flooded-bed dust scrubber on a longwall shearer through laboratory testing and CFD simulation. Ph.D. Dissertation, University of Kentucky.

2. Arya, S., & Novak, T. (2020). Numerical investigation of the effect of a novel wet scrubber on dust reduction in an underground coal mine. *Mining, Metallurgy & Exploration*, 37(1), 129-139.

3. Bilad, M. R., Discart, V., Vandamme, D., Foubert, I., Muylaert, K., & Vankelecom, I. F. (2013). Harvesting microalgal biomass using a magnetically induced membrane vibration (MMV) system: filtration performance and energy consumption. Bioresource technology, 138, 329-338.

4. Colinet, J. (1990). Laboratory evaluation of quartz dust capture of irrigated-filter collection systems for continuous miners (Vol. 9313). Washington, DC: Bureau of Mines, US Department of the Interior.

5. Colinet, J. F., & Jankowski, R. A. (2000). Silica collection concerns when using flooded-bed scrubbers. *Mining Engineering* (Littleton, Colorado), 52(4):49-54.

6. Colinet, J., Reed, W. R., & Potts, J. D. (2013). Impact on respirable dust levels when operating a flooded-bed scrubber in 20-foot cuts.

7. Coster, H. G. L., Farahani, T. D., & Chilcott, T. C. (2011). Production and characterization of piezo-electric membranes. *Desalination*, *283*, 52-57.

8. Fuchs, E.P. (1979). "Coal Mining Equipment Vibration Data Report," Donaldson Company, Inc.

9. Genkin, G., Waite, T. D., Fane, A. G., & Chang, S. (2006). The effect of vibration and coagulant addition on the filtration performance of submerged hollow fibre membranes. *Journal of membrane science*, *281*(1-2), 726-734.

10. Kim, S. C., Wang, H., Imagawa, M., Chen, D. R., & Pui, D. Y. (2006). Experimental and modeling studies of the stream-wise filter vibration effect on the filtration efficiency. *Aerosol science and technology*, 40(6), 389-395.

11. Kumar, A.R. (2015). "Computational Fluid Dynamics (CFD) Modeling and Validation of Dust Capture By a Novel Flooded Bed Dust Scrubber Incorporated Into a Longwall Shearer Operating in a US Coal Seam." pp. 1–98, M.S. Thesis, University of Kentucky.

12. Kumar, A. R., Gupta, N., & Schafrik, S. (2022). CFD modeling and laboratory studies of dust cleaning efficacy of an efficient four stage non-clogging impingement filter for flooded-bed dust scrubbers. *International Journal of Coal Science & Technology*, 9(1), 16.

13. NIOSH (2002) Exposure to Silica Dust on Continuous Mining Operations Using Flooded-Bed Scrubbers, *Applied Occupational and Environmental Hygiene*, 17:5, 322-323, DOI: 10.1080/10473220252864888.

14. NIOSH (2010). Information circular 9517. Best practices for dust control in coal mining. Morgantown, WV: U.S. Department of Health and Human Services, Centers for Disease Control and Prevention, National Institute for Occupational Safety and Health, DHHS (NIOSH) Publication No. 2010-110.

15. Pan, L., Golden, S., Assemi, S., Sime, M. F., Wang, X., Gao, Y., & Miller, J. (2021). Characterization of particle size and composition of respirable coal mine dust. *Minerals*, 11(3), 276.

16. Ren, T., Wang, Z., & Cooper, G. (2014). CFD modelling of ventilation and dust flow behavior above an underground bin and the design of an innovative dust mitigation system. *Tunneling and Underground Space Technology*, 41, 241-254.

17. Richard, D.E. "Scrubber Filter." U.S. Patent No. 4,787,920. 29 Nov 1988.

18. Schafrik, Steven J., Ashish Ranjan Kumar, and Allison Taylor. "Efficient non-clogging inertial vortex type particle scrubber." U.S. Patent No. 11,338,232. 24 May 2022.

19. Wang, X., Yuan, S., Li, X., & Jiang, B. (2019). Synergistic effect of surfactant compounding on improving dust suppression in a coal mine in Erdos, China. *Powder Technology*, 344, 561-569.

20. Wedding, W. C., Novak, T., Arya, S., & Kumar, A. (2015). CFD modeling of a flooded-bed scrubber concept for a longwall shearer operating in a US coal seam. In Proceedings of the 15th North American Mine Ventilation Symposium, Blacksburg, VA, USA (pp. 20-25).

21. Yang, X., Wang, H., & Chase, G. G. (2015). Performance of hydrophilic glass fiber media to separate dispersed water drops from ultra low sulfur diesel supplemented by vibrations. *Separation and Purification Technology*, 156, 665-672.

22. Yao, R., Jiang, G., Li, W., Deng, T., & Zhang, H. (2014). Effect of water-based drilling fluid components on filter cake structure. *Powder Technology*, 262, 51-61.